University of Technology, Sydney

Faculty of Science

A STUDY OF THIN-FOIL ROLLING AND THE DEVELOPMENT OF AN Al-Fe-Mn-Si LIGHT GAUGE FOIL ALLOY

Part 2

Course: N054 Doctorate in Science – (by Thesis)

Author: Matthew Mansell

Supervisor: Dr. Greg Heness

2007

CERTIFICATE OF AUTHORSHIP/ORIGINALITY

I certify that the work presented in this thesis has not previously been submitted for a degree nor has it been submitted as part of requirements for a degree except as fully acknowledged within the text.

I also certify that the thesis has been written by me. Any help that I have received in my research work and the preparation of the thesis itself has been acknowledged. In addition, I certify that all information sources and literature used are indicated in the thesis.

Signature of Candidate

Production Note:
Signature removed prior to publication.

14th December 2006.

CONTENTS

LIST OF FIGURES

LIST OF TABLES

CHAPTER 8 DEVELOPMENT OF AN EXPERIMENTAL PLAN

Aluminium foil is processed via seven major steps from ingot casting to final gauge saleable product. The first is direct chill or DC casting of rolling ingots. As the metal cools, alloying elements accumulate in the liquid phase until the equilibrium concentration is reached. Nucleation of a given phase can occur resulting in second-phase particles solidifying between dendrites as thin-fingered platelets.

During the second stage, homogenisation, the ingots are soaked at elevated temperatures for a specified time. This promotes dynamic recrystallisation during the hot rolling stage, while allowing diffusion at the particle-matrix interface. This allows precipitates to redistribute thereby reducing the interface area between phases and hence interfacial energy.

The next three stages in foil production are hot rolling, cold rolling and foil rolling. During hot rolling, deformation energy build-up coupled with particle stimulated nucleation increase the metal's tendency to recrystallise as the ingot thickness is reduced from 530mm to 18mm using between 15-30mm reductions per pass. At the lower end of the temperature spectrum for hot rolling, the strip is reduced from 18mm to 3mm in three passes at approximately 50% reduction.

The cold and foil rolling stages involve rolling the metal at lower temperatures to induce matrix deformation without subsequent dynamic recrystallisation and recovery. Matrix deformation increases flow stresses that fracture the intermetallic particles that have formed and is dependent on the initial microstructure as determined by the composition and casting/homogenisation conditions. The final two processes are the final separation and slitting finishing operations, followed by a final anneal to O-temper. The final annealing conditions and associated microstructural changes coupled with constituent particle break-up during the rolling operations are the crux in determining the final properties of thin-film foil products.

The Aluminium Foil Industry is relatively young, with limited published technical information on most thin-foil processing principles. Experimental work for this thesis is designed in three stages;

1. The first is to address the fundamental principles that are necessary to understand thin-foil processing, ranging from alloy development through to annealing to an extent never before published. These Chapters are integrated into the ALCOA Metallurgical Database for Foil Rolling and are located in Chapters 1 to 5.

2. The second is to establish benchmarks and optimise critical roll process variables, Chapters 6 and 7.

3. The third is to investigate the surface characteristics and microstructural evolution of alloy 8150. The focus is on the strengthening mechanisms that occur during cold and foil rolling and annealing of this near-eutectic alloy, Chapters 8 to 10. This alloy demonstrates high mechanical properties without sacrificing ductility for thin foil alloys, and was developed and registered by the author.

Literature Survey - Fundamental Principals:

- Chapter One analysed the current domestic and world supply revealing that Australia is in a vulnerable market, with AARP (ALCOA Australia Rolled Products) being the only domestic manufacturer of foil products.

- Chapter Two discussed aluminium and aluminium alloy development for thin foil alloys, concentrating on the 1XXX and 8XXX series. A discussion on strengthening mechanisms was also incorporated.

- Chapter Three examined current thin-foil rolling theory and particle break-up modelling.

- Chapter Four examined rolling lubricants and their effects on annealing.

- Chapter Five discussed web handling and creasing generation during rolling and slitting.

Benchmarking and Optimisation:

The main areas of this investigation include the following:-

- Chapter Six examines the causes of strip breaks over a 3 year period, as well as drawing from experiences of other Alcoa Foil plants. The defects are categorised according to perceived defect cause. A review of Deep Bed Filtration (DBF) and subsequent trials and results are also discussed.

  The importance of boundary lubrication is highlighted in Chapter four. The Mansell curve, an adaptation of the Stribeck curve, is developed to explain the relationship between surface marks (herringbone) and lateral tearing (ladder defect) that can occur during final pass rolling. Chapter seven discusses this.

- Chapter Seven discusses productivity improvements resulting from increasing rolling speeds for all thin-foil passes. The two obstacles that hinder rolling at faster speeds are web breaks during the rolling process, and optimal rolling parameters (unwind tension, rewind tension, load, and coolant temperature as discussed in Chapter three). A discussion into the influence of chroming work rolls on rolling speed and defect generation is included.

Alloy Investigative Design

- Chapter Eight explained the experimental procedure for analysis of AA8150. This includes sample preparation, surface studies and metallurgical examination.

- Chapter Nine collates the results for surface study at final gauge and microstructural evolution of the alloy as it is processed for two processing routes typical of an 8150 product. The surface tribology and oxide characteristics are evaluated and compared to the existing 1145 product. A study of surface roughness was carried out using an atomic force microscope was able to provide peak-to-valley difference and a three-dimensional image of the area scanned.

  The surface oxide thickness and composition is investigated using a combination of depth profiling using ion bombardment and XPS analysis of the foil samples and the results compared to existing models for aluminium purity. Previous studies indicate that surface oxides for commercial 1xxx alloys are in the range of 2.8 to 5nm thick, requiring the use of XPS and SIMS analysis techniques.

The microstructural evolution of alloy 8150 from 2.7mm down to 0.012mm (cold and foil rolling) including the effects of high pass temperatures and final annealing temperature on mechanical properties is examined using an SEM in conjunction with image analysis, EDAX and EDS to determine the phase composition and percentage. The alloy was developed and registered in response to the increased requirement of higher strength at lower gauges.

- Chapter Ten discussed the findings from Chapter Nine and states conclusions from the evidence.
- Chapter Eleven is a summary of the overall finding of this thesis.

The data collected, particularly in the case of productivity improvements, image analysis and surface oxide investigations, incorporated hundreds of pages of information. The summarised forms are included as tables or figures within this thesis. The base-line data had been burnt into a disc, referred to as Appendix CD.

The data included covers but not limited to, the following data compilation, typified as Appendix CD through-out the text:

- Rolling parameters as per Chapter 8
- Image analysis part 1
- Image analysis part 2
- Pinhole collation
- Erickson results
- Surface Oxide composition and thickness data

The disc will be attached to the inside of the cover, and will include files relevant to the thesis over the past six years.

8.1. Sample Preparation

8.1.1. Collection of 8150 Samples

Four blocks of 8150 were cast at AARP – Point Henry to the following specifications; 1426mm wide x 4600mm long x 530mm thick. The as-cast wt% composition is determined using spectra-analysis, given in Table 8.1. In accordance with ADC standards, the alloy density for 8150 has been calculated as 2729 kg/m3.

Sample	Cu %	Fe %	Mg %	Mn %	Si %	Fe/Si ratio	Cr %	Ti %
1	0.013	1.08	0.025	0.37	0.131	8.26	0.003	0.01
2	0.013	1.09	0.024	0.38	0.13	8.36	0.003	0.01
3	0.013	1.08	0.025	0.37	0.131	8.26	0.003	0.01

Table 8.1. Composition of AA8150 cast block

The blocks were scalped (surface milled) at a depth of 6mm per side to remove surface oxides and unwanted intermetallics and homogenised at 580°C for four hours after a fourteen hour heat-up time. The blocks were rolled 18 times on the hot-reversing mill with reductions between 25 to 30mm and transferred to the warm mill at 18mm, before being reduced in three passes from 18 to 2.7mm. The final pass on the warm mill was made at >280°C (actual 303°C) to help promote full dynamic recrystallisation.

One block was cut in half to make coil A and coil B to aid in facilitating the trial. Coil's A and B were rolled from 2.7mm to 0.22mm in three passes via the cold rolling process. The coils were processed via two different paths to final gauge, Figure 8.1.

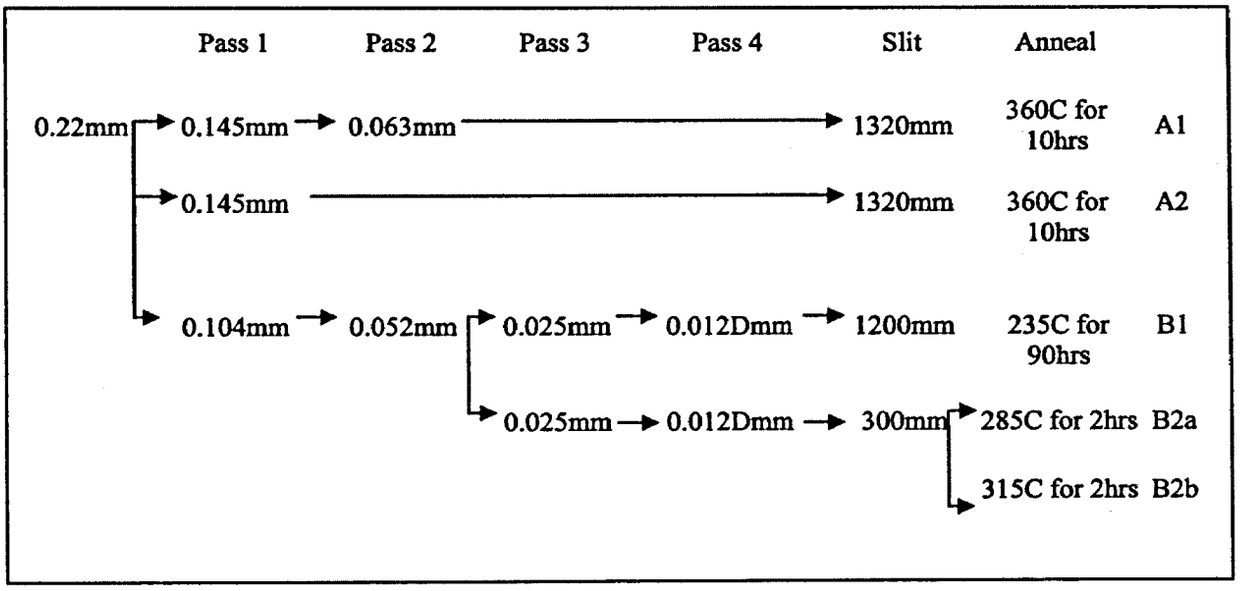

Figure 8.1. Processing routes for 8150 product used in trial.

Part A was rolled to 63μm (A1) and annealed at 360°C for 10 hours, with an intermediate step at 145μm (A2). Part B was rolled to 52μm, before being slit into two further products, 1200mm wide (B1) processed on the No2 Foil Mill with a roll roughness of between 5-7Ra, and 300mm wide (B2) processed on the No1 Foil Mill with a roll roughness of between 14-16Ra. The final gauge of the product is 12μm (or 24μm double gauge)

Sample B1 was annealed at 235°C for 90 hours, while B2 was split. Sample B2a was annealed for 2 hours at 285°C and B2b annealed for 2 hours at 315°C. The anneal time and temperature are established practices for household and light gauge foil.

The rolling parameters for thin-film and open gap rolling are discussed in Chapter 7, with additional information given in Table 8.2. From this, samples were prepared for microscopic examination of grain structure and intermetallics, and SEM/EDX to determine what the intermetallics were. The volume fraction of intermetallics was determined via image analysis.

Exit Gauge	**AGC Mode**	**Load**	**Exit Stress**	**Entry Stress**	**Speed Target**	**Speed Actual**
μm		Tonnes	Kg/mm^2	Kg/mm^2	m/min	m/min
29	TEN-SPD	360	4.6	4.6	700	≈ 490
14	TEN-SPD	460	5.0	5.0-5.5	700	≈ 600
13D	TEN-SPD				700	≈ 530

Reductions	Described/optimised in Chapter 7
Work roll camber	75μm
Work roll finish	5 – 7 Ra super finished (No2 Foil Mill)
	14 - 16 Ra super finished (No1 Foil Mill)
Work rolls – chromed vs. unchromed.	Chromed
Back up roll camber	Zero
Coolant viscosity	1.9 Ave (1.8 – 2.0)
Coolant temperature (Mansell Curve)	Min 38C for Ladder, max is 55C
	Rolled at 42°C for B1 samples
	Rolled at 49°C for B2 samples

Table 8.2. Additional rolling parameters for the sample trial metal

8.1.2. Preparation of AA8150 Samples

Metallographic examination was made on specimens obtained from samples collected during the processing of the metal. Samples were collected at the 2.7mm exit warm mill and at the 0.220mm exit cold rolling. From here samples were collected at 145μm, 63μm, and 12μm to examine second phase particles and grain structure during each rolling pass. Samples prior to and post-anneal were taken for the 145μm, 63μm and 12μm samples, with the annealing schedules described in Figure 8.1.

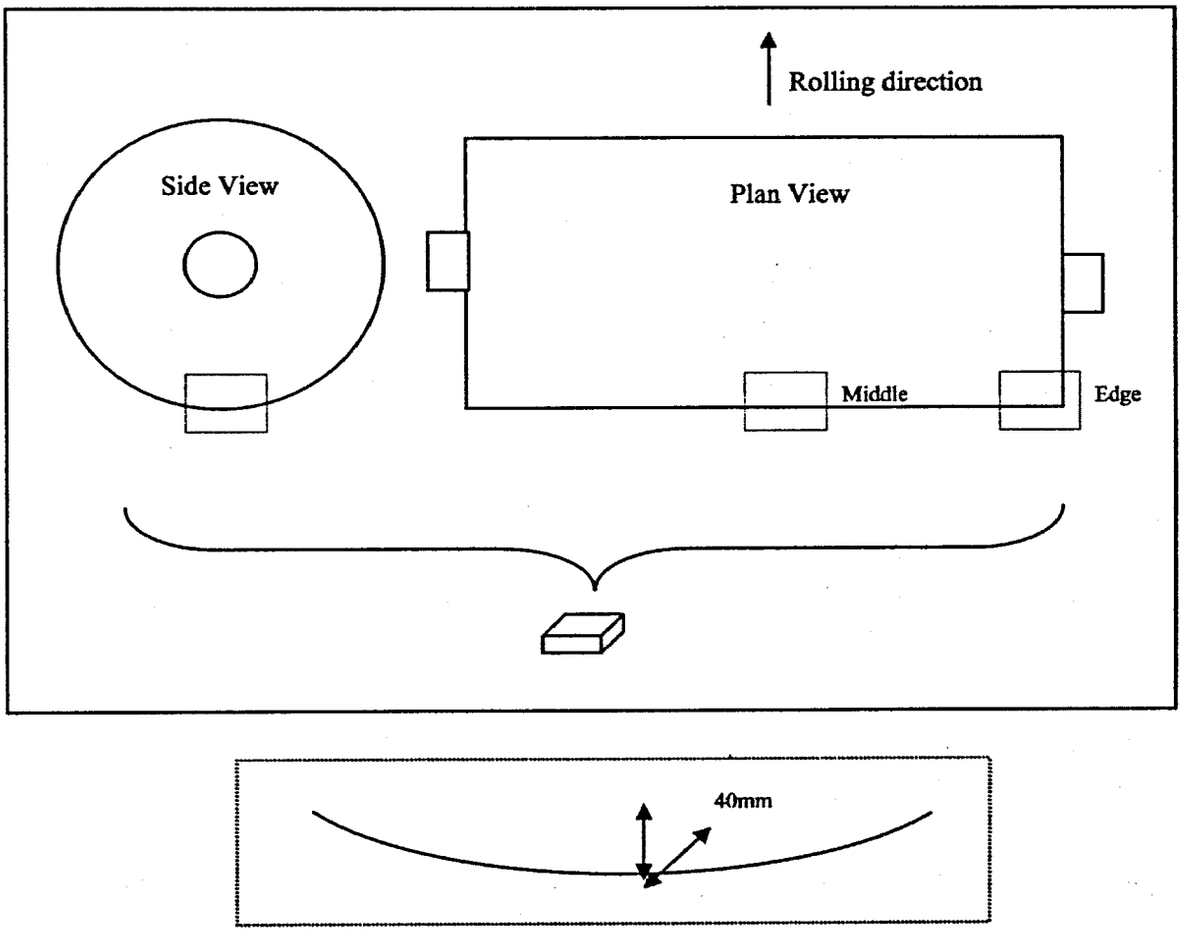

Figure 8.2. **Sample location in coil. The samples are collected 40mm in from the exposed edge, and 40mm in from the coil outer diameter**

Longitudinal-normal sections no larger than 20mm x 20mm were taken from the middle and edge of the coils at 2.7mm exit warm mill, and at the middle for all other specimens, approximately 40mm from the outer diameter, as shown in Figure 8.2.

The samples were then mounted with the leading edge exposed and polished to a one-micron finish using various grades of silicon carbide paper prior to magnesium oxide mechanical polishing. The leading edge or cross section was chosen as it best showed the elongated grains and second phase particles.

The samples were etched in a solution of Keller's reagent in an ultrasonic bath. Superficial staining was removed during the water rinse. The samples were photographed at a magnification of 500x to examine the intermetallic structure. The grain structure was examined at 200x and 400x magnification using electro-etch techniques. The standard procedure for sample preparation is given in Appendix 6.

Final anneal temperature

At lower gauges grain size is a critical factor in determining the strength of a product via the Hall-Petch equation, as discussed in Chapter 2.3.2.4. Small grain sizes are achieved by heavy cold rolling deformation of a material followed by a thermal treatment in conjunction with a pre-determined microstructure. This can be affected by modifying the Si/Fe ratio and manganese content, choosing the correct inter-anneal and final-anneal conditions and minimising recovery/recrystallisation during cold rolling.

The effect of final annealing temperature on end-use mechanical properties on 12 micron alloy 8150 was investigated. A coil of AA8150 was cold rolled to 0.22mm via the process path outlined below:

Coil	Hot Roll		Cold Roll		Cold Roll		Slit		Cold Roll
A	2.7mm	→	1.05mm	→	0.48mm	→	20mm/side	→	0.22mm

After cold rolling, the coil was processed as per the B2 samples in Figure 8.1 to final gauge and split into two, as described below:

Pass 1		Pass 2		Pass 3		Pass 4		Slit		Anneal
0.104mm	→	0.052mm	→	0.025mm	→	0.012Dmm	→	300mm	→	285°C for 2 hours
									→	315°C for 2 hours

The final product was annealed by using two consecutive furnace loads in the same furnace for 2 hours. Randomly selected coils from the furnace tree of finished product were burst strength tested. Approximately 25 samples, 150mmx150mm in size, were taken from each anneal path and the burst strength determined using a Mullen's tester (Appendix 7 – procedure for operation of a Mullen's tester).

The gauge of each sample was also checked gravimetrically to eliminate the influence of gauge on strength. Samples were taken from near the testing area for both temperatures, cold mounted and hand polished to 4000 grit before final polishing using 1μm magnesium oxide paste, Appendix 6. The samples were then lightly etched to show the grain structure.

Exit Cold Rolling Temperature

Cold work imparted on the material prior to final anneal can effect the final mechanical properties via modifications to the annealed microstructure. This effect has been seen on 3xxx series alloys with exit temperatures as low as 150°C[1].

A trial was performed were several batches of 8150 product were rolled with the entry and exit temperatures recorded for all cold passes. The pass 2 entry temperature was allow to exceed 60°C, getting as high as 100°C, resulting in exit temperature exceeding 150°C. The coils were then processed to 120μm finstock* product. Three Erickson tests were then performed at the beginning of each coil as per standard procedure, Appendix 8, and the results plotted against batch number.

* Finstock is used to make the refrigeration component for air conditioners

8.2. Surface Studies – Experimental Method

8.2.1. Introduction

One of the more critical characteristics of foil products is unwind stickiness after the final anneal. Residual coolant composition and rolling conditions are critical, and are discussed in Chapter 4 – Rolling Lubrication. While the effect of surface oxides for 1XXX series alloys during annealing has been investigated (Chapter 2.3.2.5-6) along with rolling oil residue reactions, no investigation has been published that looks at the next generation of foil alloys, namely the 8XXX high iron and manganese alloys.

Surface contamination and composition have been discussed by Treverton and Thomas[2] who showed that surface contamination causes a loss in adhesion of organic coatings used on aluminium foil products, previously attributed to enrichment of alkali and alkaline earth metal elements in the oxide. Williams concluded that for 1xxx alloys, residual surface contamination and not surface oxides were a mechanism for stickiness. As discussed in Chapter 2.3.2.5, oxide thicknesses were reported to range from 1.0 to 5.0 nm on commercially produced 1xxx series foil alloys.

Williams[3] found that at least 60% of the original rolling lubricant remaining on the strip following annealing was mainly composed of straight chain aliphatic hydrocarbons slightly polymerised to a molecular weight between 1350 and 4000, along with some alkoxy-groups, ketones, carboxylic acids and carbonates. A similar coolant composition combined with two distinct annealing cycles and surface roughness values will allow a comparison of surface oxides for alloy 8150 versus 1145. The composition of the residual rolling oil post-anneal is expected to be similar to that observed by Williams[3] and hence investigation into the residue composition is not warranted.

8.2.2. Surface Study Techniques

Surface oxides in commercially produced foils are generally less than 10nm thick, and hence to study aluminium surfaces requires highly sensitive surface techniques. Classically, surface analysis was performed using adsorption isotherms, ellipsometry and surface roughness. However due to their limited nature, highly sensitive surface techniques such as X-ray Photoelectron Spectroscopy (XPS) and Secondary Ion Mass Spectrometry (SIMS) for the examination of foil surface oxides are required.

XPS, also referred to as ESCA (Electron Spectroscopy for Chemical Analysis), employs the use of characteristic x-rays (generally Mg–Kα or Al–Kα) to irradiate a sample, exciting electrons in the surface of a material. As shown in Figure 8.3, electrons are emitted by the photoelectric effect, producing a spectrum of photoelectron intensity as a function of binding energy given by;

$$KE = h\nu - BE - \Phi s \qquad (8.1)$$

Where hν is the energy of the photon, BE the binding energy of the atomic orbital from which the electron originates and Φs is the spectrometer work function.

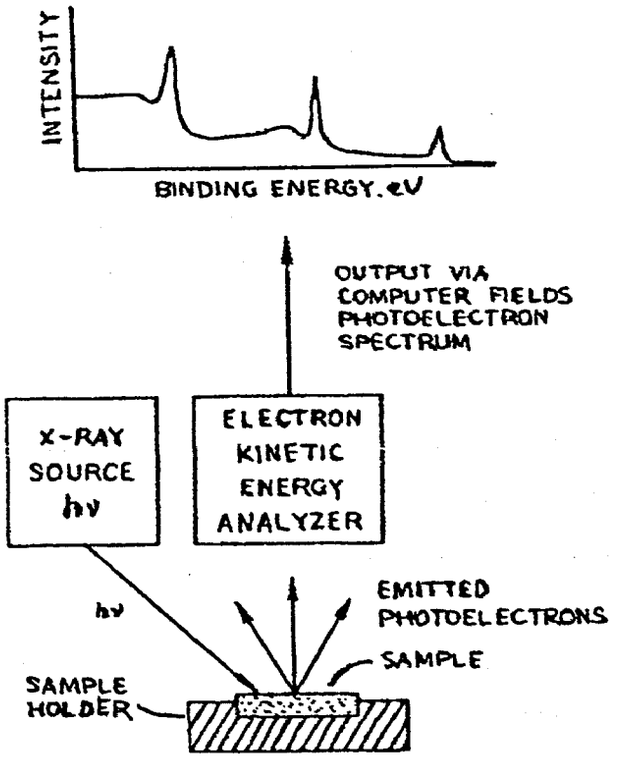

Figure 8.3 **Schematic of an X-ray photoelectron spectroscopy that employs the photoelectric effect[4].**

XPS spectra have been obtained for every element on the Periodic Table. Ionisation of the core electrons from each atomic orbital provides a list of ionisation energies for each element. These are sufficiently characteristic to be used for qualitative analysis, that is, the atoms of any element can be detected by their characteristic pattern of peaks. Further to this, variations in the elemental binding energies arise from the differences in the chemical potential and polarisability of compounds cause peak shifts. These shifts can be used to identify the chemical state of the materials being analyzed.

XPS is generally good for depths less than 3nm as electrons possess insufficient energy to escape, but when used in combination with ion etching to erode the sample in stages, a quantitative depth profile can be constructed[5]. A guide to preparing, mounting, collecting and analysing data is available[6]. The binding energy for oxygen, aluminium, silicon, manganese and iron for both Mg–Kα and Al–Kα photons is given in Appendix 9.

SIMS is a low-energy surface technique which bombards a sample with a beam of primary ions to remove the outer atomic layers as neutral particles and secondary ions. The secondary ions give an elemental analysis of the surface sample via mass spectrometry. Ion etching or 'sputtering' progressively into the surface allows a depth profile to be obtained, and is able to detect elements in very low concentrations. The aggressive nature of the ion bombardment limits the technique to inorganic material analysis; however it is able to qualitatively detect elements at very low concentrations.

It is well known that even small changes to the surface roughness of finishing rolls dramatically increases the rolling speed for thin foil products[7]. In saying this, no direct correlation between commercially used roll finishes and hence surface roughness, and surface oxides has been undertaken. To measure surface roughness, an Atomic Force Microscope (AFM) is used to essentially drag a cantilevered silicon-nitride needle across a specified surface area to give peak-to-valley difference and a mean roughness value in nm over a prescribed area. Generally roughness is measured in terms of Ra or $(um)^{-1}$.

8.2.3. Experimental Method

The experimental method is designed to compare the surface roughness, surface oxidation thickness and composition for alloy AA8150 as a function of temperature, time and surface roughness/morphology extremes for commercially used annealing cycles. The variation in oxide composition with depth was also investigated. The annealed coils were processed under similar conditions; with trial anneal samples, B1 and B2, taken from the parent coil as described in section 8.1.

Foil slab samples for both the B1 and B2 processing routes were taken from the centre axial position, approximately 50mm in from the outer radial edge were collected. The samples were approximately 5mm thick, containing between 500 – 1000 sheets or layers which were stuck together as much as possible to avoid surface contamination. In each case, samples were prepared immediately before insertion into analysis equipment by cutting several layers together to sample size, and then peeling away a layer to expose a fresh as the sample was placed into the platelet or chamber of the instrument used.

Surface Roughness

A study of surface roughness was carried out using an atomic force microscope, which in addition to mean surface roughness measures, was able to provide peak-to-valley difference and a three-dimensional image of the area scanned. A more detailed examination of a specific area that comprised approximately 2.5-4% of the total area also allowed the Ra to be calculated. Further to this, a section analysis giving a side two-dimensional profile was also performed.

Samples from the centre of both slabs approximately 10mm x 10mm were cut and separated prior to placing on a specimen platelet. The samples were placed inside a Digital Instrument 3000 AFM, and a representative product area of approximately $50\mu m^2$ was scanned at a rate of 0.4002 Hz over several minutes. The signals were then transferred to an image via an internal software package. Specific areas regarded as being representative of the sample were subjected to a section analysis and 'box' analysis. Both the shiny and matte sides were investigated.

The surface roughness of shiny and matte side of samples produced via the B1 and B2 processing routes was assessed using an on-line Digital Instrument 3000 conversion package. The information was presented in four forms, the first two presenting an overall plan view of the area examined or surface analysis; and the final two images a section analysis represented by a three–dimensional view of the same area and a cross-sectional view along a trace line. Table 8.3 has been collated to aid in understanding the terminology used to describe surface roughness measure.

LEGEND	DEFINITION
Img. Z range	Maximum vertical distance between highest and lowest data points on the image
Img. Mean	Mean value of z data contained within the image
Img. Rms	Root mean square average of height deviations taken from the mean data plane
Ing. Ra	Arithmetic average of the absolute values of surface height deviations measured from the mean plane within the image
Img. Srf. Area	Three dimensional area of the image (sum of area of all triangles formed by three adjacent data points
Z range	Peak-to-valley difference in height values within the analysed region (box)
Mean	Mean value of z data contained within the box
Rms (Rq)	Standard deviation of the Z values within the box
Mean roughness (Ra), nm	Arithmetic average of the absolute values of surface height deviations measured from the mean plane within the box
Max height (Rmax), nm	Maximum vertical distance between highest and lowest data points on the image (should equal Z range)
Surface area, um^2	Three dimensional area of the box (sum of area of all triangles formed by three adjacent data points

Table 8.3. Definitions of surface roughness measures used in defining surface roughness.

The digital instrument input parameters were the same for all four samples tested:

- Scan size: 50μm
- Scan rate: 0.4002 Hz
- Number of samples: 256
- Image data: Height
- Data Scale: 1.0000μm

Surface Oxides and Oxide Depth

With the AFM providing effectively a visual examination of the surface, XPS combined with ion etching was employed to detect the elements present in the surface oxide of both the B1 and B2 shiny and matte samples, and to provide information on compound formation. The analysis was used to indicate if any unusual components which have been linked to sticky-unwind foil were present. The effects of surface roughness, surface morphology, time and temperature in commercial applications on surface oxides can be determined

Depth profiling was carried out using ion bombardment and XPS analysis on both foil samples, shiny and matte sides. XPS general survey scans were used to compare relative oxide levels of the matte and shiny sides of the short-anneal high-temperature versus long-anneal low-temperature samples.

General wide surface scans were run to start with, followed by high resolution or region multiplex scans for oxygen, aluminium and carbon. Depth profiles were run using ion bombardment to remove top layer, and general survey scans, using XPS at progressive intervals, to examine the overall new surface characteristics.

In determining the oxide thickness using ion bombardment, it has become apparent that there is no clear definition available as to when an oxide boundary starts or finishes[8].

There are many different interpretations of an oxide boundary including:

- 50% initial value, $(\text{Metal O})_{50\%}$
- 5% initial value, $(\text{Metal O})_{5\%}$
- Start of diffusion process
- Lines of best fit

For the purpose of the thesis both the 50% and 5% values will be discussed.

Surface Composition

The samples were subject to general wide surface scans using a VG ESCALAB 220I XL X-Ray with an Al-Kα monochromatic x-ray, with an internal on-line conversion program used to interpret the results. Targeted binding energies were subjected to high resolution or region multiplex scan, with up to 50 scans required for some elements. General wide survey scans provide only an idea of surface characteristics. High resolution or region multiplex scans were made for the aluminium, carbon and oxygen components.

Depth profiles for both the shiny and matte surfaces of samples B1 and B2 were conducted using a VG ESCALAB 220i XL-Ray. Several layers were cut to size and separated prior to testing. The adjacent shiny and matte areas were profiled, with B1 assessed first. The process involves argon ion bombardment over a specified area, at a rate of 2 angstroms per sec for a period of 12.1 seconds, forty times to a depth of 50nm. For the B2 samples this was reduced to a depth of less than 20nm, with the matte side sample of B2 run for 14.2 seconds. The samples were not washed or cleaned prior to analysis.

8.3. Microstructural Evaluation – Experimental Method

The theory behind traditional strengthening mechanisms in Al-Fe-Mn thin foil alloys has been documented[9]. A near-eutectic alloy, incorporating elements that form intermetallic phases under selected casting conditions, results in rod-like intermetallic phases via "coupled growth".

When a mass of a molten alloy of eutectic or near eutectic composition is solidified by withdrawing heat form one end at a specific rate, a temperature gradient is established in the as-cast block, Figure 8.4[10]. This cellular or "colony" mode of solidification produces unaligned intermetallic phases that grow in the metal matrix to produce a strengthening effect. The intermetallic phase, described as rod-like, may vary in shape with a ratio of major axis to minor axis as high as five to one, Figure 8.5.

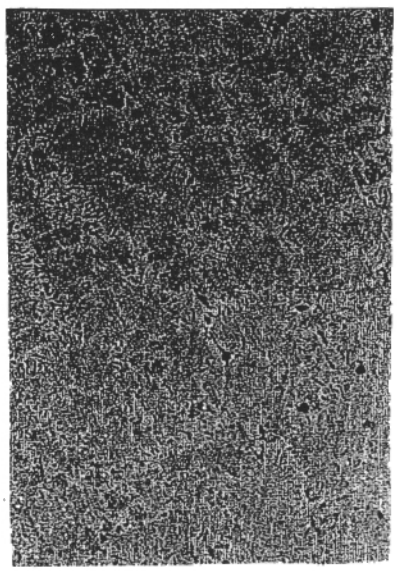

Figure 8.4. 'Colony' mode solidification[11]

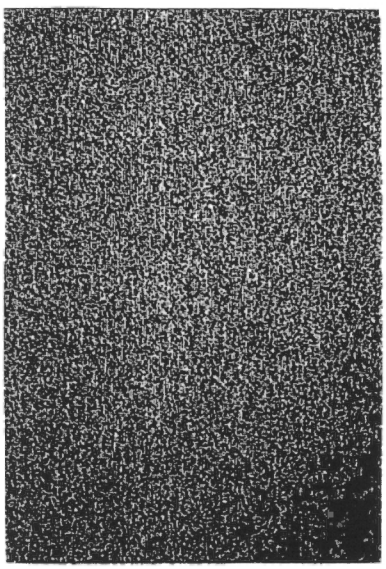

Figure 8.5. Unaligned rods[11]

In the wrought products the particle diameter of the dispersed intermetallic phase should be of sufficient size so particles will generate and stabilise a dislocation cell structure of that magnitude during cold deformation, or hold a grain diameter of that magnitude after annealing. If the particles are too small, they will not hold the high angle mis-orientation boundaries negating any yield strengthening effect.

If the intermetallic particles are too large or unevenly distributed in the products made from eutectic alloys with rod-like intermetallic phases, they will act as sites for stress concentrations or as paths for crack propagation and the material will lose its toughness or formability and yield strength will be reduced.

In general, the desired rod-like intermetallic phase may be produced without excessive growth of coarse primary intermetallic particles or excessive growth of primary aluminium dendrites. The total content of principal alloying elements must be less than 10% above or 20% below the total content of these elements at the eutectic composition to optimise strength and elongation properties. This promotes large areas free of intermetallic rods, reducing the uniformity of the particle dispersion when the cast alloy is rolled or otherwise deformed to break up and disperse the brittle intermetallic phase.

In some circumstances as much as 50 - 60% by volume of aluminium dendrites is tolerable in relatively thick ingots cast by direct-chill continuous casting procedure but the properties of rolled products decrease progressively with increase in volume of the dendrites.

With aluminium alloys with lower levels of iron and manganese, silicon additions coupled with strict control of the rolling process from hot rolling to final annealing are incorporated into the alloy design to improve strength. Alloys such as 8150 that target below the eutectic composition will form primary aluminium dendrites (in addition to the desired eutectic structure).

To increase the mechanical strength of thin-foil products, the alloy composition is best utilised in the promotion of fine grained structures via particle stimulated nucleation and retarding grain coarsening as opposed to solid solution strengthening (unless precipitates formed during cold-work enhanced strain hardening). Further to this, a fine uniform grain structure is a function of process path with casting condition, intermediate stress-relieving and final annealing all critical in developing the properties of thin-film foil alloys.

Published work on as-cast and post-homogenised structures of high strength thin-film alloys is comprehensive and requires no further evaluation. Most centre on the Al-Fe-Mn eutectic system which while giving excellent thin-film properties, has practical limitations with regards to casting and cooling rates. The Al-Fe-Mn-Si system below the eutectic is more appealing, as strength improvements are significant using more beneficial casting conditions. The end-use microstructure has improved mechanical properties while allowing up to a three-fold increase in block width is possible.

This compositions 'window' around the eutectic has resulted in the development of several alloys including alloy 8150 registered by Mansell[12]. The composition in accordance with Aluminium Association (AA) standards as submitted by Mansell to the Aluminium Association is summarized in Table 8.4, with the full correspondence given in Appendix 10.

Alloying Element	Amount
Silicon	0.30 max
Iron	0.9 – 1.3
Manganese	0.20 – 0.7
Titanium	0.05
Other, Each	0.05
Others, Total	0.15
Aluminium	Remainder

Table 8.4. Registered composition limits of AA 8150 alloy

The processing path is a critical factor in the production of this alloy, in particular the effect of final anneal temperature on AA8150 final mechanical properties and the effect of recovery relief via high entry pass temperatures during cold rolling on the mechanical properties.

This chapter will examine the current alloy's compositional limits for thin-foil alloys currently produced in Australia before discussing the development of the AA8150 microstructure and subsequent process factors.

8.2.1. Microstructure Evaluation – Initial Analysis

Samples were taken at several differing gauges during the production of 12μm foil. The samples were prepared for micrography to examine the microstructure of the intermetallic distribution and grain structure before and after annealing as discussed in section 8.1. The samples were also examined using EDAX analysis to determine the atomic and weight percentage composition of specific intermetallics. A stage micrometer was used to determine intermetallic particle size.

Image Analysis

The void fraction at various gauges was used to determine the percent intermetallics and average particle size in the aluminium matrix. The SEM micrographs were used to determine the void fraction percentage, as well as the aspect ratio of the intermetallics.

Electrical Conductivity

To confirm the presence of dispersoids in the final annealing product, conductivity measurements were used to show the amount of solute in solution. The electrical conductivity of an aluminium alloy is sensitive to elements in solid solution with the solute atoms interfering with electron motion through the aluminium. A drop in conductivity is associated with an increase of elements in solution. The size and the shape of the phases precipitated have little effect on conductivity, only volume.

Room temperature samples were prepared using a sandwiched 12μm specimen from pre and post annealing and comparing them to a 0.22mm sample.

8.2.2. Detailed Microstructure Evaluation

An evaluation of selected microstructures was performed to explain the effect of intermetallics on grain size and hence strength. Evaluations were performed on 2.7mm hot-rolled product, 0.22mm cold rolled product, and 12μm thin-foil product pre and post anneal.

The samples were examined using a FEI SIRION FEG Scanning Electron Microscope. The SEM used captive backscatter and image analysis to separate the particles from the matrix (i.e. iron precipitates appear bright). The software uses ZEISS KS400 system which allows EDS on specific precipitates from the image. The accelerating voltage was originally set to 10kV to improve resolution of the intermetallics, but was increased to 15kV to aid in the EDS analysis. To improve the EDS analysis, the accelerating voltage should be a minimum 1.5x the binding energy.

The samples were examined at various magnifications designed to optimise precipitate detection in the hot rolled (2.7mm), cold rolled (220μm), pre and post annealed foil samples (12μm). EDS analysis was performed on all samples examining the bright and dull particles, and dispersoids/precipitates. The matrix was also examined for the 2.7mm hot rolled samples as baselines.

The software permitted the measurement of the area distribution of particle sizes to be performed. The areas were grouped according to bins and a particle count completed and allotted to each bin. This in turn provided information on particle density and aspect ratio according to area bin size. This was performed on the cold rolled and pre-post annealed foil samples to quantify the effects of >99% cold work and subsequent annealing.

Phase Identification

The elemental atomic percentage obtained from the EDS spectrum was examined in conjunction with the phase diagram to determine the phases present. The results were also compared to standards at Alcoa Technical Centre (ATC)[13]. One problem with the EDS technique is that the small size of the phases, particularly the precipitates, results in the area analysed to incorporate a small amount of the surrounding matrix. This was due to the minimum area required to complete the analysis being greater than the precipitate area. The effect of this was to dilute the iron and manganese atomic volume percentages and increase the aluminium and silicon percentages[13].

8.2.3. Mechanical Testing for Light Gauge Samples

Samples were collected from both the B1 and B2a and B2b process streams. The samples were prepared for Burst testing (also known as Mullen's testing). This involved cutting a sample A4 in size from the final coil and testing in accordance to the procedure described in Appendix 7. The results were compared to standard 1145 results from standard 12 micron coils.

RESULTS, DISCUSSION AND CONCLUSION

CHAPTER 9 ALLOY INVESTIGATION - RESULTS

9.1. Surface Studies

In designing the experiment to replicate typical operational conditions, several factors were kept constant to reduce external influences outside that of the annealing furnace operating parameters and surface roughness. These factors are listed below in Table 9.1.

Rolling parameter theory has been discussed in Chapter 3, with optimal parameters determined in Chapter 7. The roll camber, finish and surface compositions remained constant, and coolant viscosity, discussed in Chapter 4, is to remain approximately within parameters set using the Mansell Curve.

Unwind tension	Described/optimised in Chapter 7
Rewind tension	Described/optimised in Chapter 7
Roll load	Described/optimised in Chapter 7
Speed	Described/optimised in Chapter 7
Reductions	Described/optimised in Chapter 7
Work roll camber	75μm
Work roll finish	5 – 7 Ra super finished (No2 Foil Mill)
	14 - 16 Ra super finished (No1 Foil Mill)
Work rolls – chromed vs. unchromed.	Chromed
Back up roll camber	Zero
Coolant viscosity	1.9 Ave (1.8 – 2.0)
Coolant temperature (Mansell Curve)	Min 38C for Ladder, max is 55C
	Rolled at 41°C for B1 samples
	Rolled at 49°C for B2 samples

Table 9.1. Additional rolling parameters for the sample trial metal

The results are divided into three categorises. The first examines surface roughness; the surface contour examined using an AFM to provide an effective visual examination of the surface. This is performed on both sides of the sheet, matte and shiny, for two different roll finishes listed in Table 9.1.

The surface oxide composition is determined using XPS analysis on both foil samples, shiny and matte sides. XPS general survey scans were employed to detect the elements present in the surface oxide of both the B1 and B2 shiny and matte samples. This is expanded to compare relative oxide levels of the matte and shiny sides of the short-anneal high-temperature versus long-anneal low-temperature samples and to provide information on compound formation.

Depth profiling of the surface oxides is carried out using ion bombardment or etching and XPS ion etching. Ion bombardment removes the existing top layer of metal oxide or carbide, and high resolution or region multiplex scans for oxygen, aluminium and carbon were performed to determine the oxide and carbon penetration.

This provides a range of samples representing maximum operation ranges for surface roughness include matte finish, annealing temperature and anneal time, as listed in Table 9.2.

	Min	Max
Surface Roughness	5-7 Ra	14-16 Ra
Surface Finish	Bright/Shiny	Matte/Dull
Annealing temperature	235°C	285°C
Annealing time	90 hours	2 hours

Table 9.2. Operational thin-foil rolling boundaries used at Yennora to produce aluminium foils

The effects of surface roughness, surface morphology, annealing time and temperature in commercial applications on surface oxides composition and depths are determined. This represent the operational boundaries currently used for the production of thin-film (<20 micron) foil in Australia.

9.1.1. Surface Roughness

Surface analysis

Surface analysis allows a small box section of the original image to be examined giving a localized area analysis. The box analysis results were generally lower than the image analysis due to the localized area of the box. This is reflected in the change in units from nm to μm. The average results for the image and box analysis are listed in Table 9.3 with the image definitions given in Table 8.3.

Image	B1 – Shiny	B1 – Matte	B2 – Shiny	B2 – Matte
Z range, μm	0.8522	2.093	0.8862	2.368
Mean, nm	0.101	0.030	0.037	0.026
Raw mean, nm	126.87	-156.55	-20.658	-161.43
Rms (Rq), nm	58.125	310.44	62.515	373.87
Ra, nm	45.152	242.45	52.215	299.13
Rmax, μm	0.8631	2.154	0.8824	2.248
Srf. area, μm^2	2509.7	2545.9	2509.3	2552.1
Srf. area diff, %	0.387	1.837	0.371	2.086
Box	B1 – Shiny	B1 – Matte	B2 – Shiny	B2 – Matte
Z range, nm	312.91	787.04	166.04	1052
Mean, nm	-20.567	-68.822	-8.470	-119.17
Rms (Rq), nm	22.634	163.13	27.946	188.49
Ra, nm	17.645	138.24	22.666	140.90
Rmax, nm	221.29	778.27	167.17	1087
Srf. Area, μm^2	93.355	69.039	97.974	67.038
Box X dim., μm	15.686	11.569	15.882	13.529
Box Y dim., μm	14.706	13.529	14.314	11.176

Table 9.3. Image and box analysis results for surface roughness for matte and shiny surfaces of samples annealed at 235 °C and 285°C.

While the values for the box analysis for Rms, Ra and Rmax were lower than the overall section analysis, a relative comparison between the shiny and matte surfaces for both analysis demonstrated a similar trend. Observations made on Rms, Ra and Rmax with a 15-20% difference between the B1 and B2 samples with slightly different roll surfaces, but with the matte surface over five times greater than the shiny surfaces.

The box statistics correlated well with the surface image statistics, mirroring the higher difference between matte and shiny rather than different roll finishes. Discussion will focus on surface image analysis as box analysis, being a subset of the surface analysis, is less quantitative of the sample surface providing isolated areas of information.

The Z ranges for the two shiny samples were both 0.87 +/-0.02μm, while the matte results were 2.2 +/-0.2μm. The variation between shiny and matte was 1.25-1.5μm, which is one to two orders of magnitude greater than similar surface variations, indicating one smooth side and one rough side, or two contrasting surface morphologies. The mean results demonstrated no real pattern, with the shiny side of B1 showing an unexpectedly high result.

Sample AFM analysis results for the surface and box analysis are given in Figures 9.1 to 9.4 for the matte and shiny sides of both samples. This is separated into shiny and matte sides for the two roll finished used in the production of the light gauge foil. In conclusion, the matte surface had a far more prominent effect than the roll surface Ra. Note that the dark/black spots are fissures in the surface of the aluminium foil.

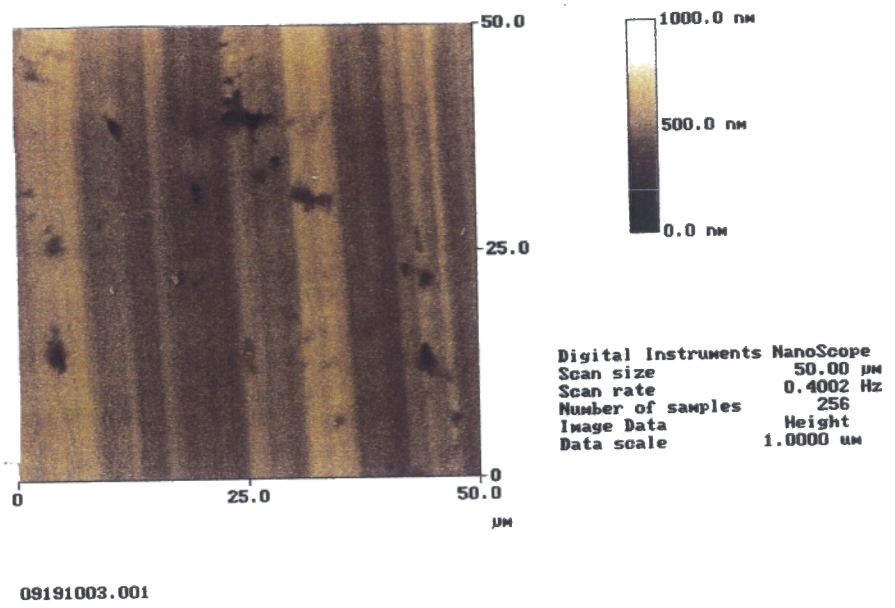

(a)

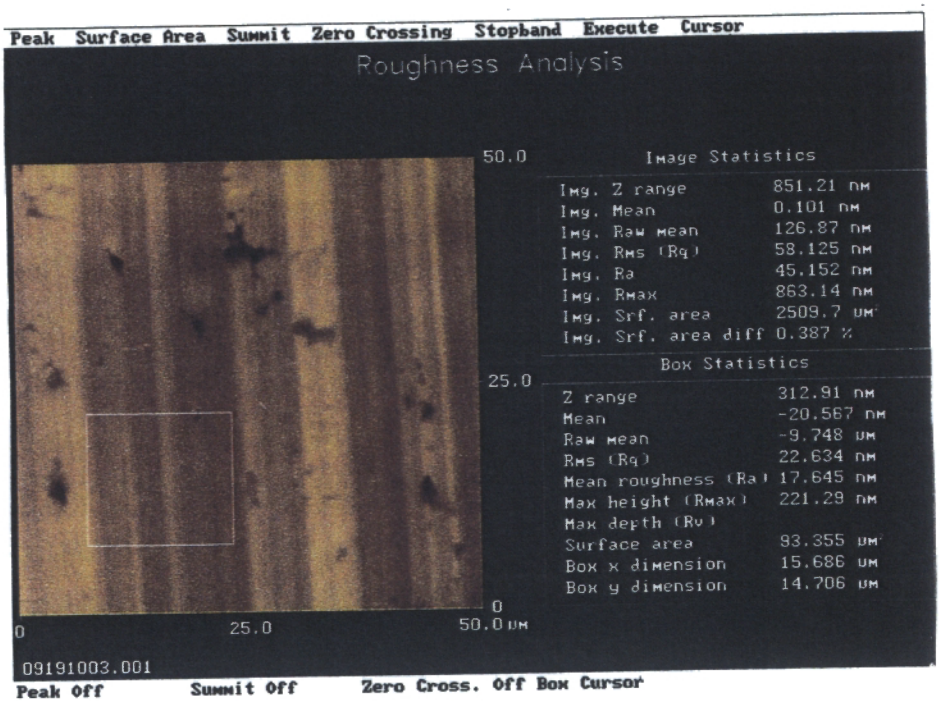

(b)

Figure 9.1. **Surface roughness for shiny sample processed using 5-7 Ra roll finish – B1 (a) surface scan (b) box analysis**

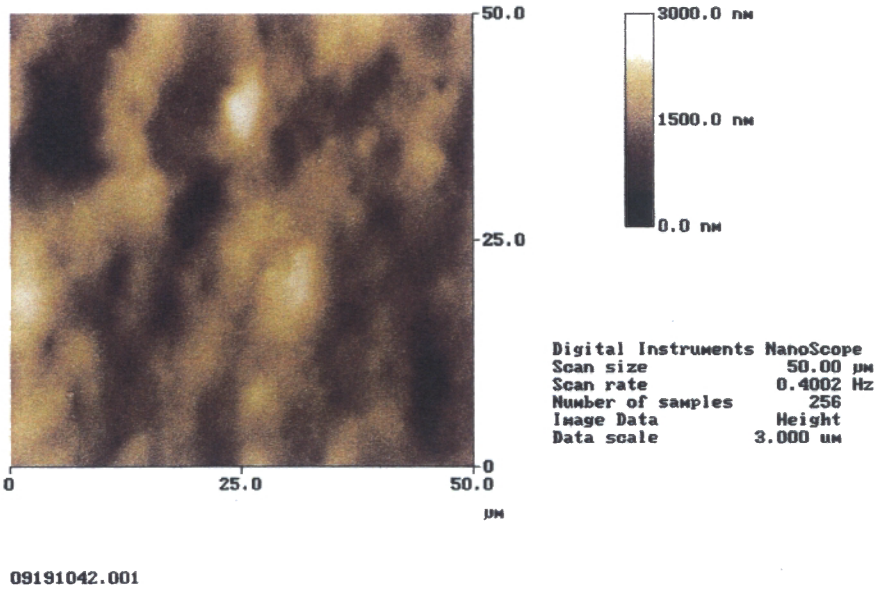

(a)

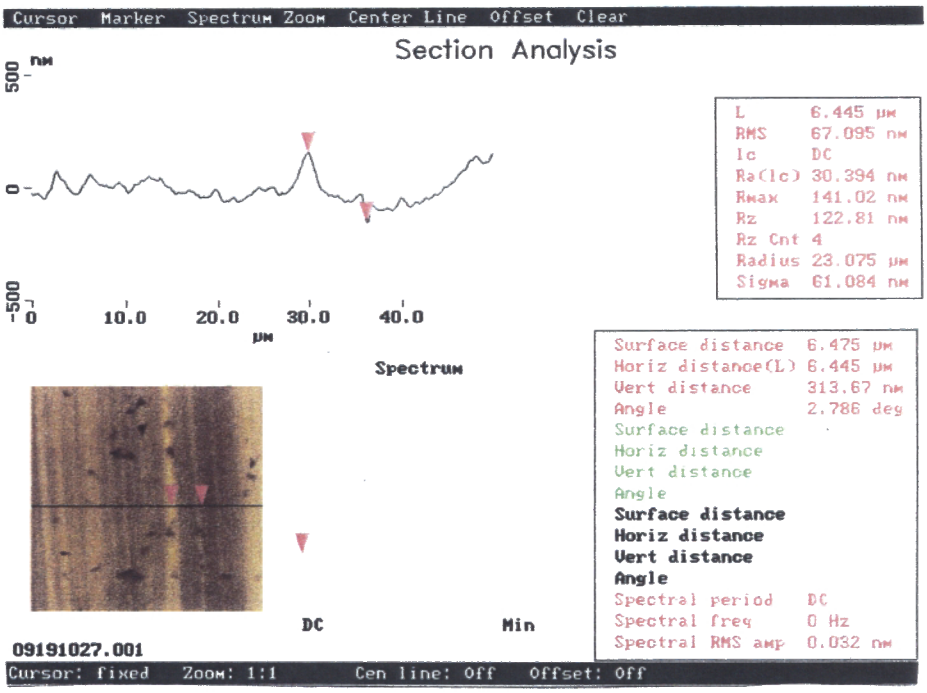

(b)

Figure 9.2. **Surface roughness for matte sample processed using 5-7 Ra roll finish – B1 (a) surface scan (b) box analysis**

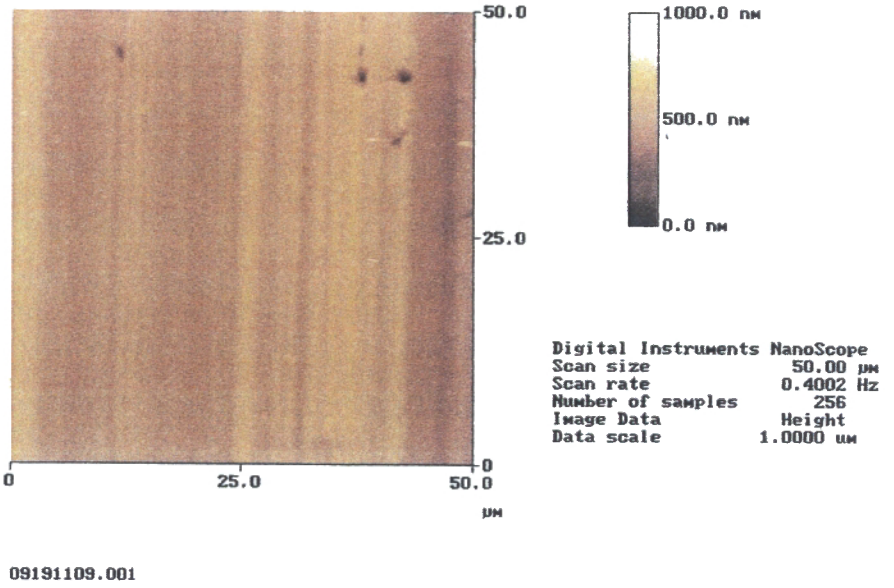

(a)

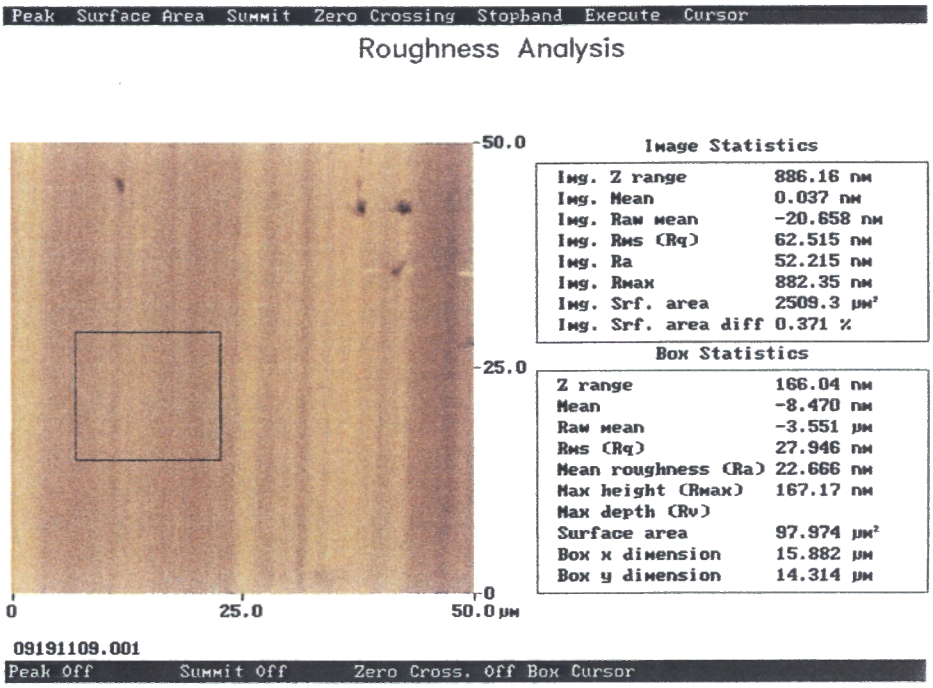

(b)

Figure 9.3. **Surface roughness for shiny sample processed using 14-16 Ra roll finish – B2 (a) surface scan (b) box analysis**

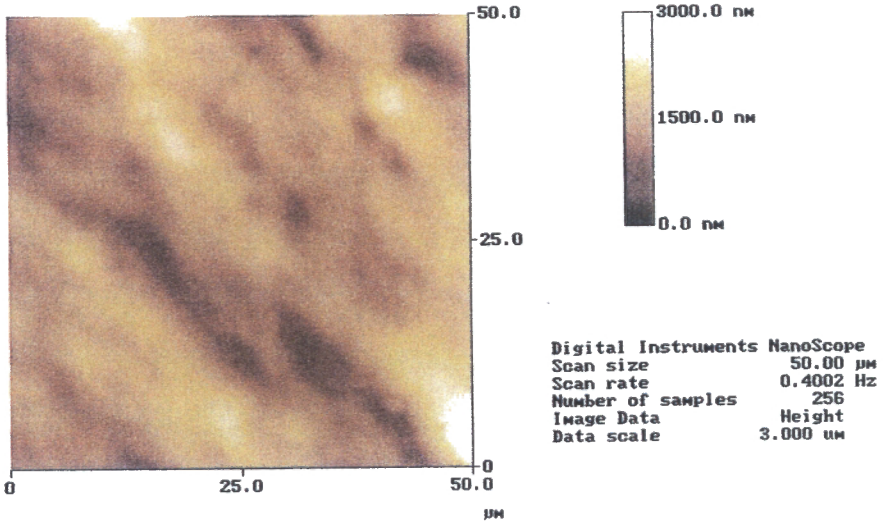

(a)

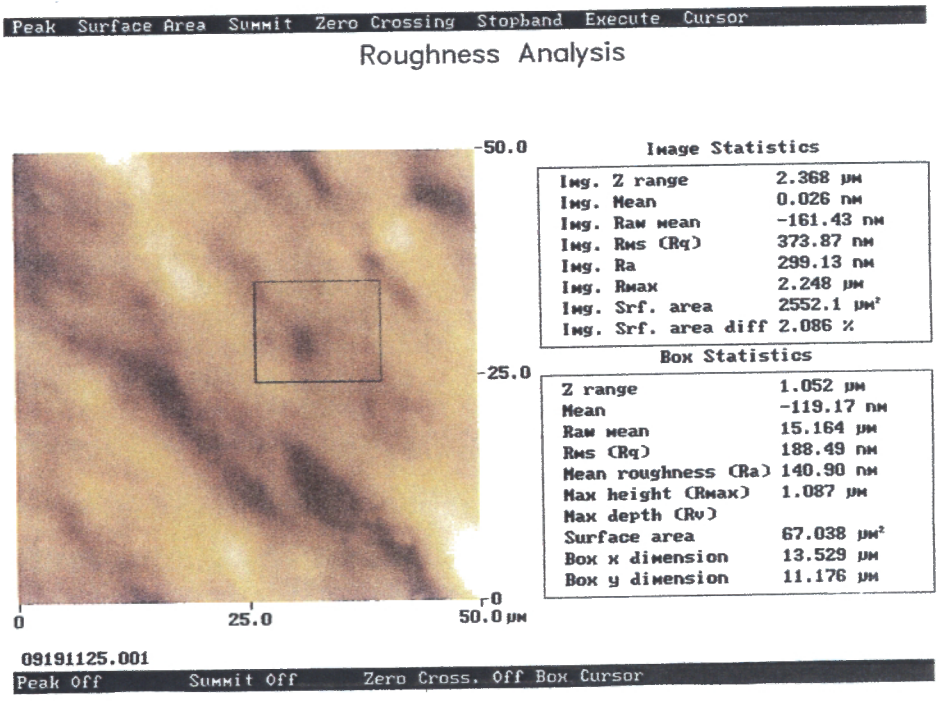

(b)

Figure 9.4. **Surface roughness for matte sample processed using 14-16 Ra roll finish – B2 (a) surface scan (b) box analysis**

Section Analysis

The section analysis provided a surface trace along a defined line as well as giving a three dimensional schematic of the surface. This was then combined to give a three dimensional image of the surface. A representative sample from the analysis is presented in Table 9.4.

Image	B1 – Shiny	B1 – Matte	B2 – Shiny	B2 – Matte
L, μm	8.984	23.828	21.289	8.594
Rms, nm	44.094	282.88	71.749	494.56
Ra (lc), nm	31.569	174.08	51.690	84.22
Rmax, nm	124.65	728.96	201.57	367.04
Surf Dist, μm	9.002	24.171	21.348	8.816
Horiz Dist, μm	8.984	23.828	21.289	8.594
Vert Dist, nm	194.27	1261	283.53	1650
Angle, deg	1.239	3.029	0.763	10.868

Table 9.4. Section analysis results for surface roughness for the matte and shiny surfaces of samples annealed at 235 °C and 285°C.

The results from the section analysis, with L the arbitrary line length between two points, confirm the surface and box analysis made on Rms, Ra and Rmax values with the surface morphology significantly more influential than the roll finish used in process the material. There is a slight difference in results when compared to the box and image analysis due to the localized nature of the reading, however the trend is consistent.

Representative section analysis results for the surface and box analysis are given in Figures 9.5 to 9.8. This is separated into shiny and matte sides for the two roll finished used in the production of the light gauge foil.

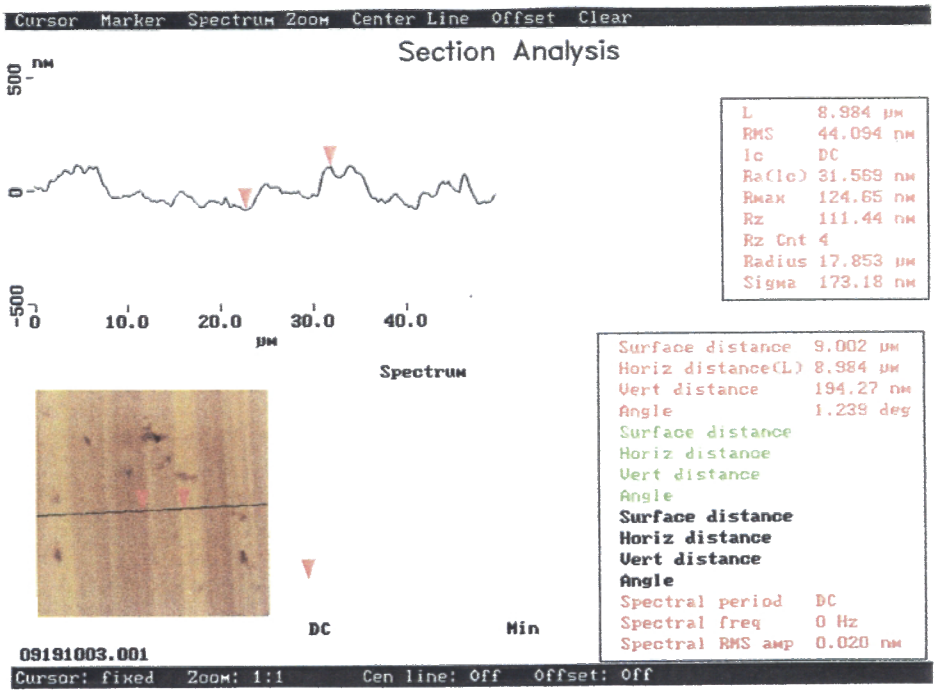

(a)

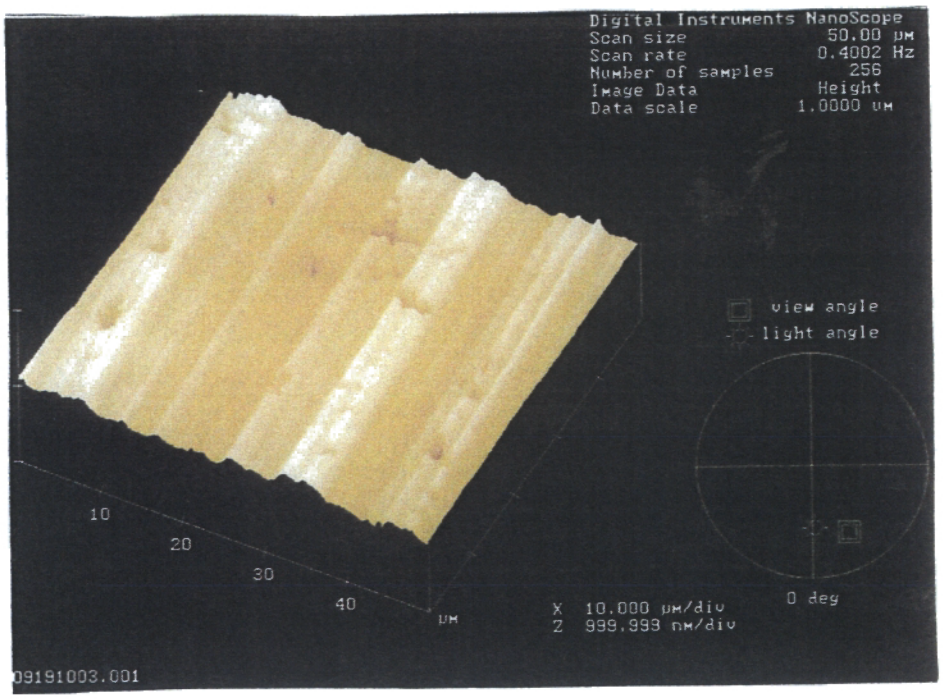

(b)

Figure 9.5. **Surface roughness for shiny sample processed using 5 - 7 Ra roll finish – B1 (a) section scan (b) three dimensional image**

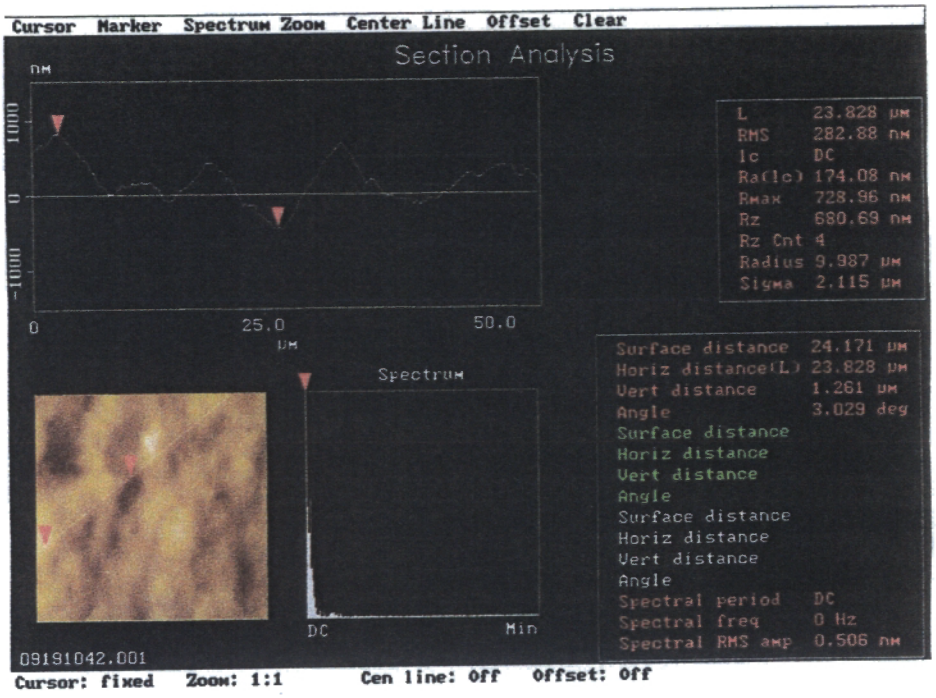

(a)

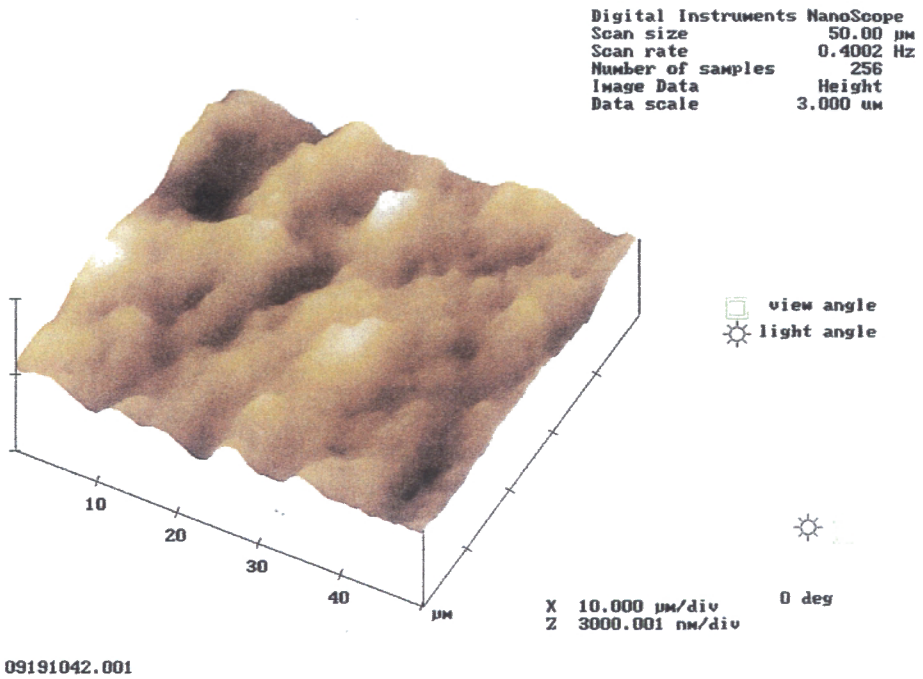

(b)

Figure 9.6. Surface roughness for matte sample processed using 5 - 7 Ra roll finish – B1 (a) section scan (b) three dimensional image

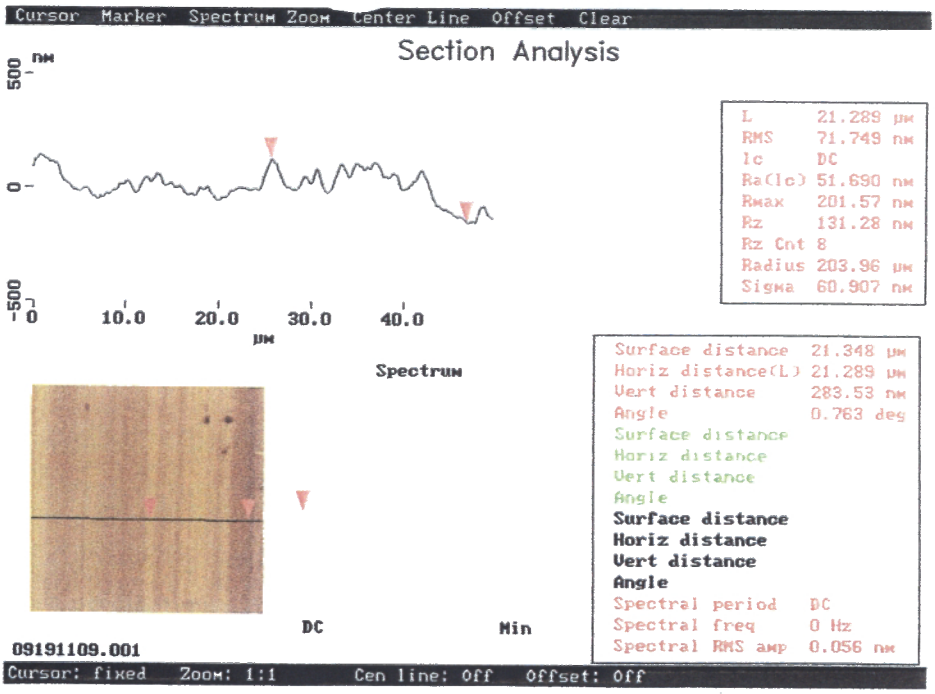

(a)

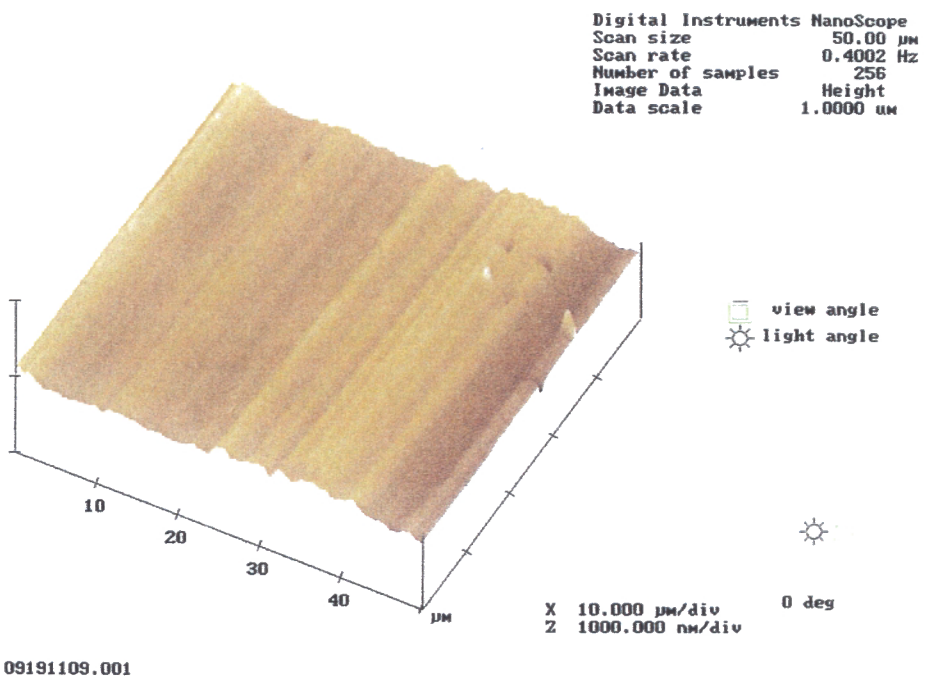

(b)

Figure 9.7. **Surface roughness for shiny sample processed using 14-16 Ra roll finish – B2 (a) section scan (b) three dimensional image**

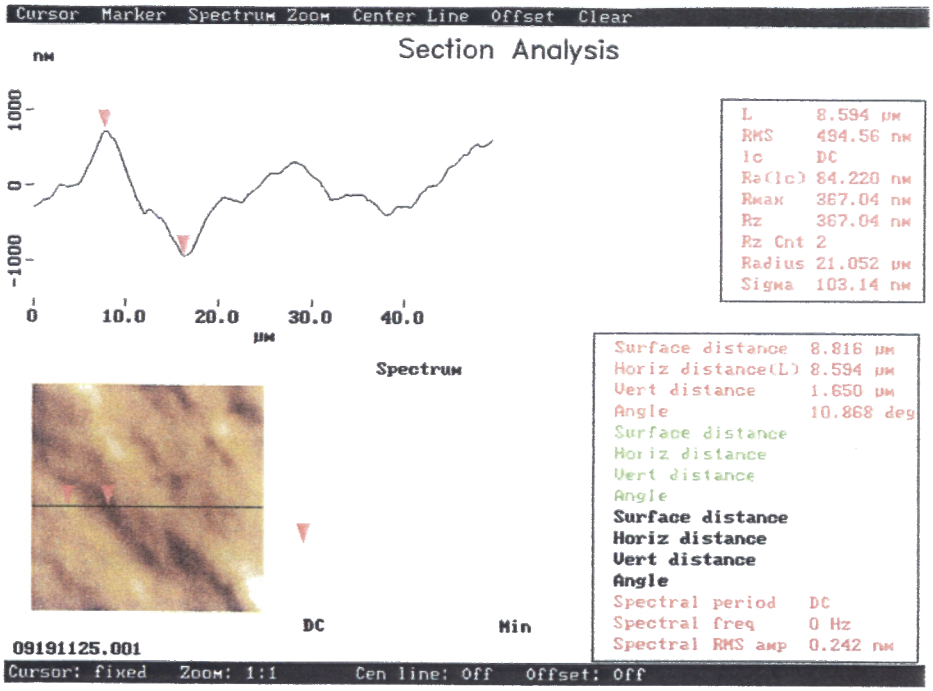

(a)

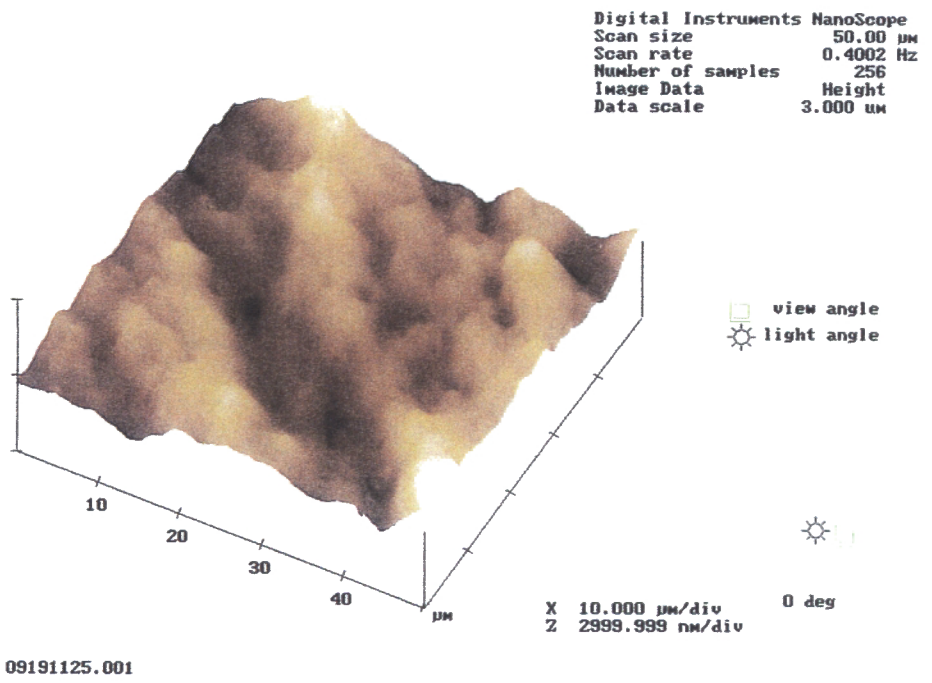

(b)

Figure 9.8. **Surface roughness for matte sample processed using 14-16 Ra roll finish – B2 (a) section scan (b) three dimensional image**

9.1.2. Surface Oxides and Oxide Depth

All four samples show trends with surface aluminium oxide levels at around 33.5-34.5%, while the metallic aluminium levels were at 9-10% for both samples. The remainder was 'other' oxygen compounds including (C_xO_y) compounds and trace elements where x and y represent various molecule combinations.

Aluminium oxide levels visually increased slightly to about the 0.4nm mark, before dropping to less than 50% of their start values at around the 4nm, and less than 5% by 10nm. Work by Williams[3] showed the carbon layer due to entrapped coolant to be approximately 0.3nm thick, which supports the results of the depth profile. The 'other' oxide compounds also drop at a similar rate. The oxide depth appears to follow an inverse logarithmic growth pattern.

The oxygen, aluminium and aluminium oxide atomic percentages were plotted versus depth on an x-y axis chart. This was based on three dimensional depth profile for the above named metal and oxides. Representative results are presented in Figures 9.9 to 9.16, for both surface morphologies and roll finishes. The first figure will be the depth profile with the second figure being the oxygen and aluminium three dimensional peak count representations.

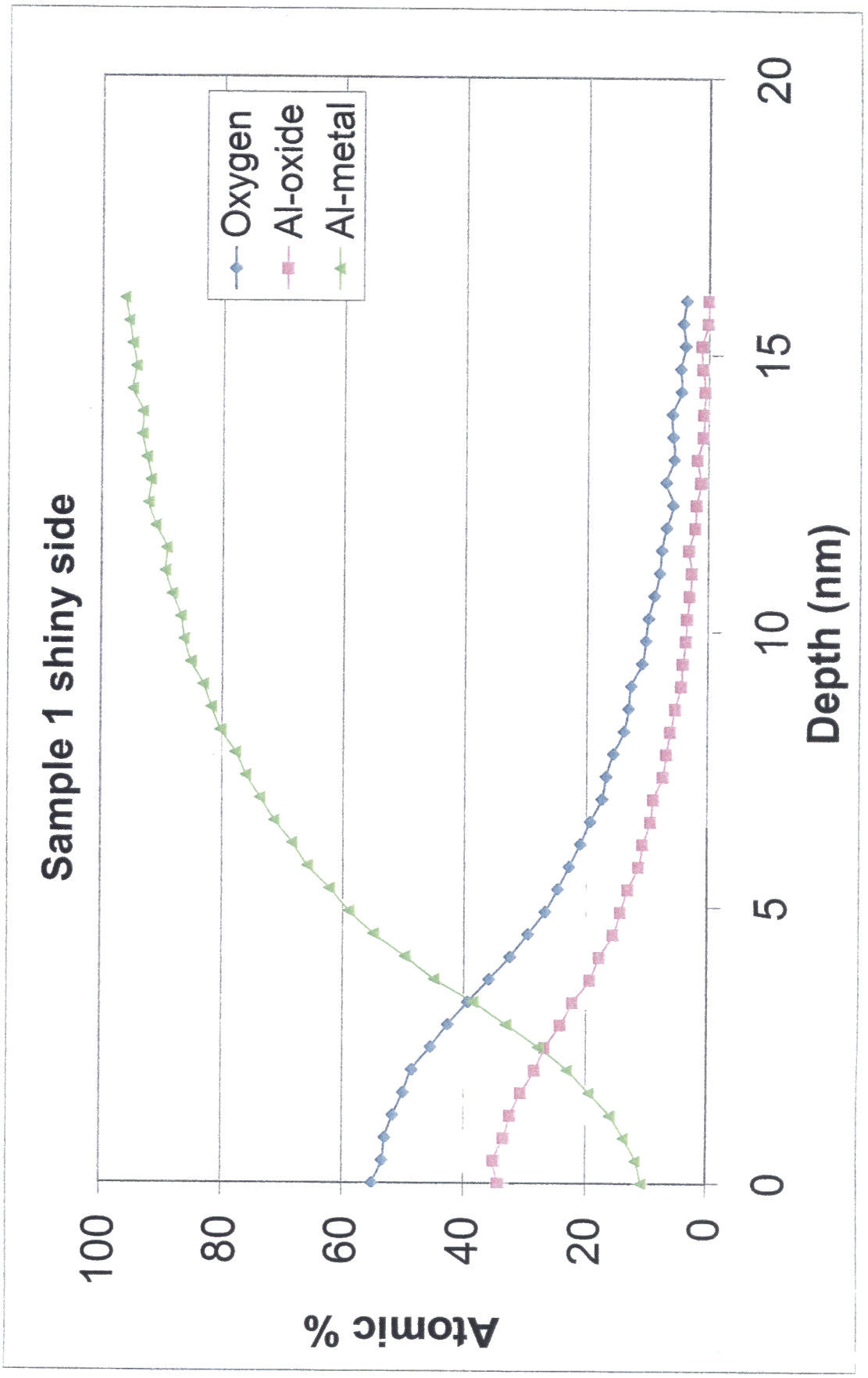

Figure 9.9. **Depth profile for oxygen, aluminium and oxides for shiny thermal treated sample processed using 5 - 7 Ra roll finish –B1**

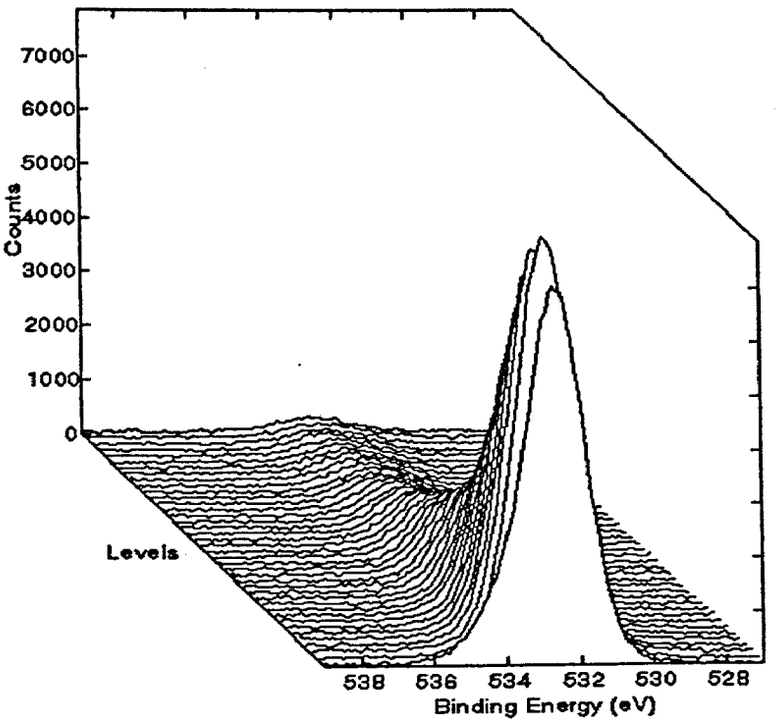

(a)

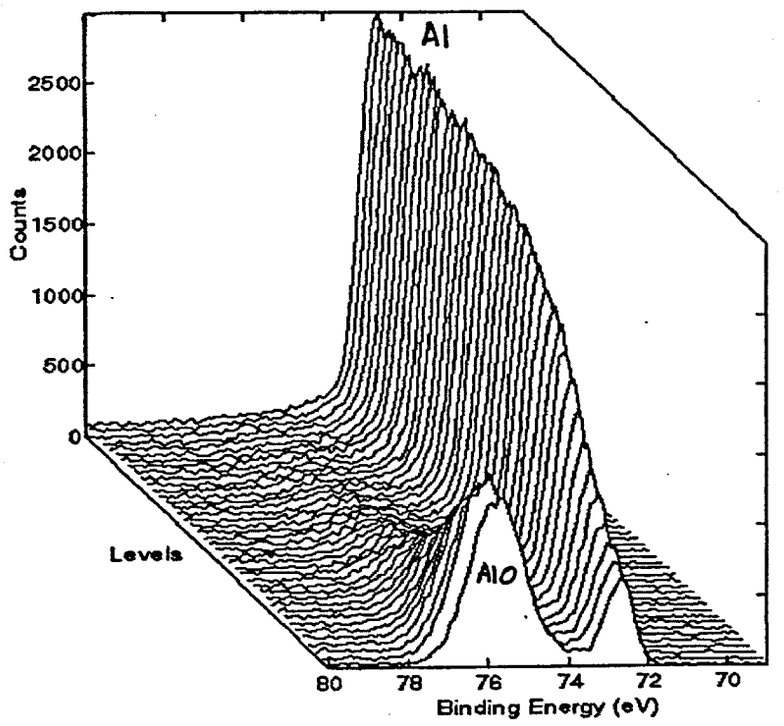

(b)

Figure 9.10. **Three dimensional representation of peak count for shiny thermal treated sample processed using 5 - 7 Ra roll finish –B1, (a) oxygen (b) aluminium and aluminium oxide**

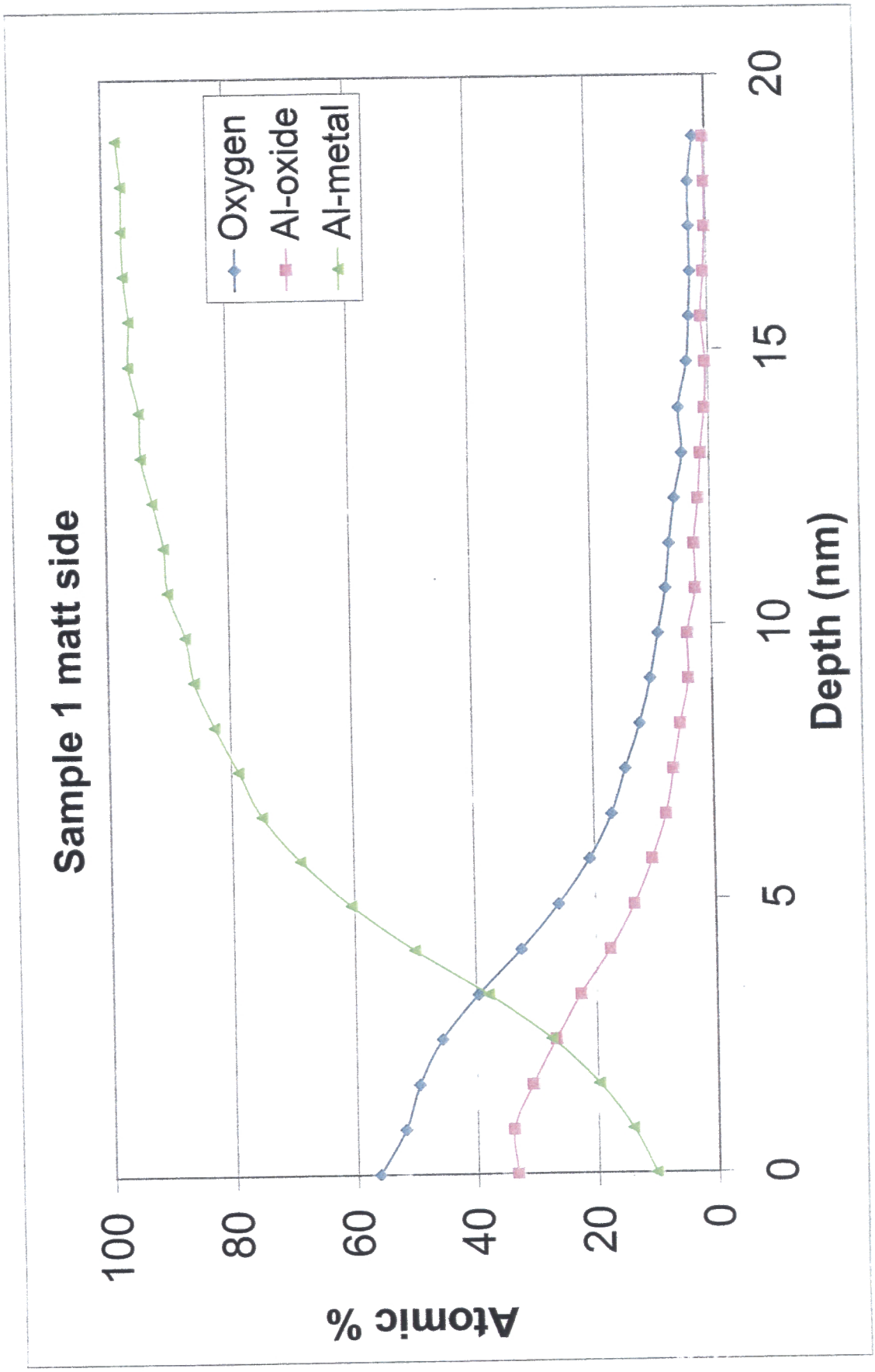

Figure 9.11. **Depth profile for oxygen, aluminium and oxides for matte thermal treated sample processed using 5 - 7 Ra roll finish –B1**

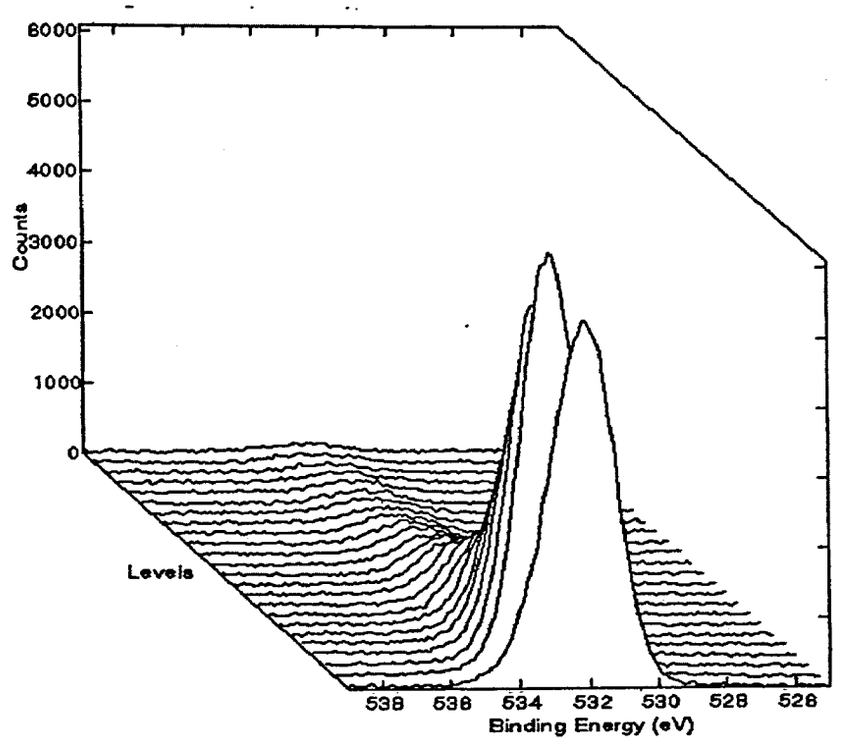

(a)

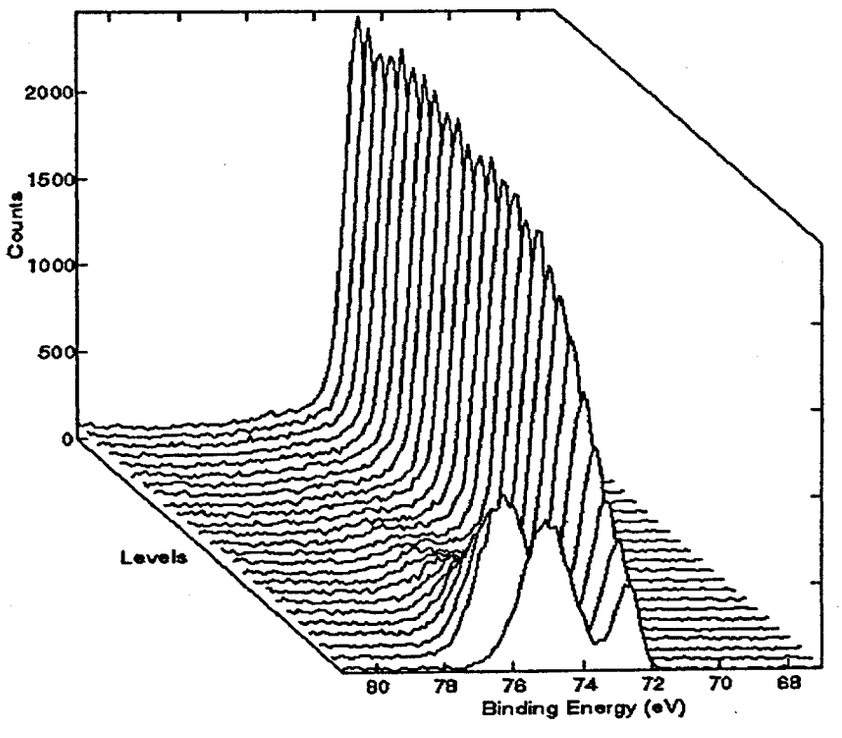

(b)

Figure 9.12. **Three dimensional representation of peak count for matte thermal treated sample processed using 5 - 7 Ra roll finish –B1, (a) oxygen (b) aluminium and aluminium oxide**

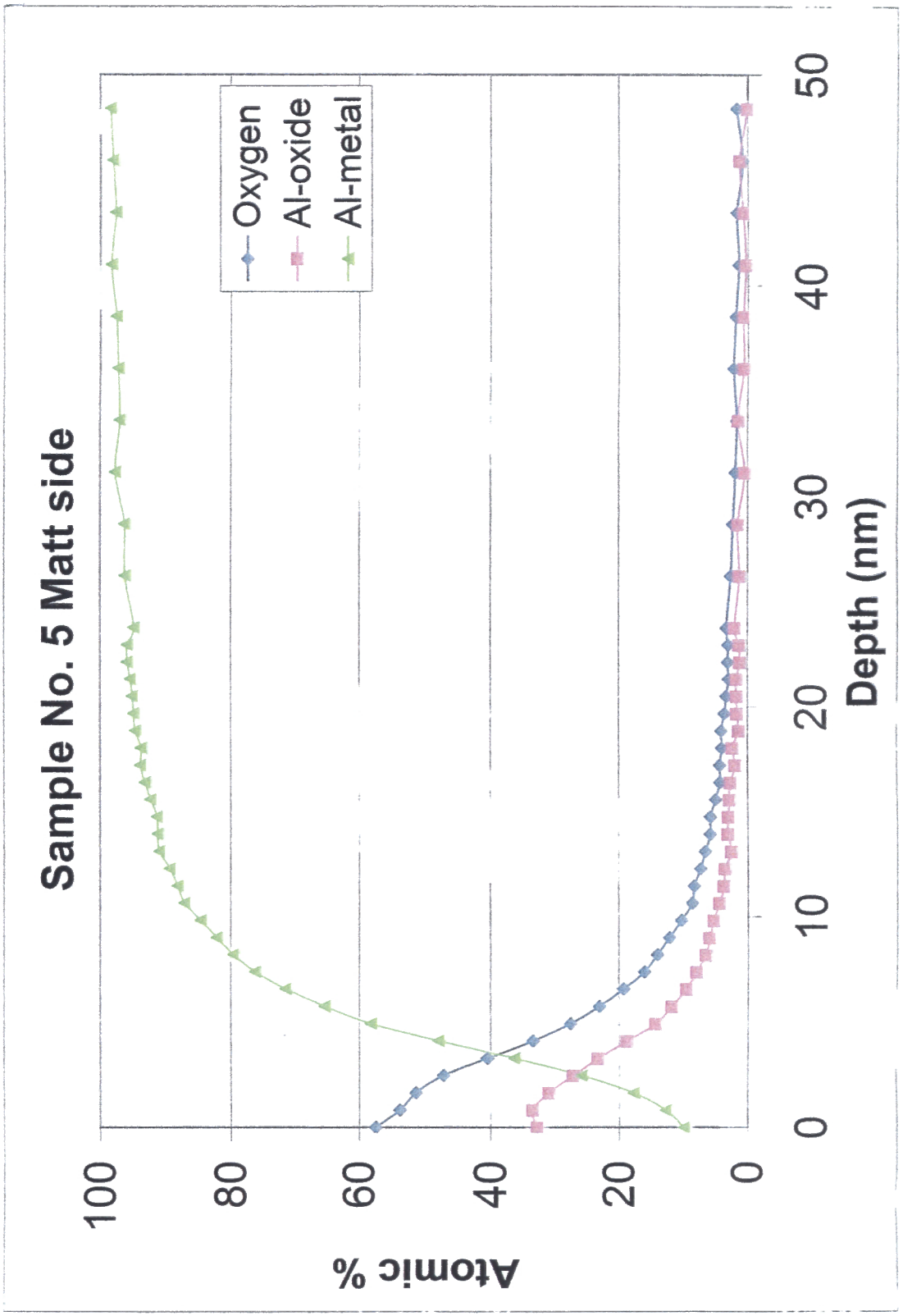

Figure 9.13. **Depth profile for oxygen, aluminium and oxides for shiny thermal treated sample processed using 14 - 16 Ra roll finish – B2**

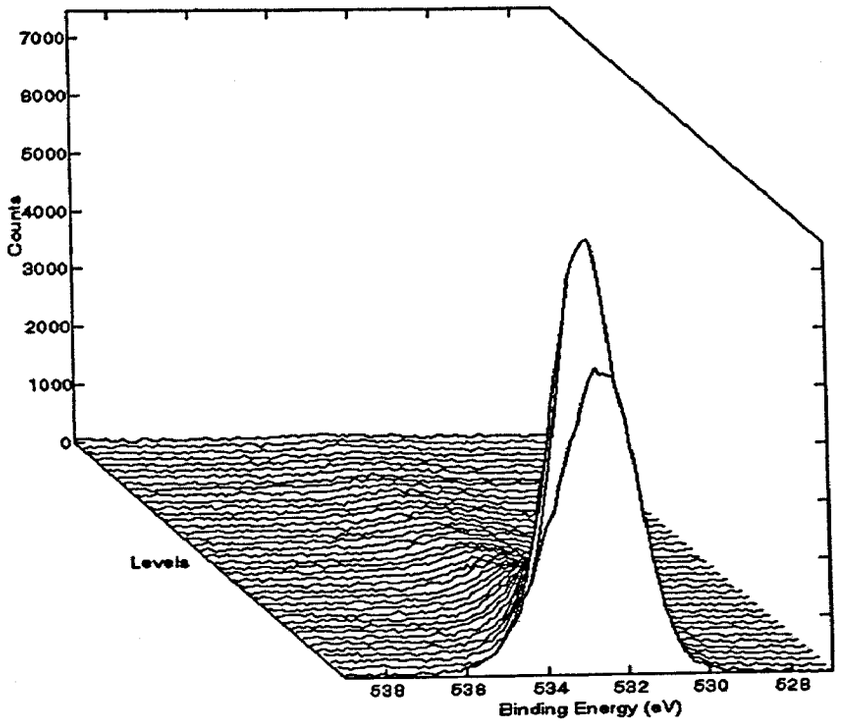

(a)

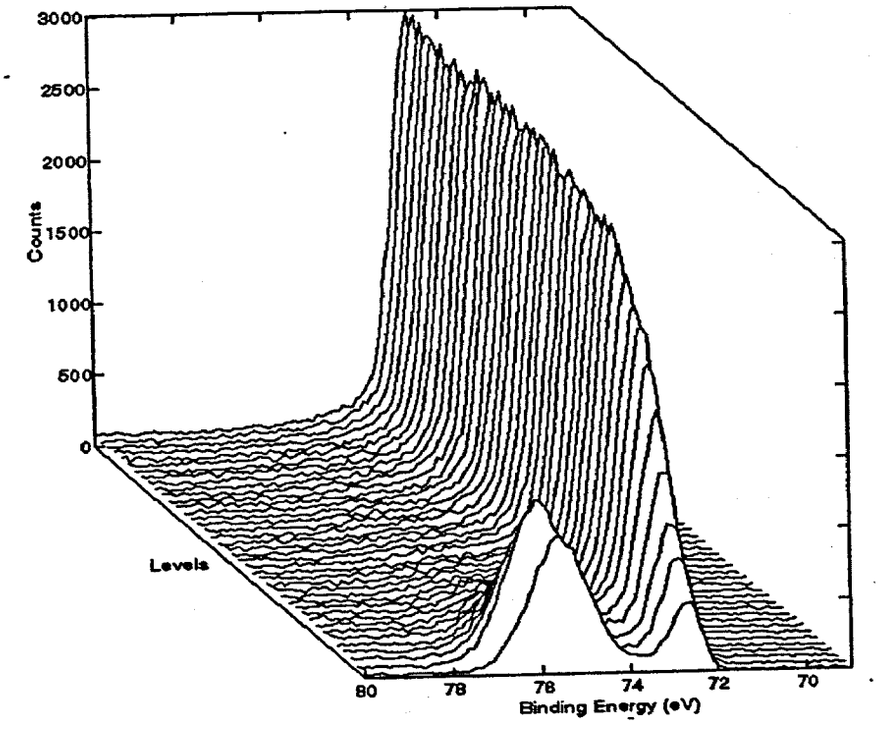

(b)

Figure 9.14. **Three dimensional representation of peak count for shiny thermal treated sample processed using 14 - 16 Ra roll finish – B2, (a) oxygen (b) aluminium and aluminium oxide**

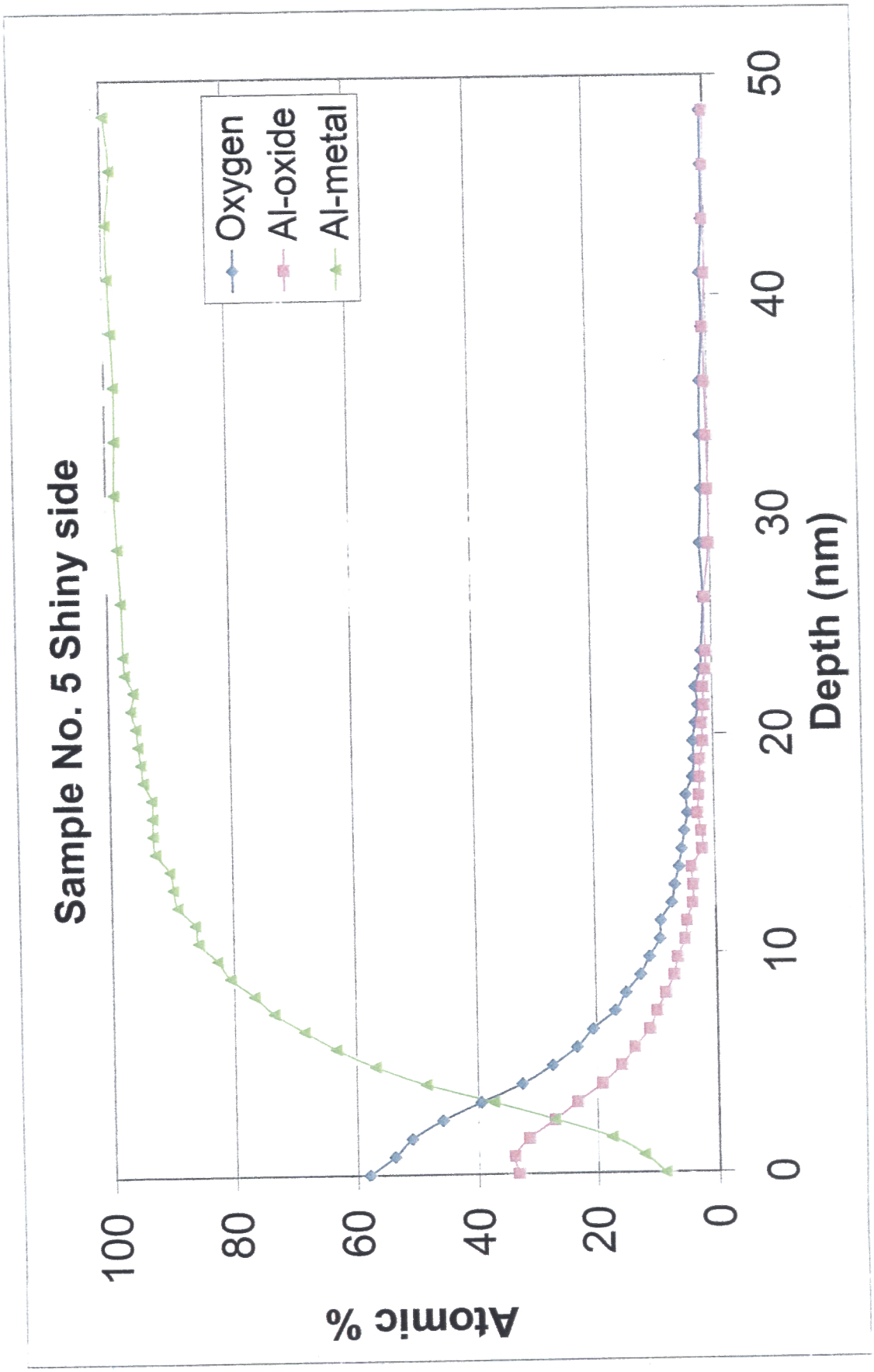

Figure 9.15. **Depth profile for oxygen, aluminium and oxides for matte thermal treated sample processed using 14 - 16 Ra roll finish – B2**

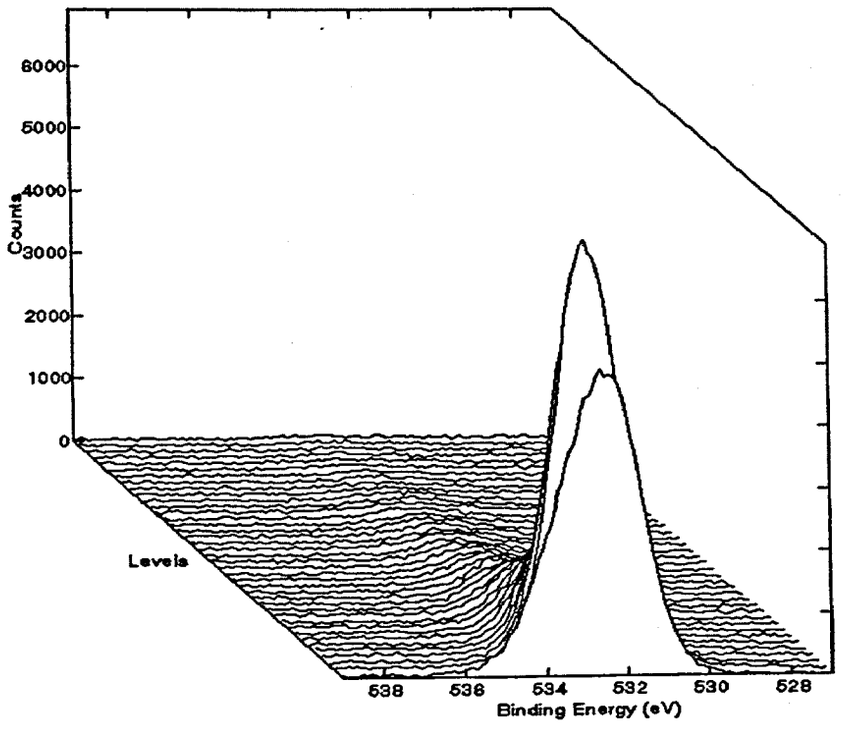

(a)

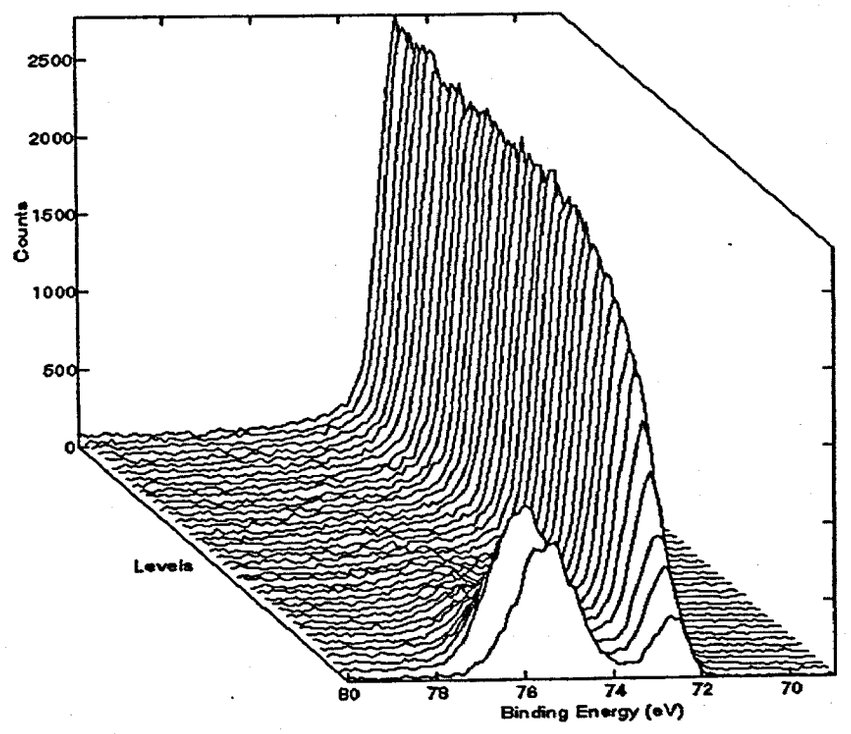

(b)

Figure 9.16. **Three Dimensional representation of peak count for matte thermal treated sample processed using 14 - 16 Ra roll finish – B2, (a) oxygen (b) aluminium and aluminium oxide**

9.1.3. Surface Composition

The samples were submitted to a general surface scan, Figure 9.17 - 18, with the composition summarized in Table 9.5. The surface composition, taken at the very surface of the shiny and matte surfaces for both samples, are composed of principally of oxygen, aluminium and carbon based species, with trace elements manganese, magnesium, tin, copper, fluorine and nitrogen present in amounts less than 0.30%, with most amounts less than 0.05%.

Sample	B1 – 5-7 Ra		B2 – 14-16 Ra	
Classification	Shiny - 235°C	Matte – 235°C	Shiny - 285°C	Matte - 285°C
Al – Oxide	27.23	26.43	28.25	28.85
Al – metal	6.58	7.34	7.01	8.8
O – Al oxide	24.51	24.55	17.87	28.11
O – Al hydroxide	15.03	13.46	20.48	14.60
O – Other	6.57	7.61	7.61	5.66
C – Hydrocarbon	16.6	16.05	16.03	11.45
C – Org Hydroxyl	1.34	1.70	0.81	0.93
C – Carboxyl	2.02	2.33	1.75	1.38
Sn – Oxide			0.02	0.01
Sn – Metal			0.03	0.05
Mn – Oxide	0.02	0.02	0.02	0.02
Mn – Metal	0.04	0.04	0.03	0.04
Mg – Oxide		0.15	0.10	
Cu – Oxide	0.05	0.05		
F				0.10
N		0.28		

Table 9.5. **Summary of XPS quantification (atomic %) for surface composition of samples thermally treated at 235 °C and 285°C**

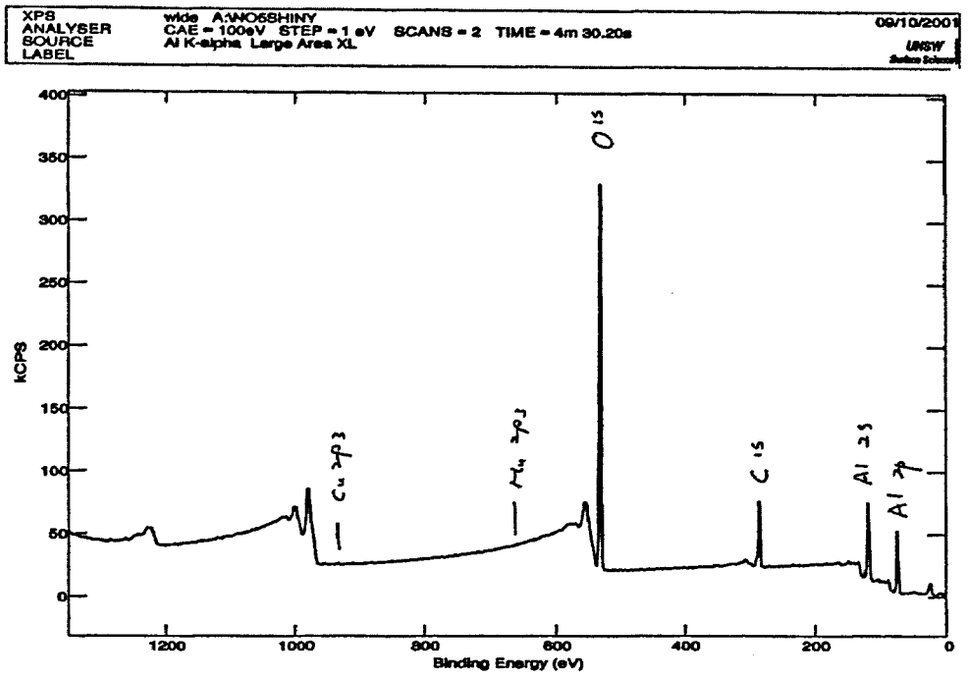

(a)

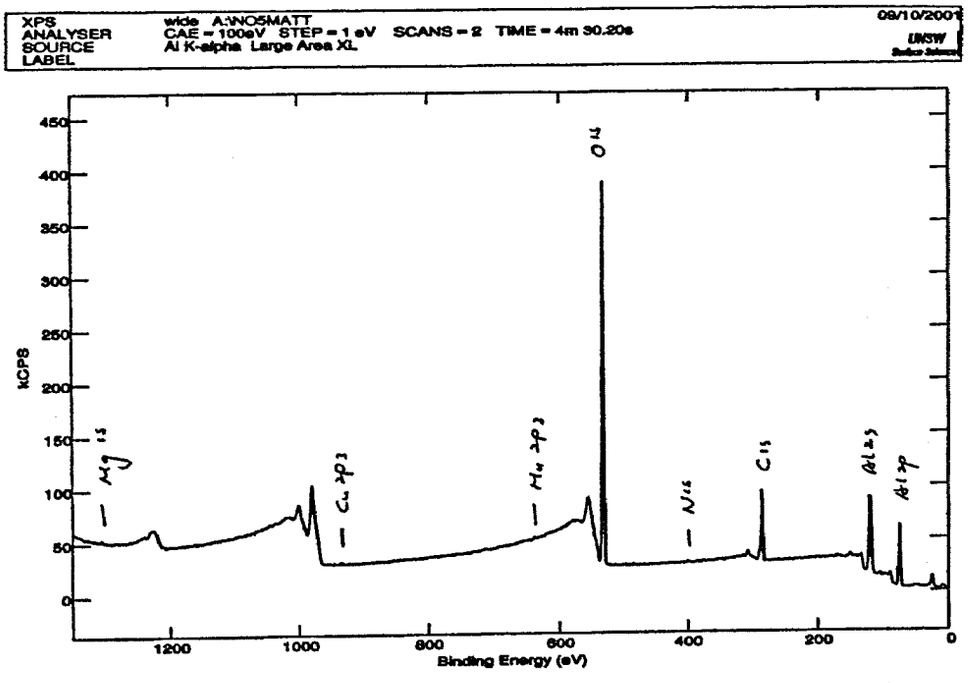

(b)

Figure 9.17. **General surface scans on aluminium sample processed using 5 – 7 Ra roll finish – B1 samples thermally treated at 235°C, (a) shiny surface (b) matte surface**

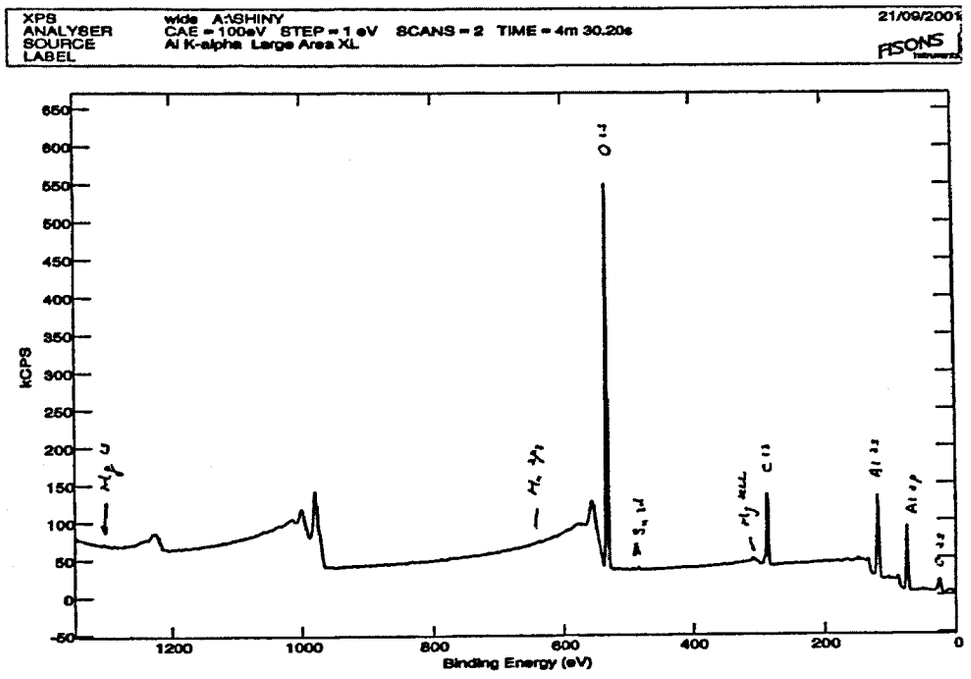

(a)

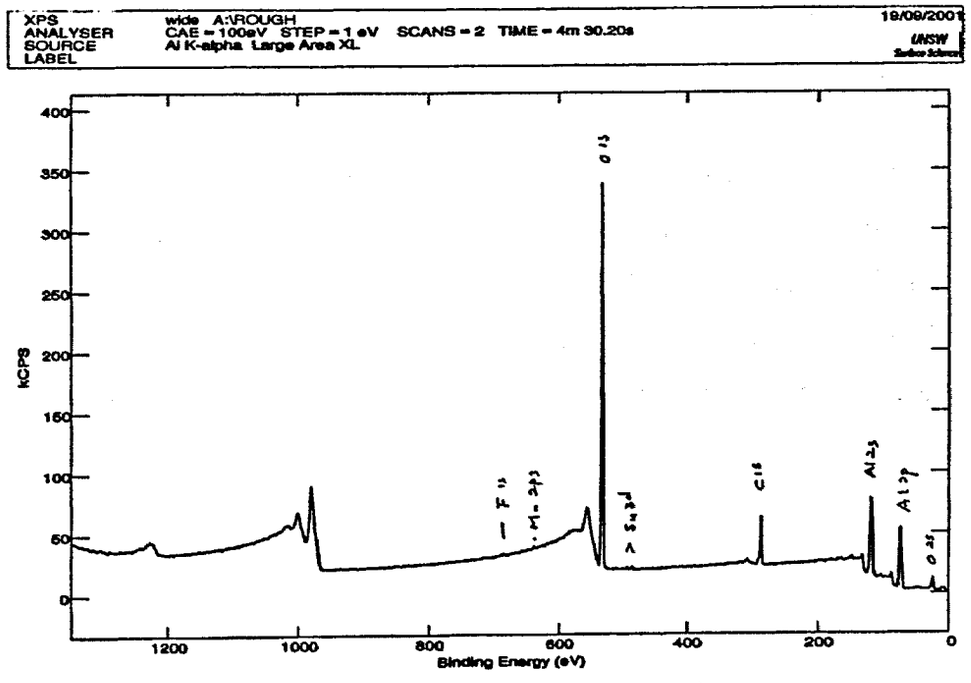

(b)

Figure 9.18. **General surface scans on aluminium sample processed using 14 - 16 Ra roll finish – B2 samples thermally treated at 285°C, (a) shiny surface (b) matte surface**

The peaks were further subject to a high resolution scan using standards, to aid in determining the component present and the atomic percentage. The Quantification table for each of the four samples is given in Appendix 11. The schematic of the results are represented in Figures 9.19 to 9.31. A sample calibration was run prior to the sample run analysis to determine the cleanliness of the vacuum chamber

The carbon scans showed a double peak, as well as some peak width spread in both peaks. The double peak spread indicated the presence of carbonaceous material, probably composed of CH_n groups as well as a small amount of oxidised carbon functional groups. Oxidised carbon groups occur at a slightly higher binding energy than the hydrocarbon group (287-290eV versus 286ev) due to the difference in electronic environment of each atom, and were found to be organic hydroxyls and carboxyls. All elements detected are curve fitted in accordance with a known organic sample.

The source of the oxidized carbon molecules and other hydrocarbon groups was the oxidation and polymerization of the surface lubricant used during the rolling process. The annealing process is performed in an air atmosphere at temperatures greater than 200°C.

The oxygen scan showed a double peak with the presence of hydroxides, while the aluminium scan showed two distinct peaks, the lower one for aluminium metal, and the higher one for aluminium oxide in the form Al_2O_3. The composition for each sample also contained some unexpected elements. One or more fractional atomic percentage amounts of copper, fluorine, nitrogen or tin were present on the sample surface.

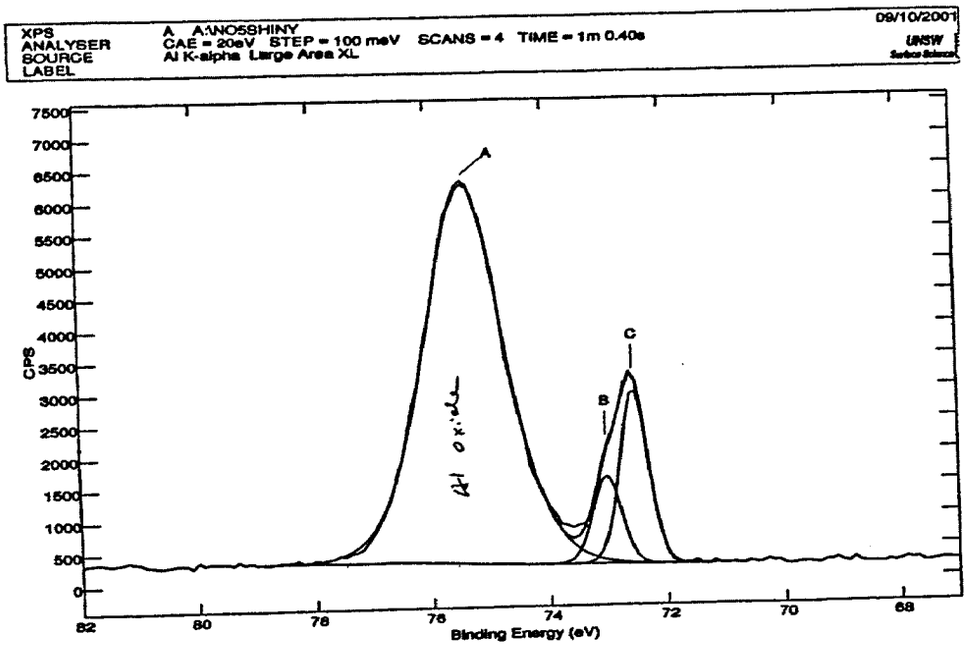

(a)

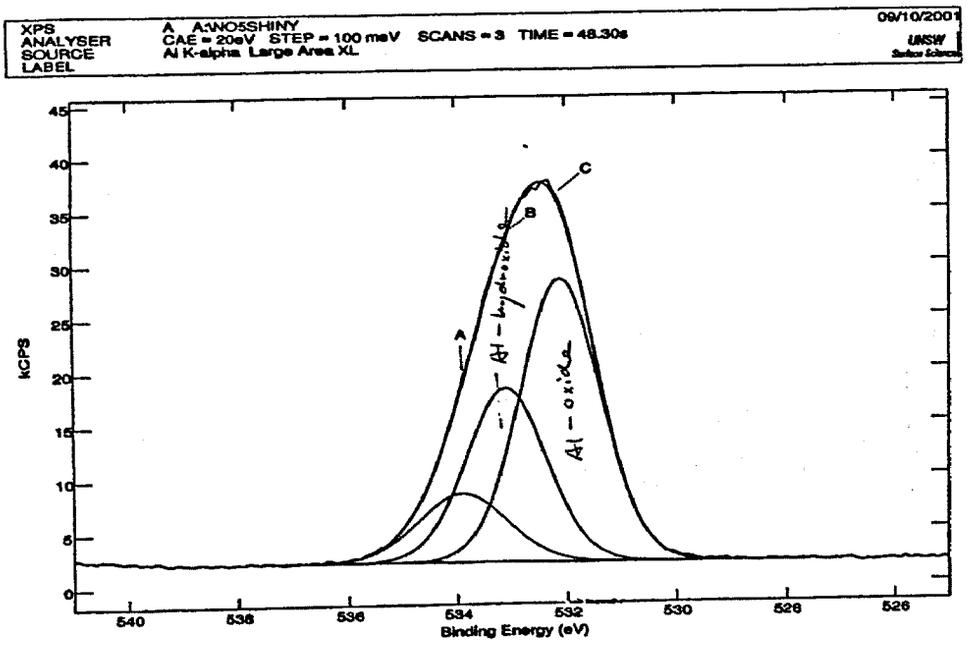

(b)

Figure 9.19. **High resolution scan for shiny sample processed using 5 - 7 Ra roll finish – B1 samples thermally treated at 235 °C, (a) aluminium (b) oxygen**

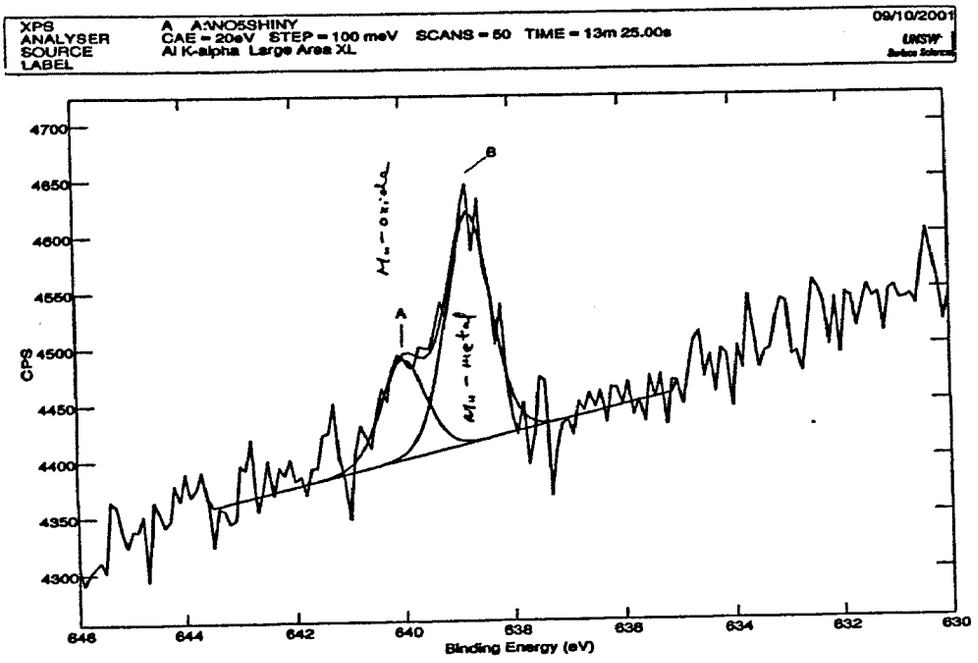

(a)

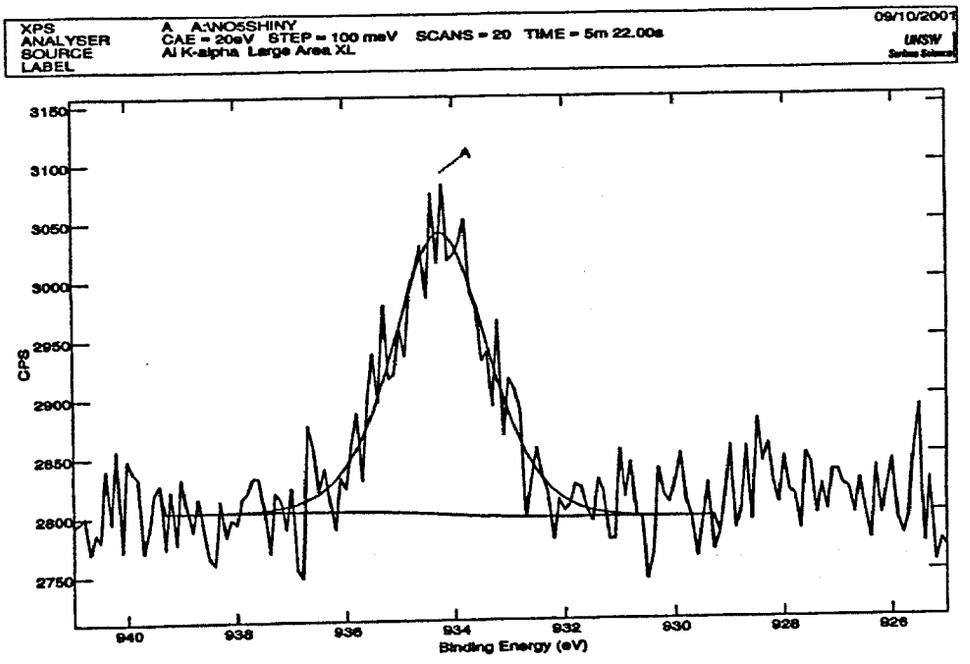

(b)

Figure 9.20. **High resolution scan for shiny sample processed using 5 - 7 Ra roll finish – B1 samples thermally treated at 235 °C, (a) manganese (b) copper**

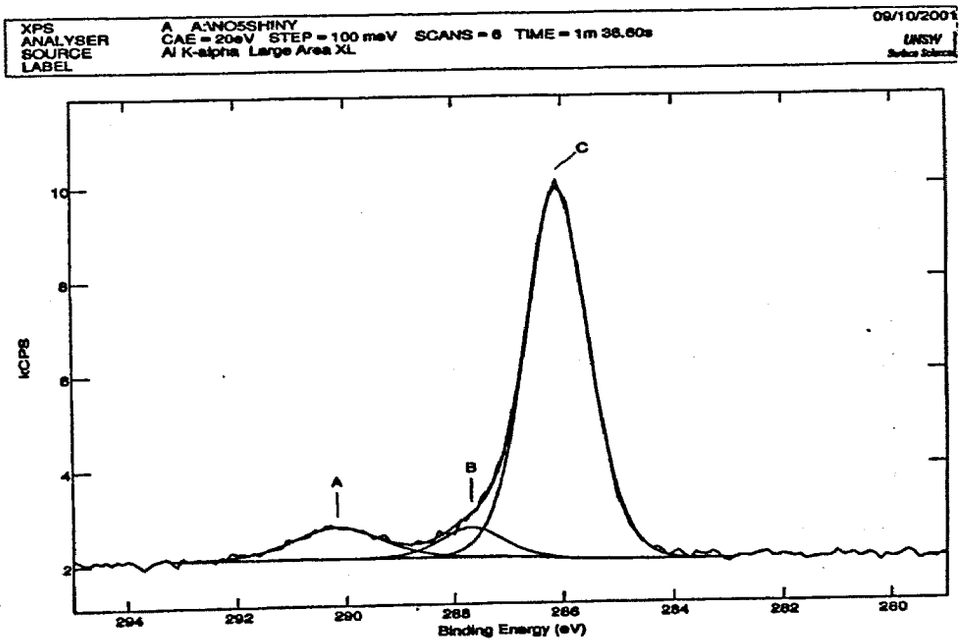

(a)

Figure 9.21. **High resolution scan for shiny sample processed using 5 - 7 Ra roll finish – B1 samples thermally treated at 235 °C, (a) carbon**

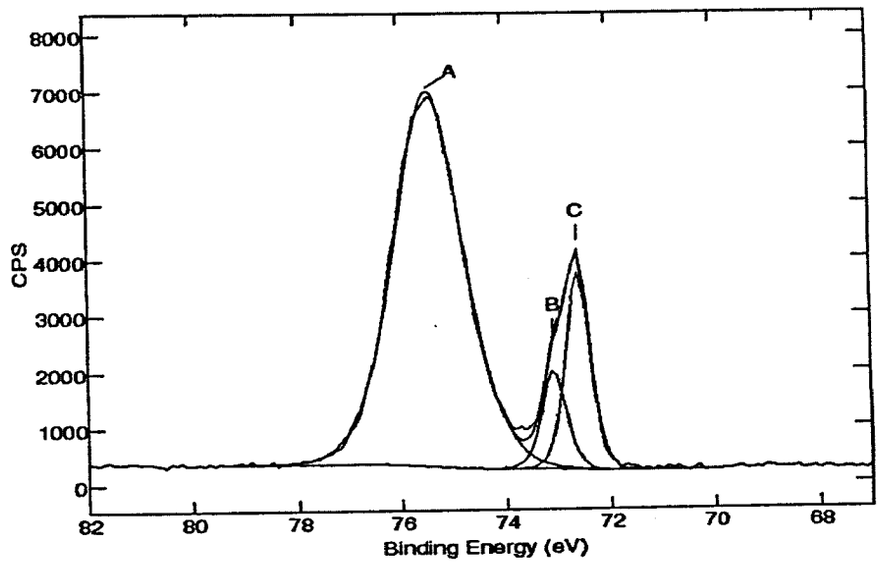

(a)

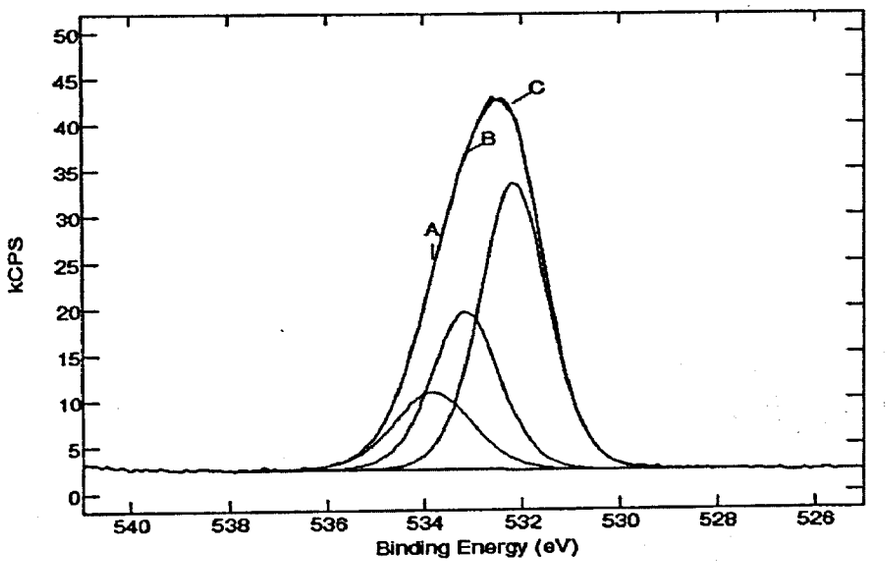

(b)

Figure 9.22. **High resolution scan for matte sample processed using 5 - 7 Ra roll finish – B1 samples thermally treated at 235 °C, (a) aluminium (b) Oxygen**

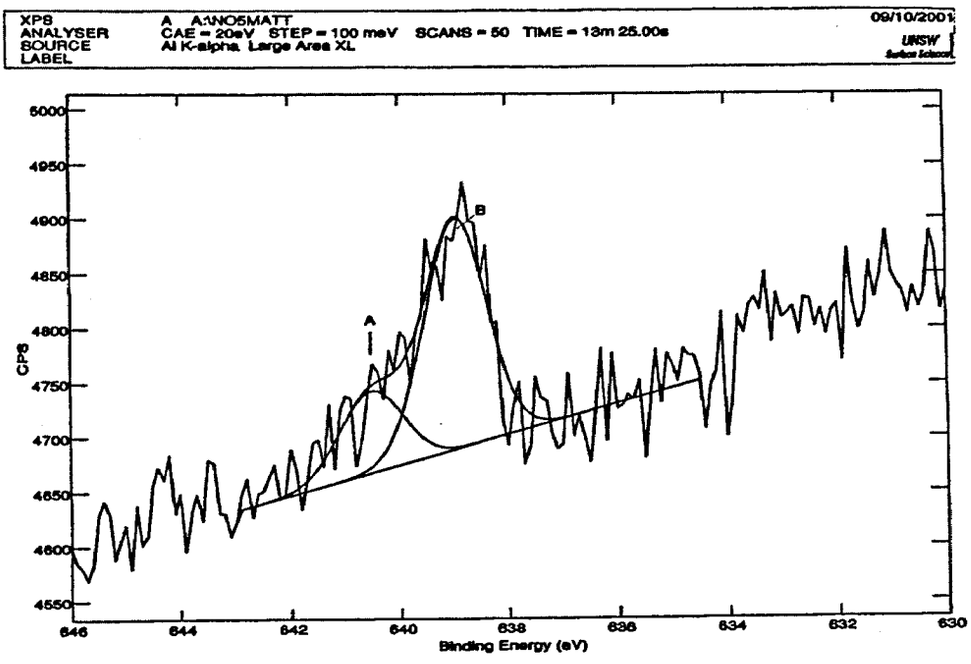

(a)

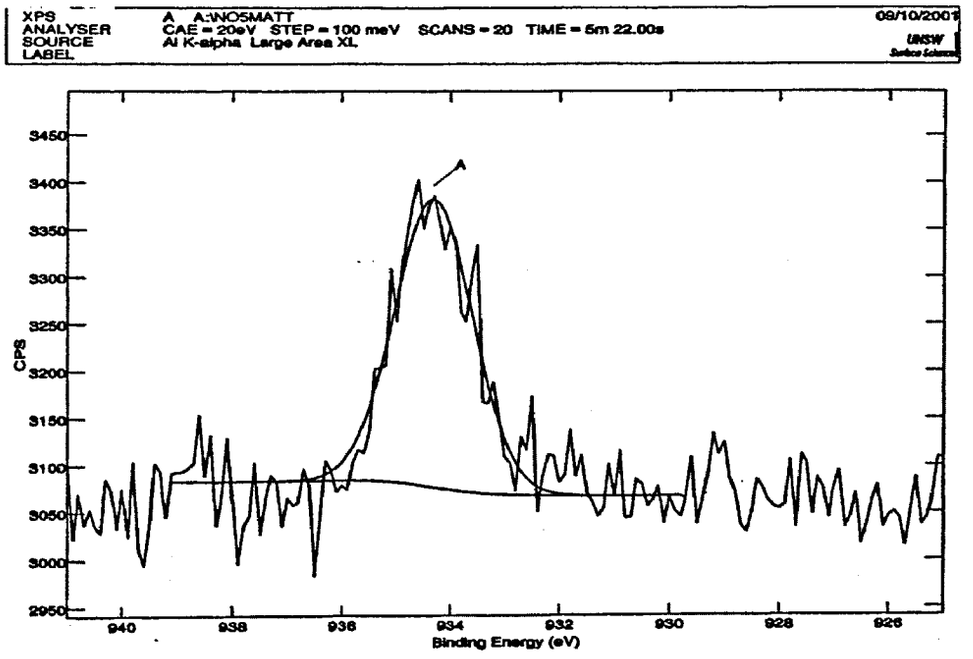

(b)

Figure 9.23. **High resolution scan for matte sample processed using 5 - 7 Ra roll finish – B1 samples thermally treated at 235 °C, (a) manganese (b) copper**

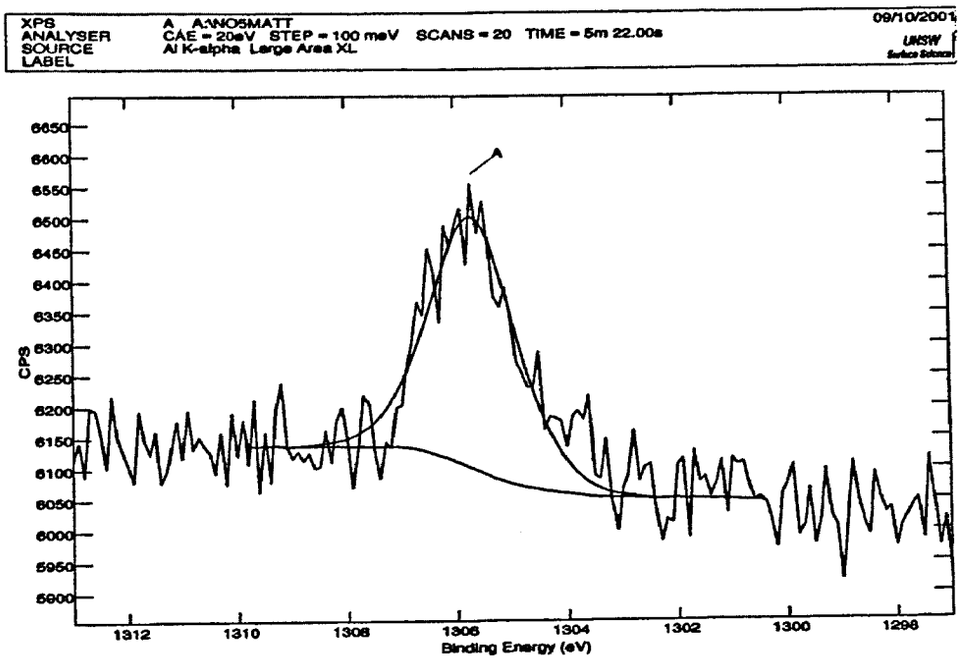

(a)

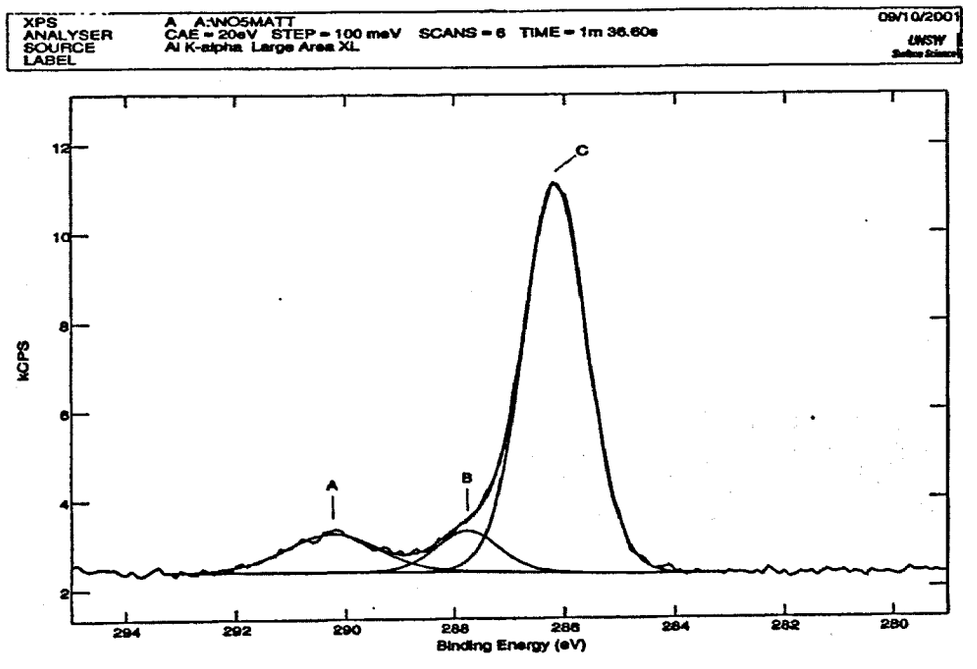

(b)

Figure 9.24. **High resolution scan for matte sample processed using 5 - 7 Ra roll finish – B1 samples thermally treated at 235 °C, (a) magnesium (b) carbon**

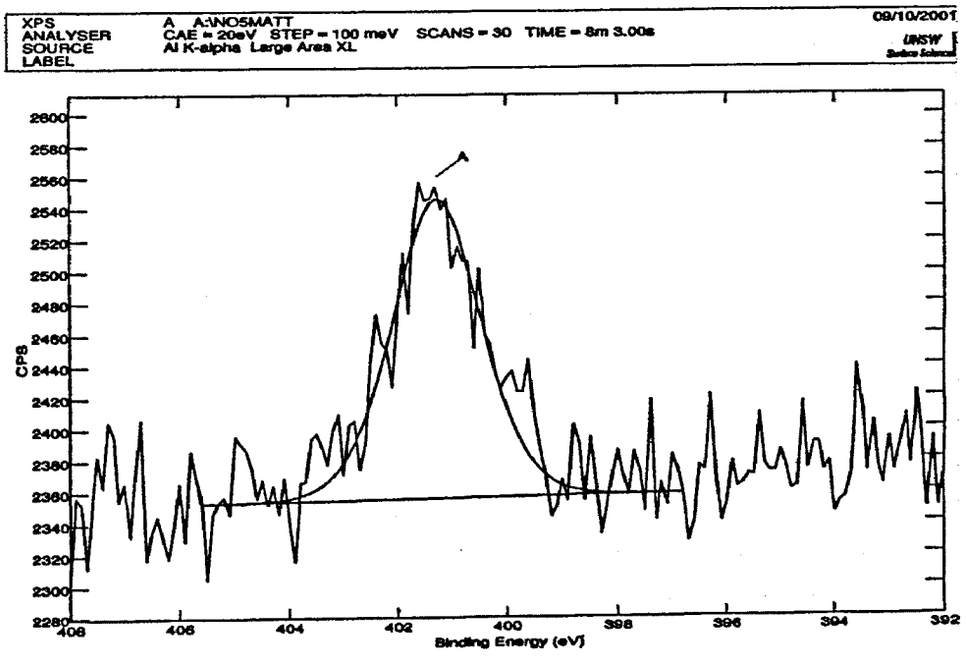

(a)

Figure 9.25. **High resolution scan for matte sample processed using 5 - 7 Ra roll finish – B1 samples thermally treated at 235 °C, (a) nitrogen**

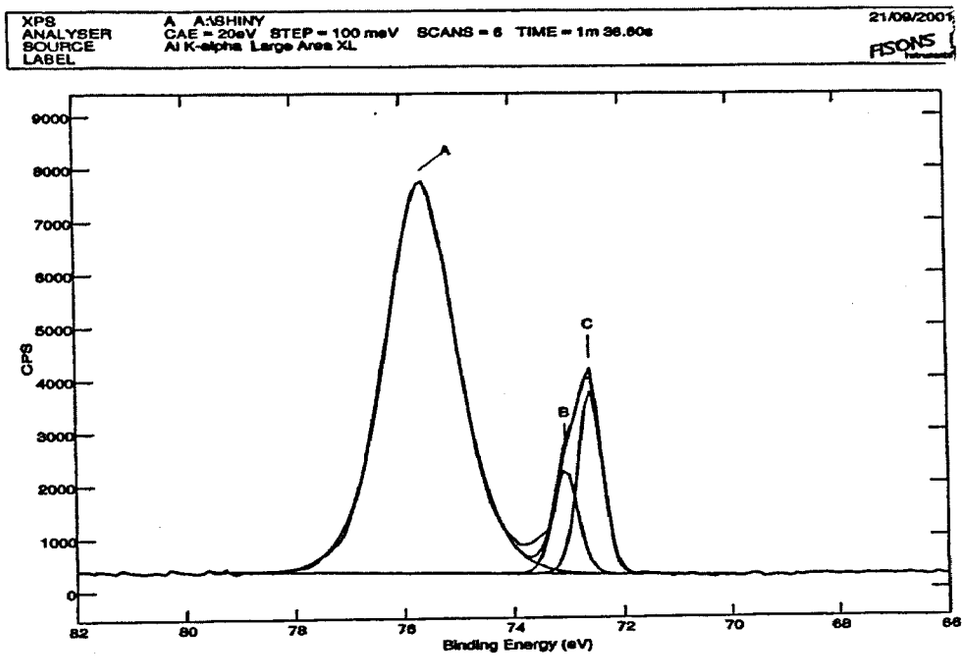

(a)

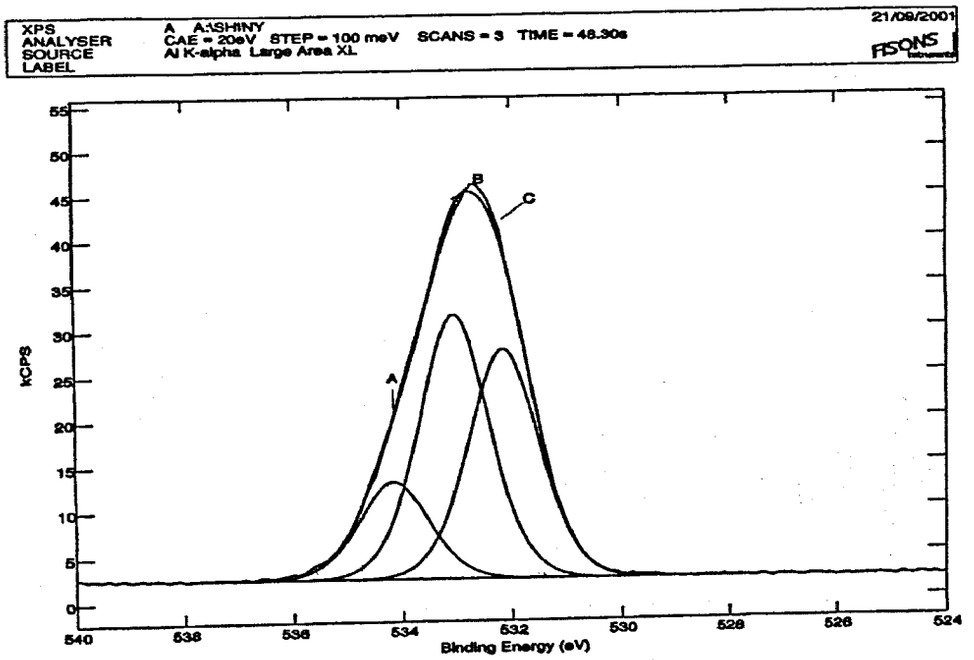

(b)

Figure 9.26. **High resolution scan for shiny sample processed using 14 - 16 Ra roll finish – B2 samples thermally treated at 285 °C, (a) aluminium (b) oxygen**

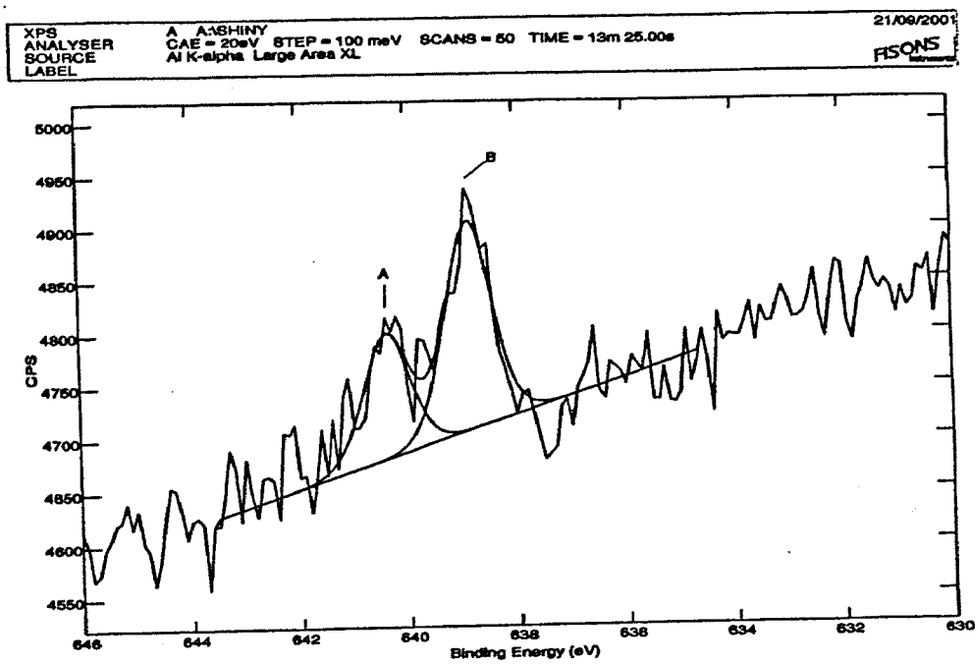

(a)

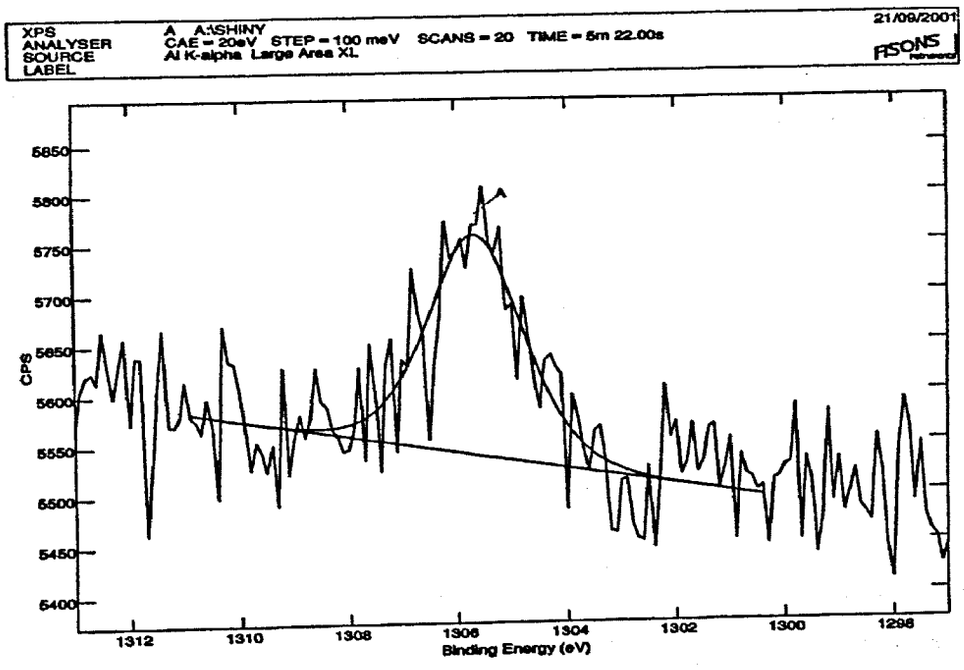

(b)

Figure 9.27. **High resolution scan for shiny sample processed using 14 - 16 Ra roll finish – B2 samples thermally treated at 285 °C, (a) manganese (b) magnesium**

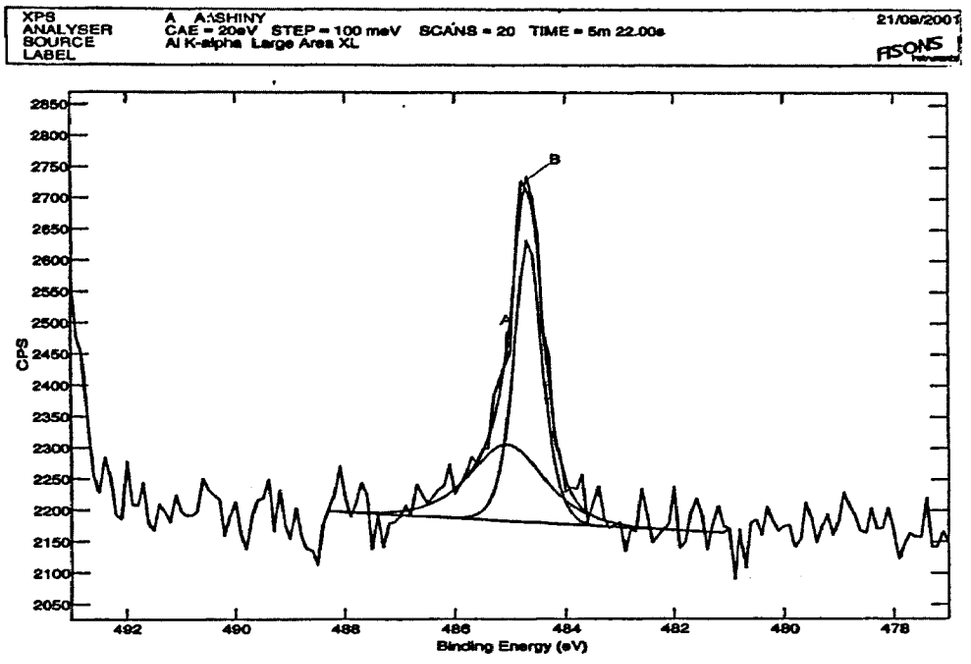

(a)

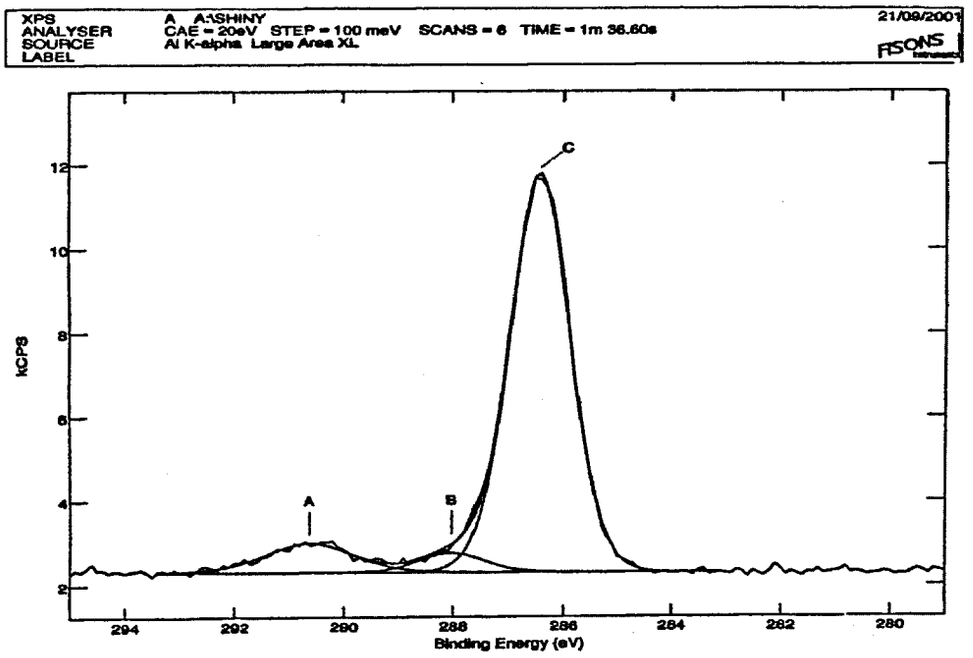

(b)

Figure 9.28. **High resolution scan for shiny sample processed using 14 - 16 Ra roll finish – B2 samples thermally treated at 285 °C, (a) tin (b) carbon**

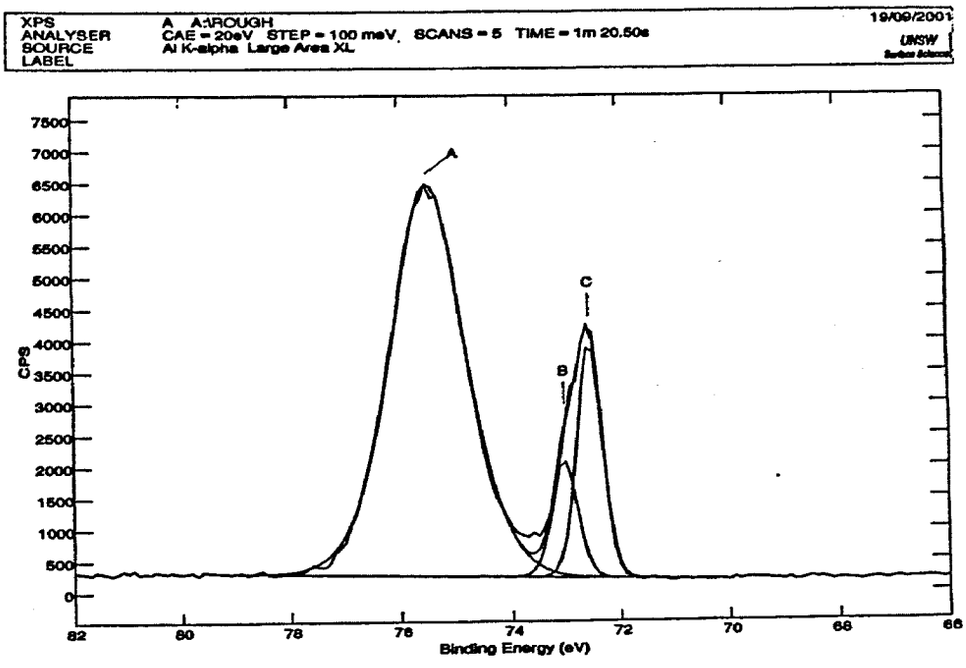

(a)

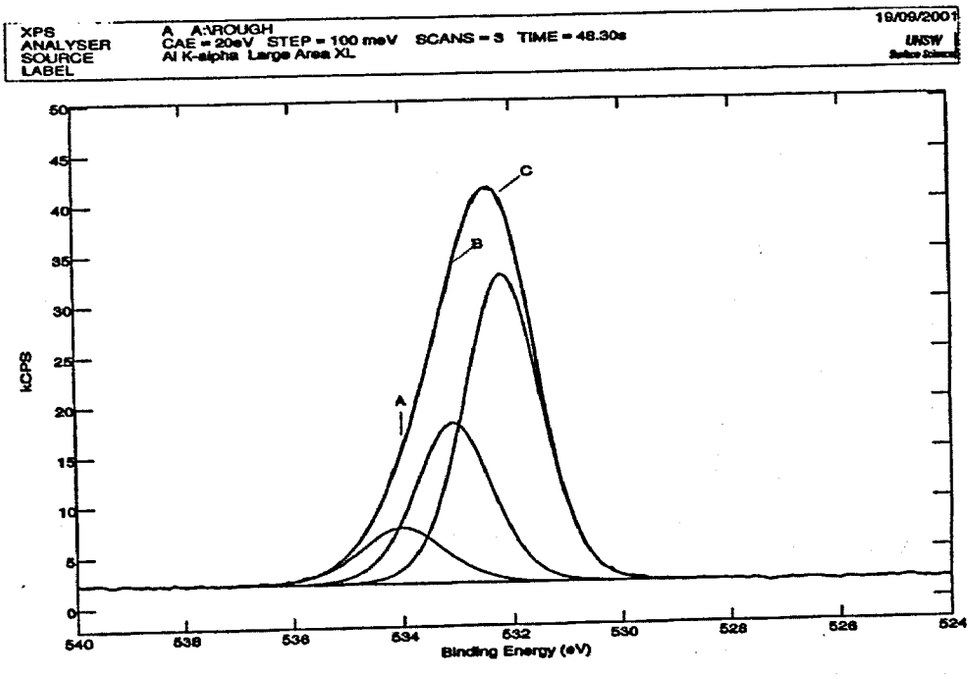

(b)

Figure 9.29. **High resolution scan for matte sample processed using 14 - 16 Ra roll finish – B2 samples thermally treated at 285 °C, (a) aluminium (b) oxygen**

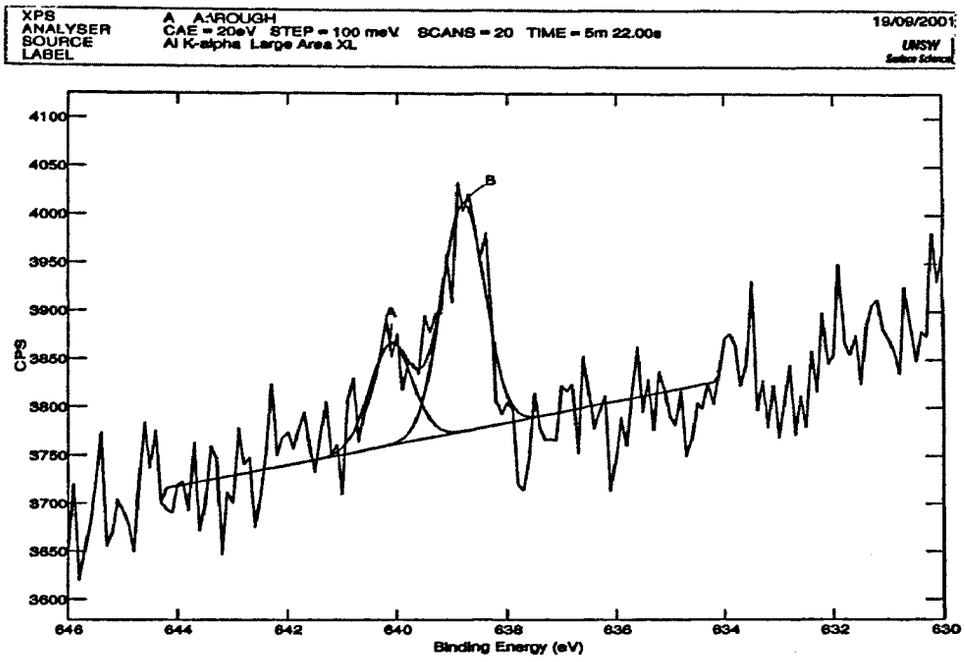

(a)

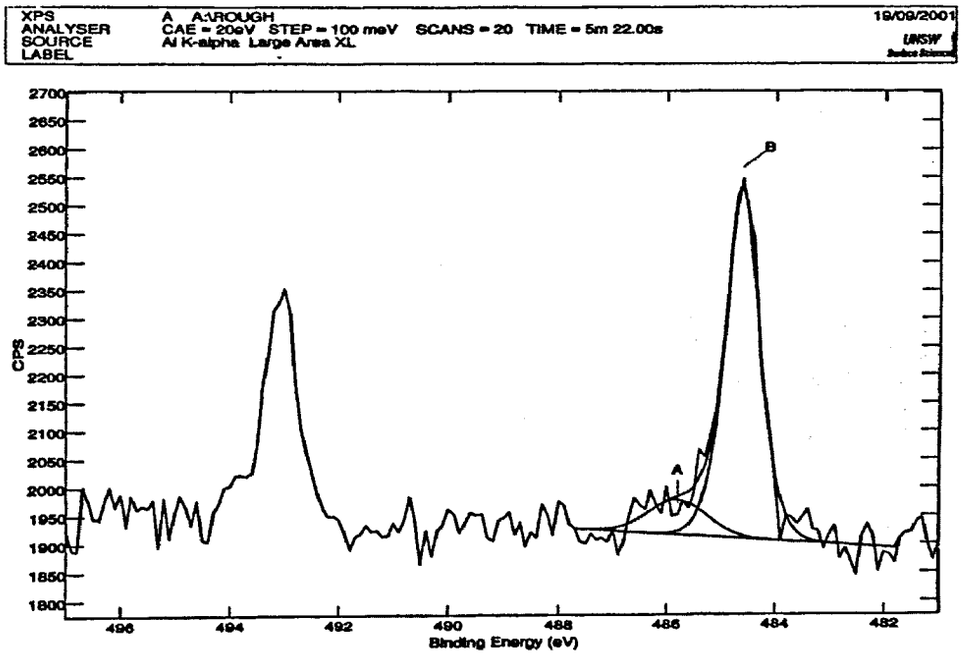

(b)

Figure 9.30. **High resolution scan for shiny sample processed using 14 - 16 Ra roll finish – B2 samples thermally treated at 285 °C, (a) manganese (b) tin**

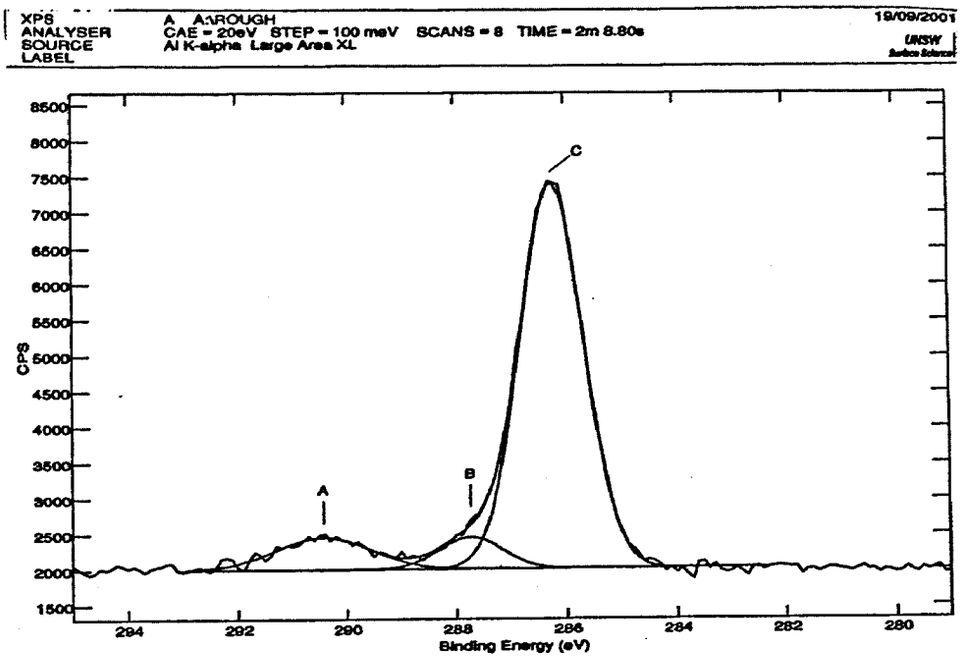

(a)

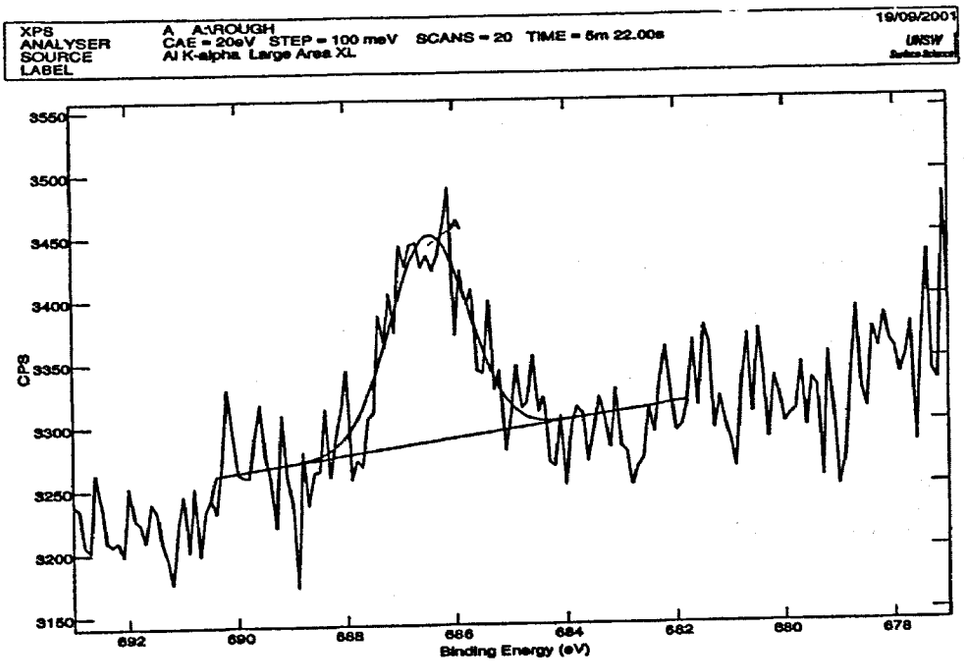

(b)

Figure 9.31. **High resolution scan for matte sample processed using 14 - 16 Ra roll finish – B2 samples thermally treated at 285 °C, (a) carbon (b) fluorine**

9.2. Microstructural Evaluation of AA8150

9.2.1. Microstructure Evaluation – Initial Analysis

Results were collated from the Burst testing performed on both the 1145 and 8150 samples. The results are shown in Table 9.6. There is a clear differentiation between 1145 and 8150 regardless of processing route with 8150 at least double the burst strength of 1145. Subsequent testing in production has confirmed these observations.

Sample	Alloy 1145 (MPa)	Alloy 8150 (MPa)
1	42	112
2	51	108
3	48	103
4	45	110
5	45	105
6	43	115
7	49	106
8	51	108
Range	40-51 (MPa)	>100

Table 9.6. Burst test comparison between AA1145 and AA8150 (B2a) samples thermally treated at 285°C

Samples were taken at several intermediate gauges during the production of 12μm foil to determine the microstructural factors that resulted in this dramatic strength improvement. All 8150 samples started with an initial cast block size that exceeds 500mm and with no thermal treatments resulting in a cold work reduction from hot work depth of between 10 to 100 times. The samples were prepared for micrography to examine the microstructure of the intermetallic distribution and grain structure during processing and before and after annealing.

The samples were examined using EDAX analysis to determine the composition of specific intermetallics. A void fraction at various gauges was used to determine the percent intermetallics and average particle size in the aluminium matrix. A stage micrometer was used to determine intermetallic particle size.

Samples from Coil A

220μm

AA8150 processing does not include an inter-anneal during cold rolling due to the detrimental effect on mechanical properties. As the process path does not vary until foil gauges (<200μm), only the intermetallic non-annealed structure was examined at 500x at the middle and edge locations. A stage micrometer with one division equalling 10 microns is used as a length unit reference, Figure 9.32.

The matrix appears to contain between 5-10% intermetallics, generally elongated in the direction of rolling, varying in size from fractions of a micron to several microns in size, Figures 9.33 - 34. There is evidence of matrix stresses splitting intermetallics, as discussed by the particle break-up model as described in Chapter 3. Void fraction data was obtained and is discussed later in the chapter.

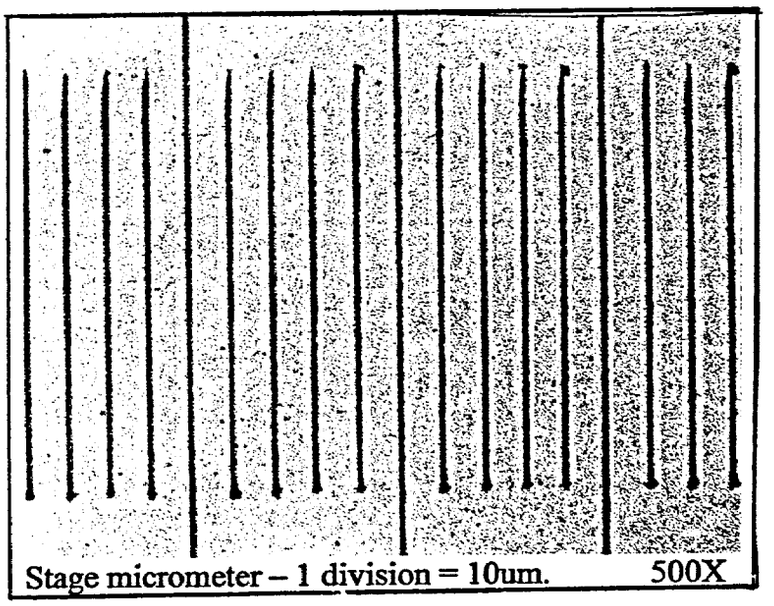

Figure 9.32. **Stage micrometer at 500x, 1 division = 10 microns**

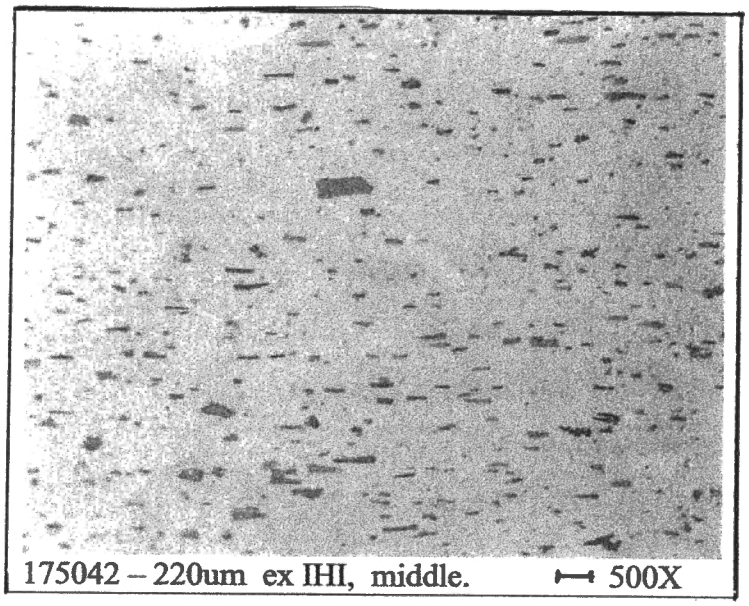

Figure 9.33. **Microstructure at 220μm for AA8150 – middle sample. There is a large number of darker rectangular particle as well as some lighter more oval particles**

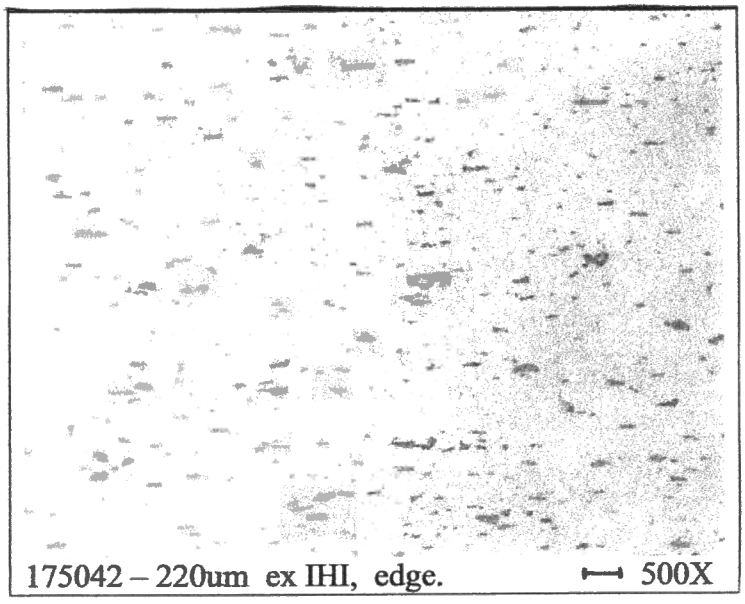

Figure 9.34. **Microstructure at 220μm for AA8150 - edge sample. Similar microstructure to the middle sample, with a large number of darker rectangular particle as well as some lighter more oval particles**

145μm

Micrographs of the intermetallic phases at 500x magnification were taken for both annealed and non-annealed states. Samples were taken at 145μm product from the middle of the coil and near the edge, Figure 9.35 - 36. There appears to be little differentiation between middle to edge, non-anneal to anneal. The particle void fraction and size is similar to 220μm.

The grain size was not homogeneous. While there was evidence of recrystallisation, grain size varies from a few microns to tens of microns. The edge did appear to have a slightly finer structure when magnified to 400x, Figures 9.37 – 38.

The grain structure of the edge sample appeared to have a finer grain structure than the middle samples due to surface shear forces. This was particularly evident at 200x magnification, were M represents the middle sample and E the edge sample. In both cases evidence of complete recrystallisation was present; however the non-homogenous grain growth was also apparent.

63μm

The microstructure for the 63μm product appears similar to that of 145μm product, with intermetallic size and grain size comparable, Figure 9.39 - 40. There was again evidence of large non-homogenous grains, with the annealed sample exhibiting a fine distribution of intermetallics. This indicates that precipitation may occur during annealing.

Like the 145μm sample, the grain structure of the edge sample has a finer grain structure than the middle samples. At 200x magnification, M represents the middle sample and E the edge sample. Excessive inhomogeneous grain growth is particularly evident on the M – middle sample. In both samples, complete recrystallisation occurred, Figures 9.41 – 9.42.

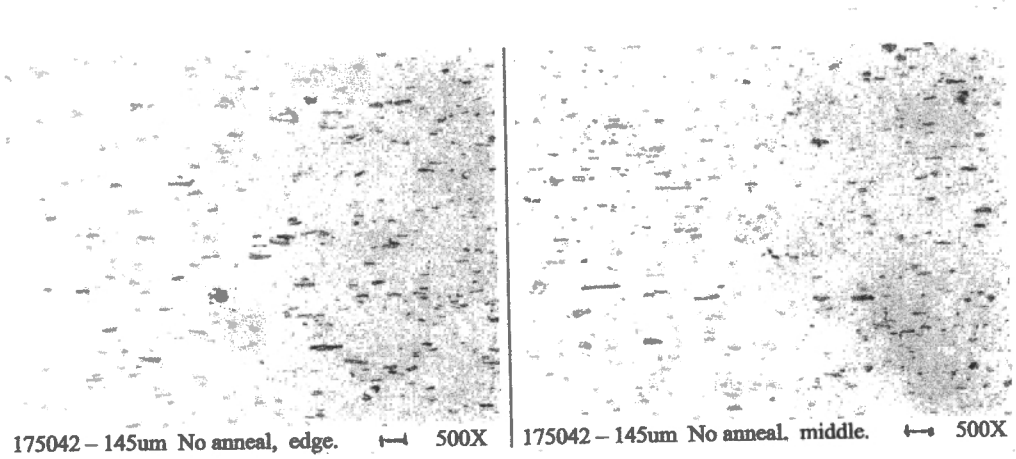

Figure 9.35. **Microstructure at 145µm - pre-anneal, middle and edge sample. Like the 220µm samples, both samples appear similar in appearance.**

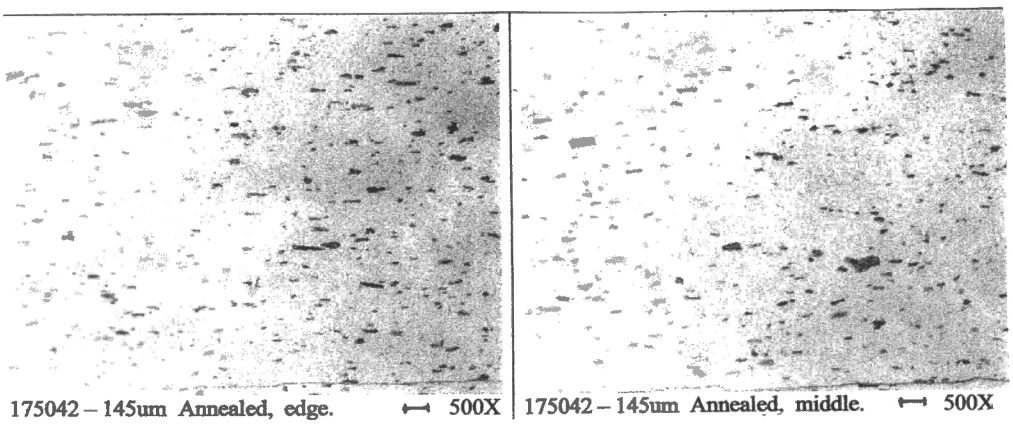

Figure 9.36. **Microstructure at 145µm – post-anneal, middle and edge samples. There does not appear to be any significant differentiation between pre and post annealed sample, middle to edge.**

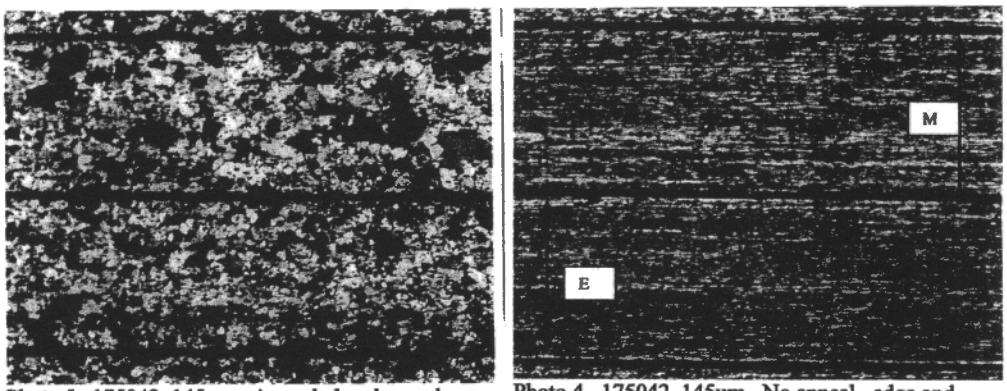

Photo 5. 175042 145um. Annealed, edge and middle. 200X

Photo 4. 175042 145um. No anneal, edge and middle. 200X

Figure 9.37. **Grain structure at 145μm – Sample taken at 200x to pre-anneal, middle and edge sample. 'M' represents the middle sample and 'E' the edge sample. Evidence of complete recrystallisation is present with some large in-homogenous grain growth.**

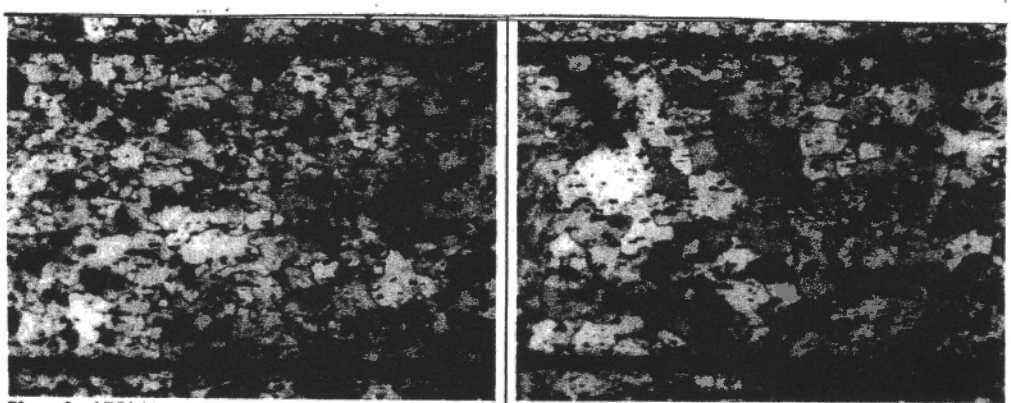

Photo 3. 175042 145um annealed at edge. 400X

Photo 4. 175042 145um annealed at middle. 400X

Figure 9.38. **Grain structure at 145μm – post-anneal, middle and edge samples at 400x. The present of a higher number of small rains is apparent on the edge samples when compared to the middle samples**

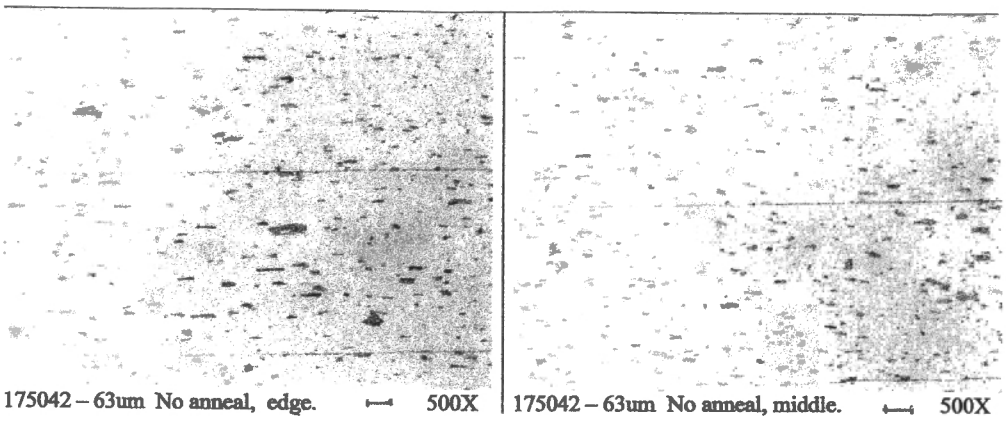

Figure 9.39. **Microstructure at 63μm – pre-anneal, middle and edge sample. Like the 220μm and 145μm samples the structure for edge and middle samples pre anneal is similar.**

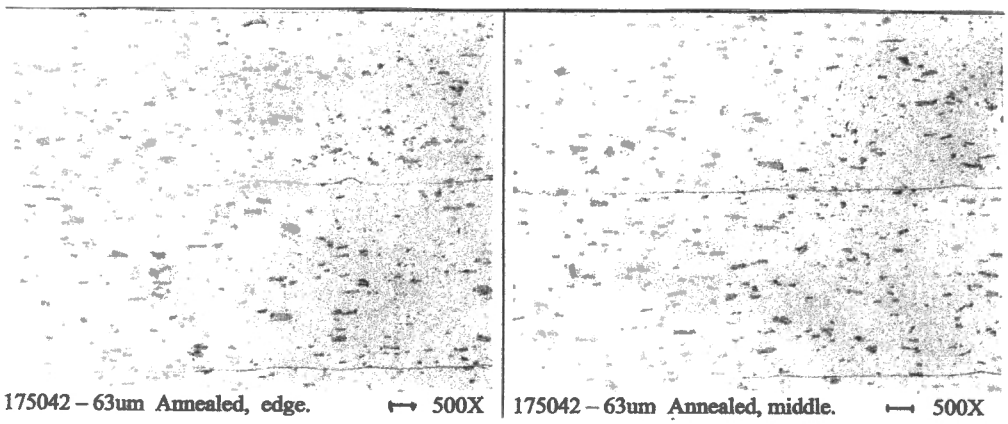

Figure 9.40. **Microstructure at 63μm – post-anneal, middle and edge samples. There does not appear to be any significant difference in appearance between middle and edge. The presence of fine precipitates in both samples is evident on close inspection.**

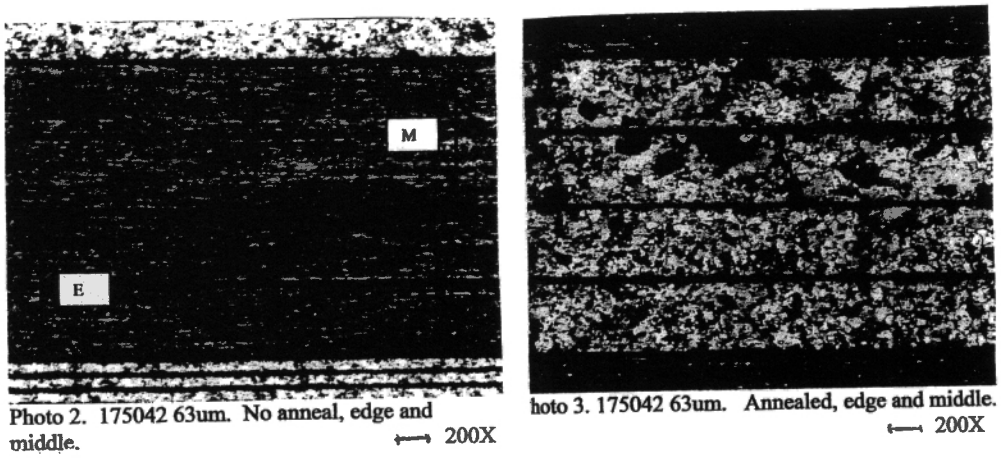

Photo 2. 175042 63um. No anneal, edge and middle. 200X

Photo 3. 175042 63um. Annealed, edge and middle. 200X

Figure 9.41. **Grain structure at 63µm – sample taken at 200x to pre-anneal, middle and edge sample. 'M' represents the middle sample and 'E' the edge sample. Evidence of complete recrystallisation is present with large in-homogenous grain growth occurring in the M samples.**

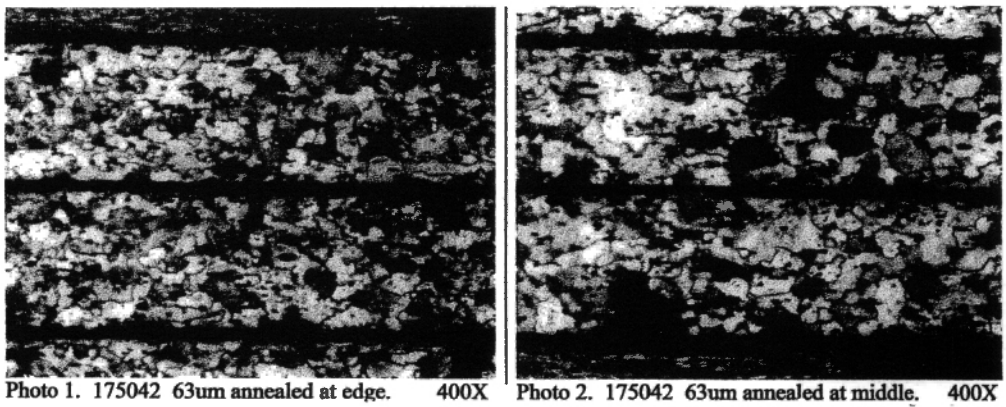

Photo 1. 175042 63um annealed at edge. 400X

Photo 2. 175042 63um annealed at middle. 400X

Figure 9.42. **Grain structure at 63µm – post-anneal, middle and edge samples at 400x. The present of a higher number of small grains is apparent on the edge samples when compared to the middle samples**

Samples from Coil B

The B sample product followed the same processing until the penultimate rolling stage. The coils were divided into two, rolled to 12μm and slit to either 1200mm or 300mm final width, B1 and B2 respectively. The 300mm product was annealed for 2 hours, with the anneal temperature set at 285°C – B2a, or 315°C – B2b. Wider product is annealed at lower temperatures, 235°C, but higher times, 100 hours, to prevent sticky or wet unwind coils.

Samples were collected 40mm in from the edge and 40mm from the outer surface, and micrographs showing the intermetallic particles were taken at 500x for the B1 and B2a sample. As 2 hours at 285°C (B2a) is a developed practice for 300mm 8150 household foil, the higher annealing temperature, 315°C (B2b), will be discussed at the end of the chapter in relation to the effect of temperature on mechanical properties.

Both samples showed a similar proportion of intermetallic particles (5-10%) as the heavy gauge samples from coil A, along with some fine dispersoids/precipitates in the anneal state. The larger particles were aligned in the direction of rolling and were generally block-like in shape, with an aspect ratio up to 5. The intermetallics varied in size from tenths of a micron up to about five microns again with evidence of particle fracture due to matrix stresses.

Sample B1 (235°C for 100 hours), had a significantly courser grain structure than B2a (2 hours at 285°C). Generally, the B1 samples showed about 25-50% full width coverage, that is the grain size was approximately 25 – 50% of the foil width, while the B2a sample appeared to have <10% full width coverage. This was evident at 400x magnification, with higher magnification having poor resolution. The B1 samples (235°C for 100 hours) are shown in Figures 9.43, 9.45 and 9.47 and the B2a samples (2 hours at 285°C) are shown in figures 9.44, 9.46 and 9.48.

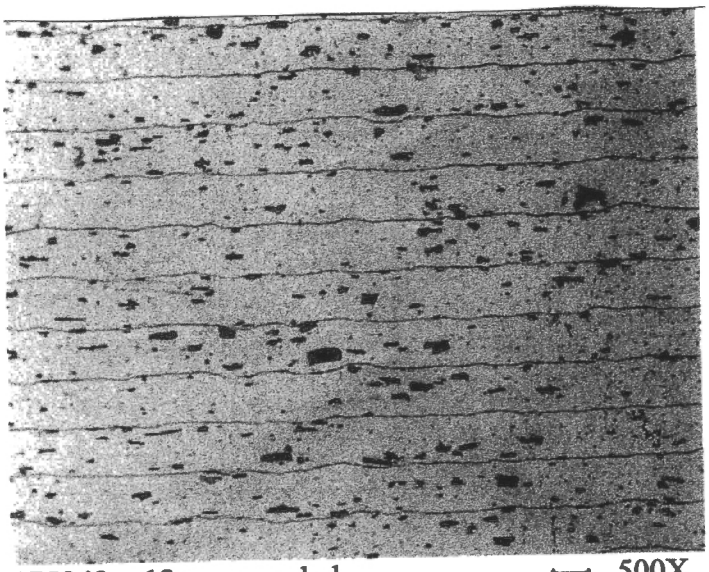

175042 – 12um annealed. ⟷ 500X

Figure 9.43. **Microstructure at 12μm (500x) – B1 (235°C for 100 hours) post-anneal taken 40mm inform edge. The intermetallic particles are aligned in the rolling direction, with some several microns in length. There is a fine distribution of dispersoid particles through the matrix.**

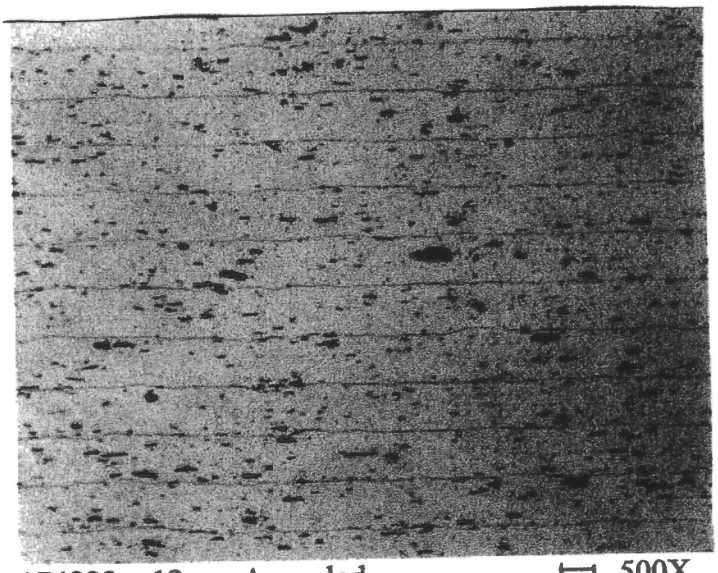

174823 – 12um Annealed. ⟷ 500X

Figure 9.44. **Microstructure at 12μm (500x) – B2a (285°C for 2 hours) post-anneal taken 40mm inform edge. The intermetallic particles are aligned in the rolling direction, with some several microns in length. There is a fine distribution of dispersoid particles through the matrix.**

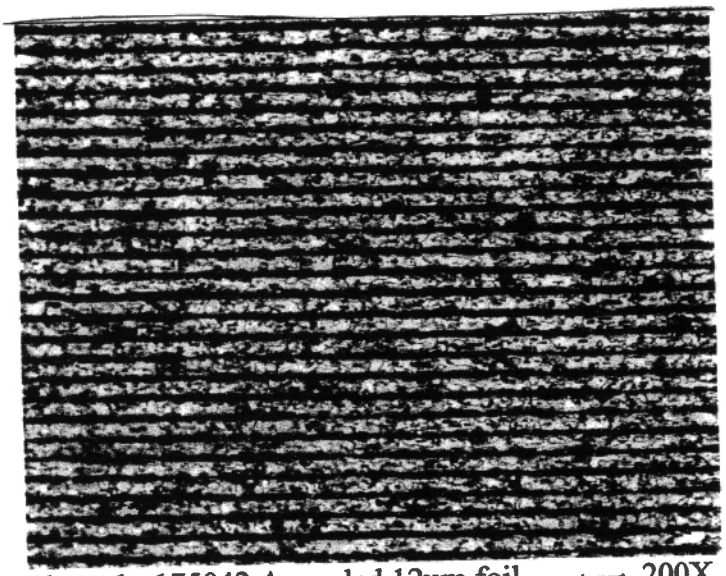

Photo 1. 175042 Annealed 12um foil. ⟼ 200X

Figure 9.45. **Grain structure at 12μm (200x) – B1 (235°C for 100 hours). Evidence of complete recrystallisation with large in-homogenous grain growth across the full width of the sample.**

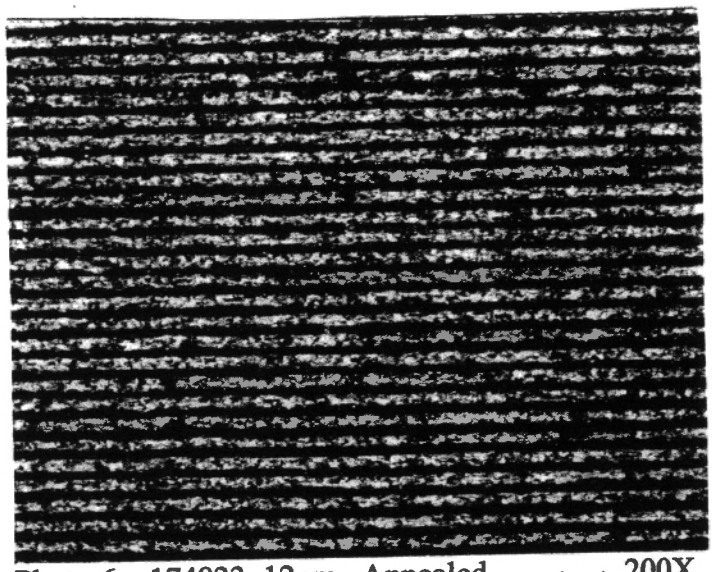

Photo 6. 174823 12um. Annealed. ⟼ 200X

Figure 9.46. **Grain structure at 12μm (200x) – B2a (285°C for 2 hours). The present of a higher number of small homogenous grains which are less than half width of the sample.**

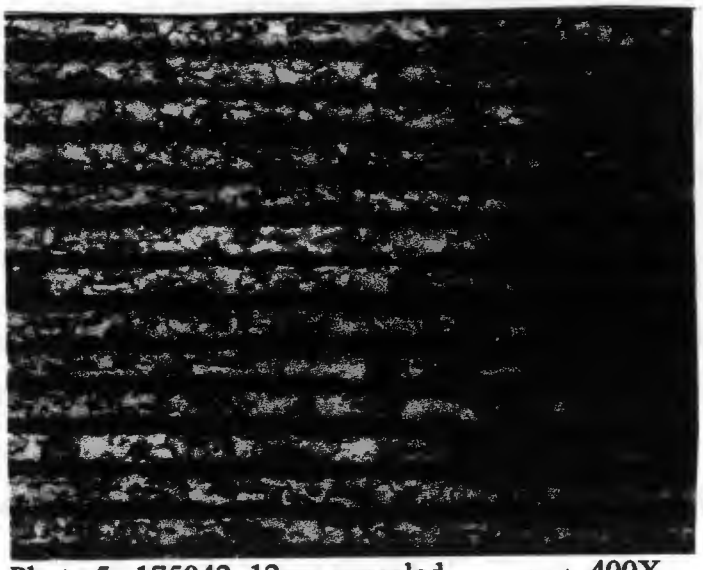

Photo 5. 175042 12um annealed. ⟷ 400X

Figure 9.47. **Grain structure at 12μm (400x) – B1 (235°C for 100 hours) Closer inspection of the sample confirms complete recrystallisation with large in-homogenous grain growth across the full width of the sample.**

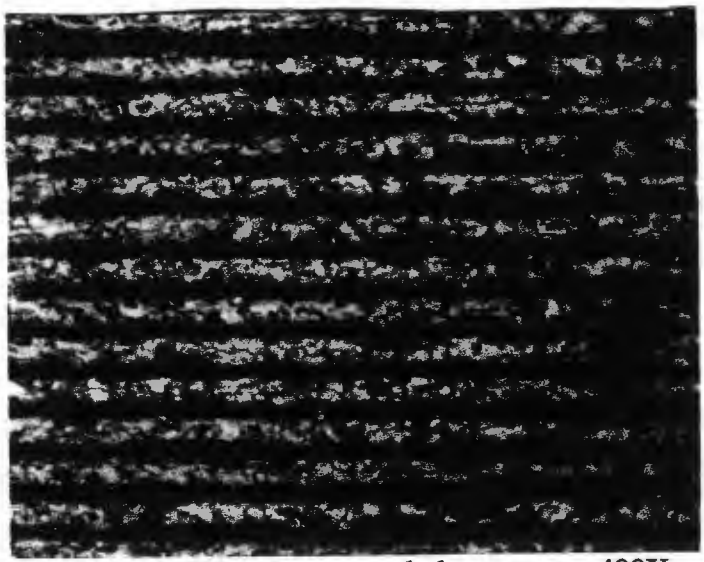

Photo 6. 174823 12um annealed. ⟷ 400X

Figure 9.48. **Grain structure at 12μm (400x) – B2a (285°C for 2 hours). Closer inspection of the sample confirms complete recrystallisation the presence of a higher number of small grains less than half sample width.**

SEM analysis

Several samples at 2.7mm, 220μm, 145μm, 63μm and 12μm were subjected to SEM investigation. Evidence of particle break-up, the particle size and the composition were found. EDX analysis of several particles was performed along with SEM micrographs taken at various magnifications to give an initial semi-quantitative indication.

The 2.7mm gauge sample metallic matrix was analysed and found to be composed of aluminium with large bright intermetallic particles aligned to the direction of rolling. At higher magnifications the particle aspect ratios were observed to vary greatly with a significant number found with aspect ratios exceeding 5. Several particles were in various stages of fracture as predicted by the break-up model (Chapter 3). Particles were analysed at various gauges and found to contain combinations of iron, manganese, aluminium and silicon generally form $(Fe,Mn)Al_x$ or $(Fe,Mn)_xSiAl_x$. The EDX analysis along with a collection of micrographs of the 2.7mm samples are given in Figures 9.49 – 51.

The 220μm and 145μm samples showed a similar arrangement of intermetallic's aligned to the direction of rolling with particle fracture evident. Like the 2.7mm sample, the EDX analysis of the particles revealed large intermetallic's with aspect ratios up to 10 largely composed of aluminium, iron, manganese and silicon. The EDX analysis along with a collection of micrographs of the 220μm samples is given in Figures 9.52 – 54. The EDX analysis along with a collection of micrographs of the 145μm samples is given in Figures 9.55 – 57.

The micrographs of the 63μm sample had a comparable microstructure to the previous gauges. Several particles were measured and found to be up to 8 microns in length with aspect ratios around 5 and below. There were also numerous dark areas on the surface which when tested for composition were found to be voids in the surface matrix and composed of aluminium. The intermetallics particles were difficult to evaluate, with two 'shades' of particles observed. The EDX analysis of the void, along with a collection of micrographs of the 63μm samples is given in Figures 9.58 – 60.

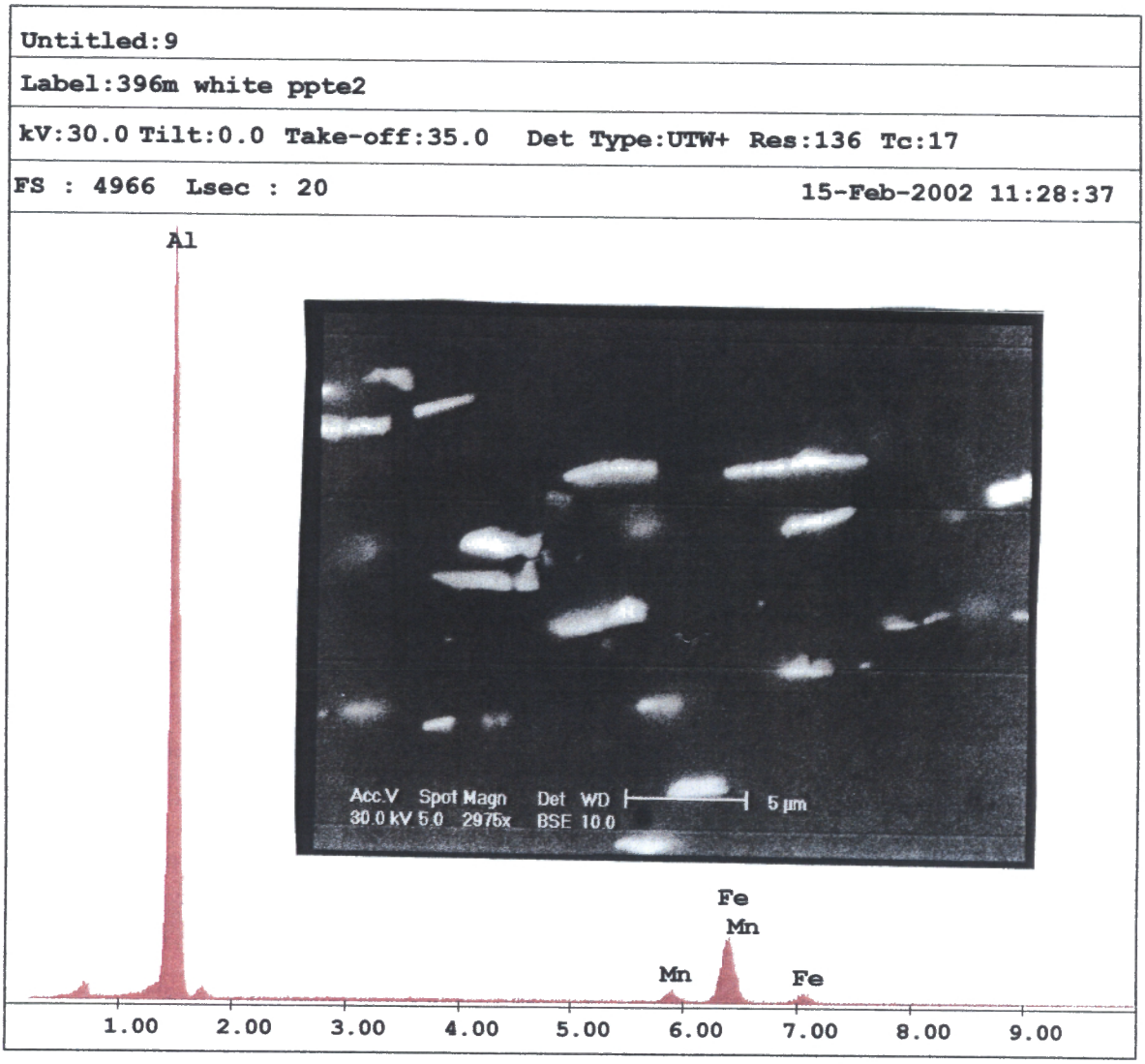

Figure 9.49. **EDX analysis with Particle inset (2975x) for 2.7mm sample exit hot rolling. Bright rectangular particles aligned in rolling direction with fracture evident. Particles found to be composed of aluminium, iron, manganese and silicon.**

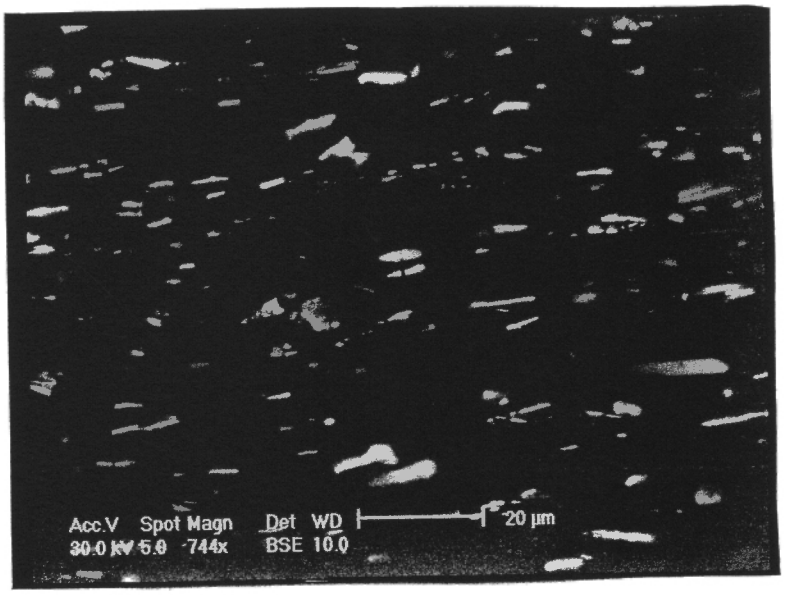

Figure 9.50. **Micrograph of 2.7mm structure showing large bright rectangular particles up to 20µm with high aspect ratios. Fracture is evident.**

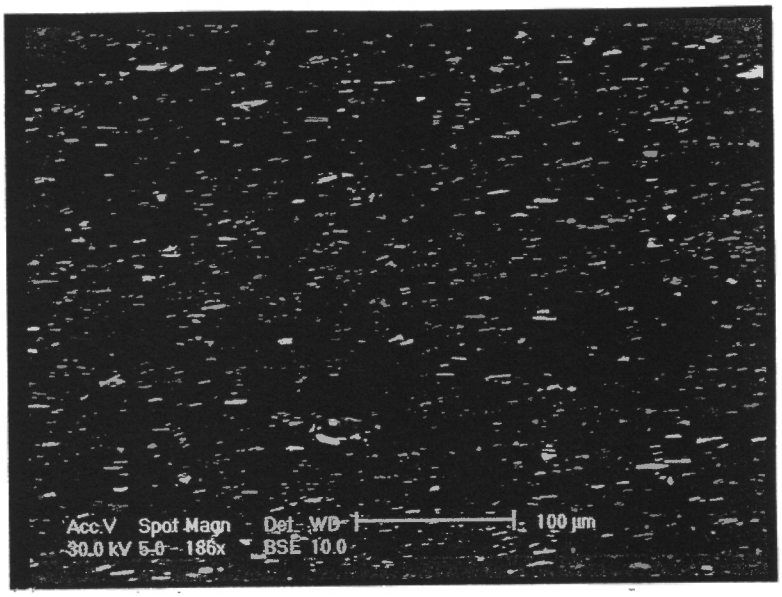

Figure 9.51. **Micrograph of 2.7mm structure showing high volume of large bright rectangular particles in aluminium matrix.**

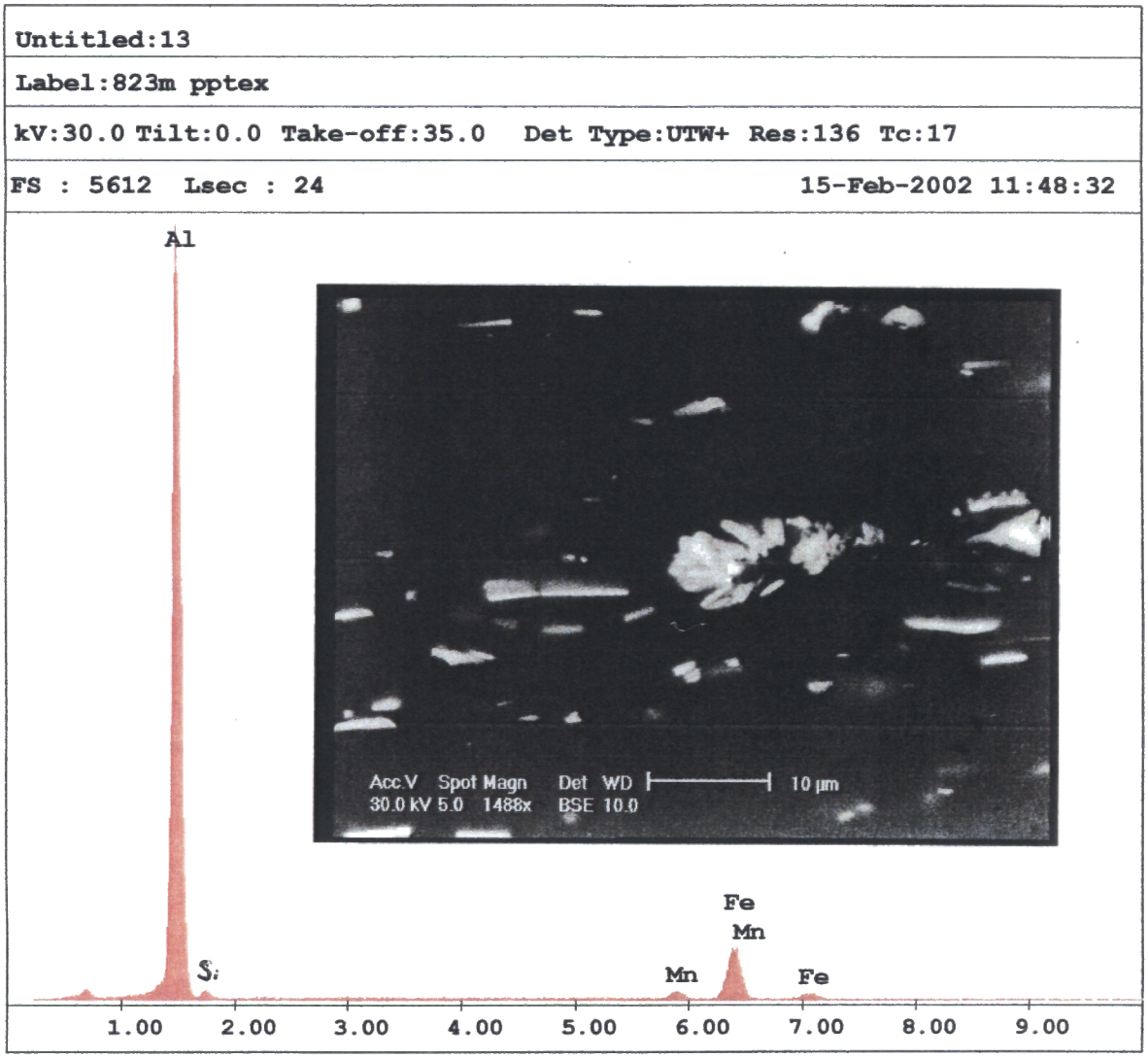

Figure 9.52. **EDX analysis with Particle inset (1488x) for 220µm sample in W-temper. Bright feather shaped particle aligned in rolling direction with fracture evident. Particles found to be composed of aluminium, iron, manganese and silicon.**

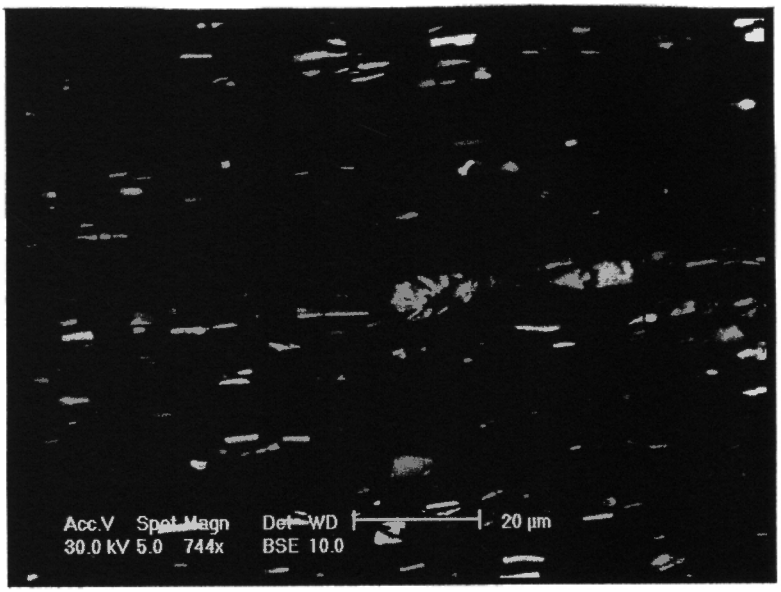

Figure 9.53. **Micrograph of 220µm structure showing large bright rectangular particles up to 20µm. Fracture is evident.**

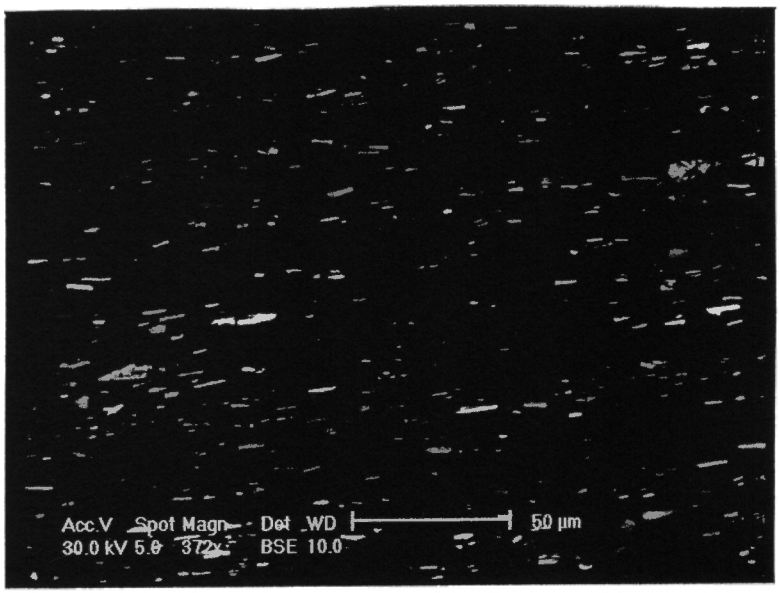

Figure 9.54. **Micrograph of 220µm structure showing high volume of large bright rectangular particles in aluminium matrix with aspect ratios up to 10.**

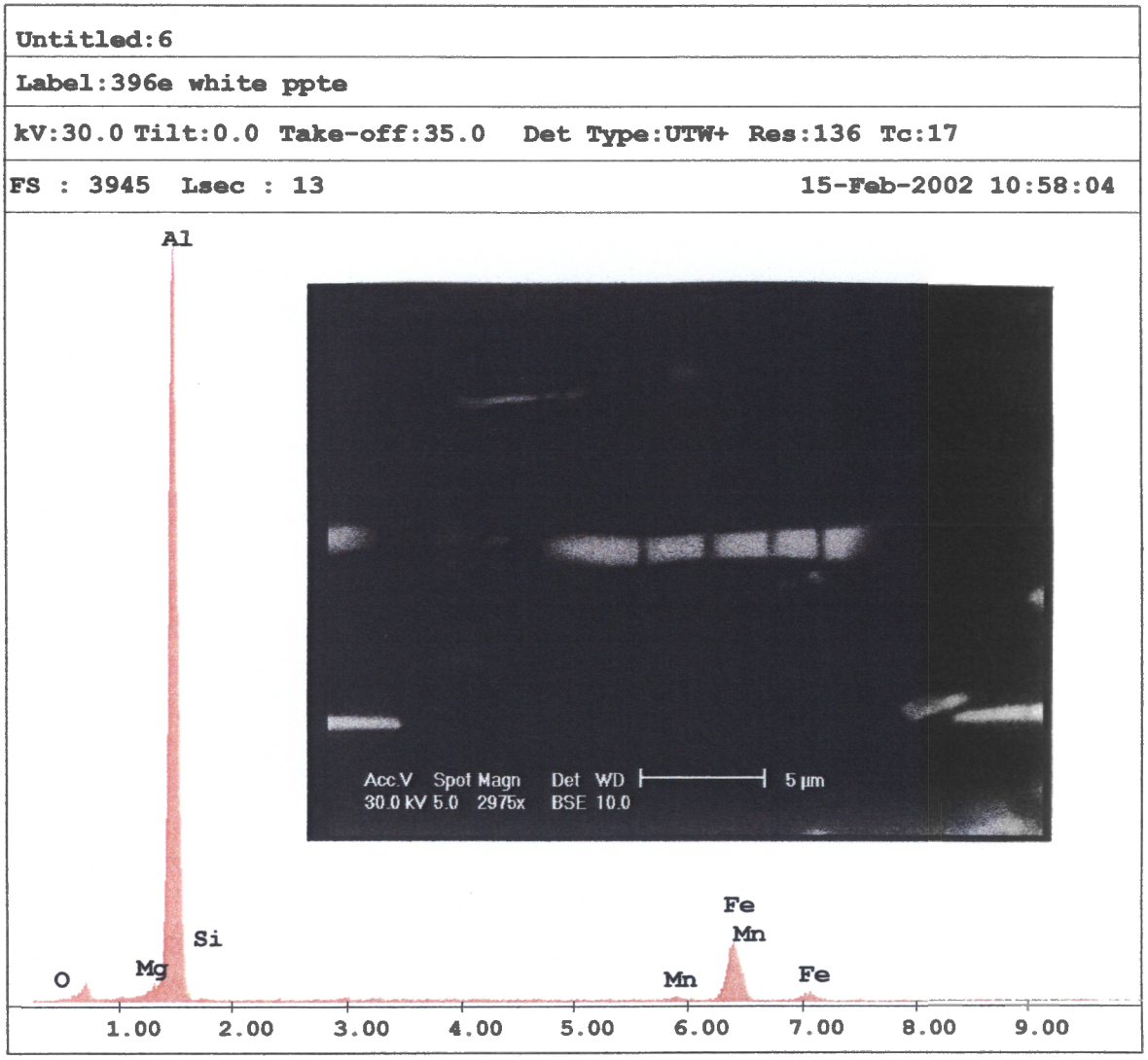

Figure 9.55. **EDX analysis with Particle inset (2975x) for 145µm sample in O temper. Bright rectangular particle aligned in rolling direction with multiple fractures evident. Particles found to be composed of aluminium, iron, manganese and silicon.**

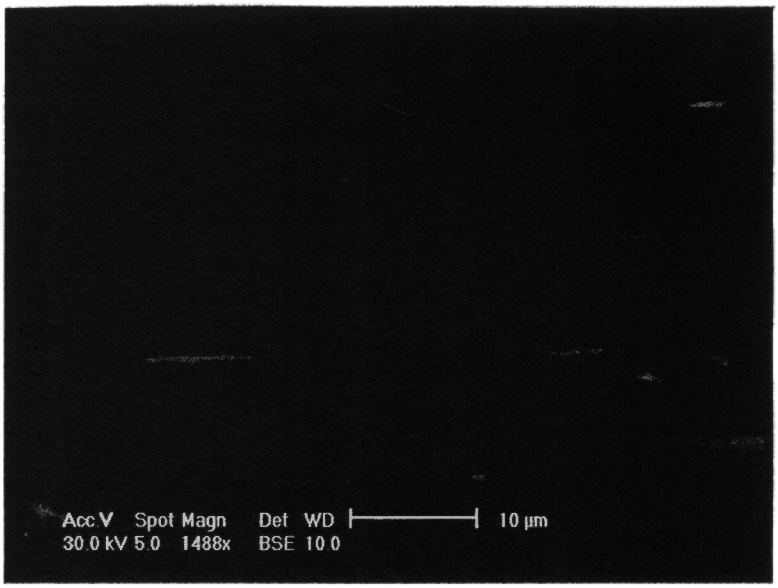

Figure 9.56. **Micrograph of 145µm structure showing large bright rectangular particles with multiple fractures and aspect ratios between 5-10.**

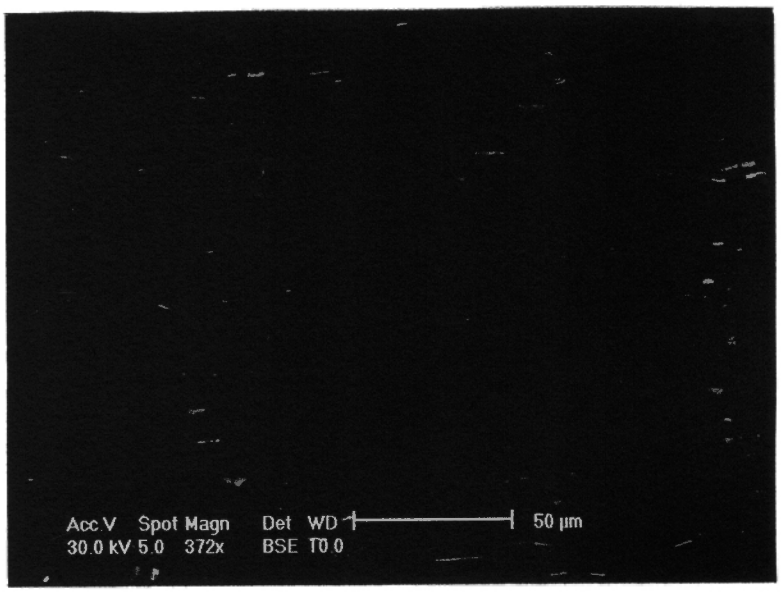

Figure 9.57. **Micrograph of 145µm structure showing high volume of large bright rectangular particles in aluminium matrix up to 10µm in length.**

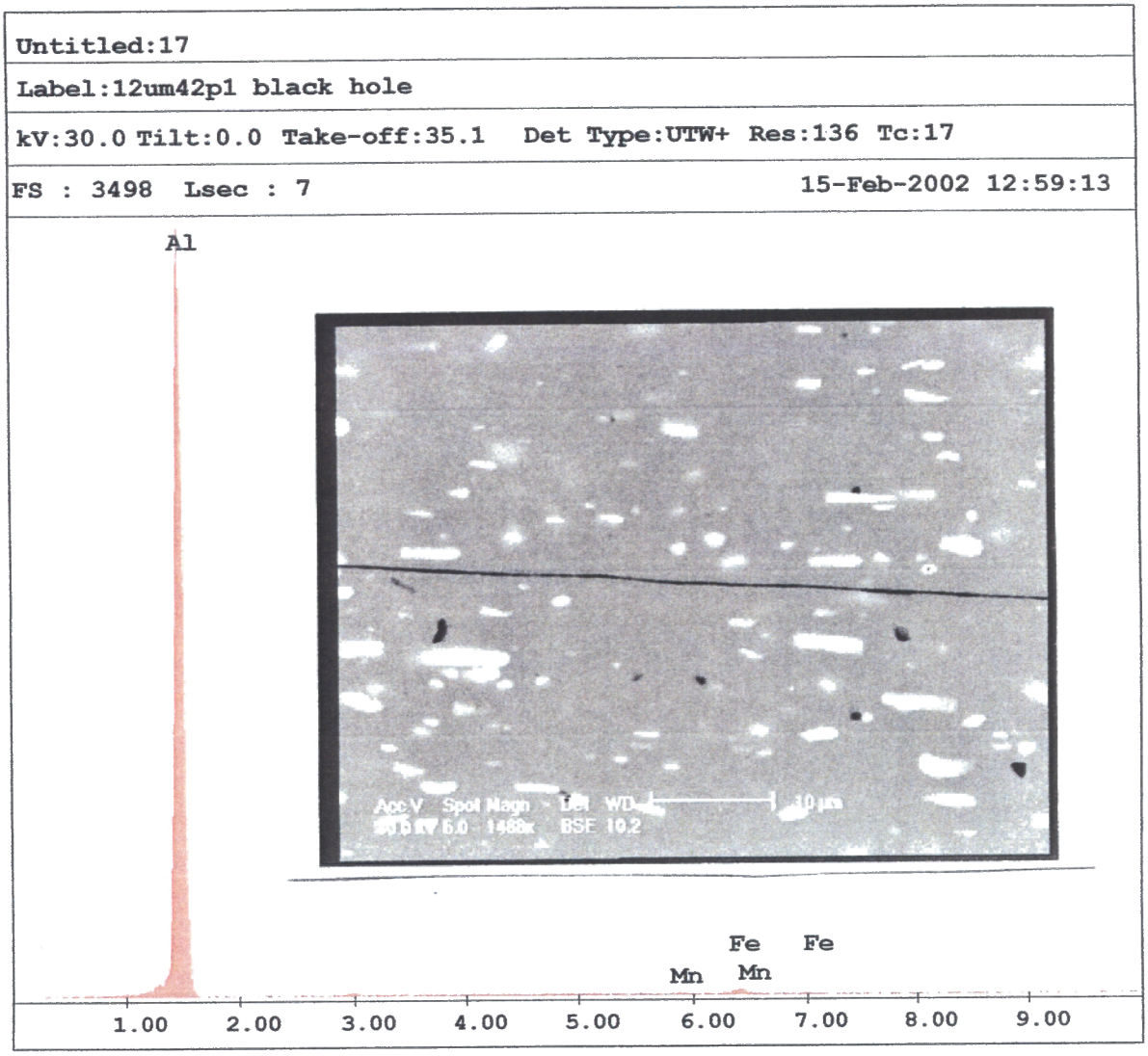

Figure 9.58. **EDX analysis of dark areas with Particle inset (1488x) for 63µm sample. Bright rectangular particles aligned in rolling direction generally less than 10µm with aspect ratio around 5. Dark area found to voids in aluminium matrix.**

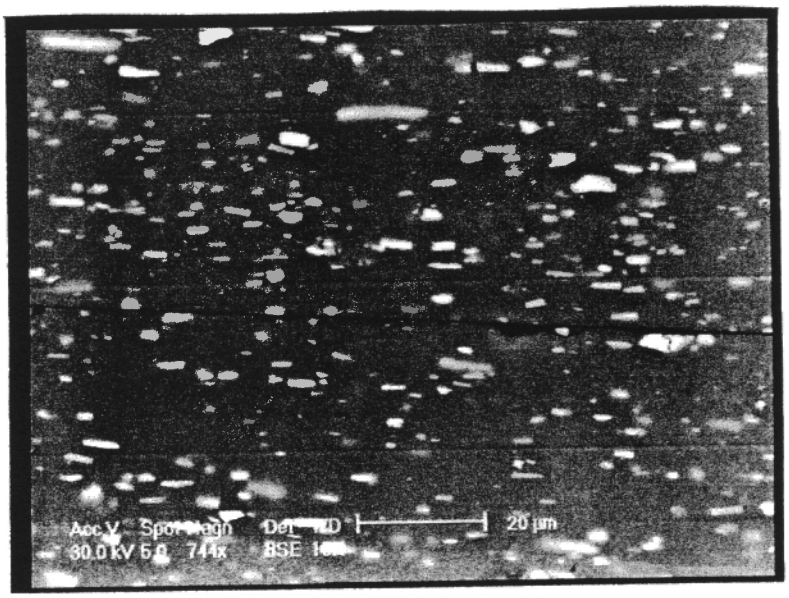

Figure 9.59. **Micrograph of 63µm structure showing large bright rectangular particles with multiple fractures. The larger one were measured and found to be below 10µm with aspect ratios around 5.**

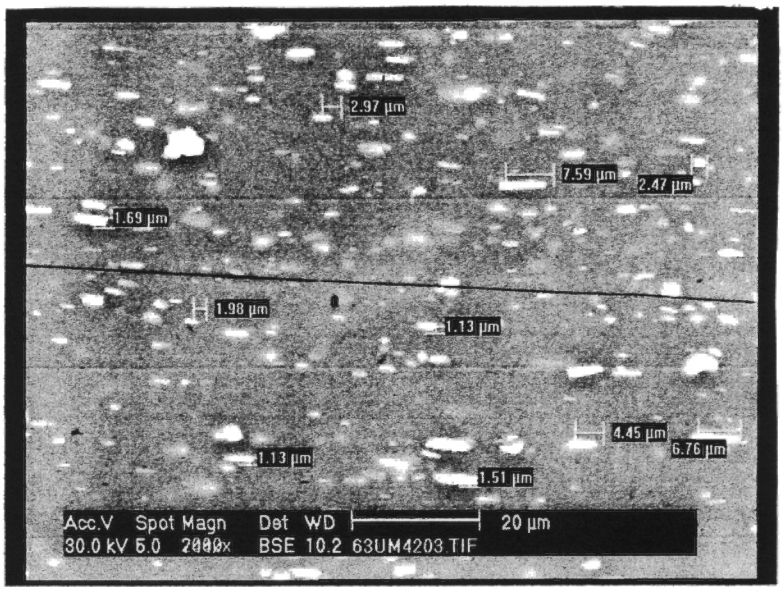

Figure 9.60. **Micrograph of 63µm structure showing high volume of large bright rectangular particles in aluminium matrix generally below 10µm in length. No evidence of precipitation or dispersoids. Bright rectangular particles contrast smaller duller, no oval particles**

Samples collected at 12μm were subjected to SEM investigation at various magnifications. Evidence of particle break-up, particle size and composition was found to agree with previous observations made of heavier gauges. The EDX analysis of several bright particles found a combination of iron, manganese, aluminium and silicon were present in the particles. This was present in the form of $(Fe,Mn)Al_x$ or $(Fe,Mn)_xSiAl_x$ intermetallics.

The metallic matrix contained aluminium with large bright intermetallic particles aligned to the direction of rolling present. At lower magnifications, dull, more oval particles were observed aligned to the direction of rolling. At higher magnifications up to 2975x, no precipitates or dispersoids were identified.

The particle aspect ratios were generally lower than that observed at higher gauges, with particles rarely longer than 5 microns. This resulted in many particles having aspect ratios at 5 or less, largely believed due to particle fracture. Several particles were in various stages of fracture, with stringers of particles observed. This supports the theory that particle fracture resulting from matrix stresses fracturing and moving particles in the direction of rolling being more dominant than crushing from the roll load forces.

A typical EDX analysis of the bright particles along with a collection of micrographs of the 12μm sample is given in Figures 9.61 – 63. They clearly show the rectangular bright particles along side the smaller duller oval particles.

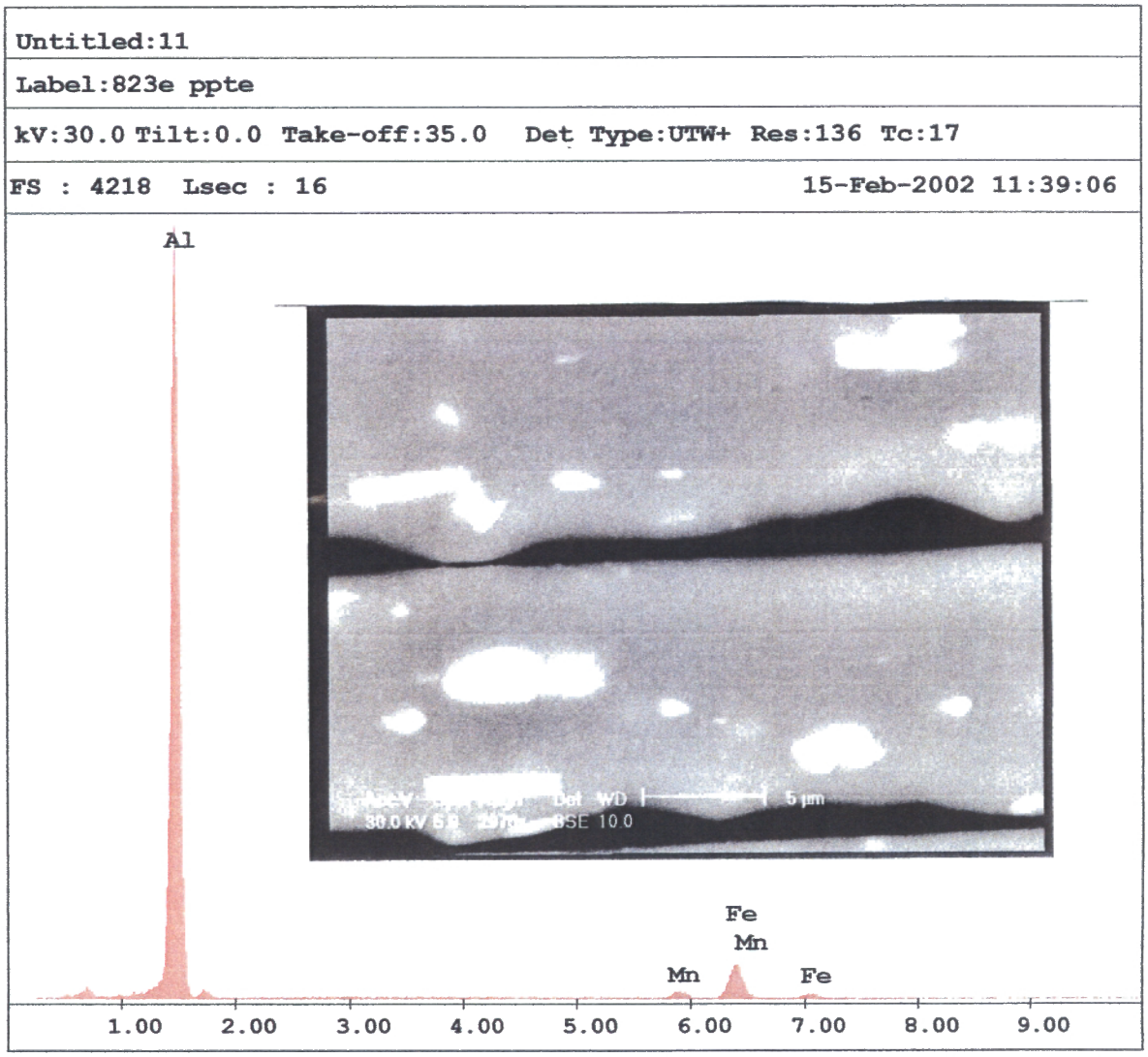

Figure 9.61. **EDX analysis with Particle inset (2975x) for 12μm sample in O temper at 285°C for 2 hours. Bright rectangular particle aligned in rolling direction with multiple fractures evident. Particles found to be composed of aluminium, iron, manganese and silicon. No evidence of dispersoids or precipitates in matrix.**

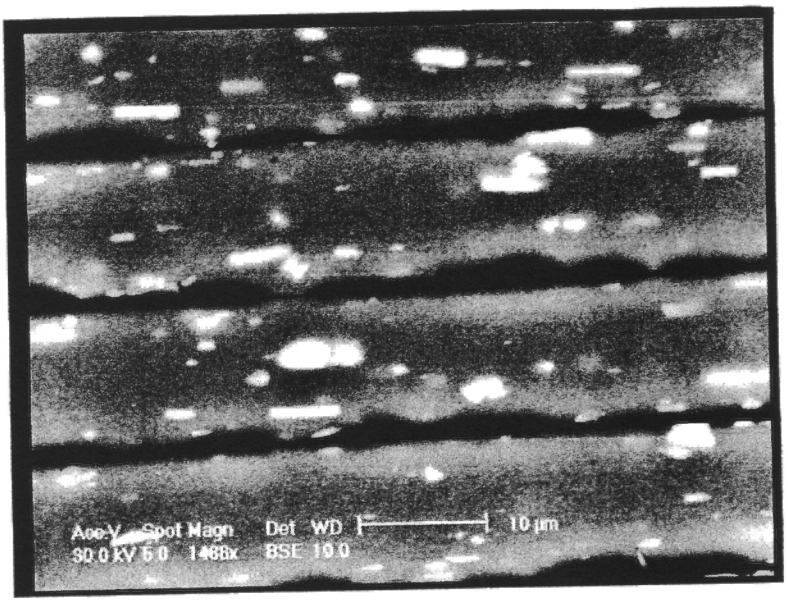

Figure 9.62. **Micrograph of 12µm structure showing bright and dull particles in aluminium matrix below 10µm in length. No evidence of precipitation or dispersoids.**

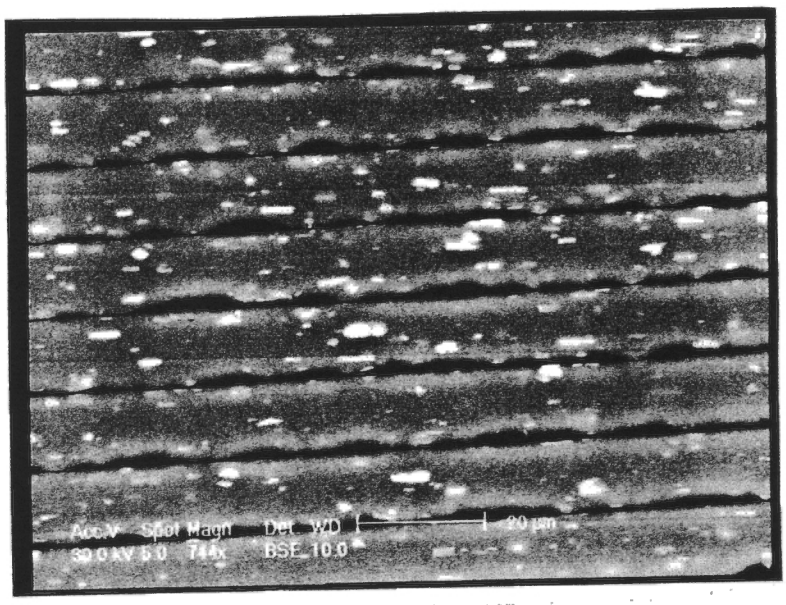

Figure 9.63. **Micrograph of 12µm O temper structure showing high volume of large bright rectangular particles and duller more oval particles in aluminium matrix generally below 10µm in length. No evidence of precipitation or dispersoids. Bright rectangular particles contrast smaller duller, no oval particles**

Image Analysis

To determine the volume of particles present, the SEM micrographs were used to determine the intermetallic or void fraction percentage, as well as the aspect ratio of the intermetallics. The void fraction percentage increased as the metal was processed, increasing from around 6% to 8% or a 30% increase after annealing. This promotes the theory of dispersoids precipitating out of solution on annealing, and was most prevalent at lower gauges despite being difficult to observe.

The aspect ratio of the intermetallic/voids was measured and was found to average around 2, dropping slightly by about 5% as the metal was processed, with the standard deviation increasing slightly over the same data range. This is not deemed significant as the high standard deviation indicating minimal particle fracture during processing. A summary of the results is given in Tables 9.7 and 9.8 with the raw data is give in the attached CD.

Coil ID	Gauge	Zoom	Red Lower	Red Upper	Area	Average
A	220um	33%	115	220	7342	6.13%
B	220um	33%	130	220	7310	6.20%
A	220um	33%	120	220	7643	6.30%
B	2.7mm	33%	105	220	7440	6.30%
A	145um	33%	140	222	7506	7.07%
A	63um	33%	150	220	7508	7.73%
B2	12um	33%	138	220	7183	7.10%
B1	12um	33%	140	222	7473	8.27%
B2	12um	To many gaps				

Table 9.7. Void Fraction Results

Despite several attempts to mount the sample, the B2 12μm second samples gave inaccurate readings due to the gap spacing between the foil sheets showing up as a large particle.

Coil ID	Gauge	Zoom	Red Lower	Red Upper	Breadth	Width	Aspect ratio	Stdev (l)
A	220um	33%	115	220	2.1	1.00	2.10	1.68
B	220um	33%	130	220	1.9	0.91	2.09	1.45
A	220um	33%	120	220	2.1	1.00	2.10	1.65
B	2.7mm	33%	105	220	1.9	0.93	2.04	1.75
A	145um	33%	140	222	2.1	1.05	2.00	1.70
A	63um	33%	150	220	2.1	1.05	2.00	1.68
B2	12um	33%	138	220	1.9	0.94	2.02	1.57
B1	12um	33%	140	222	2.3	1.10	2.09	1.86
B2	12um	To many gaps						

Table 9.8. Aspect Ratio Fraction Results

Electrical Conductivity

To confirm the presence of dispersoids in the final annealing product, conductivity measurements were used to show the amount of solute in solution. The electrical conductivity of an aluminium alloy is sensitive to elements in solid solution with the solute atoms interfering with electron motion through the aluminium. The size and the shape of the phases precipitated have little effect on conductivity. The volume of precipitates has a measurable effect on conductivity with the more elements in solution reducing the conductivity.

Room temperature samples were prepared using a sandwiched 12μm specimen from pre- and post-annealing and comparing them to a 0.22mm sample. A slight increase in conductivity for the pre-annealing sample was determined along with a more significant increase after annealing. This indicates some minor precipitation of particles during processing, with increased precipitation of particles during the annealing stage of processing. In line with work described in the literature survey, the initial precipitation was not expected, with only minor precipitation during annealing expected due to the compositional equilibrium and hence a further more detail microstructural evaluation is required.

9.2.2. Detailed Microstructure Evaluation

An evaluation of selected microstructures was performed to explain the effect of intermetallics on grain size and hence strength. Evaluations were performed on 2.7mm hot-rolled product, 0.22mm cold rolled product, and 12μm thin-foil product pre and post anneal.

The samples were examined using a FEI SIRION FEG Scanning Electron Microscope. The SEM used captive backscatter and image analysis to separate the particles from the matrix (i.e. iron precipitates appear bright). The software is a ZEISS KS400 system which also allows EDS on specific precipitates from the image. The accelerated voltage was originally set to 10kV to improve resolution of the intermetallics, but was increased to 15kV to aid in the EDS analysis. To improve the EDS analysis, the accelerated voltage should be a minimum 1.5x the binding energy.

The samples selected were exit hot rolling at 2.7mm, exit cold rolling at 220μm and pre and post annealing for the 12μm gauge. The micrographs were studied for the presence of dispersoids or precipitation, dull and bright intermetallics and the aluminium matrix composition. EDS was performed on the matrix in the initial sample, and all particles observed in the matrix.

The different magnifications are designed to optimise the visual observation of the expected precipitates to be found, with no precipitation expected until foil gauges are reached (based on conductivity tests). EDS analysis was performed on all samples examining the bright and dull particles, and dispersoids. The matrix was also examined for the 2.7mm hot rolled samples as baselines. Sample EDS analysis and micrographs are given for all gauges to assist in future reference within the ALCOA metallurgical database.

In the context of the thesis, dispersoids refer to small particles that occur prior to any rolling process or as a consequence of rolling, while precipitates result from thermal treatments.

Hot Rolled 2.7mm Sample

The microstructure of the 2.7mm sample was found to contain large intermetallics in excess of 10μm in an aluminium matrix with fine evenly dispersed dispersoids. The dispersoids observed are believed to occur during homogenisation. This agrees well with current 8xxx series literature on Al-Fe-Mn alloys as discussed earlier. There is also confirmation of bright and dull particles that are observed at lower gauges in the previous analysis, but at a much higher gauge.

The bright intermetallic demonstrated both vertical and horizontal fracture as discussed in the particle break-up modelling, while the upper right duller particle appears to be plastically deforming giving it an oval shape, Figure 9.64 - 65. At higher magnifications dull spherical dispersoids can be seen intermittently through-out the matrix. The accompanying EDS spectrums of the particles are given in Figures 9.66 – 9.69, with a summary of the EDS shown in Table 9.9. These are included for future reference within the ALCOA network at all gauges.

Intermetallic	Al (wt%/at%)	Mn (wt%/at%)	Fe (wt%/at%)	Si (wt%/at%)
Matrix	98/98	0/0	0/0	2.4/2.4
Bright Particle	72/81	2.2/1.2	19.8/10.8	6.1/6.6
Dull Particle	80/88	2.2/1.2	15.5/10.8	2/2.2
Dispersoid/ppt	91/94	3.2/1.6	1.5/0.8	3.4/3.3

Table 9.9. EDS summary for 2.7mm 8150 alloy

The bright and dull particles have higher levels of iron than the dispersoids with similar manganese levels (indicating a slightly different Al:Fe ratio). Manganese is the dominant alloy addition for the dispersoids. The density of the dispersoids is given in the image analysis data.

Figure 9.64. **SEM micrograph of 2.7mm sample (1000x). Intermetallic's are generally rectangular in shape, with several larger more rounded phases present. The matrix appears to have undergone particle and possibly full recrystallisation.**

Figure 9.65 **SEM micrograph of 2.7mm sample (2000x). Large bright block-shaped intermetallic particle shows multiple fraction sites. Above right is a duller, more rounded intermetallic which shows signed of plastic deformation. The matrix appears to have undergone particle and possibly full recrystallisation with intermittent dull spherical dispersoids visible.**

File: C:\PGT_Data\Data\808362hr2_5_matrix.pgt
Collected: July 20, 2005 11:07:59

Live Time: 100.00 Count Rate: 7776 Dead Time: 53.54 %
Beam Voltage: 10.00 Beam Current: 2.00 Takeoff Angle: 33.50

■ 808362hr2_5_matrix.pgt FS: 36000

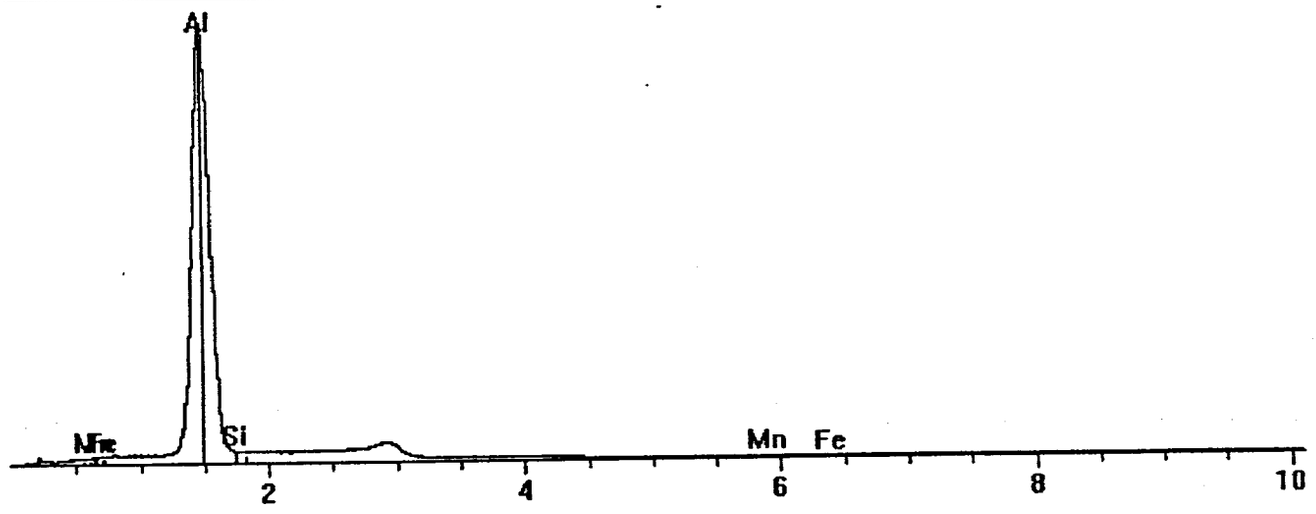

Element	Line	keV	KRatio	Wt%	At%	At Prop	ChiSquared
Al	KA1	1.487	0.9751	97.55	97.64	0.0	47.56
Mn	KA1	5.898	0.0000	0.00	0.00	0.0	
Fe	KA1	6.403	0.0000	0.00	0.00	0.0	
Si	KA1	1.740	0.0160	2.45	2.36	0.0	47.56
Total			**0.9911**	**100.00**	**100.00**	**0.0**	**73.90**

Element	Line	Gross (cps)	BKG (cps)	Overlap (cps)	Net (cps)	P:B Ratio
Al	KA1	4511.1	92.8	0.3	4417.9	47.6
Mn	KA1	14.8	18.0	0.0	0.0	0.0
Fe	KA1	12.0	14.7	0.0	0.0	0.0
Si	KA1	199.4	97.7	31.8	69.9	0.7

Element	Line	Det Eff	Z Corr	A Corr	F Corr	Tot Corr	Modes
Al	KA1	0.895	1.000	1.000	1.000	1.000	Element
Mn	KA1	0.976	1.226	1.006	1.000	1.233	Element
Fe	KA1	0.981	1.216	1.003	1.000	1.219	Element
Si	KA1	0.885	0.982	1.563	1.000	1.535	Element

Figure 9.66. **Spectrum of matrix is essentially purity aluminium with pseudo-silicon reading**

File: C:\PGT_Data\Data\808362hr2_brighter_particle.pgt
Collected: July 20, 2005 10:32:44

Live Time:	100.00	Count Rate:	5547	Dead Time:	46.40 %
Beam Voltage:	10.00	Beam Current:	2.00	Takeoff Angle:	33.50

808362hr2_brighter_particle.pgt

FS: 20000

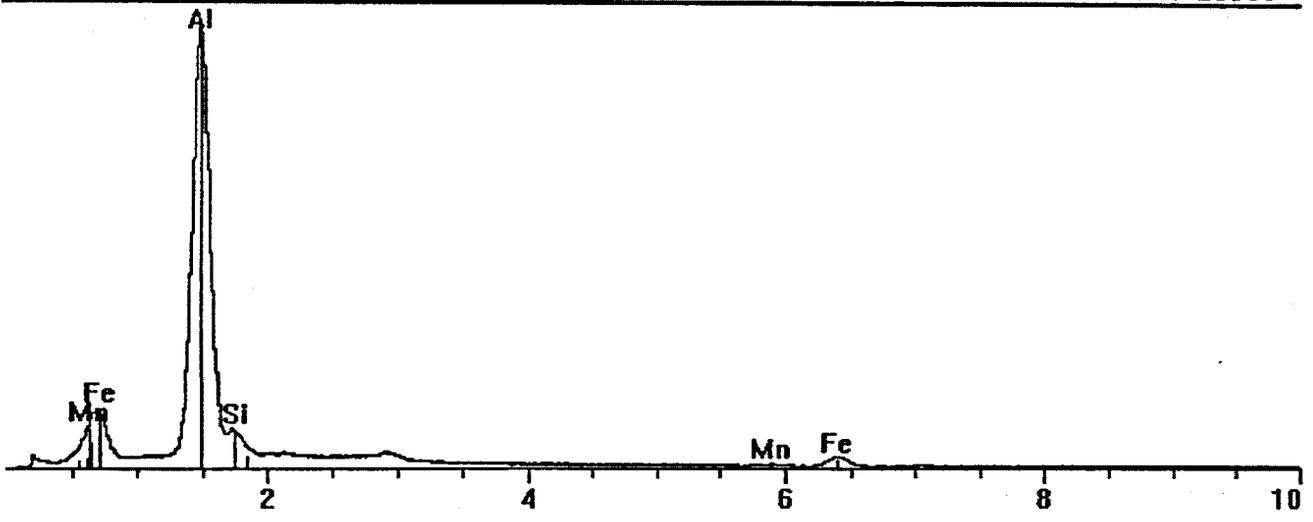

Element	Line	keV	KRatio	Wt%	At%	At Prop	ChiSquared
Al	KA1	1.487	0.6602	71.92	81.34	0.0	40.38
Mn	KA1	5.898	0.0186	2.17	1.20	0.0	1.88
Fe	KA1	6.403	0.1689	19.80	10.81	0.0	1.88
Si	KA1	1.740	0.0433	6.12	6.64	0.0	40.38
Total			**0.8910**	**100.00**	**100.00**	**0.0**	**31.36**

Element	Line	Gross (cps)	BKG (cps)	Overlap (cps)	Net (cps)	P:B Ratio
Al	KA1	2556.3	94.3	0.7	2461.3	26.1
Mn	KA1	30.2	19.8	0.0	10.4	0.5
Fe	KA1	77.0	17.5	1.0	58.4	3.3
Si	KA1	271.1	97.6	17.8	155.8	1.6

Element	Line	Det Eff	Z Corr	A Corr	F Corr	Tot Corr	Modes
Al	KA1	0.895	0.970	1.124	0.999	1.089	Element
Mn	KA1	0.976	1.181	1.005	0.984	1.168	Element
Fe	KA1	0.981	1.169	1.002	1.000	1.172	Element
Si	KA1	0.885	0.952	1.483	1.000	1.412	Element

Figure 9.67. EDS spectrum of large bright particle show high percentage of iron and some secondary manganese and silicon readings.

File: C:\PGT_Data\Data\808362hr2_2_dull_particle.pgt
Collected: July 20, 2005 10:41:47

Live Time:	100.00	Count Rate:	5849	Dead Time:	47.45 %
Beam Voltage:	10.00	Beam Current:	2.00	Takeoff Angle:	33.50

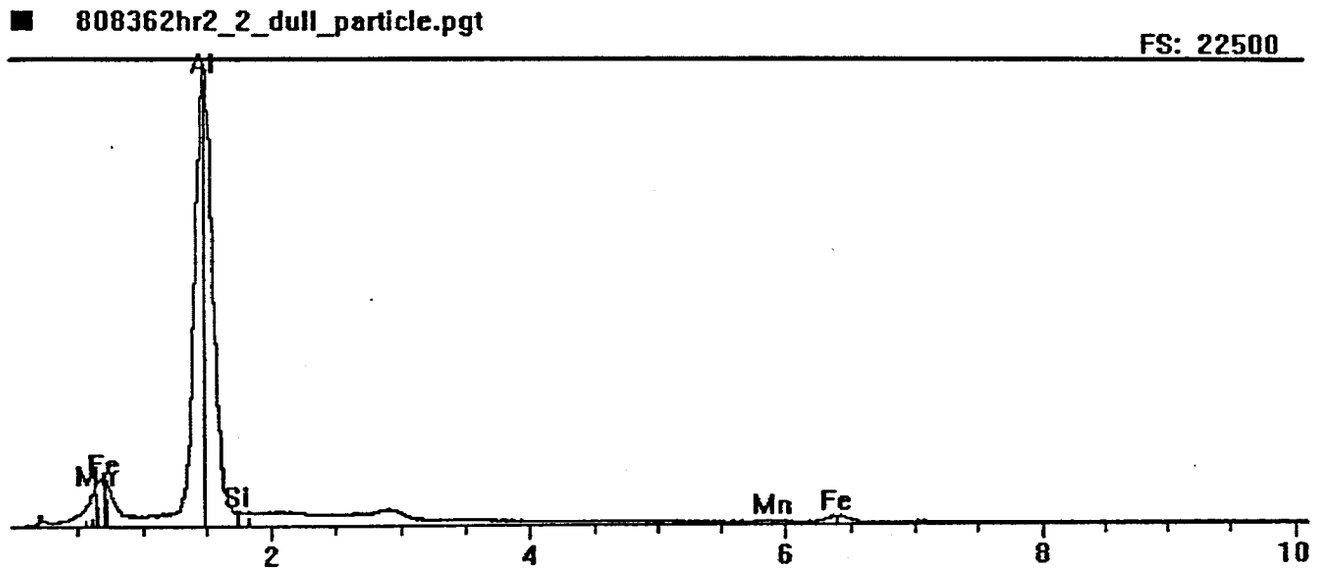

Element	Line	keV	KRatio	Wt%	At%	At Prop	ChiSquared
Al	KA1	1.487	0.7480	80.19	88.37	0.0	54.58
Mn	KA1	5.898	0.0191	2.26	1.22	0.0	1.92
Fe	KA1	6.403	0.1315	15.53	8.26	0.0	1.92
Si	KA1	1.740	0.0140	2.03	2.15	0.0	54.58
Total			**0.9127**	**100.00**	**100.00**	**0.0**	**47.89**

Element	Line	Gross (cps).	BKG (cps)	Overlap (cps)	Net (cps)	P:B Ratio
Al	KA1	2958.3	76.8	0.2	2881.3	37.5
Mn	KA1	29.8	18.8	0.0	11.0	0.6
Fe	KA1	64.4	16.3	1.1	47.0	2.9
Si	KA1	153.1	80.4	20.8	51.9	0.6

Element	Line	Det Eff	Z Corr	A Corr	F Corr	Tot Corr	Modes
Al	KA1	0.895	0.975	1.100	1.000	1.072	Element
Mn	KA1	0.976	1.189	1.005	0.988	1.180	Element
Fe	KA1	0.981	1.178	1.002	1.000	1.180	Element
Si	KA1	0.885	0.957	1.517	1.000	1.452	Element

Figure 9.68. **EDS spectrum of dull oval particle show iron and some secondary manganese and silicon readings.**

File: C:\PGT_Data\Data\808362hr2_6_dispersoid spherical.pgt
Collected: July 20, 2005 11:13:00

Live Time: 100.00 Count Rate: 7490 Dead Time: 52.72 %
Beam Voltage: 10.00 Beam Current: 2.00 Takeoff Angle: 33.50

■ 808362hr2_6_dispersoid spherical.pgt

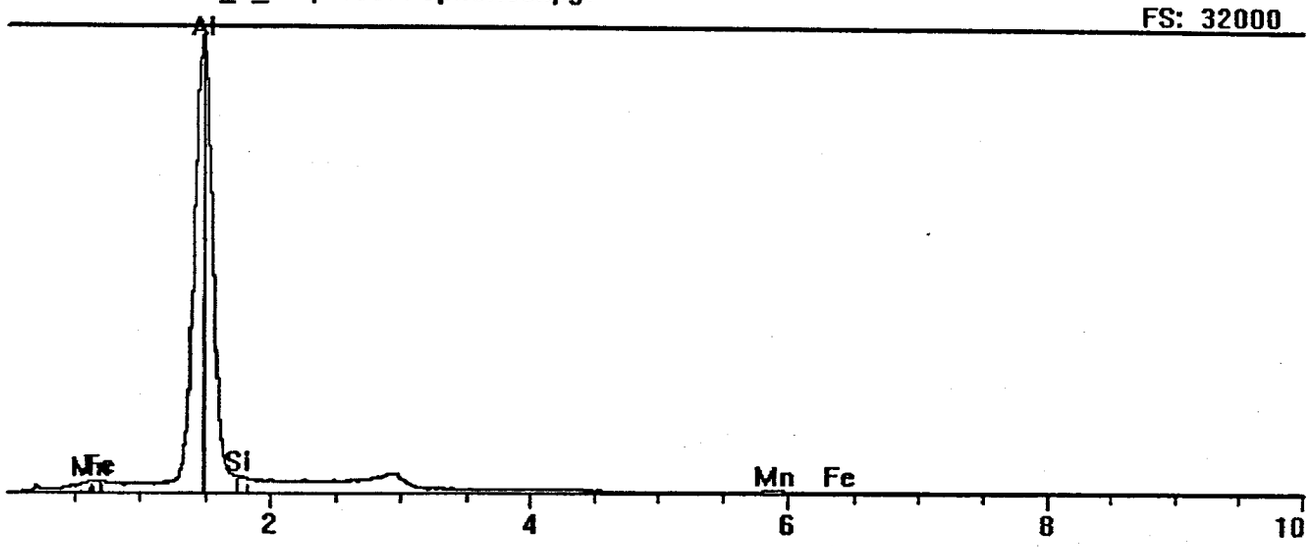

Element	Line	keV	KRatio	Wt%	At%	At Prop	ChiSquared
Al	KA1	1.487	0.9099	92.45	94.63	0.0	44.66
Mn	KA1	5.898	0.0250	3.06	1.54	0.0	1.42
Fe	KA1	6.403	0.0099	1.20	0.59	0.0	1.42
Si	KA1	1.740	0.0219	3.29	3.24	0.0	44.66
Total			**0.9667**	**100.00**	**100.00**	**0.0**	**57.12**

Element	Line	Gross (cps)	BKG (cps)	Overlap (cps)	Net (cps)	P:B Ratio
Al	KA1	4213.8	106.0	0.4	4107.3	38.7
Mn	KA1	34.1	17.2	0.0	16.9	1.0
Fe	KA1	20.6	14.8	1.7	4.1	0.3
Si	KA1	236.4	111.4	29.6	95.4	0.9

Element	Line	Det Eff	Z Corr	A Corr	F Corr	Tot Corr	Modes
Al	KA1	0.895	0.994	1.023	0.999	1.016	Element
Mn	KA1	0.976	1.217	1.005	0.999	1.222	Element
Fe	KA1	0.981	1.206	1.003	1.000	1.210	Element
Si	KA1	0.885	0.976	1.541	1.000	1.504	Element

Figure 9.69. EDS spectrum of spherical dispersoids contain manganese and possibly silicon, with lower levels of iron.

Cold Rolled 0.22mm product

The microstructure of cold rolling gauges demonstrates the even distribution of particles through out the matrix parallel to the direction of rolling. The particle distribution shows a peak in particle count around $1\mu m^2$ with a noticeable drop in the average aspect ratio at the same value while the maximum aspect ratio remained high, Figure 9.70.

The micrographs are taken at several magnifications. The presence of bright and dull particles is observed, with random dull spherical dispersoids being visible at higher magnifications. Particle fracture is observed in several particles, but predominately bright particles, Figures 9.71-9.73. EDS spectrums for the bright and dull particles and dispersoids are given in Figures 9.74 – 9.76 with a summary given in Table 9.10.

There is no increase in dispersoid/precipitate amounts, nor the relative amounts of iron to manganese. This indicates that reductions up to 90% do not induce 'shear' precipitation or substitution of elements in the constituent particles, either light or dull. The dispersoids are manganese rich, with the particles iron rich.

Intermetallic	Al (wt%/at%)	Mn (wt%/at%)	Fe (wt%/at%)	Si (wt%/at%)
Bright Particle	71/81	2.3/1.3	19.5/10.6	6.7/7.2
Dull Particle	82/90	2.1/1.1	14.6/7.7	1.4/1.5
Dispersoid/ppt	92/95	3/1.5	1.2/0.6	3.3/3.2

Table 9.10. EDS Summary for 0.22mm 8150 alloy

The bright and dull particles have higher levels of iron than the dispersoids with similar manganese levels (indicating a slightly different Al:Fe ratio). Manganese is the dominate alloy addition for the dispersoids.

S# 808362 0.22mm exit Cold Rolling 8150 Sheet

file: 808362CRIA-1

MEASURED AREA DISTRIBUTION OF PARTICLE SECTION SIZES

Group number	Area of sections microns	Area%	Number	Number density (no./mm2)	Number density (no./um2)	Maximum aspect ratio	Average aspect ratio
2	63.0957 - 39.8107	0.0263	9	6	0.000006	3.54	2.46
3	39.8107 - 25.1189	0.0546	29	18	0.000018	5.72	3.24
4	25.1189 - 15.8489	0.1435	117	74	0.000074	9.81	2.99
5	15.8489 - 10.0000	0.2767	357	226	0.000226	13.68	3.40
6	10.0000 - 6.3096	0.4255	873	552	0.000552	15.09	3.61
7	6.3096 - 3.9811	0.5437	1755	1109	0.001109	12.64	3.60
8	3.9811 - 2.5119	0.6385	3221	2035	0.002035	15.61	3.70
9	2.5119 - 1.5849	0.6511	5167	3264	0.003264	12.70	3.60
10	1.5849 - 1.0000	0.6277	7836	4950	0.004950	12.13	3.25
11	1.0000 - .6310	0.4573	9009	5691	0.005691	14.42	2.90
12	.6310 - .3981	0.3178	9914	6263	0.006263	10.30	2.62
13	.3981 - .2512	0.1505	7168	4528	0.004528	6.18	2.59
14	.2512 - .1585	0.0697	4545	2871	0.002871	4.12	2.51

statistics
Average area = 1.3875 Average diameter = 1.0402
Median area = .7282 Median diameter = 1.0672
No. of particles/mm2 = 31587
Area percent = 4.383

Figure 9.70. **The measured area distribution of particle sizes for the cold-rolled 220μm sample. There is a notable increase in particle count for particles with areas below 6μm^2. The average aspect ratio falls below three for particles less than 1μm^2 implying a change in the morphology of the predominate phase.**

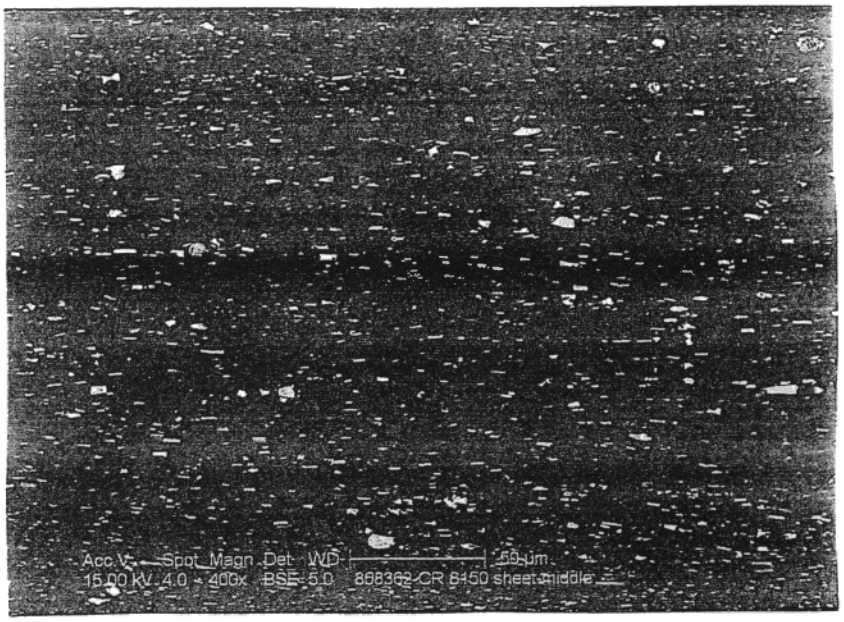

Figure 9.71. **SEM micrographs of 220μm sample (x400). Intermetallic's are evenly distributed across the matrix, varying in size and shape. They are generally rectangular in shape with several larger more rounded particles.**

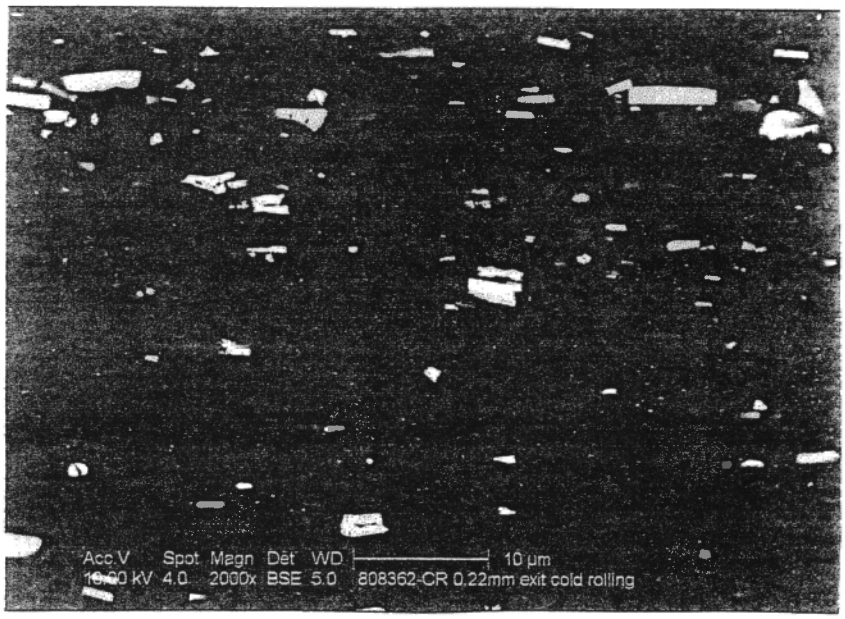

Figure 9.72. **SEM micrograph of 220µm sample (2000x). Several brighter particles are fracturing in several locations resulting in intermetallic stringers in the rolling direction. The matrix has a elongated grain structure with intermittent dull spherical dispersoids visible.**

Figure 9.73. **SEM micrograph of 220µm sample (5000x). Dispersoids are clearly seen intermittently spread through the matrix. Particles showing multiple fracture sites with some voiding visible.**

File: C:\PGT_Data\Data\808362cr3_bright particle.pgt
Collected: July 20, 2005 11:49:32

Live Time:	100.00	Count Rate:	5811	Dead Time:	47.31 %
Beam Voltage:	10.00	Beam Current:	2.00	Takeoff Angle:	33.50

■ 808362cr3_bright particle.pgt

FS: 20000

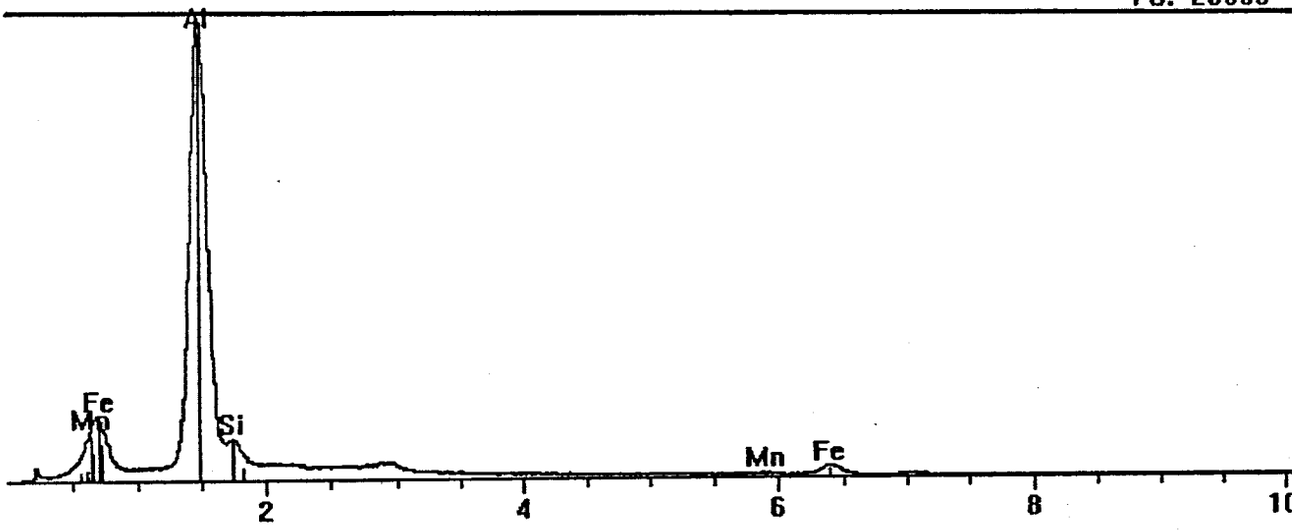

Element	Line	keV	KRatio	Wt%	At%	At Prop	ChiSquared
Al	KA1	1.487	0.6567	71.50	80.83	0.0	43.09
Mn	KA1	5.898	0.0200	2.34	1.30	0.0	1.47
Fe	KA1	6.403	0.1662	19.49	10.64	0.0	1.47
Si	KA1	1.740	0.0473	6.66	7.23	0.0	43.09
Total			**0.8903**	**100.00**	**100.00**	**0.0**	**34.02**

Element	Line	Gross (cps)	BKG (cps)	Overlap (cps)	Net (cps)	P:B Ratio
Al	KA1	2657.9	92.8	0.8	2564.4	27.6
Mn	KA1	31.2	19.4	0.0	11.7	0.6
Fe	KA1	78.5	17.1	1.2	60.2	3.5
Si	KA1	293.3	96.7	18.5	178.1	1.8

Element	Line	Det Eff	Z Corr	A Corr	F Corr	Tot Corr	Modes
Al	KA1	0.895	0.971	1.123	0.998	1.089	Element
Mn	KA1	0.976	1.181	1.005	0.985	1.169	Element
Fe	KA1	0.981	1.170	1.002	1.000	1.173	Element
Si	KA1	0.885	0.952	1.480	1.000	1.409	Element

Figure 9.74. **EDS spectrum of large bright particles show a high percentage of iron and some secondary manganese and silicon readings.**

File: C:\PGT_Data\Data\808362cr3_1_dull particle.pgt
Collected: July 20, 2005 11:55:57

Live Time:	100.00	Count Rate:	6281	Dead Time:	48.90 %
Beam Voltage:	10.00	Beam Current:	2.00	Takeoff Angle:	33.50

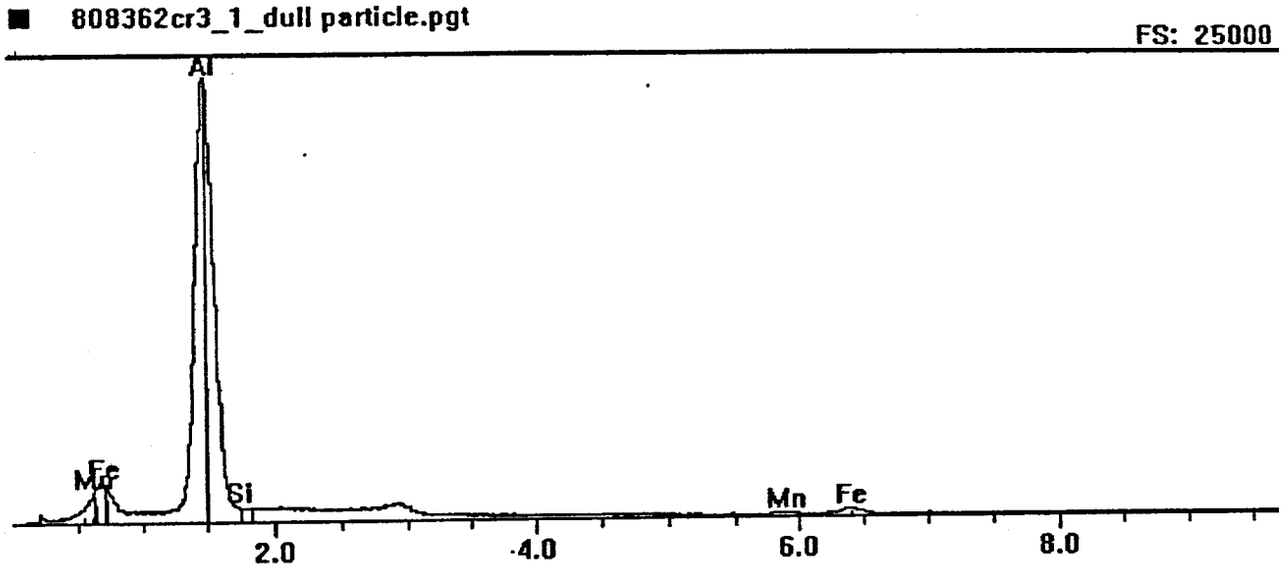

Element	Line	keV	KRatio	Wt%	At%	At Prop	ChiSquared
Al	KA1	1.487	0.7678	81.95	89.70	0.0	49.00
Mn	KA1	5.898	0.0175	2.07	1.11	0.0	1.41
Fe	KA1	6.403	0.1230	14.55	7.69	0.0	1.41
Si	KA1	1.740	0.0098	1.43	1.50	0.0	49.00
Total			**0.9181**	**100.00**	**100.00**	**0.0**	**42.97**

Element	Line	Gross (cps)	BKG (cps)	Overlap (cps)	Net (cps)	P:B Ratio
Al	KA1	3231.7	98.4	0.2	3133.2	31.9
Mn	KA1	29.7	19.0	0.0	10.7	0.6
Fe	KA1	64.3	16.7	1.1	46.6	2.8
Si	KA1	163.0	101.9	22.6	38.5	0.4

Element	Line	Det Eff	Z Corr	A Corr	F Corr	Tot Corr	Modes
Al	KA1	0.895	0.977	1.093	1.000	1.067	Element
Mn	KA1	0.976	1.191	1.005	0.988	1.183	Element
Fe	KA1	0.981	1.180	1.002	1.000	1.183	Element
Si	KA1	0.885	0.959	1.524	1.000	1.460	Element

Figure 9.75. **EDS spectrum of dull oval particle show iron and some secondary manganese and silicon readings.**

File: C:\PGT_Data\Data\808362cr3_2_dispersoid.pgt
Collected: July 20, 2005 12:01:25

Live Time: 100.00 Count Rate: 7400 Dead Time: 52.42 %
Beam Voltage: 10.00 Beam Current: 2.00 Takeoff Angle: 33.50

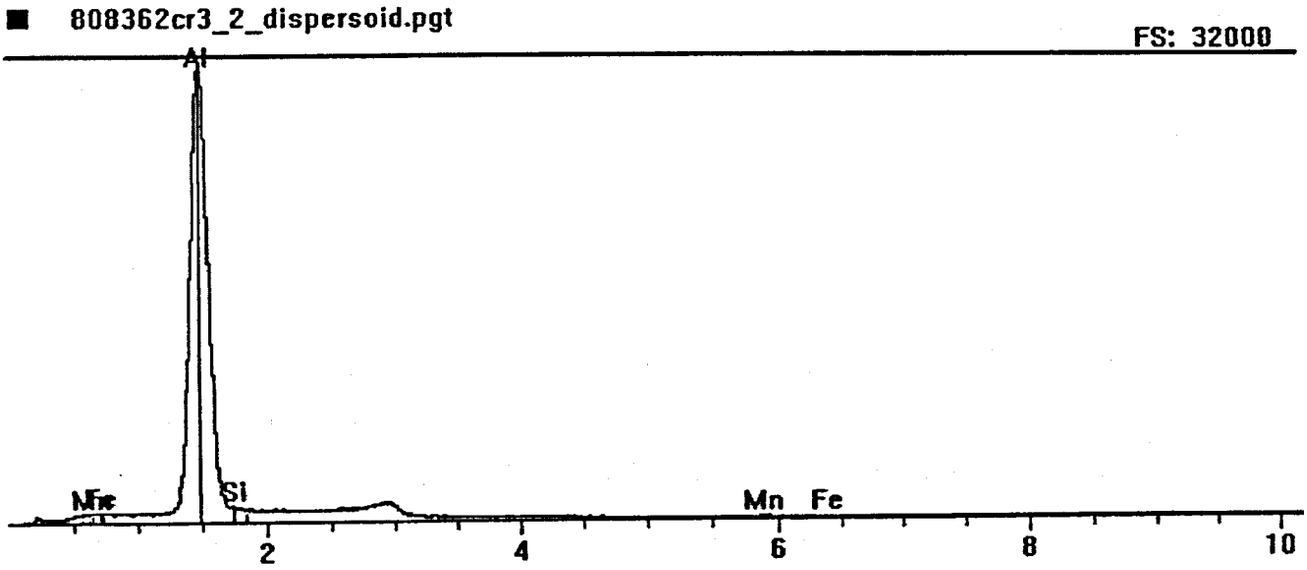

Element	Line	keV	KRatio	Wt%	At%	At Prop	ChiSquared
Al	KA1	1.487	0.9483	95.46	96.40	0.0	51.60
Mn	KA1	5.898	0.0123	1.51	0.75	0.0	2.11
Fe	KA1	6.403	0.0016	0.19	0.09	0.0	2.11
Si	KA1	1.740	0.0187	2.84	2.76	0.0	51.60
Total			**0.9809**	**100.00**	**100.00**	**0.0**	**64.70**

Element	Line	Gross (cps)	BKG (cps)	Overlap (cps)	Net (cps)	P:B Ratio
Al	KA1	4227.6	100.5	0.4	4126.7	41.1
Mn	KA1	25.7	17.7	0.0	8.0	0.5
Fe	KA1	15.9	14.5	0.8	0.6	0.0
Si	KA1	213.6	105.4	29.7	78.6	0.7

Element	Line	Det Eff	Z Corr	A Corr	F Corr	Tot Corr	Modes
Al	KA1	0.895	0.998	1.009	0.999	1.007	Element
Mn	KA1	0.976	1.222	1.006	1.000	1.229	Element
Fe	KA1	0.981	1.212	1.003	1.000	1.216	Element
Si	KA1	0.885	0.979	1.551	1.000	1.519	Element

Figure 9.76. **EDS spectrum of spherical dispersoids contain manganese and possibly silicon, with lower levels of iron.**

Thin Foil Pre-Anneal 12μm product

The microstructure yields an un-recrystallised sub-grain type structure of less than 1μm, with random spherical dispersoids less than 0.1μm in size and a mean spacing of between 2μm to 10μm. Larger constituent intermetallics greater than 2μm are also present.

The particle distribution shows an order of magnitude increase in particles less than $1\mu m^2$ supporting the conductivity results that indicate precipitation during foil rolling. The precipitate aspect ratio drops to 2 from the dispersoid aspect ratio of between 2-3, Figure 9.77. There is a shift in the top end distribution of particles with the maximum particle size being below $10\mu m^2$. The micrographs are shown in Figures 9.78-9.81, with the EDS spectrum shown in Figures 9.82-9.84 with a summary given in Table 9.11.

There is a slight change in the composition of the dispersoid/precipitate composition, indicating that precipitation is occurring. The precipitates that are coming out of solution are iron rich. This implies that reductions greater than 99% without thermal treatment results in 'precipitates' shearing out of solid solution.

Intermetallic	Al (wt%/at%)	Mn (wt%/at%)	Fe (wt%/at%)	Si (wt%/at%)
Bright Particle	72/82	3.2/1.7	18.2/9.9	6.3/6.8
Dull Particle	80/89	2.8/1.5	14.9/7.9	1.6/1.7
Dispersoid/ppt	94/95	1.2/0.6	2.4/1.2	2.9/2.8

Table 9.11. EDS Summary for 12μm Pre-annealed 8150 alloy

The aspect ratio falls to two for particles less than $0.40\mu m^2$. This implies the manganese rich dispersoid range in size predominately from $0.07 - 1.6\mu m^2$, with iron rich precipitates below and iron rich intermetallics above this range.

S# 909362 F 8150 sheet 12 micron exit foil rolling double

file: 808362MF-1

MEASURED AREA DISTRIBUTION OF PARTICLE SECTION SIZES

Group number	Area of sections microns	Area%	Number	Number density (no./mm2)	Number density (no./um2)	Maximum aspect ratio	Average aspect ratio
5	15.8489 - 10.0000	0.1845	1	184	0.000184	2.67	2.67
6	10.0000 - 6.3096	0.2927	2	368	0.000368	6.71	4.96
7	6.3096 - 3.9811	0.6666	7	1290	0.001290	4.86	3.74
8	3.9811 - 2.5119	0.7833	13	2395	0.002395	7.83	3.73
9	2.5119 - 1.5849	0.5431	15	2763	0.002763	7.79	3.77
10	1.5849 - 1.0000	0.3871	16	2948	0.002948	7.64	4.28
11	1.0000 - .6310	0.4157	28	5158	0.005158	13.52	4.30
12	.6310 - .3981	0.2707	30	5527	0.005527	12.70	3.92
13	.3981 - .2512	0.1747	30	5527	0.005527	6.83	2.89
14	.2512 - .1585	0.0952	27	4974	0.004974	8.84	2.84
15	.1585 - .1000	0.0550	23	4237	0.004237	4.03	2.06
16	.1000 - .0631	0.0534	37	6816	0.006816	3.60	1.99
17	.0631 - .0398	0.0349	38	7001	0.007001	10.21	2.68
18	.0398 - .0251	0.0584	104	19159	0.019159	8.86	2.26
19	.0251 - .0158	0.0487	135	24870	0.024870	11.15	2.50
20	.0158 - .0100	0.0411	180	33160	0.033160	7.42	2.16
21	.0100 - .0063	0.0272	186	34266	0.034266	13.72	2.10
22	.0063 - .0040	0.0171	183	33713	0.033713	8.98	1.78
23	.0040 - .0025	0.0096	165	30397	0.030397	7.40	1.71
24	.0025 - .0016	0.0052	141	25976	0.025976	10.45	1.72
25	.0016 - .0010	0.0017	72	13264	0.013264	5.09	1.72
26	.0010 - .0006	0.0016	98	18054	0.018054	6.13	1.84

statistics
Average area = .1478 Average diameter = .1866
Median area = .0080 Median diameter = .0920
No. of particles/mm2 = 282047
Area percent = 4.167

Figure 9.77. **The measured area distribution of particle sizes for the foil rolled 12µm sample pre-annealed. There is a notable increase in particle count for particles with areas below 1µm^2 and a further increase for particles with area below 0.40µm^2.**

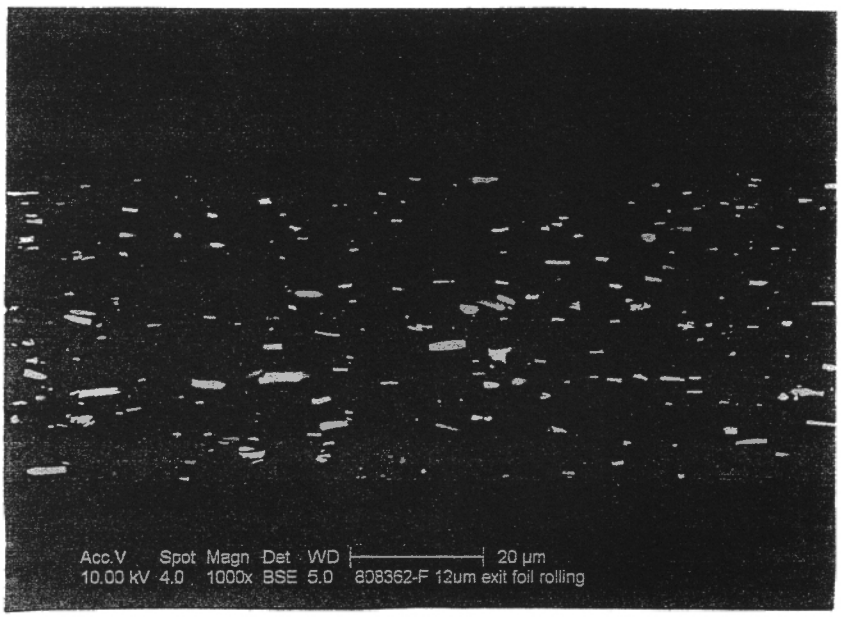

Figure 9.78. **SEM micrograph of 12µm pre-annealed sample (1000x). Intermetallic's are generally rectangular in shape aligned in the direction of rolling.**

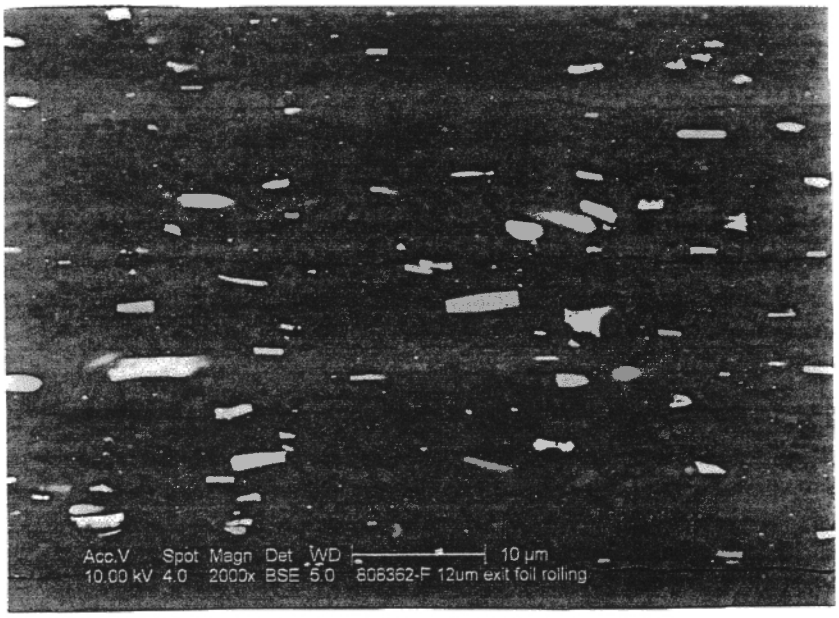

Figure 9.79. **SEM micrograph of 12µm pre-annealed sample (2000x). Bright and dull intermetallic particles 'string' in the rolling direction. The matrix has an un-recrystallised sub-grain type structure of less than 1µm, with random spherical dispersoids visible.**

Figure 9.80. **SEM micrograph of 12µm pre-annealed sample (5000x). Dispersoids are clearly seen intermittently spread through the matrix with a mean spacing of between 2µm to 10µm.**

Figure 9.81. **SEM micrograph of 12µm pre-annealed sample (9000x). The microstructure yields an un-recrystallised sub-grain type structure of less than 1µm. Spherical dispersoids less than 0.1µm in size are clearly seen intermittently spread randomly the matrix with a mean spacing of between 2µm to 10µm.**

File: C:\PGT_Data\Data\808362f2_1_bright particle.pgt
Collected: July 20, 2005 13:13:31

Live Time:	100.00	Count Rate:	5792	Dead Time:	47.24 %
Beam Voltage:	10.00	Beam Current:	2.00	Takeoff Angle:	33.50

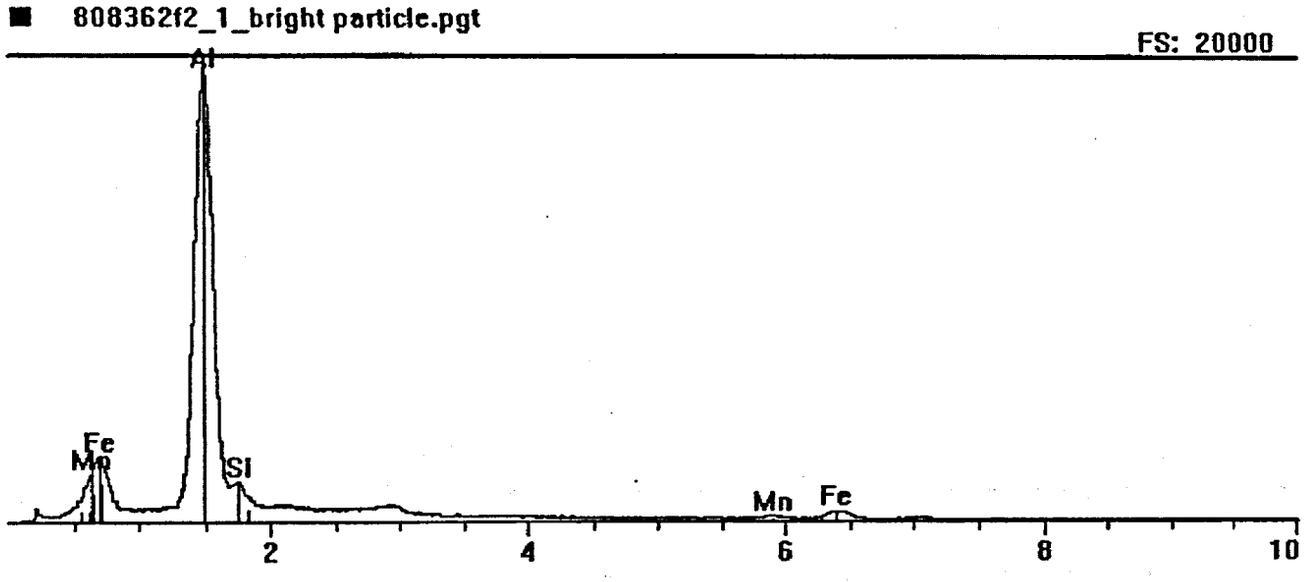

Element	Line	keV	KRatio	Wt%	At%	At Prop	ChiSquared
Al	KA1	1.487	0.6669	72.42	81.60	0.0	47.51
Mn	KA1	5.898	0.0269	3.15	1.74	0.0	1.55
Fe	KA1	6.403	0.1549	18.18	9.89	0.0	1.55
Si	KA1	1.740	0.0443	6.26	6.77	0.0	47.51
Total			0.8929	100.00	100.00	0.0	37.13

Element	Line	Gross (cps)	BKG (cps)	Overlap (cps)	Net (cps)	P:B Ratio
Al	KA1	2652.6	93.0	0.7	2558.9	27.5
Mn	KA1	34.5	19.1	0.0	15.4	0.8
Fe	KA1	73.8	17.1	1.5	55.2	3.2
Si	KA1	279.0	96.7	18.5	163.9	1.7

Element	Line	Det Eff	Z Corr	A Corr	F Corr	Tot Corr	Modes
Al	KA1	0.895	0.971	1.120	0.999	1.086	Element
Mn	KA1	0.976	1.182	1.005	0.986	1.171	Element
Fe	KA1	0.981	1.171	1.002	1.000	1.174	Element
Si	KA1	0.885	0.953	1.483	1.000	1.413	Element

Figure 9.82. **EDS spectrum of large bright particles show a high percentage of iron and some secondary manganese and silicon readings.**

File: C:\PGT_Data\Data\808362f2_dull particle.pgt
Collected: July 20, 2005 13:04:57

Live Time:	100.00	Count Rate:	5995	Dead Time:	47.95 %
Beam Voltage:	10.00	Beam Current:	2.00	Takeoff Angle:	33.50

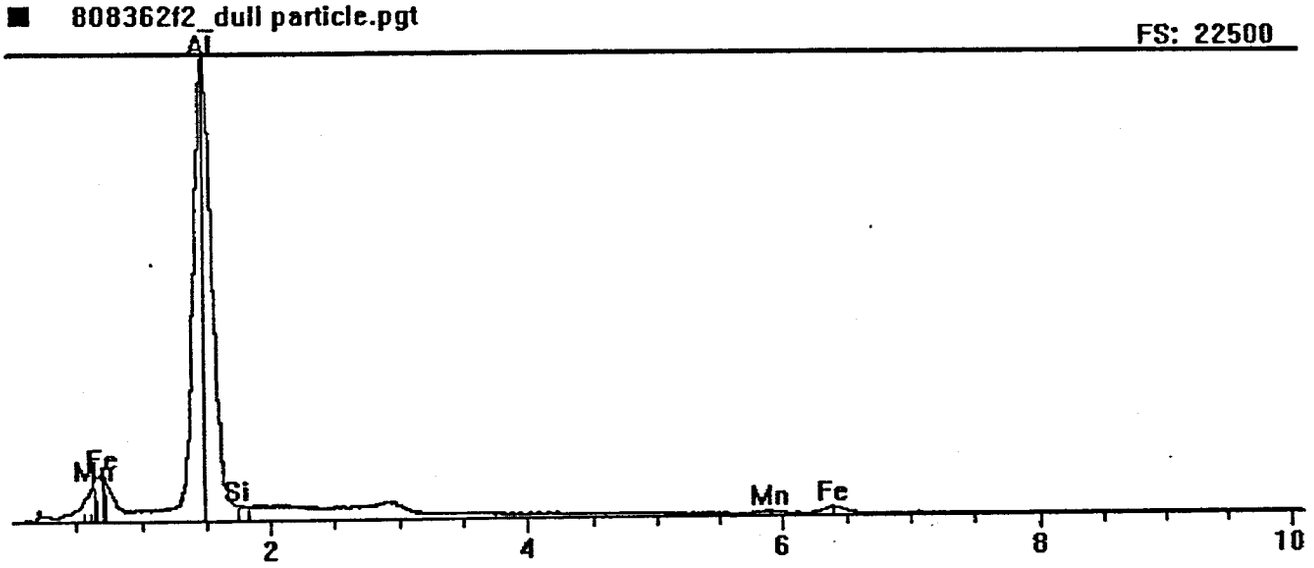

Element	Line	keV	KRatio	Wt%	At%	At Prop	ChiSquared
Al	KA1	1.487	0.7534	80.70	88.88	0.0	48.23
Mn	KA1	5.898	0.0237	2.80	1.52	0.0	1.65
Fe	KA1	6.403	0.1264	14.92	7.94	0.0	1.65
Si	KA1	1.740	0.0108	1.57	1.67	0.0	48.23
Total			**0.9144**	**100.00**	**100.00**	**0.0**	**41.40**

Element	Line	Gross (cps)	BKG (cps)	Overlap (cps)	Net (cps)	P:B Ratio
Al	KA1	3029.9	91.1	0.2	2938.7	32.3
Mn	KA1	33.2	19.3	0.0	13.9	0.7
Fe	KA1	64.0	16.9	1.4	45.8	2.7
Si	KA1	156.6	94.7	21.2	40.7	0.4

Element	Line	Det Eff	Z Corr	A Corr	F Corr	Tot Corr	Modes
Al	KA1	0.895	0.975	1.099	1.000	1.071	Element
Mn	KA1	0.976	1.189	1.005	0.988	1.181	Element
Fe	KA1	0.981	1.178	1.002	1.000	1.180	Element
Si	KA1	0.885	0.957	1.520	1.000	1.454	Element

Figure 9.83. **EDS spectrum of dull oval particle show iron and some secondary manganese and silicon readings.**

File: C:\PGT_Data\Data\808362f2_2_dispersoid.pgt
Collected: July 20, 2005 13:13:31

Live Time:	100.00	Count Rate:	7375	Dead Time:	52.35 %
Beam Voltage:	10.00	Beam Current:	2.00	Takeoff Angle:	33.50

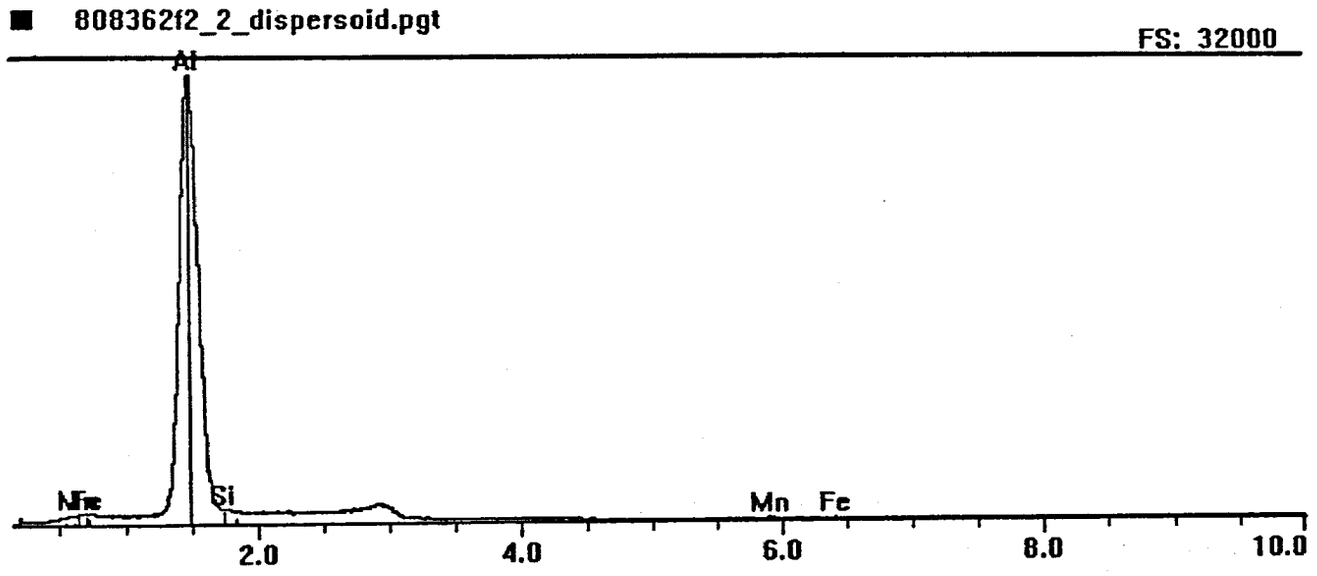

Element	Line	keV	KRatio	Wt%	At%	At Prop	ChiSquared
Al	KA1	1.487	0.9222	93.58	95.43	0.0	53.67
Mn	KA1	5.898	0.0099	1.21	0.60	0.0	1.85
Fe	KA1	6.403	0.0195	2.36	1.16	0.0	1.85
Si	KA1	1.740	0.0189	2.86	2.80	0.0	53.67
Total			0.9704	100.00	100.00	0.0	66.47

Element	Line	Gross (cps)	BKG (cps)	Overlap (cps)	Net (cps)	P:B Ratio
Al	KA1	4190.9	96.4	0.4	4094.2	42.5
Mn	KA1	23.9	17.3	0.0	6.6	0.4
Fe	KA1	23.2	14.5	0.6	8.0	0.6
Si	KA1	211.7	101.1	29.5	81.1	0.8

Element	Line	Det Eff	Z Corr	A Corr	F Corr	Tot Corr	Modes
Al	KA1	0.895	0.995	1.020	0.999	1.015	Element
Mn	KA1	0.976	1.219	1.005	0.998	1.223	Element
Fe	KA1	0.981	1.208	1.003	1.000	1.212	Element
Si	KA1	0.885	0.977	1.546	1.000	1.511	Element

Figure 9.84. **EDS spectrum for the spherical dispersoids show higher levels of iron than manganese. This implied that the precipitation of iron rich particles have occurring during foil processing.**

Thin Foil Post-Anneal 12μm product

The microstructure of the post annealed thin foil product is significantly different to the pre-anneal sample. Recrystallisation is present with grainsize observed to be generally greater than 1μm and most 2-5μm sized grains. There is no significant change to the shape, orientation, size or number of constituent particles. The precipitate number has increased considerably, with the mean spacing less than 1μm. An area distribution analysis showed a 100% increase in particle count for particles with areas less than $0.0400\mu m^2$ while little to no change occurred for particles greater than $0.0400\mu m^2$, Figure 9.85.

There was a small decrease in aspect ratio for the new precipitates, implying that the precipitates were spherical in shape when compared to the constituents. The micrographs are shown in Figures 9.86 - 9.90 with the EDS spectrum shown in Figures 9.91 – 9.93 with a summary given in Table 9.12. Figures 10.45 –10.46 show the measure area distribution of particle section sizes pre and post anneal.

The manganese atomic percentage has dropped slightly with a corresponding increase in iron observed from the pre-annealed samples. This implies that cold work greater than 99% following by thermal processing produces both iron rich precipitates prior to thermal treatment and manganese rich precipitates post thermal treatment. There is also some substitution of iron for manganese in the larger bright and dull particles, with the overall ratio remaining fairly constant.

Intermetallic	Al (wt%/at%)	Mn (wt%/at%)	Fe (wt%/at%)	Si (wt%/at%)
Bright Particle	71/81	1.7/0.94	20.5/11.2	6.2/6.7
Dull Particle	81/89	1.8/1.0	15.1/8.0	1.6/1.7
Dispersoid/ppt	93/95	2.2/1.1	1.2/0.6	3.5/3.4

Table 9.12. EDS Summary for 12μm Post-annealed 8150 alloy

S# 808362 8150 sheet O 12 micron exit foil, rolled in annealed condition

file: 808362MO-1

MEASURED AREA DISTRIBUTION OF PARTICLE SECTION SIZES

Group number	Area of sections microns	Area%	Number	Number density (no./mm2)	Number density (no./um2)	Maximum aspect ratio	Average aspect ratio
1	10.0000 - 6.3096	0.1282	1	177	0.000177	6.40	6.40
2	6.3096 - 3.9811	0.1588	2	353	0.000353	6.07	4.13
3	3.9811 - 2.5119	0.4294	8	1412	0.001412	5.66	3.14
4	2.5119 - 1.5849	0.1734	5	883	0.000883	9.34	4.57
5	1.5849 - 1.0000	0.6187	28	4943	0.004943	8.98	3.80
6	1.0000 - .6310	0.2901	20	3531	0.003531	7.39	3.56
7	.6310 - .3981	0.2179	24	4237	0.004237	10.25	3.04
8	.3981 - .2512	0.1903	34	6002	0.006002	9.25	3.39
9	.2512 - .1585	0.0737	21	3707	0.003707	3.94	2.39
10	.1585 - .1000	0.0704	30	5296	0.005296	8.02	2.34
11	.1000 - .0631	0.0303	22	3884	0.003884	6.32	2.18
12	.0631 - .0398	0.0305	36	6355	0.006355	6.31	2.63
13	.0398 - .0251	0.0697	131	23125	0.023125	8.98	2.59
14	.0251 - .0158	0.0941	271	47839	0.047839	10.59	2.23
15	.0158 - .0100	0.0820	370	65316	0.065316	8.27	2.08
16	.0100 - .0063	0.0547	388	68493	0.068493	9.60	1.92
17	.0063 - .0040	0.0359	394	69552	0.069552	7.82	1.74
18	.0040 - .0025	0.0216	376	66375	0.066375	7.14	1.69
19	.0025 - .0016	0.0114	322	56842	0.056842	7.51	1.64
20	.0016 - .0010	0.0046	202	35659	0.035659	4.05	1.73
21	.0010 - .0006	0.0028	182	32128	0.032128	4.06	1.77

statistics
Average area = .0551 Average diameter = .1117
Median area = .0062 Median diameter = .0569
No. of particles/mm2 = 506109
Area percent = 2.789

Figure 9.85. **The measured area distribution of particle sizes for the foil rolled 12µm sample post-annealed. There is a notable increase in particle count for particles with areas below 0.40µm^2 and a corresponding decrease in average aspect ratio.**

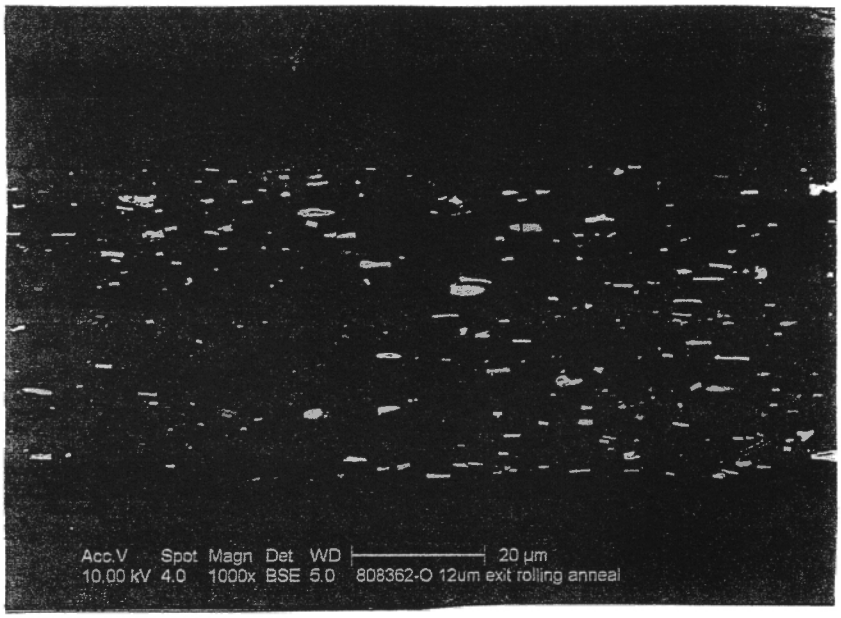

Figure 9.86. **SEM micrograph of 12µm post-annealed sample (1000x). Intermetallic's are generally rectangular in shape aligned in the direction of rolling.**

Figure 9.87. **SEM micrograph of 12µm post-annealed sample (2000x). Bright and dull intermetallic particles are aligned in the rolling direction. The matrix has a recrystallised grain structure of generally greater than 1µm and below 5µm with random spherical precipitates and dispersoids visible.**

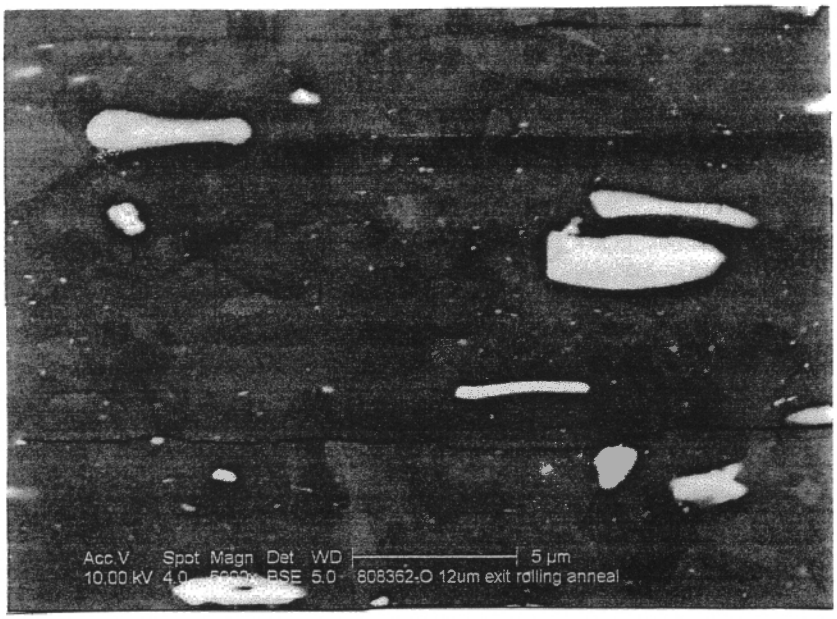

Figure 9.88. **SEM micrograph of 12µm post-annealed sample (5000x). Dispersoids are clearly seen intermittently spread through the matrix with a mean spacing below 1µm.**

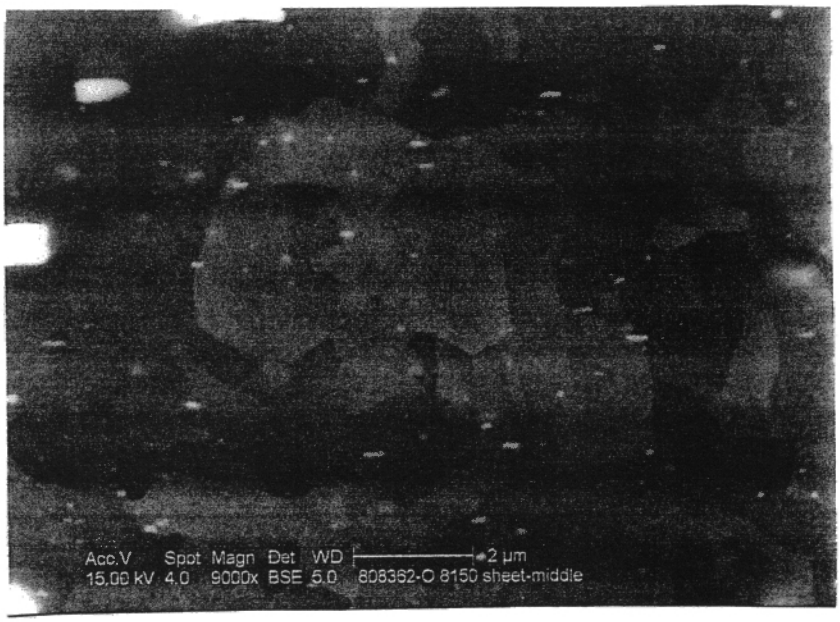

Figure 9.89. **SEM micrograph of 12µm post-annealed sample (9000x). The precipitates/dispersoids are randomly distributed in the homogenously recrystallised matrix.**

Figure 9.90. **SEM micrograph of 12µm post-annealed sample (9000x). The accelerate voltage is reduced from 15kV to 10kV to emphasize the precipitates/dispersoids embedded in the matrix.**

File: C:\PGT_Data\Data\80836202_bright particle.pgt
Collected: July 20, 2005 13:31:46

Live Time:	100.00	Count Rate:	5728	Dead Time:	47.08 %
Beam Voltage:	10.00	Beam Current:	2.00	Takeoff Angle:	33.50

■ 80836202_bright particle.pgt

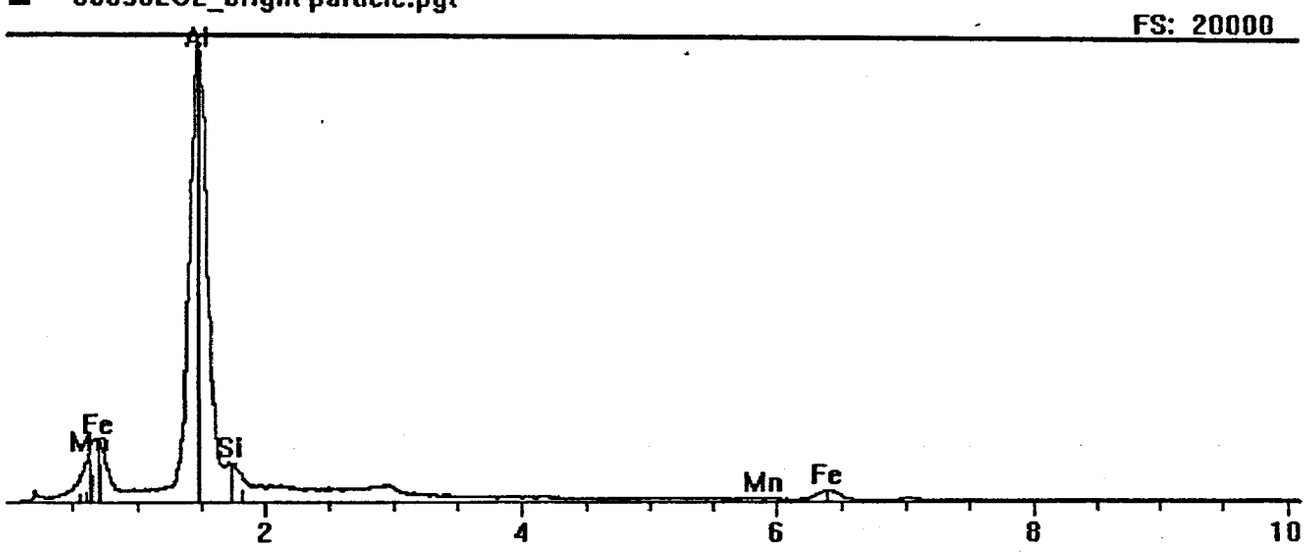

Element	Line	keV	KRatio	Wt%	At%	At Prop	ChiSquared
Al	KA1	1.487	0.6565	71.61	81.12	0.0	43.44
Mn	KA1	5.898	0.0144	1.68	0.94	0.0	1.46
Fe	KA1	6.403	0.1752	20.53	11.23	0.0	1.46
Si	KA1	1.740	0.0438	6.18	6.72	0.0	43.44
Total			**0.8899**	**100.00**	**100.00**	**0.0**	**33.35**

Element	Line	Gross (cps)	BKG (cps)	Overlap (cps)	Net (cps)	P:B Ratio
Al	KA1	2630.9	93.8	0.7	2536.3	27.0
Mn	KA1	28.3	20.0	0.0	8.3	0.4
Fe	KA1	81.1	17.5	0.8	62.8	3.6
Si	KA1	278.8	97.3	18.3	163.2	1.7

Element	Line	Det Eff	Z Corr	A Corr	F Corr	Tot Corr	Modes
Al	KA1	0.895	0.970	1.126	0.999	1.091	Element
Mn	KA1	0.976	1.180	1.005	0.984	1.167	Element
Fe	KA1	0.981	1.169	1.002	1.000	1.172	Element
Si	KA1	0.885	0.952	1.482	1.000	1.411	Element

Figure 9.91. **EDS spectrum of large bright particles show a high percentage of iron and some secondary manganese and silicon readings.**

File: C:\PGT_Data\Data\80836202_1_dull particle.pgt
Collected: July 20, 2005 13:36:00

Live Time:	100.00	Count Rate:	6220	Dead Time:	48.70 %
Beam Voltage:	10.00	Beam Current:	2.00	Takeoff Angle:	33.50

■ 80836202_1_dull particle.pgt

FS: 25000

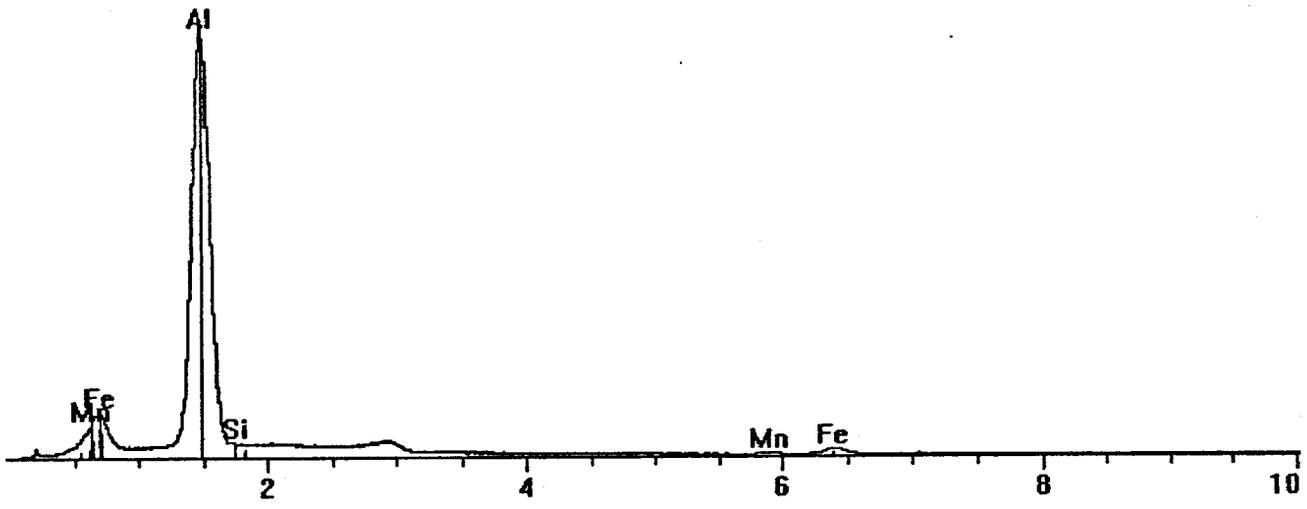

Element	Line	keV	KRatio	Wt%	At%	At Prop	ChiSquared
Al	KA1	1.487	0.7634	81.57	89.40	0.0	52.47
Mn	KA1	5.898	0.0151	1.79	0.96	0.0	1.58
Fe	KA1	6.403	0.1273	15.05	7.96	0.0	1,58
Si	KA1	1.740	0.0109	1.59	1.68	0.0	52.47
Total			**0.9167**	**100.00**	**100.00**	**0.0**	**44.76**

Element	Line	Gross (cps)	BKG (cps)	Overlap (cps)	Net (cps)	P:B Ratio
Al	KA1	3134.9	95.3	0.2	3039.4	31.9
Mn	KA1	28.4	19.4	0.0	9.0	0.5
Fe	KA1	65.0	17.1	0.9	47.0	2.8
Si	KA1	162.8	99.0	21.9	41.9	0.4

Element	Line	Det Eff	Z Corr	A Corr	F Corr	Tot Corr	Modes
Al	KA1	0.895	0.977	1.094	1.000	1.069	Element
Mn	KA1	0.976	1.191	1.005	0.988	1.182	Element
Fe	KA1	0.981	1.180	1.002	1.000	1.182	Element
Si	KA1	0.885	0.958	1.522	1.000	1.459	Element

Figure 9.92. **EDS spectrum of dull oval particle show iron and some secondary manganese and silicon readings.**

File: C:\PGT_Data\Data\808362O2_2_dispersoid.pgt
Collected: July 20, 2005 13:40:17

Live Time: 100.00 Count Rate: 7434 Dead Time: 52.55 %
Beam Voltage: 10.00 Beam Current: 2.00 Takeoff Angle: 33.50

■ 808362O2_2_dispersoid.pgt

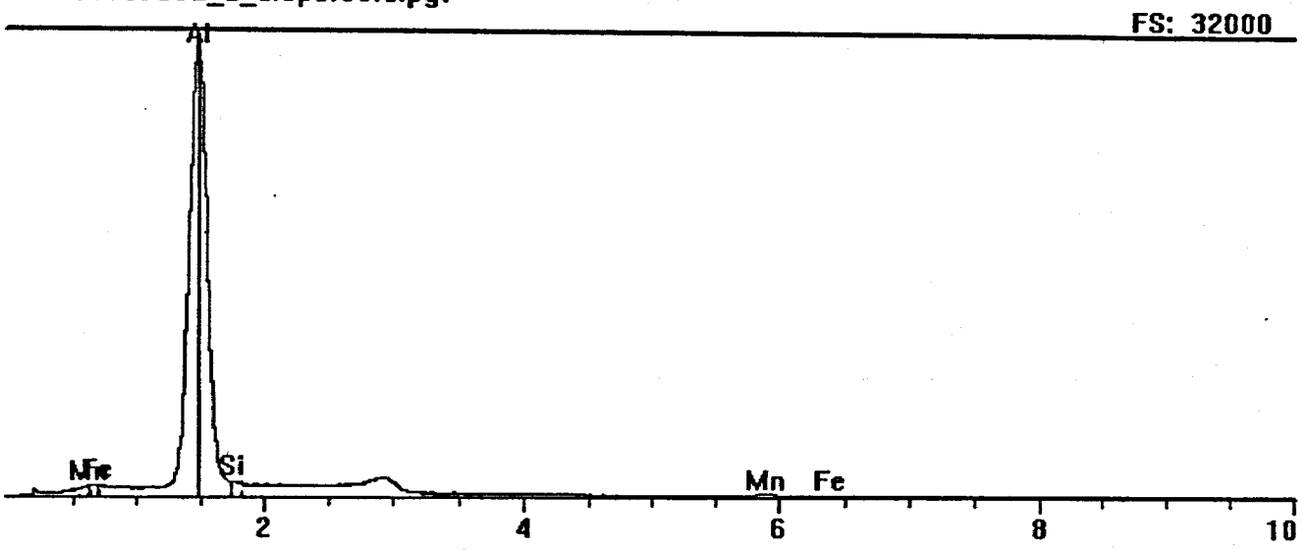

Element	Line	keV	KRatio	Wt%	At%	At Prop	ChiSquared
Al	KA1	1.487	0.9193	93.15	94.93	0.0	49.74
Mn	KA1	5.898	0.0183	2.24	1.12	0.0	1.73
Fe	KA1	6.403	0.0096	1.16	0.57	0.0	1.73
Si	KA1	1.740	0.0229	3.46	3.38	0.0	49.74
Total			**0.9701**	**100.00**	**100.00**	**0.0**	**67.87**

Element	Line	Gross (cps)	BKG (cps)	Overlap (cps)	Net (cps)	P:B Ratio
Al	KA1	4211.0	88.8	0.5	4121.7	46.4
Mn	KA1	31.0	18.7	0.0	12.3	0.7
Fe	KA1	20.7	15.5	1.2	4.0	0.3
Si	KA1	222.3	93.4	29.7	99.2	1.1

Element	Line	Det Eff	Z Corr	A Corr	F Corr	Tot Corr	Modes
Al	KA1	0.895	0.996	1.018	0.999	1.013	Element
Mn	KA1	0.976	1.219	1.005	0.999	1.224	Element
Fe	KA1	0.981	1.208	1.003	1.000	1.212	Element
Si	KA1	0.885	0.977	1.543	1.000	1.507	Element

Figure 9.93. **EDS spectrum of spherical dispersoids return to higher concentrations of manganese and possibly silicon, with lower levels of iron.**

Phase Identification

The elemental atomic percentage obtained from the EDS spectrum was examined in conjunction with the phase diagram to determine the phases present. The results were also compared to standards at Alcoa Technical Centre (ATC)[13]. A problem with the EDS technique is that the small size of the phases, particularly the precipitates, results in the area analysised to incorporate a small amount of the surrounding matrix. This was due to the minimum area required to complete the analysis being greater than the precipitate area. The effect of this was to dilute the iron and manganese atomic volume percentages and increase the aluminium and pseudo-silicon percentages[13].

The matrix was found to be essentially aluminium with only trace amounts of iron and manganese. The surprisingly high silicon content, which was an order of magnitude greater than the maximum composition, could be explained by an inherent error in the in-house software (due to silicon/aluminium overlap), and hence is regarded as negligible[13].

At all gauges, the bright particles had similar compositions and alloy ratios. With cold work levels greater than 90%, with 99% typical there is some substitution of iron and manganese. This is reversed during thermal treatment. This will be explained in the discussion. When compared to ATC standards, the high iron levels with low atomic volumes of silicon and even lower manganese levels confirmed the particle as $Al_{12}(FeMn)_3Si$. In some literature the phase is also referred to as $Al_{15}(FeMn)_3Si$[13]. The phase is iron dominant with only minor manganese substitution.

Similarly the dull phases were evaluated and found to match $Al_6(FeMn)$ particles. Again the phase was dominated by the iron atomic percentage when compared to manganese. The silicon levels were similar to that seen in the matrix analysis and hence discounted. The dispersoid/precipitate analysis was complicated by the above mentioned area limitations. The dispersoids were higher in atomic percentage until final annealing. During the final thermal treatment stage, the manganese content increase to be greater than the iron content. As a result the precipitates were richer in manganese than the dispersoids.

In summary, Table 9.13 describes the phases from each sample, with the iron atomic percentage approximately an order of magnitude greater than the manganese percentage for the phases. Literature indicted that the detrimental $Al_3(FeMn)$ or equivalent may be present, however none was detected[14]. The silicon to iron ratio and overall content was not high enough to induce higher silicon phases such as $Al_9Fe_2Si_2$ or Al_8Fe_2Si[15].

There is some substitution in all phases of iron and manganese as a result of either excessive cold work (>99% reduction)[60] or thermal treatment. This is due to the rolling temperatures providing sufficient temperature or energy (up to 100°C) to allow the iron saturated solution to 'precipitate' iron rich spherical particles.

Phase	Composition
Matrix	Essential 100% aluminium
Bright Phases - all samples	$Al_{12}(FeMn)_3Si$
Dull Phases – all samples	$Al_6(FeMn)$
Dispersoids – before final heat treatment	$Al_{12}(FeMn)_3Si$
Precipitates – after final heat treatment	$Al_{12}(MnFe)_3Si$

Table 9.13. Phases in 8150 alloy during thermo-mechanical processing

9.2.2. Other Observations

9.2.2.1. Anneal Temperature

The burst strength results for the trial 12 micron material which compared a 30C difference in annealing temperature over a 2 hour soak period is shown in Figure 9.94. The product produced fell into one of two distinct burst strength distributions; the lower strength distribution with an average burst strength of 92kPa, annealled at 315°C (red – B2b), or the higher strength distribution with an average burst strength of 117.6kPa annealed at 285°C (blue – B2a).

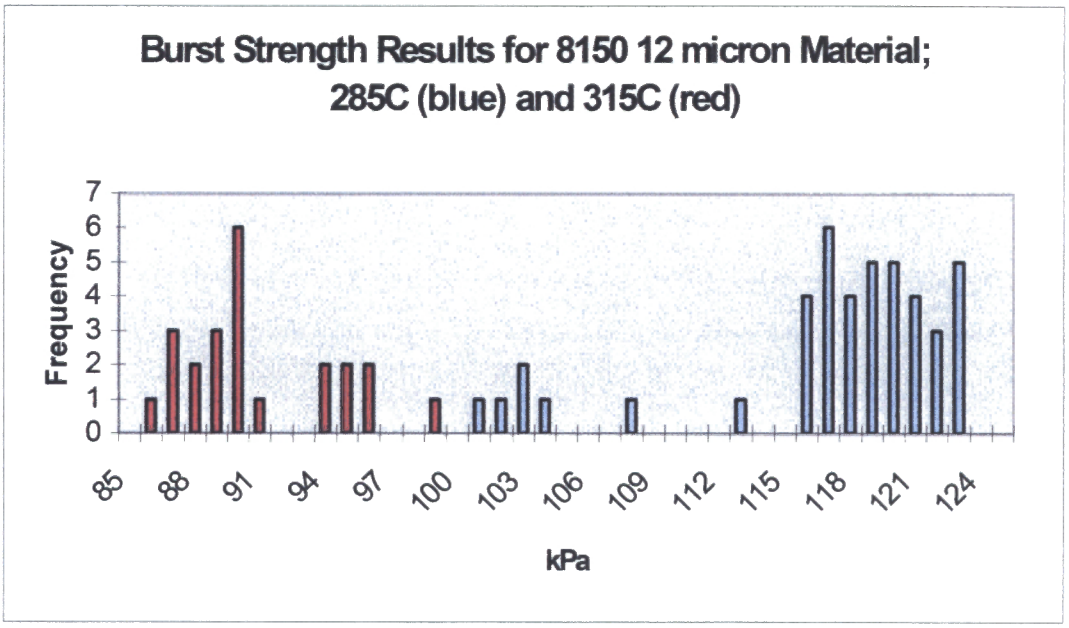

Figure 9.94. **The distribution of Mullen's results for 8150 alloys demonstrates the sensitivity of mechanical properties to final annealing temperature. The red results are for a 20°C higher annealing temperature than the blue.**

9.2.2.2. The Effects of Recovery during Cold Rolling.

Subsequent Erickson testing of the final product showed a 10-15% drop in Erickson strength (refer to Appendix 8 for Erickson testing procedure)[16]. This is shown in Figure 9.95, with the raw data in Appendix 11.

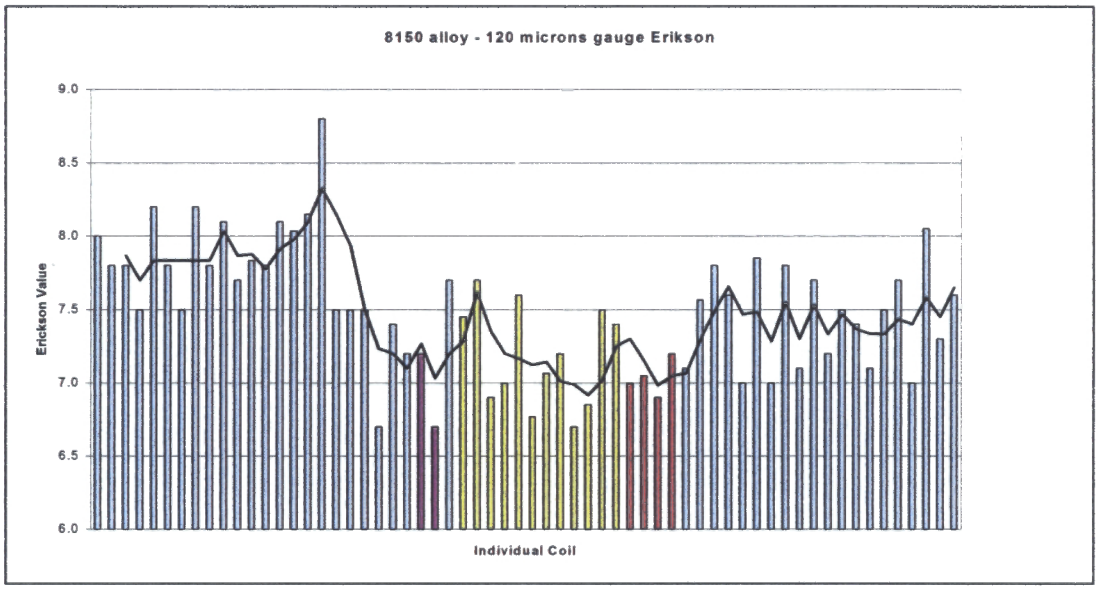

Figure 9.95 **Erickson results of 120um 8150 product versus time. The Erickson values decrease by over 10% once the rolling temperatures exceeded 160°C.**

Samples were collected from the coils with high and low Erickson results, polished and etched to determine the grain structure, Figure 9.96. The macrographs showed the presence of larger grains (approximately 2-5 times normal size) in the coils with lower properties.

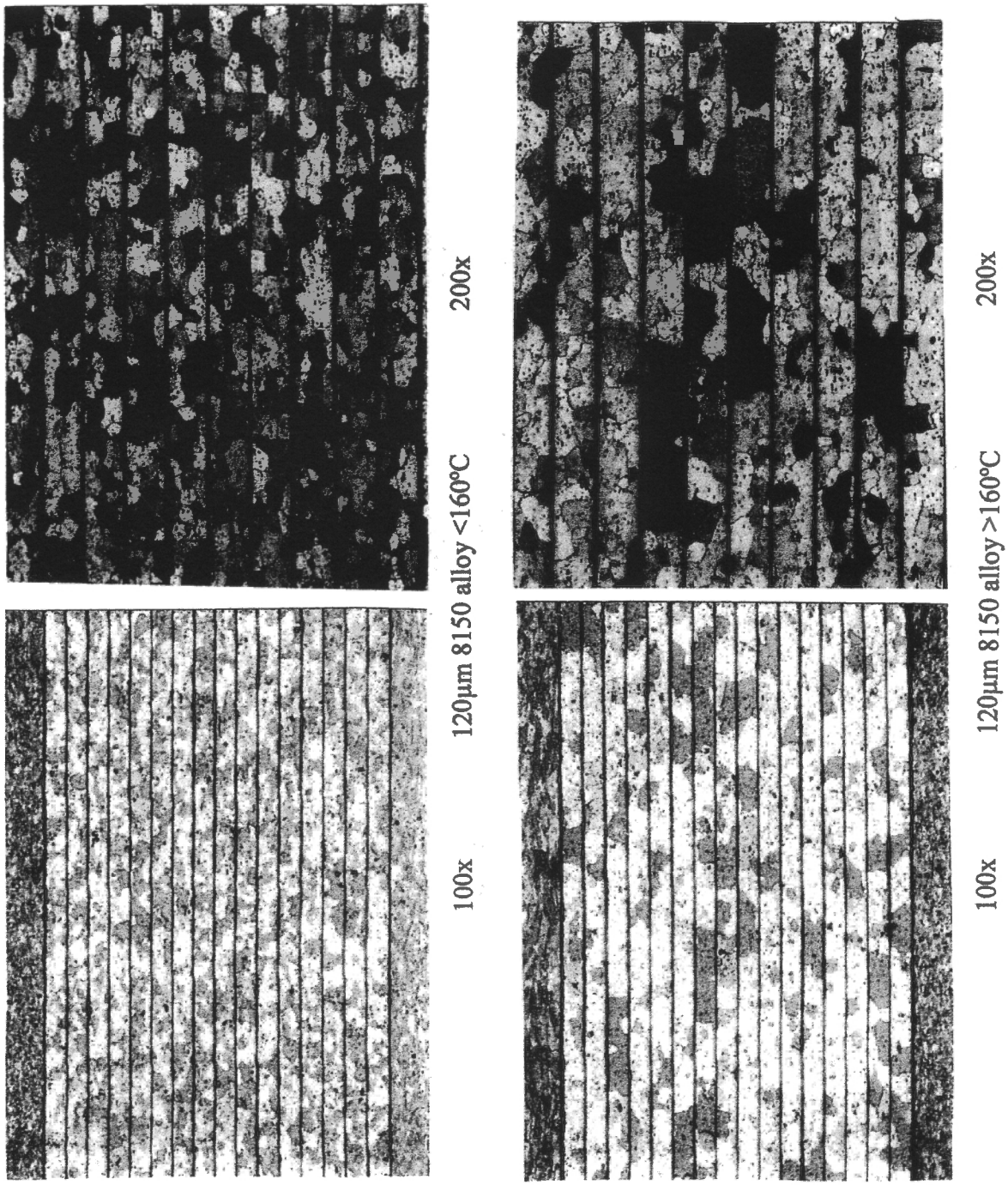

Figure 9.96. **Metallurgical comparison of 8150 rolled at below 160°C compared to those rolled at greater than 160°C. The presence of Large Random Grains at 100x and 200x explains the Loss in Strength via the Hall-Petch Relationship.**

CHAPTER 10 ALLOY INVESTIGATION – DISCUSSION AND CONCLUSIONS

10.1. Surface Studies

An examination of the shiny and matte sides revealed no significance difference in total oxygen or carbon levels. One matte sample had much lower surface hydrocarbon contamination, believed related to the application technique rather than reaction kinetics. The application technique involves a localized 'drip' of matting fluid onto the sheet. This then relies on the rolling process to spread the matting fluid across the strip. Failure to do this can result in broken matte or in more extreme cases streaky matte (as described in Chapter 6).

A more preferred method of matte fluid application is to spray the fluid onto the sheet. It highlights the need to improve the current matte application technique from a non-uniform drip system to a more uniform spray system. This will also aid in controlling streaky and broken matte defects.

XPS analysis of the thin foil surface showed the presence of carbonaceous surface contaminates along with various oxides and alkali and alkali earth metals. General wide surface scans gave little information other than identifying the presence of oxygen, aluminium and carbon, as well as several trace elements. High resolution scans were made on the elemental compounds detected to allow a closer examination of surface contaminates, particularly carbon and oxygen.

Carbon

The carbon spectra showed three peaks for all samples with the larger peak at 286.1 – 286.4eV assumed to be a slightly shifted (2eV) hydro-carbon group. The charging shift is associated with insulating materials[17]. The broad base was found to be due to the presence of alkoxy-groups in the form of organic hydroxyls that would occur at a shifted value of 287.7-287.8eV. The third peak consisted of an oxidised carbon functional group in the form of carboxylic acids at 290.2-6eV.

The carbonaceous residues were found to be composed mainly of hydrocarbons, with traces of organic hydroxyls and carboxylic acids an order of magnitude less. There was a small increase in binding energy and base spread for carbon based products as the annealing temperature increased, but time decreased. At temperature below 250°C (B1), oxidation rather than polymerisation occurs. At temperatures of around 300°C (B2), some polymerisation occurs although oxidation dominates[3]. This indicated that for temperatures below 300°C where oxides start to crystallize, the heating process time is critical in promoting oxidation and even polymerisation.

Depth profiles obtained using ion bombardment and XPS analysis revealed a slight increase in aluminium oxide at the surface with a corresponding drop in 'other' oxides to about the 0.3-0.5nm mark. This corresponded with William's[3] observations that the carbonaceous residue appeared to be approximately 0.3nm thick. It appeared that the organic oxides substitutionally diffuse into the metal surface at a similar rate to that of aluminium hydroxide[3]. The exact transition point is difficult to establish as there is no recognized international guidelines on measuring oxide thickness using XPS data.

Oxides

High resolution scans for oxygen showed a broad single oxygen peak that was due to the presence of both aluminium oxide and aluminium hydroxides at 533.1eV and 532.1eV respectively, as well as a smaller peak at 533.9eV which further supports the presence of alkoxy-groups. The depth profiles for aluminium oxides and other oxides corresponded that those observed in carbon. Both oxides then follow an inverse logarithmic growth pattern until a depth of between 5 to 15nm. The oxygen diffusion layer starts for a further 10-20nm back with the exact transition point difficult to determine.

In lieu of any defined method of determining an oxide thickness, the aluminium spectra resulting from high resolution XPS multiplex surveys can be used to calculate the oxide thickness, as shown by Clark and Tripathi:

$$\frac{A_{oxide}}{A_{metal}} = \frac{(1-\exp^{(-d/\Delta)}}{\exp^{(-d/\Delta)}} \qquad (9.2)$$

Where A_{oxide} and A_{metal} are the respective areas obtained from Al(2p) XPS spectra, d is the oxide film thickness and Δ is the escape depth. The value for Δ is estimated at 1.2 ± 0.2nm for KE ~ 1180 eV[18]. Using this equation, the oxide thickness is 2.8 ± 0.5nm for all samples.

The presence of hydroxides at the surface indicated either humid slitting and/or annealing conditions, or the production of water from the chemical reactions during annealing bonding, the aluminium metal surface to produce aluminium hydroxides. While the atomic percentage values were proportionally high, work by Williams indicated that they had a negligible effect on stickiness[3]. As all samples unwound easily with no addition force, this observation was supported in this thesis.

While William's work suggested that residual lubricant polymerization is the main mechanisms for stickiness, there is still a train of thought that surface oxidation of the residual lubricant and aluminium interface are factors[3]. The observations from this trial are consistent with William's observations of non-sticky foil, with lubricant polymerisation the main mechanism for stickiness. The ratio of time to temperature still requires further investigation, with heat-up and cooldown rates to remain constant.

Other

The presence of trace elements such as fluorine, nitrogen and tin are thought to be contaminates from either the natural gas supply that is used to fire the furnaces, or in the case of tin, impurities in the coolant from gear-oil and other heavy oil leaks. Some manganese was expected, and was present in oxide trace amounts.

The presence of copper and magnesium was anticipated as furnaces used to cast the alloys also cast high copper and magnesium alloyed products. These two alloys, along with manganese, leach into refractory bricks, and can contaminate purity alloys such as 1xxx and 8xxx series alloys if not 'washed out' correctly. Alloy additions are not unheard of in 8xxx series alloys, with Alcan having a patent on the addition of copper and magnesium to alloy 8006, itself a patented alloy[19,20,21].

Copper promotes a finer grain structure and increased burst strength but also increases the corrosion susceptibility of the metal, particularly when used in frozen food applications. Magnesium is detrimental on laminated product as magnesium oxide 'islands' can reduce the adhesions at the lamination boundary, similar to the effects of poor wettability coils. The mechanism for this is given in Chapter 2.3.2.6. The presence of these elements must be kept at below 0.05% as was done in this instance.

Based on the work by Williams, the effect of humidity, and atmospheric conditions in general were not examined. The annealing cycles have been based on previous work, and are consistent with the finding of the thesis[3]. As a result heating rates and subsequence de-greasing kinetics related to this area were not examined. Work in determining a more exact nature of the carbon compounds was not performed as all annealing temperatures were below 300°C. The results agree with the work of Williams[3].

Surface Roughness

The matte surface roughness is far more pronounced than roll finish surface roughness. The mean Ra and peak-to-valley data indicated that the roll-metal interface was significantly less aggressive on the surface morphology than the metal-metal interface. This implies that roll grind has a secondary influence when looking exclusively at surface roughness.

This phenomenon can be explained by examining the surface interface friction conditions for metal-to-metal interfaces. Insufficient lubrication at the roll bite results in discrete fractures in the lubrication film between the roll and the strip. Consequently, metal-to-metal contact occurs with friction dependent on the physical properties of the surface films formed by the lubrication on the metal surface as well as the environmental and operational conditions. The process of dripping matting solvent or rolling oil onto the surface promotes lubrication breakdowns at the metal-to-metal interface resulting in metal-to-metal contact.

While roll grind roughness is found to have a secondary effect on surface roughness when compared to metal-to-metal interactions, roll grind roughness is known to be a major variable that can influence rolling speeds. Increasing roll roughness increases rolling speeds, but has the opposite effect on coolant entrainment. Increasing the rolling speed increases the coolant film thickness, moving the rolling boundary conditions towards hydrodynamic surface fissures, Figure 10.1. To counter this, coolant temperature should also be increased.

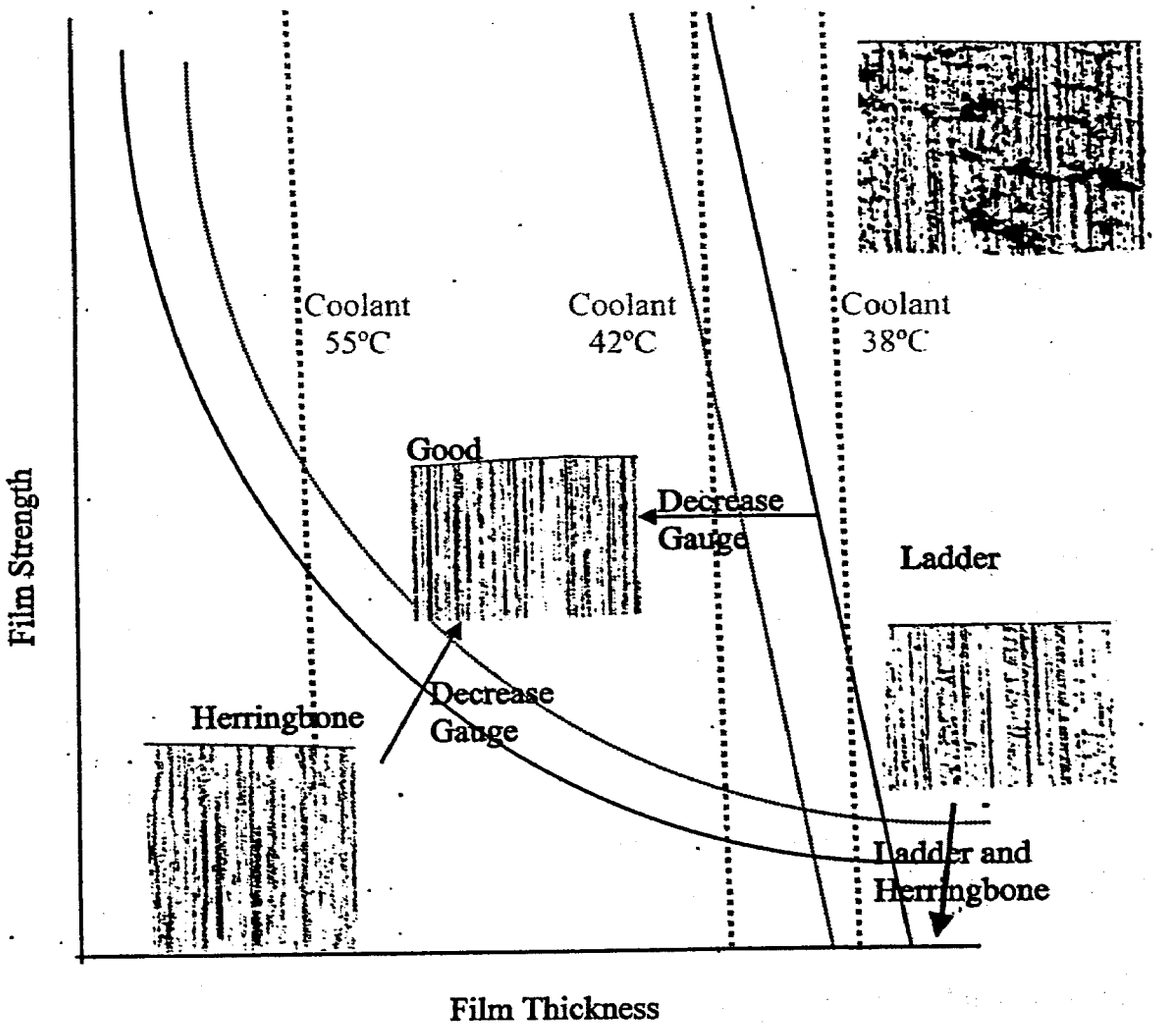

Figure 10.1. **Mansell Curve – Film thickness versus film strength expressed as a function of rolling lubricant temperature. Thinner gauges reduce the "good" operational window, increasing the likelihood of ladder, herringbone or both occurring**

The effect of increased coolant entrainment leading to increased fissure density was seen on the shiny surface of lower roll grind samples B1, 5-7 Ra. This indicates a higher film strength and/or thickness than on the higher roll grind product B2, 14-16 Ra. As roll finish has a significant effect on coolant entrapment, higher roll roughness is expected to increase surface fissures as more coolant is present at the roll-metal interface boundary.

This discrepancy can be explained using the Mansell curve, where increased film thickness is a function of viscosity which in turn is related to coolant temperature. The lower rolling lubricant temperature used on the B1 samples has been shown to increase the size and number of hydrodynamic lubrication pockets which plastically deform the localized areas at the surface. The increased gauge and hardness of the metal reduces the fissure density due to the increase in tension required to fracture the surface. This implies that coolant temperature has a greater effect than roll grind.

10.1.1. Summary

Surface carbonaceous layer and oxide layer thicknesses and compositions were found to be independent of standard operational time and temperatures windows as represented by B1 and B2. The presence of trace elements in the surface oxide while not unexpected indicates variation in the casting and rolling processes can result in alloy contamination with a review of quality controls required. The carbonaceous layer was found to be less than 0.5nm thick, with the subsequent oxide layer composed mainly of hydrocarbons, organic hydroxyls and carboxylic acids. The presence of moisture led to the formation of hydroxides.

The oxide layer penetrated to 4-6nm, following an inverse logarithmic growth pattern. At temperatures below 300°C, there appeared to be a time/temperature correlation which allows shorter annealing times without inducing stickiness. No evaluation was carried out for temperatures greater than 300°C and further work is justified to reduce cycle time. Tears or lesions in the surface indicate the effect of coolant entrainment as discussed using the Mansell Curve.

Inadequate film strength or film thickness allows metal-to-roll contact promoting herringbone. Increasing the film properties using viscosity can result in 'pockets' of coolant resulting in ladder and/or herringbone. A balance between coolant temperature and additives is required to produce an acceptable surface finish.

10.2. Microstructure Evaluation

In the context of this discussion, constituents or primary phase particles occur during casting of the metal. They are also referred to as intermetallics. Dispersoids or secondary particles precipitate during homogenisation prior to hot rolling. Precipitates, which are also termed secondary particles, are particles that form as a result of thermal treatment after cold work. It has been documented that the nature of the particle population first laid down during casting can have a strong influence on downstream behaviour[22]. However, the downstream thermo-mechanical processes have not been well documented, with little or no documentation on the roll of processing on final mechanical properties.

In a synopsis of the casting influence, iron segregates strongly to cell or dendrite arm boundaries during solidification where it takes part in eutectic and peritectic reactions principally with aluminium, silicon and manganese. Although the Al-Fe phase diagram predicts Al_3Fe in aluminium based alloys, metastable phases can form via eutectic reactions during solidification, even under normal production conditions. Typically the particles formed occupy a few volume percent of the wrought microstructure and are generally up to 10μm in size at final gauge. They are insoluble and may undergo phase transformation and modify their morphology during ingot homogenisation, or be fractured and re-distributed during rolling[23].

Large ingots cast by the direct-chill continuous casting process have resulted in growth rates varying from centre to edge. The temperature gradients in the liquid are not well defined and are reduced by convective mixing in the molten ingot sump. As a result, it is difficult to produce eutectic Al-Fe-Mn alloys such as 8006 in blocks greater than 225mm thick while maintaining improved mechanical properties[11].

The thesis provides an alloy, 8150 and method (lower cold rolling temperatures and no interanneal) for producing a prototype thin-film high-strength aluminium alloy using a relatively ductile metal and cast blocks with thickness up to 610mm. The mechanical properties of a dispersion/intermetallic-strengthened alloy are governed by relatively coarse intermetallics promoting nucleation sites for grains, while a fine dispersion of microscopic insoluble particles impede boundary migration[11,14,24].

The microstructure of the alloy 8150 uniquely promotes improved mechanical properties without a significant reduction in ductility. This is achieved without an interanneal, which is of secondary benefit in the production of alloy 8150. The product has been successfully rolled to gauges below 10μm with mechanical properties up to twice that of tradition 1xxx series while maintaining ductility in excess of 30%.

The microstructure of the alloy 8150 depends on both the phases produced during casting and also on the modifications they undergo during preheating. Little work has been done on the effects of downstream processing on microstructure. The phases and microstructure depend on the thermodynamics of the system, but they are also quite sensitive to kinetic factors because of the many possible metastable equilibria.

These factors, in combination with the dislocation structure or grain structure result from high levels of cold-work with no inter-thermal relief, resulting in grains that cover 20-50% of the through thickness of thin foil products which is optimal for tensile strength and elongation. The large intermetallics provide nucleation sites while the smaller precipitates and dispersoids pin grain growth resulting in a fine grain structure.

To help understand the impact of intermetallics on grain structure, it is necessary to discuss the effects of recovery and recrystallation on mechanical properties[25].

10.2.1. Recrystallisation and Recovery

The grain size is a balance between nucleation, growth rates and recovery, increasing with work-hardening and temperature respectively. As most nuclei form at or near grain boundaries, smaller original grain size enhances nucleation. In aluminium, lightly strained fine-grained samples are either heated very slowly or passed slowly through a sharp temperature gradient to induce nucleation[26].

Particles in metallic matrices are usually divided into groups based on size and distribution. Coarse particles are defined as having a diameter greater than 1μm, fine particles are less than 1μm. Dispersion is based on the nearest-neighbour particle centre-to-centre distance[27].

The effects of second phase particles on primary recrystallisation, often termed Particle Stimulated Nucleation (PSN) have been reviewed in recent years by many workers such as Humphreys, Hansen and Bay, and Doherty and Martin[28,29,30]. The key conclusions are as follows:

i) Acceleration of recrystallisation occurs when large particles are present. The deformation zone around the large particle has a higher stored energy and larger misorientations than in the matrix. Higher particle density results in smaller recrystallised grain sizes.

ii) Retardation of recrystallisation occurs in the presence of fine particles where the mean spacing (Δ_3) is of the order of the sub-grain size. Fine dispersions retard sub-grain coarsening inhibiting nucleation.

iii) Nucleation originates in the deformation zone, but not always at the particle/matrix interface. Nucleation occurs by a rapid polygonisation process involving sub-boundary migration.

iv) Particles barely affect the growth of recrystallised grains, suggesting that retardation of recrystallisation is largely a consequence of the inhibition of nucleation. This further implies that particles affect the final grain size, depending on nucleation rates.

Constituents or primary particles play an important role in grain size control with coarse, widely spaced constituents promoting fine grain structures on recrystallisation. Subgrains form at lattice rotations within the metal matrix and have a highly misorientated random alignment making them effective recrystallisation nuclei sites[31].

Dispersoids or second phase particles have the opposite effect to constituents. Grain size is increased due to fine particles acting as pinning points for the low angle subgrain boundaries stabilizing the structure impeding subgrain growth. Similar detrimental effects occur when precipitation and recrystallisation occur concurrently, with the relative kinetics of each determining the influence of precipitation on recrystallisation. If precipitation occurs before recrystallisation, cell walls and subgrain boundaries inhibit the formation of nuclei yielding large recrystallised grains. If the reverse occurs then interference is minimal[31,26].

Solute elements have a strong influence on recrystallisation in aluminium. The effects of additions up to 1% for copper, silicon, iron, manganese, magnesium and zinc have all been studied[32]. Iron and manganese rapidly reduce the amount of recrystallisation; copper and silicon have little effect and zinc and magnesium tend to accelerate recrystallisation. Generally the addition of solute elements increases recrystallisation temperature, but at the same time decreases the tendency for dynamic recovery. This apparently contradictory statement is not fully understood.

Generally, in coarser grained products, strength follows a Hall-Petch type of relationship with grain diameter, however yield strength has been found to vary with the reciprocal of grain size for thinner products, implying stronger grain-size dependence[33]. The strong grain boundary hardening effect is accompanied by a loss of further hardening ability during tensile deformation, which inturn limits ductility at room temperature. This is understood in terms of small mean free path for dislocations being limited by the grain size resulting in less dislocation-dislocation interaction. This puts the lower grain size limit for grain boundary hardening at $1\mu m$[34].

10.2.2. Phase-Particle Discussion

The locally developed alloy 8150 is unique in it approach to producing high-strength high-ductility thin film foils from standard block feed. The removal of an interanneal is also unique with the final product undergoing in excess of 99.9% work without web failure or non-homogenous final properties.

Strengthening of thin-film aluminium foils has in the past relied on large (>1μm) iron-bearing constituent particles (usually $FeAl_3$) to promote recrystallisation by inducing a deformation zone around the large particle. This results in a higher stored energy and larger misorientations in the matrix promoting nucleation. Increasing the iron content increases the particle volume resulting in smaller recrystallised grain sizes as the particles tend to pin dislocations. However, once a critical upper limit for iron is reached, typically between 1-1.7%, the coarse $FeAl_3$ particles tend to crack and produce notches reducing formability and fatigue resistance. Silicon is generally present as a impurity and at low levels remains in solution.

During thermal treatment, increased levels of silicon can result in the precipitation of various meta-stable Al-Fe-Si phases which, if thermo-mechanically controlled, can further enhance the mechanical properties of an end product. The fields of existence of the ternary phases in the solid state are mostly outside their range of primary crystallisation, the completion of peritectic reactions is necessary for equilibrium to be established. For this reason most commercial alloys are not in equilibrium and it is not uncommon to find a meta-stable phase present and even dominate.

Of these, $FeAl_6$ has been found to disperse more finely than $FeAl_3$, reducing the effects of increased iron on formability while maintaining strength. However, to promote $FeAl_6$ formation, freezing rates must be between 1 - 10°C/second compared to the more tradition freezing rates of less than 1°C/second. If the Fe/Si ratio is greater than one, adequate quantities of some transitional metals allow substitution in the constituent phases. In the case of high manganese alloys, this permits the formation of the Al_6(FeMn) phase as the manganese and iron substitute freely with each other.

Combining the effects iron, manganese and to a less extent silicon have enabled alloys to be developed such as 8006 for low-gauge high-strength applications. The alloy's composition is within 10% of the eutectic resulting in a matrix of unaligned intermetallic rods essentially free of intermetallic particles. However, due to the high freezing rates required to promote $Al_6(FeMn)$, casting block thickness should not exceed 225mm or a reduction in mechanical properties will occur.

The iron and manganese levels for alloy 8150 were decreased to the bottom end of the eutectic formation range at 1.1% iron and 0.45% manganese. Note that iron and manganese levels must be tightly controlled to prevent the formation of large intermetallics which are insoluble.

The aluminium-iron equilibrium phase diagram shows that solubility of iron is very low at less than 0.05%. This promotes iron-bearing phases to come out of solution while much of the manganese stays in solution. High iron levels in alloy 8150 also promote dynamic recovery when rolling to high strains which in turn reduce the driving force to recrystallise, adding a further reason to lower the iron levels.

Having produced a cast alloy of the necessary structure, the block is pre-heated to produce an appropriate microstructure, and aid in reducing the slab thickness to the desired gauge. Manganese is the most effective solid solution strengthener, generally remaining in solution to levels up to 0.3%, requiring large misorientations in the matrix to come out of solution in any great volume.

Transition elements especially manganese, also come into play during the heat-treatment of Al-Fe-Si alloys, as in the presence of high Fe/Si ratios they enhance and/or stabilise the formation of the cubic α-Al(Fe,Mn)Si phase, $Al_{12}(FeMn)_3Si$[35]. Silicon levels were increased to around 0.3% to promote $Al_{12}(FeMn)_3Si$ formation during casting, homogenisation and final thermal treatment. Silicon also impedes dynamic recovery and promotes strain hardening though dislocation multiplication.

When an ingot having the proper structure is hot-rolled or extruded, the brittle intermetallic Al(Fe,Mn) and Al(Fe,Mn)Si phases are subjected to local mechanical loading due to deformation of the surrounding aluminium matrix, causing them to fracture and fragment evenly along their length, creating uniform but somewhat elongated particles aligned to the rolling direction[36]. This was observed in the 2.7mm samples for the $Al_{12}(FeMn)_3Si$ constituents in alloy 8150. The $Al_6(Fe,Mn)$ phase appeared to have some limited plastic deformation during hot working or rolling supporting other observations[37]. It is expected that other Fe-containing phases with higher transition temperatures, such as Al_3Fe and $Al_{12}(Fe,Mn_3)Si$ would not plastically deform.

The major part of the reduction of the initial ingot by hot-rolling re-arranges the particles evenly throughout the ductile metal matrix during the deformation of the ingot. The subsequent cold-rolling operation imparts at least 90% reduction of the hot-rolled slab to generate the desired dislocation cell structure in the aluminium matrix without any further controlled thermal processing.

During the "cold-work" stage of production, recovery must be avoided to prevent irregular grain growth in the final product as this has a negative effect on final tensile properties. Recovery reduces the intensity of the deformation zone adjacent to the particles reducing their effectiveness as nucleation sizes for recrystallisation.

This effect was highlighted by drop in Erickson values for 120μm 8150 product. The alloy was subjected to cold-work at temperatures above 150°C. The metal starts to recover which in turn affects the final anneal recrystallisation process resulting in a 10-20% drop in Erickson properties. This highlights the criticality in removing the interanneal from the process path. This is a necessary process in the production of all other thin-film foil products in Australia due to the inability of other foil alloys to achieve consistent properties at final gauge due to unhindered grain growth.

The microstructures for alloy 8150 at 0.22mm gauge showed no significant dispersoid formation from hot rolling to 2.7mm. The particles are a combination of $Al_6(Fe,Mn)$ constituents formed during casting and $Al_{12}(FeMn)_3Si$ dispersoids formed during homogenisation and to a lesser degree casting. The aspect ratio of the particles is generally less than 6, with most between 3-4.

When rolled to thin foil gauges of less than 20μm, the metal has been reduced by 99.9+% without thermal relief, a unique process for this strength/ductility combination. In the production of rolled products of good formability for such purposes as container and household foil, it is permissible to sacrifice some of the potential strength of the product in order to ensure the desired formability characteristics. As a result, the final anneal temperature is critical to the development of final properties, with recovery and/or recrystallisation initiating at relatively low temperatures due to the high cold work coupled with the heat generated during sheet rolling.

The optimisation of tensile yield and elongation properties in thin-film foil alloys employs a final thermal treatment to produce a fine grain structure, thereby utilising grain boundary hardening. Constituents are required to act as a catalyst for nucleation, with dispersoids and precipitates pinning or hindering grain boundary migration. This combines with the latent effect of solid solution hardening and high stored energy, with large misorientations in the matrix, resulting in a very fine grain or sub-grain size. For a more detailed explanation of recrystallisation and recovery in aluminium and its alloys, please refer to Appendix 12.

The microstructure of the 12μm 8150 sample prior to annealing shows a highly stressed matrix with a sub-grain structure less than 1μm. Subgrains form at lattice rotations within the metal matrix and have a highly misorientated random alignment making them effective recrystallisation nuclei sites[31]. The constituent and dispersoid phases resulting from casting are of equal size and volume to that seen during upstream processing, with some precipitation of $Al_{12}(FeMn)_3Si$ evident.

In 12μm foil, the constituents are generally between 0.5 to 5μm in length, evenly dispersed and aligned to the rolling direction with an aspect ratio greater than 2. The precipitates resulting from the final thermal treatment appear spherical, are sparsely distributed through the matrix in no specific location and generally less than 0.1μm in size.

The high matrix stresses resulting from the extremely high cold work reductions and the solid solution effects of manganese and silicon effectively shorten the precipitation spacing. This makes lower volumes of precipitates more effective in pinning grain boundary movement once recrystallisation occurs, with particle strengthening proportional to spacing:

$$\boxed{\tau \alpha Gb/l} \qquad (10.1)$$

where τ is the shear stress, G the matrix shear modulus, b the Burgers vector, and l the interparticle spacing.

Fine particles or precipitates will tend to retard sub-grain coarsening inhibiting nucleation if the spacing is in the order of subgrain size. Hence a balance is required between pinning the grain boundaries, resulting barriers to dislocation motion, and development of higher dislocation densities adjacent to the particles. The alloy 8150 coupled with the processing route achieve tis balance

The dispersoids in alloy 8150 were found to be $Al_{12}(FeMn)_3Si$ and $Al_{12}(MnFe)_3Si$ and complement the constituents for form fine grains on annealing. A TEM of a 8150 type alloy (1.35%Fe, 0.6%Mn) is illustrated in Figure 10.2. A well-defined substructure exists with particles pinning many of the boundaries[33].

The volume concentration of constituent particles is critical as large particles with small spacing inhibit recrystallisation by particle pinning effects (Zener drag) promoting large grain sizes. Previous work identified that the void fraction percentage of particles should fall in a range of between 5-20%[14]. The data indicated that for alloy 8150, the void fraction was effective at between 5-10% with no results tested with concentrations outside this range. This value increases during the final stages of rolling, and after final thermal treatment.

Figure 10.2. **TEM of an 8150 type alloy (1.35%Fe, 0.6%Mn) cold rolled to 130μm and partially annealed. A well defined substructure exists with particles pinning many of the boundaries**

The microstructure of the 12μm AA8150 thin film product after annealing showed well defined grain boundaries indicating that substantial recovery/recrystallisation had occurred. The grain structure generally appeared uniform, with two to four grains through the foil thickness. The grains were irregular in shape, indicating that boundary migration was being impeded. This agrees with the theory of high matrix stress levels in conjunction with large constituent promoted nucleation while the fine dispersoids pin the grain growth.

The $Al_6(Fe,Mn)$ constituents and $Al_{12}(FeMn)_3Si$ dispersoids in alloy 8150 were present in similar quantities greater than $0.400\mu m^2$, however the volume of particles below this figure effectively doubled. The high flow stresses from work hardening combined with the thermal treatment, allowed the non-equilibrium manganese to precipitate out of solution replacing iron as the dominant transition metal resulting in a $Al_{12}(MnFe)_3Si$ phase. These particles were effective in restricting grain growth by pinning the grain boundaries and hindering dislocation motion.

Unlike intermetallics, dispersoids and precipitates reduce the energy of the high angle boundaries as the second phase particles 'pin' the boundary causing a new boundary to be formed as it curves around the particle. This is achieved by increasing the average misorientations between neighbouring subgrains through particle hindering and eventually pinning, enhancing the nucleation of recrystallisation sites.

10.2.3. Synopsis

The unique strengthening mechanisms for alloy 8150 enables the casting of a standard block with a thickness of up to 610mm, while providing a microstructure that promotes high tensile properties at thin-foil gauges, was described. At thin foil gauges, subgrains form at lattice rotations within the metal matrix as a result of the high cold reductions with no intermediate thermal treatments. This results in highly misorientated random alignments in the deformation zone that surround large constituent particles making them effective recrystallisation nuclei sites. Intermediate thermal treatments including recovery have a detrimental effect on this process.

Dispersoids and precipitates reduce the energy of the high angle boundaries as dispersoids 'pin' the boundary causing a new boundary to be formed as it curves around the particle. This is achieved by increasing the average misorientations between neighbouring subgrains through particle hindering and eventually pinning, enhancing the nucleation of recrystallisation sites. These are effective barriers to dislocation motion and higher dislocation densities develop adjacent to the particles. This results in a thin foil product (<20μm) that exhibits twice the tensile properties (via burst strength) of traditional 1xxx series foil alloys.

The constituent phases $(FeMn)Al_6$ and some $Al_{12}(FeMn)_3Si$ form during solidification with the dispersoid $Al_{12}(FeMn)_3Si$ developing during homogenisation. The constituents were observed to fracture during processing due to high matrix stresses being the more dominant force as opposed to crushing. The dispersoids/precipitates that occurred during the final thermo-mechanical stages were found to be $Al_{12}(FeMn)_3Si$ and $Al_{12}(MnFe)_3Si$.

The lower solubility of iron results in a dominant transition metal in the dispersoid until the final thermal process is reached. The high stress levels combined with the thermal treatments allow manganese to substitute and precipitate out of solution.

The wrought aluminium alloy 8150 contains iron, manganese and silicon at greater than 20% from the eutectic composition. The alloying constituents comprise iron to a maximum of 1.3%, manganese at a maximum of 0.7% and silicon at a maximum of 0.3%. The principal alloying constituents present in a total amount supply about 4.0-10% by vol.% of dispersed intermetallic particles with a size range of 0.1 to 10 microns, promoting high strength and formability.

The preferred composition for the Al-Fe-Mn 8150 alloy has an iron and manganese content laying within the coordinates 1.3% Fe, 0.2% Mn; 1.3% Fe, 0.4% Mn; 0.9% Fe, 0.2% Mn; 0.9% Fe, 0.7% Mn. The alloy also including silicon up to 0.30% max; others up to 0.15% max. total and up to 0.05% each, Al balance. It is, however, most preferred that the alloy should contain Fe and Mn within the coordinates 1.2% Fe, 0.3% Mn; 1.0% Fe, 0.3% Mn; 1.1% Fe, 0.6% Mn; 1.0% Fe, 0.3% Mn, the alloy also containing Si up to 0.3%, others preferably below 0.15% total (0.05% max. each), Al balance.

To further illustrate the compositional boundaries, reference is made to Figure 10.3, which shows in simplified form the liquidus boundaries between Al-Al_3Fe and Al-Al_6Mn for the alloy developed. The area indicated by the outer dotted line defines a general composition range which may conveniently be employed for the production of cast alloys having intermetallic phases of the required diameter for use in the production of high-strength high-formability wrought aluminium alloy products.

The area indicated by the inner solid line defines a preferred range of compositions with which cast alloys having the desired phases may be more easily produced without growth of undesirable excessively coarse intermetallic particles. Figure 10.4 provides a three dimensional interpretation of the alloy 8150 compositional boundaries taking into account silicon.

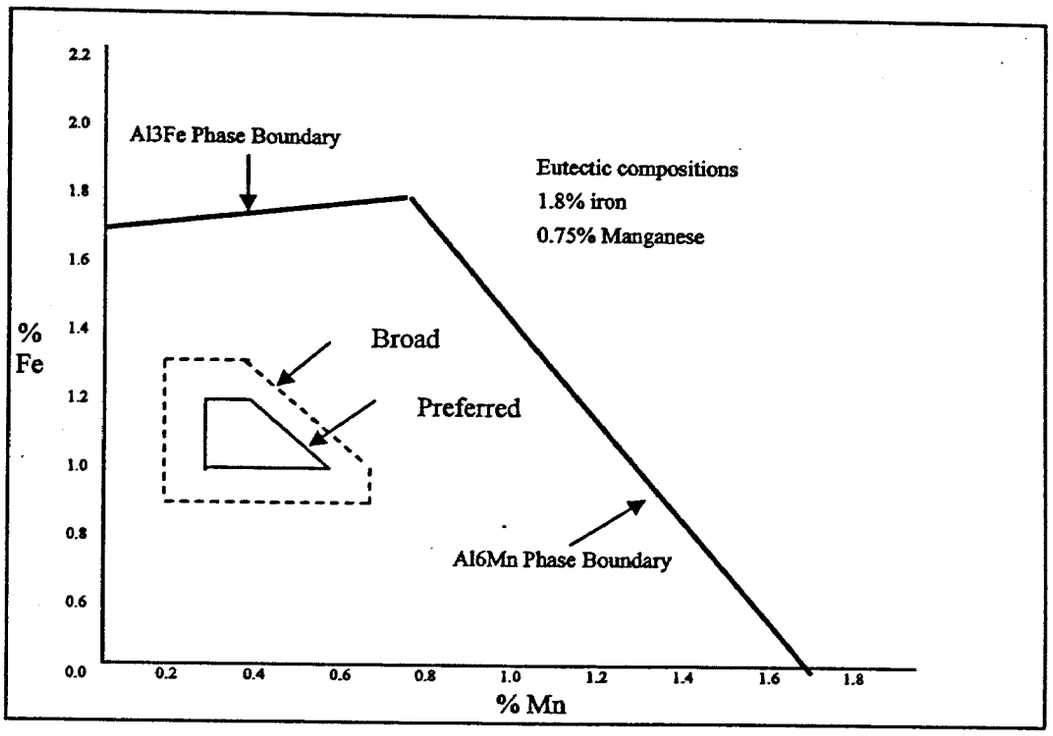

Figure 10.3. **Al-Fe-Mn compositional limits using a two dimensional chart to based on the 8150 alloy compositional boundaries.**

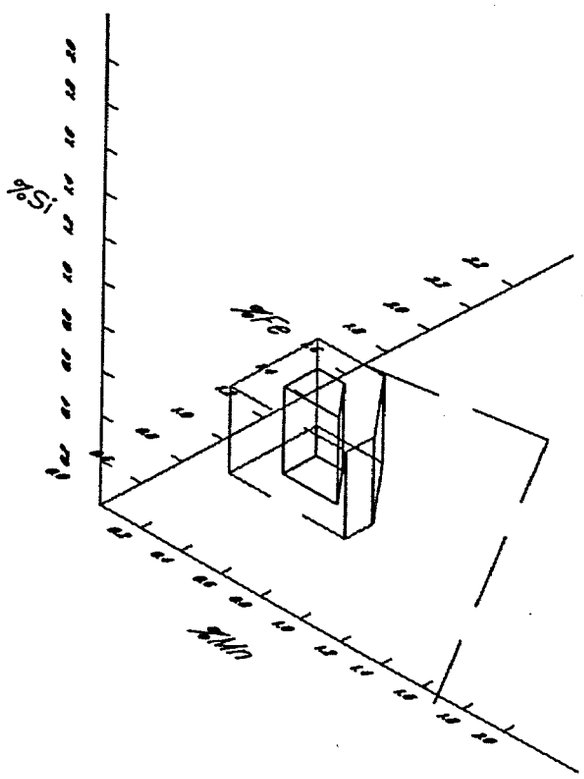

Figure 10.4. **Al-Fe-Mn-Si compositional limits using a three dimensional graph based on the 8150 alloy composition boundaries**

Work has been performed to improve strength by introducing small proportions of copper and/or magnesium which remain in solid solution in the aluminium phase[14]. They have known strength-providing properties when subjected to a final thermal treatment at a temperature in the range of 200-400°C after cold-working. Their applications in the thin-foil market are limited as copper promotes corrosion while magnesium can result in excessive MgO formation at the surface (refer to Chapter 2.3.2.6), both of which are unacceptable to the end user.

10.3. Processing Variables

10.3.1. Annealing Temperature

The 8150 alloy and the processing schedule designed for these trials were targeting an average burst strength of ~110kPa with a minimum strength of 100kPa. As discussed earlier, results obtained for approximately half of the material met pre-determined expectations. Results falling in the lower half of the distribution did not.

Reliability of the Yennora burst strength tester was checked using a sample of known burst strength and found to be within specification. The reliability of the Yennora burst strength tester during these trials is not under question.

It is understood that a low burst strength result can be due to either under or over annealing of the metal. In the case of under annealing, the metal will be only partially recrystallised; through-coil burst strength will be inconsistent and areas in the coil will test low (i.e. will have very little ductility). For an over annealed coil, full recrystallisation plus undesirable further grain growth will occur; a large grain size will result, and the material will test consistently low.

Samples from the low strength distribution were laboratory annealed at temperatures of 300°C and 350°C, and then retested for burst strength. Neither sample group showed a difference in resultant burst strength indicating a full annealed microstructure. This confirmed that the material sent for trial was fully annealed and, since there was no movement in burst strength for the annealed samples, possibly over annealed. Both high and low strength samples were prepared for microstructural comparison, Figure 10.5[38].

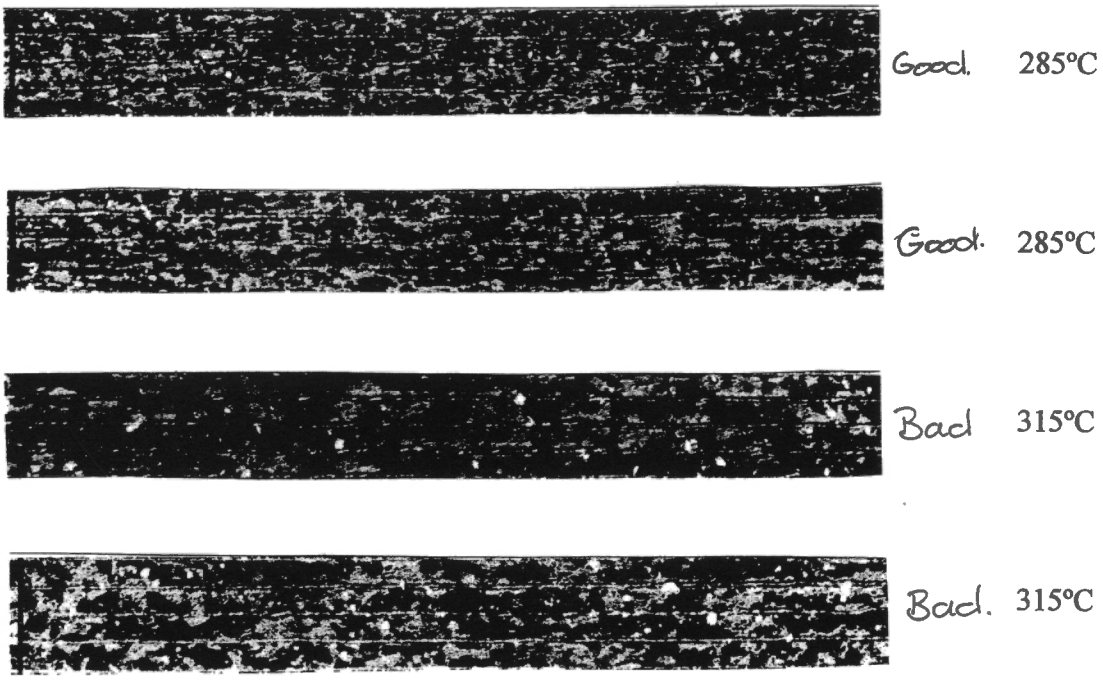

Figure 10.5 **Microstructural comparison of alloy 8150 annealed at different temperatures. (200x)**

From Figure 10.5, the grain size of the low burst strength material is clearly much larger than for the high burst strength metal, confirming over annealing of the low testing product.

There are a number of process stages that can contribute to a larger grain size in the final product; most notably, these include:

(i) Too high a temperature soak

(ii) Excessively long soak time in the final anneal

(iii) An increase in the %cold work imparted on the material prior to the final anneal

(iv) Incorrect alloy composition

(v) Recrystallisation during processing (eg. exit warm mill)

(vi) Unsuitable preheat of the ingot leading to a non homogeneous distribution of secondary precipitates.

The contribution of each of these has been considered:

(i) Soak temperature of the final anneal

The principle focus of the trial was to qualify the effect of final annealing conditions on 8150 microstructure. Small grain size is required to maximise mechanical properties while maintaining ductility, and is achieved by heavy cold rolling deformation of a material after interannealing.

If the number of small particles becomes too high, a majority of grain boundary movement is hindered, leading to discontinuous growth of a few grains and a coarse final grain size. Large numbers of small particles are formed by the precipitation of Fe or Mn in 8xxx series alloys from solid solution during annealing or final annealing, promoting discontinuous grain growth at higher annealing temperatures.

In this instance, even a small change (20°C) has a dramatic effect on thin gauge foils with high iron-manganese contents. However in saying this, we cannot discount other factors that may influence excessive grain growth.

(ii) Soak time of the final anneal

The annealing cycle used for the 8150 alloy incorporates a 2 hour soak for both 285°C and 305°C. This soaking period is not considered excessive, however longer periods of time must be qualitatively tested.

(iii) % cold work imparted on the material prior to final anneal

As the rolling schedule was constant for both products, this is not expected to be a factor, however refer to point (v).

(iv) Incorrect alloy composition

Samples are taken three times during a standard cast, at the start, middle and end. The results, given in Table 10.1, show no change in composition during the cast. Compositional analysis indicates the presence of titanium. TiB grain refinement was conducted for the trial casts, and there were no abnormalities found in the casting data records.

cast #	cast date	Cu	Fe	Mg	Mn	Si	Fe/Si ratio	Cr	Ti
454,073	27/07/01	0.001	1.11	0.001	0.42	0.147	7.54	0.002	0.005
454,073	27/07/01	0.001	1.11	0.001	0.42	0.147	7.54	0.002	0.005
454,073	27/07/01	0.001	1.11	0.001	0.42	0.147	7.54	0.002	0.005

Table 10.1. 8150 Alloy Composition Used on Trial Coils

(v) Recrystallisation/Recovery during processing

No interanneals were given to the trial material during the cold rolling process. Cold rolling was hence performed without any metal recrystallisation. Final pass warm mill temperatures have also been checked. All warm mill exit temperatures were below 290°C which historically is below the exit temperature required to self annealed. Any degree of recrystallisation during warm rolling can hence be discounted.

There is a concern that excessive temperature during cold rolling can cause the metal to recover, increasing the amount of cold work on subsequent passes which may affect final properties. This is discussed in the next section.

(vi) Preheat practice

The trial 8150 ingot was processed with a 4 hour at 510°C preheat to ensure adequate homogenisation. It is during homogenisation that secondary particles precipitate. The size and distribution of these secondary precipitates influence the rate of recrystallisation during the final anneal, and hence are critical to the grain size observed in the finished product.

Conclusion

From the results, final annealing temperatures had a major effect on final end property results. Changes in final annealing temperature, even as little as 20°C, resulted in a 21% drop in final properties at the higher temperature. Here the driving force for recrystallisation and grain growth is greater than the pinning force provided by the particles, due in part to both the high level of residual stress and increased number of small particles.

Increased annealing temperatures will increase precipitation and hinder a majority of grain boundary movement, but will promote random discontinuous growth of a few grains and a resultant coarse final grain size will occur.

The results also highlighted the importance of recovery/recrystallisation during processing and hence an investigation into processing limits during cold rolling was initiated.

10.3.2. Cold Rolling Recovery – Exit Temperature

The microstructures for the lower rolling temperature product show grain sizes 50-75% smaller than for high temperature product. The lower Erickson values were found to correlate with entry temperatures in excess of 60°C, with rolling conditions set at constant values for load, speed and tension. In these instances, exit temperatures often exceed 160°C which can result in partial recovery.

As the deformation temperature increases, the dislocation recovery processes of cross-slip and climb is enhanced, reducing the effect of particle stimulated nucleation in subsequent thermal processes. Partial recovery in the matrix results in increase work hardening on subsequent passes, promoting discontinuous grain growth as the iron-manganese rich dispersions have a similar effect to excessive highly soak temperatures. The entry cold rolling temperatures of the coil is to be kept below 60°C in order to keep the exit temperature below 160 °C i.e. no back-to-back rolling.

This also confirms that thermal treatments during processing and prior to a final anneal, are detrimental to final properties due to the negative effect on grain size. This criterion includes partial recovery to full recrystallisation.

CHAPTER 11 SUMMATION

The Aluminium Rolling Industry has had limited published technical information on thin-foil processing principles. The fundamentals of thin-film rolling unlike open-gap rolling have never been collated and discussed. Experimental work for this thesis was designed in three stages;

1. To discuss the fundamental principles that are necessary to understand thin-foil processing. This included but was not limited to alloy development, rolling models, surface lubrication and annealing to an extent never before published. These Chapters are integrated into the ALCOA Metallurgical Database for Foil Rolling.

2. To establish benchmarks and optimise several processing variables, and investigate other areas of process improvement as-raised.

3. To investigate the surface characteristics and microstructural evolution of Al-Fe-Mn-Si alloy 8150 during cold and foil rolling and annealing. The final alloy composition and registration by completed by the author.

The first five Chapters were a literature survey that discussed several aspects of thin-foil rolling. To achieve objectives two and three, the fundamentals needed to be understood. Examining each Chapter in more detail:

- Chapter One analysed the current domestic and world supply revealing that Australia is in a vulnerable market, with AARP (ALCOA Australia Rolled Products) being the only domestic manufacturer of foil products.

- Chapter Two discussed aluminium and aluminium alloy development for thin foil alloys, concentrating on the 1XXX and 8XXX series. With the market requiring thinner gauges at higher strengths, there has been a move away form the traditional 1xxx series alloys to more exotic alloys that utilise iron, silicon and manganese. A discussion on strengthening mechanisms was also incorporated.

- Chapter Three examined current thin-film rolling theory and particle break-up modelling.

- Chapter Four examined rolling lubricants and their effects on annealing.

- Chapter Five discussed web handling and creasing generation during rolling and slitting.

The investigation moved on to current rolling practices with the objective of reducing web failures and increasing productivity. Productivity improvements were based on the interpretation of rolling models to focus efforts on variables that would best achieve the desired production improvements. Examining each Chapter:

- Chapter Six examined the causes of strip breaks over a 3 year period at Yennora foil plant, as well as drawing from experiences of other Alcoa Foil plants. The defects were categorised according to perceived defect cause. A 75% reduction in strip breaks was achieved over this period. A review of Deep Bed Filtration (DBF) and subsequent trials and results were also discussed.

  The detailed examination of boundary lubrication, as highlighted in Chapter four, resulted in the development of the Mansell curve, an adaptation of the Stribeck curve, to explain the relationship between surface marks (herringbone) and lateral tearing (ladder defect) that can occur during final pass rolling.

- Chapter Seven discussed productivity improvements resulting from increased rolling speeds for all thin-foil passes. The two obstacles that hindered rolling at faster speeds were found to be web breaks during the rolling process, and optimal rolling parameters (unwind tension, rewind tension, load, and coolant temperature as discussed in Chapter three). By concentrating on these specific variable, rolling speeds and hence productivity were increased by up to 20%.

  A discussion into the influence of chroming work rolls in a foil mill on rolling speed and defect generation was included. Chrome rolls being unique to Yennora, providing the benefit of long runs without frequent roll changes. The chrome surface was more resistant to wear caused by the rolling process, maintaining its Ra and hence maintaining rolling speeds.

The final section focused on a fourth generation alloy 8150. For thin foil rolling it incorporated iron-manganese eutectic constituent phases with iron-manganese-silicon precipitation to promote high strength coupled with formability. The surface characteristics were examined and suitability for the industry and potential annealing problems evaluated. The strengthening mechanism was discussed with the alloy currently in the patent process for ALCOA.

- Chapter Eight documents the experimental procedure for further alloy studies. It details the process for collecting samples and evaluating the samples using image analysis, surface analysis techniques and microscopy.

- Chapter Nine contains the results of both the surface study analysis and microstructural development during processing and annealing from 2.7mm to 12 micron annealed product.

- Chapter Ten discussed the effect of alloy, surface roughness, time and temperature on oxide thickness and composition and found that the current generation of foil alloy compositions have little effect on surface oxides. The importance of this is that surface oxides are a proposed mechanism for surface stickiness which may be a consequence of annealing. The effect of current manufacturing operational windows, namely roll grind and annealing temperature and time is discussed.

Studies reviewed for this thesis indicate that surface oxides for commercial 1xxx alloys are in the range of 2.8 to 5nm thick, requiring the use of XPS and SIMS analysis techniques. The 8xxx series alloy was found to be compatible with current 1xxx thermal treatment procedure.

The microstructural evolution of Alloy 8150 during cold and foil rolling is discussed. The alloy was developed and registered in response to the increase requirement of higher strength at lower gauges. The alloy utilises a unique combination of high cold reductions, solid solution strengthening, constituent and dispersion strengthening to produce a fine grained structure with high strength and formability characteristics.

In addition to discussing the evolution of microstructure of alloy 8150 from 2.7mm down to 0.012mm (cold and foil rolling), the effects of high pass temperatures and final annealing temperature on mechanical properties are examined. It was found that temperature is critical in providing the final mechanical properties during the manufacturing process.

- Chapter Eleven summarises the findings from the thesis.
- The Appendices contain additional information on the sampling and testing procedure and alloy information. Recovery and recrystallisation and examined in further detail.

In the development of alloy 8150, the process is critical in determining the microstructure that promotes high strength with good ductility. What is claimed is:

1. A method of producing primary/dispersion-strengthened aluminium alloy products to achieve a 95+% reduction of cast aluminium alloy without an intermediate thermal.
2. An alloy composition that allows for the casting of blocks between 500 to 650mm thick while providing a microstructure that promotes high mechanical properties including elongation.
3. An alloy composition according to point 2 that shall contain not more than 1.3% iron, 0.7% manganese and 0.3% silicon.
4. A method according to point 1, in which the cast aluminium alloy mass is subjected to an initial reduction by hot working, followed by cold working to further reduce the hot worked depth by at least a factor 10.
5. A method according to point 1 and 4 in which the hot worked depth is reduced by at least a further 90% by cold working. This incorporates reductions of between 15-30mm per pass.
6. A process according to points 1, 4-5 that allows final product down to 10μm to be achieved without intermediate annealing, including that induced during cold rolling.

The following microstructural metallurgical features were found to determine the improved mechanical properties:

7. A final microstructure, in accordance with point 2 and 3, which contains 4 - 10% by volume of unaligned intermetallic dispersoids of an average diameter in the range of 0.5-10 microns with some coarse primary intermetallic particles. This is inclusive of 0 - 5% precipitates from cold work and subsequent thermal treatment.

8. The principle intermetallics in the final product are Al-Fe, Al-Fe-Si, Al-Fe-Mn and Al-Fe-Mn-Si phases.

9. The intermetallic phases, due to their small initial size show some evidence of fracturing during the hot rolling stage of the product at 2.7mm.

10. The $Al_3(Fe,Mn)$ phase is expected to fracture during hot-rolling more readily than $Al_6(Fe,Mn)$ or $Al_{12}(FeMn)_3Si$ phases.

11. A final microstructure, in accordance with points 2-3 and 7 that consists of intermetallic dispersoids being composed of an intermetallic compound of Al with two or more of iron, manganese and silicon.

12. The final particle size for 90% by area of particles is between $0.5\mu m^2$ and $6\mu m^2$.

13. A final microstructure that incorporates precipitates less than $0.400\mu m^2$. These impede grain growth.

14. The precipitates are composed of an intermetallic compound of Al with two or more of iron, manganese and silicon, the most likely being $Al_{12}(FeMn)_3Si$ and $Al_{12}(MnFe)_3Si$ phases.

15. The precipitates can occur prior or post final annealing.

16. A final microstructure, in accordance with points 2-3, 7-11, in which the intermetallics are aligned to the direction of rolling, and may be elongated during the hot working process.

17. A final microstructure, in accordance with points 2-3, 7-11 in which the intermetallics may fracture during hot work/cold work due to the matrix forces being imposed on to the intermetallic.

18. A final microstructure, in accordance with points 2-3, 7-11 in which the intermetallics have an aspect ratio of between 1 and 6.

19. A final microstructure that employs solid solution strengthening, dispersion hardening, strain hardening to induce a fine grain structure in thin foils.

20. A method according to points 1, 4-6 in which the cold worked alloy is subjected to a final heat treatment at temperatures in the range of 200-350°C.

21. A final microstructure, in accordance with points 12-16, that is influenced greatly by relatively small changes in temperature. Time has a secondary effect

22. A final microstructure, in accordance with point 5, in which the cold work temperature may induce partial recovery.

23. The final product which when processed to induce the required microstructure, in accordance with points 1-18, results in an average burst strength 100% greater than traditional 1xxx series alloys thin-film foils.

24. The effect of dispersoids and precipitates is only for thin-film foils (less than 20μm). At more typical foil gauges (20-200μm), these intermetallics are less effective in promoting finer grain sizes.

In summary, a detailed literature review of thin-foil rolling was completed. Existing rolling practises were evaluated and optimised resulting in a 75% drop in break-rate coupled with a 20% improvement in productivity. A new Al-Fe-Mn-Si alloy, AA8150, was developed utilising a unique combination of strengthening mechanisms to produce a high-strength high-formability thin-foil product with superior annealing characteristic's to existing 1xxx alloys.

APPENDICES

APPENDIX 1 PROPERTIES OF PURITY ALUMNIUM.

Property	Value	
Colour – Reflected Light	Silvery While	
Reflection of incident visible radiation	80 – 85%	
Emissivity (10 to 38°C)		
Wavelength – 10.0 (μm)	0.02 – 0.04	
5.0 (μm)	0.03 – 0.08	
1.0 (μm)	0.08 – 0.27	
Crystallographic Structure	Face-centred cube	
Lattice constant α at 25°C	0.40414 nm	
Minimum inter-atomic distance	0.28577 nm	
Slip plane – primary twinning plane	(1, 1, 1)	
Density at 20°C	2.699 g/cm^3	
Solid at 600°C	2.55 g/cm^3	
Liquid at just above melting point 600°C	2.38 g/cm^3	
Volume change near solidification	6.7%	
Casting contraction (linear)	1.7 – 1.8%	
Heat of Combustion	200 Kcal per g-atom	
Melting Point	660.2°C	
Boiling Point	2057°C / 2480°C	
Vapour pressure at 1200°C	1 x 10^{-3} mm mercury	
Property (cont.)	Value	
Specific heat	J (kgK)	Cal/g/°C
at 20°C	930	0.222
at 100°C	935	0.223
at 500°C	1110	0.266

Mean specific heat 0 to 658°C solid	1045	0.25
	J/g	Cal/g
Heat of Fusion	387	92.4
Heat of Vapourisation	8200 – 8370	7950 – 2000
Linear coefficient of thermal expansion x 10^6	23.0	(20° - 100°C)
Linear coefficient of thermal expansion x 10^6	28.1	(20° - 600°C)
Linear coefficient of thermal expansion x 10^6	31.1	(at 500°C)
Viscosity at melting point	130 m Nsm^{-2}	
Surface tension at melting point	914 m Nm^{-1}	
Thermal Conductivity	W/mK	cal/s/cm^2/cm/°C
at 0°C	209	0.50
at 100°C	213	0.51
at 200°C	217	0.52
Electrical conductivity at 20°C (International Annealed Copper Standard (IACS) = 100)	65.5%	
Electrical resistivity at 20°C	2.69 μΩcm	2.63 ohm cm
Temperature coefficient of electrical resistance at 20°C	0.0041	
Thermo-electric force (relative to Pt with cold junction at 0°C)	+0.416 at 100°C	
Magnetic susceptibility at 18°C x 10^6	0.63	
Standard potential at 25°C	-1.69V	
Electrochemical equivalent Al^{+++}	0.3354 g/A/h	
Velocity of sound in Aluminium	5100 m/s	

APPENDIX 2 AFFECTS OF ADDITIONS TO 1XXX SERIES ALLOYS.

Arsenic:	Must be controlled to very low limits were aluminium is used as foil for food packaging.
Beryllium:	Not to be used in aluminium alloys that may contact food or beverages as may result in beryllium poisoning.
Boron:	Used as a grain refiner either alone or in combination with Titanium. Not recommended in light gauge alloys due to agglomerated TiB_2 particles that may result in strip breaks.
Calcium:	Very small amounts (10ppm) increase the tendency of molten aluminium alloys to pick-up hydrogen.
Carbon:	Currently being assessed as a possible replacement Boron in grain refining. Carbides decompose in the presence of water that may lead to surface pitting.
Cerium	In alloys containing high iron (>0.7%), is reported to transform acicular $FeAl_3$ into a noncircular compound.
Chromium:	Can be used as a grain refiner. May leave a yellow tinge to the metal.
Copper:	Small amounts of copper in solid solution are particularly effective in increasing the H1X and O-temper yield strengths of lxxx alloys, however can promote corrosion.
Hydrogen:	Due to the higher solubility in the liquid state than solid, can result in porosity during solidification.
Iron:	The most common impurity found in aluminium, appearing as an intermetallic second phase in combination with aluminium and often with other alloys. Iron reduces grain size in wrought alloys, and when combined with manganese near the eutectic content, producing useful combination of strength and ductility.
Lithium:	Levels greater than 5ppm can promote the discolouration (blue corrosion) of aluminium foil under humid conditions.
Magnesium:	Levels greater than 0.05% can result in dark patches, often termed "Magnesium bloom" (Mg oxide), on the surface of annealed light gauge foil.
Manganese:	A common impurity in primary aluminium, it increases strength either in solid solution or as a finely precipitated intermetallic phase with no adverse effect on corrosion. Manganese remains in solution when chill cast, increasing the recrystallisation temperature and promotes a fibrous structure in hot-rolling. As a dispersed precipitate, it is effective in slowing recovery and preventing grain growth. Manganese is also used to correct the shape of acicular or of platelike iron constituents and to decrease their embrittling effect

Nickel:	Promotes pitting corrosion in dilute alloys such as 1100.
Silicon:	The second highest impurity after iron at 0.01 to 0.15%.
Tin:	As little as 0.01% tin in commercial-grade aluminium will cause surface darkening on annealing and increase the susceptibility to corrosion.
Titanium:	Primarily used as a grain refiner in aluminium alloy castings and ingots. See boron.
Vanadium:	Present in levels between 10 to 200 ppm, lowers conductivity, raises the recrystallisation temperature and can have a grain refining effect on solidification.

APPENDIX 3 1145 SPECIFICATIONS.

Specifications:

AMS, 4011
ASTM, B 373
Government, QQ-A-1876

Chemical Composition Limits:

Al min.	99.45
Si + Fe max	*0.55*
Cu max	*0.05*
Mn max.	0.05
Mg max.	0.05
Zn max.	0.05
V max.	*0.05*
Ti max.	0.03
Max. other each	0.03

Applications

Typical uses: Foil for packing, insulating and heat exchanges

Fabrication Characteristics

Annealing temperature: 345 °C (650°F)

Mass Characteristics

Density: 2.705 g/cm3 (0.0977 lb/in3) at 20°C (68°F)

Thermal Properties

Liquidus Temperature: 657°C (1215°F)

Solidus Temperature: 646°C (1195°F)

Mechanical Properties

	Tensile Strength		Yield Strength		Elongation
Temper	MPa	Ksi	MPa	Ksi	%
Typical properties					
O	75	11	34	5	40
H18	145	21	117	17	5
Tensile strength limits (a)					
O	95 max	14 max			
H19	140 min	20 min			
(a) Unmounted foil 0.02 to 0.15mm (0.007 to 0.059 in.) thick					

Corrosion and fabrication Characteristics

Alloy / Temper	Applications	Resistance to Corrosion		Weldability		
		General	SCC	Gas	Arc	Spot / seam
1145 O	Foil, Finstock	A	A	A	A	B
1145 H12		A	A	A	A	A
1145 H14		A	A	A	A	A
1145 H16		A	A	A	A	A
1145 H18		A	A	A	A	A

Alloy / Temper	Workability	Machinability	Brazeability	Solderability
1145 O	A	E	A	A
1145 H12	A	E	A	A
1145 H14	A	D	A	A
1145 H16	B	D	A	A
1145 H18	B	D	A	A

Coefficient of Thermal Expansion

Linear:

Temperature Range		Average Coefficient	
°C	°F	μm/m • K	μin./in. • °F
-50 to 20	-58 to 68	21.8	12.1
20 to 100	68 to 212	23.6	13.1
20 to 200	68 to 392	24.5	13.6
20 to 300	68 to 572	25.5	14.1

Volumetric:	68 x 10^{-6} m^3/m^3 • K (3.8 x 10^{-5} $in.^3/in.^3$ • °F)
Specific Heat:	904 J/kg • K (0.216 Btu/lb • °F) at 20°C (68°F)
Thermal Conductivity: At 20°C (68°F):	O temper, 230 W/m • K (133 Btu/ft • h • °F) H18 temper, 227 W/m • K (131 Btu/ft • h • °F)

Electrical Properties

Electrical Conductivity: Volumetric at 20°C (68°F):	O temper: 61% IACS	H18 temper: 60% IACS
Electrical Resistivity: at 20°C (68°F):	O temper: 28.3 nΩ•m	H18 temper: 28.7nΩ ft•m
Temperature coefficient: at 20°C (68°F):	O/H18 tempers: 0.1 nΩ•m per K	

Optical Properties

Reflectance:	95 to 97% for λ = 0.3 to 10 μm
Emittance:	3 to 5% for λ = 9.3μm at 20°C (68°F)

APPENDIX 4 LUBRICANTION VISCOSITY FACTORS

1. Material

Metal Brightness after pack pass
Fissure density
Burst strength of feed material
Erickson strength of feed material
Hotline rolling variables (Scalping, Homogenizing, Hot and Warm rolling).
Metal composition
Temper measure at 0.48mm
Ra of feed metal at 0.029um

2. Roll Parameters

Roll Data	
Camber on hot rolls	Ovality of journals
Camber on coil rolls	Relief measurements
Chrome Data	
Thickness	Stabilise time/temperature
Etch time	Chrome time
Chrome solution temperatures	Amps and ripples
Roll Grind	
Wheel Data	Coolant data
Microfinish	
Tape data	Platten pressure
Platten roll data	Clutch pressure
Tape speed	Coolant data
Work roll rpm	Coolant flow
Tape feed speed	

3. Mill Parameters for Intermediate and Finishing Mills

Mill load
Unwind tensions
Rewind tensions
Forward and backward slip
Coolant pressure and temperature
Mill load tilt
Coolant properties
Mill speed
Matting fluid properties, flow and temperature

APPENDIX 5 TAKING A MEVIL MEASURE

A mevil is used to measure mass of a coil based on millimetre wall build-up at the side of a coil. A measuring tool, termed a "mevil stick", is used to take the measure, in units of kg/cm

The mevil stick is placed against the side of the coil, with the base of the stick even with the core.

At the intersection of the top of the coil with the mevil stick, a number is shown and this gives the final size of the coil ie. 26 mevils.

The mevils are multiplied by the width (in centimetres) to give a final mass in kilograms. For example, a 26 mevil coil, 1480mm width yields:

26 x 148 = 3770 kg's (3.8 t)

It is accurate to about ±1.5% for wide, large coils. The imperial equivalent is called a gevil.

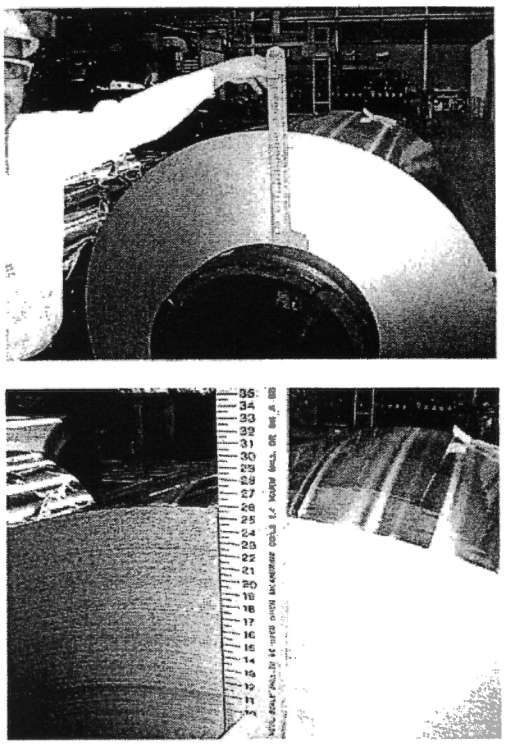

APPENDIX 6 SAMPLE PREPARATION SOP

Making Pack Mounts

Pack mounts are useful for producing longitudinal or transverse metallographic sections. Several samples can be mounted and polished at one time in a pack mount. Also, superior edge retention can be obtained on single samples which have been pack mounted. Pack mounting is recommended for single samples less than 0.064" (1.6mm) in thickness.

Materials

Pack mounts consist of binders, spacers, samples, bolts and nuts.

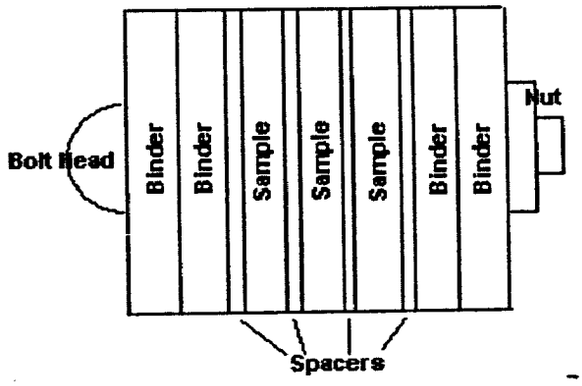

Binders serve to flatten the pack by transmitting the compressive load from the vice to the pack. We use 2024-T3 which is 0.064" (1.6mm) thick for binder material. The use of relatively hard alloys for binders is recommended so the binders can resist deformation and transmit the compressive forces to the inside of the pack. Two pieces of binders are generally used on each side of the pack mount.

Spacers are used between the binders and the samples and between samples if there are multiple samples in the pack mount. The spacers deform to the contours of the sample surfaces during preparation of the mount. This helps to keep polishing liquids and etchants out of the spaces between samples. High purity aluminium foil which is 0.010" (0.25mm) thick is a good choice for a spacer material. High purity foil is relatively difficult to polish and has a tendency to retain particles during polishing. If the polish on the high purity spacer material is good and there are few retained particles, then the polish on the samples is likely to be acceptable and free from artefacts. Spacers made from 2024-O also work.

Bolts (8/32) and nuts used to secure the pack mount are preferably made from aluminium. The use of aluminium bolts rather than steel avoids the possibility of contamination of polishing solutions and etchants if one accidentally exposes the bolts in the mount during polishing.

Assembly of the Pack Mount

Binders, spacers and samples are typically cut to 1.25" x 1" (32mm x 25mm). The longer edge of the sample is the orientation which will be polished. The pack is organized as is illustrated and placed securely in a vice. The bottom of the mount extends upwards in the vice. Two holes are drilled in the pack to accept the 8/32 aluminium bolts. The spacing between the bolts should be about 0.50" (13mm) so that both bolts will fit in a standard mount. The bolts are placed through the pack and tightened securely. It is important to compress the pack mount as tightly as possible to prevent polishing and etching solutions from getting between the spacers and samples. These liquids will tend to ooze from the pack mount and produce artefacts on the finished sample. As an aid in sample location, we generally put the heads of the bolts on the side of the pack which contains the sample at the top of our sample list. Alternatively, the number of spacers or binders can be made asymmetric to aid sample identification after mounting.

After the bolts have been tightened, the pack is removed from the vice. The top and ends of the pack are trimmed on the band saw. The distance between the bolts and the surface to be polished should be kept as large as possible (3/8", 10mm) to minimize the possibility of polishing into the heads of the bolts. The length of the pack should be reduced to less than 1" (25mm) so it will fit in a standard 1.25" (32mm) mount. Wooden blocks should be used to safely push the pack mount through the band saw. The edges of the mount are then rounded on a rough polishing wheel to prevent the sharp edges from tearing polishing materials in later steps. At this point, the pack can be mounted and polished using conventional techniques.

Mounting Techniques

Samples for metallographic analysis are typically mounted in cylindrical mounts prior to polishing. Mounting allows one to develop very safe polishing procedures which yield consistent, high quality results. Larger samples can be polished without mounting. However, results obtained in this manner can be ambiguous. Often, more time is wasted in repolishing unmounted samples than if the sample was mounted at the beginning of the examination.

The sample should be cleaned for a short time using soap and water in an ultrasonic cleaner. This will help the mounting material bind firmly to sample and minimize gaps which may form in the mount. The sample should be thoroughly dried after the cleaning procedure.

Samples can be supported in the mounting press with commercially available clips. Also, samples can be glued to the piston of the mounting press with Duco cement. This minimizes the chance that samples will move as pressure is applied to the mounting material. Duco seems to react with non-lucite mounting materials leaving voids in the mount. Thus, Duco cement should only be used with lucite-type mounting materials.

We use several types of mounting materials depending on the nature of the sample and the investigation which may be required.

- Lucite, TR-1 Transoptic Mounting Powder from Mark V Laboratory

This is our most widely used mounting material for aluminium. The hardness of this material is appropriate for polishing aluminium alloys. It is clear which allows one to see the actual location on the sample where the polished section is taken. This is necessary when trying to polish into a specific location on the sample.

- Fina-Met, UT-5 Mounting Powder from Mark V Laboratory

This is a harder material than lucite which improves edge retention on hard samples. Fina-Met is used when polishing steels, or other very hard materials. It is opaque.

- Konducto Met I Mounting Powder Form

This material forms a mount which is electrically conductive. Konducto Met is used when the mount will be examined in a scanning electron microscope or microprobe. This mounting material can drain electrical charge from the sample which can accumulate from exposure to an electron beam. Electrically insulating mounting materials tend to charge and decompose upon exposure to electron beams making imaging of the sample difficult. The use of Konducto Met is especially important when the SEM/microprobe examination will be done near the edge of the sample where the electron beam will unavoidably contact the mounting material. Konducto Met is opaque.

- Epoxy Mounting Materials

Epoxy can be used to mount samples when exposure to elevated temperature and pressure might cause the microstructure of the sample to be altered. However, mounting with epoxy is messy and produces inferior mounts.

The parameters used to mount with lucite and the other solid mounting materials will vary with the type and condition of the mounting press. However, it should be possible to produce mounts in less than 20 minutes. Several types of imperfections can be found in mounts. These include "snowballs" - Cloudy areas seen in clear lucite mounts which are caused by reaction of moisture with the lucite. Water trapped in a pack mount can escape during mounting and cause snowballs.

Polishing Techniques

Polishing aluminium alloys is typically required to reveal important microstructural features. Aluminium is not the easiest material to polish because it is relatively soft. Embedded particles and artefacts are often introduced during the polishing process.

The advent of automatic polishing machines has increased the reproducibility and the rate at which samples can be prepared. Although hand polishing techniques are still used for some specialized investigations, an automatic polisher is the workhorse in today's metallographic lab.

The following procedure is used at ATC for polishing aluminium alloys using an Abrapol polisher from Struers. Slight modifications may be necessary for other polishers.

1. Insert mounted samples into the polishing fixture. At least four specimens need to be placed in our six position fixture to ensure proper operation.

2. Polish on 240 grit (US nomenclature, paper from Leco) for 20 seconds at 300 rpm. Maintain water flow to the paper during polishing. Polishing pressure for this step and subsequent steps is 20 nt. Examine the mounts to determine if planar surfaces have been created on each mount. If not, repeat this step. The example illustrates what the surface of a typical sample will look like after this step.

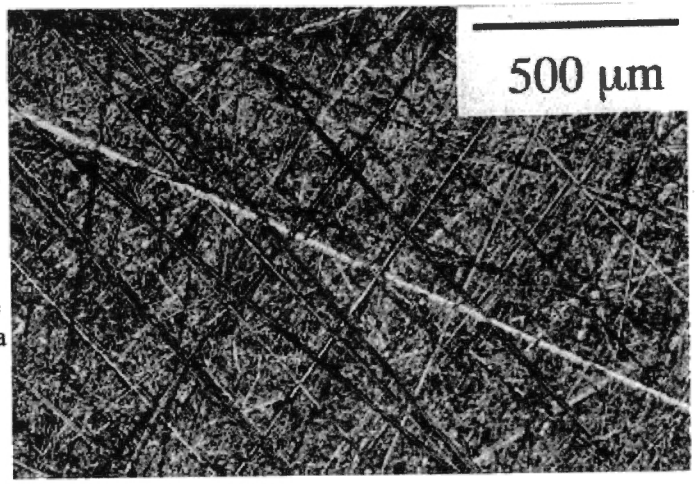

3. Rinse under running water.

4. Polish on 320 grit paper for 20 seconds reducing the speed to 150 rpm. Maintain water flow to the paper during polishing. (Some metallographers omit the 320 grit step.)

5. Rinse under running water.

6. Polish on 400 grit paper for 20 seconds at 150 rpm. Maintain water flow to the paper during polishing. The example shows what the sample should look like after this step.

7. Rinse under running water.

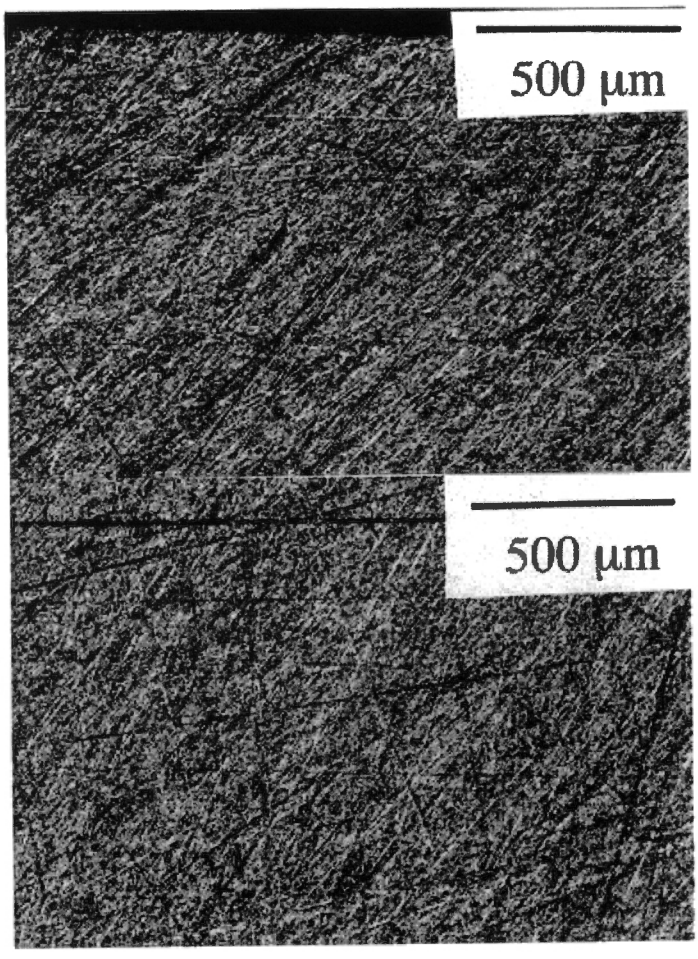

8. Polish on 600 grit paper for 20 seconds at 150 rpm. Maintain water flow to the paper during polishing. The example shows what the sample should look like after this step.

9. Rinse under running water.

10. This step is used to reduce the amount of embedded SiC. This step should be used for pure aluminium and whenever a very good polish is required. Polish for 2 minutes on DP-Mol cloth (Struers) using 3 Micron Diamond Suspension Spray (Leco) and DP Red Lubricant HQ (Struers). This step will round the edges of the samples slightly. If embedded particles persist, increase time and pressure for this step.

11. Clean using a wet cotton ball and water with dish soap. Be sure that the cotton ball is saturated before touching the samples as dry cotton can produce scratches. Blow off water with compressed air.

12. Polish for 2 minutes on Technotron Cloth (Leco) using 3 Micron Diamond Suspension Spray (Leco) and Microid Diamond Extender (Leco). The example shows what the sample will look like after this step. For softer alloys, the samples should be examined under the microscope at this point to determine of embedded particles are present.

13. Repeat cleaning as in 11.

14. Polish for 2 minutes on Technotron Cloth (Leco) using 1 Micron Diamond Suspension Spray (Leco) and Microid Diamond Extender (Leco). The example shows what the sample should look like after this step.

15. Repeat cleaning as in 11.

16. Polish for 30 seconds on OP-Chem Cloth (Struers) using about 100 ml of 50% solution of OPS Suspension (Struers) in water. Longer polishing times and/or higher concentrations of OPS will stain the constituent phases. Wet the polishing wheel with OPS solution before beginning polishing. The example shows what the sample will look like after this step.

17. Repeat cleaning as in 11.

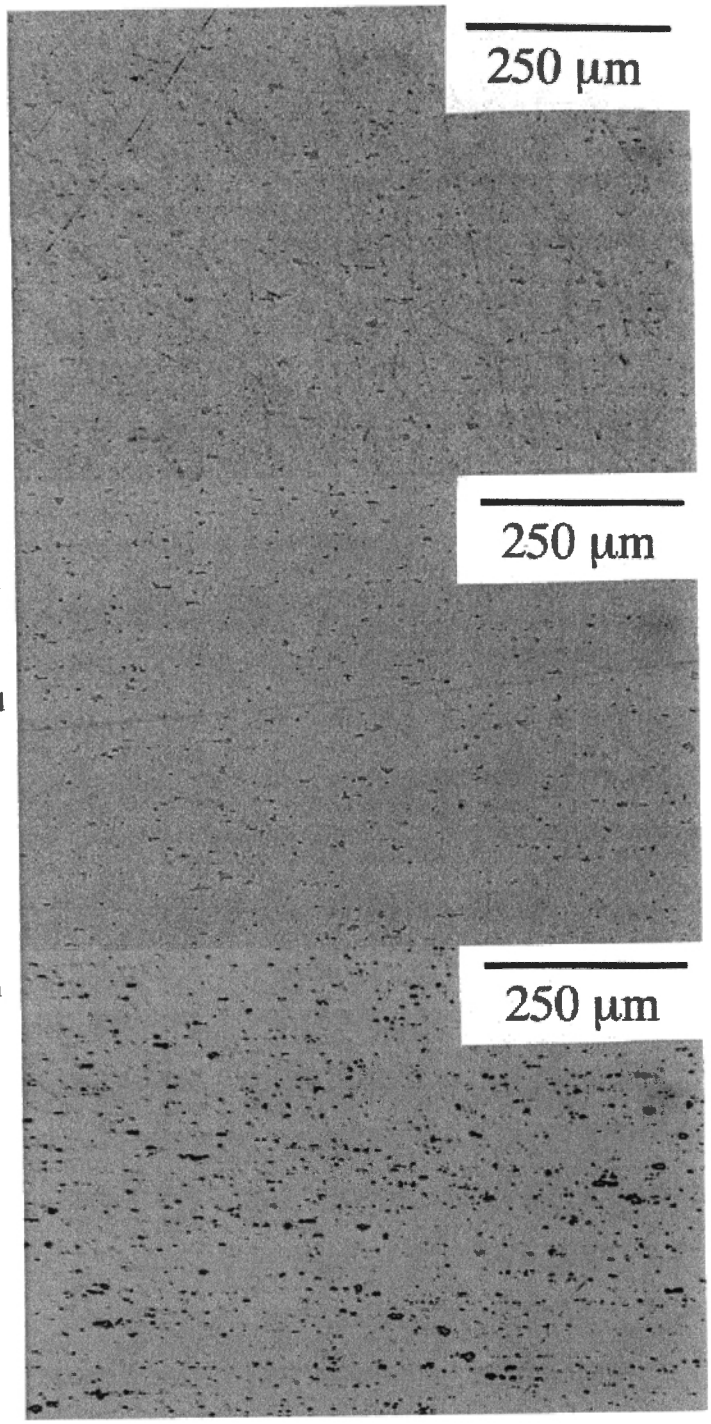

Etching Techniques

Aluminium alloys are often etched to reveal aspects of metallurgical structure which cannot be seen in the as-polished condition. While etching is very useful, there are some microstructural evaluations which should be done in the as-polished condition. For example, identification of phases such as Mg_2Si or S-phase is much more straight forward on as-polished samples. Therefore, etching is generally done only after a thorough examination has been completed on the as-polished sample.

Etchants

The following section contains a list of the most commonly used etchants for aluminium alloys.

IMPORTANT SAFETY INFORMATION: Safety procedures for making or using etchants will not discussed here. These etchants use hazardous materials which must be handled carefully and disposed of properly. Knowledge of proper procedures for handling HF is especially critical.

The actual times and conditions for using these etchants vary and will be discussed in a later section for each alloy family.

- Graff-Sargent Etch

Graff-Sargent (G/S) etch performs in a similar manner to Keller's etch, but it is less aggressive. G/S can be used to reveal more structure without the tendency to over-etch the entire sample. G/S will attack oxides more slowly than Keller's and G/S can be used to reveal the presence of forging laps or oxide stringers. Light etches with G/S will highlight constituents. G/S is used on most alloys, but to a lesser extent on 5xxx and 6xxx alloys.

15.5ml	HNO_3
0.5ml	HF
3.0gm	CrO_3
84 ml	H_2O

- Keller's Etch

Keller's etch is a standard etch for aluminium alloys. Keller's is quite aggressive and care must be taken not to over-etch. An application of G/S before etching with Keller's almost always improves the final result. Keller's etch is useful for identification of Al_7Cu_2 Fe.

2.5 ml HNO_3
1.5 ml HCl
0.5 ml HF 95.5 ml H_20

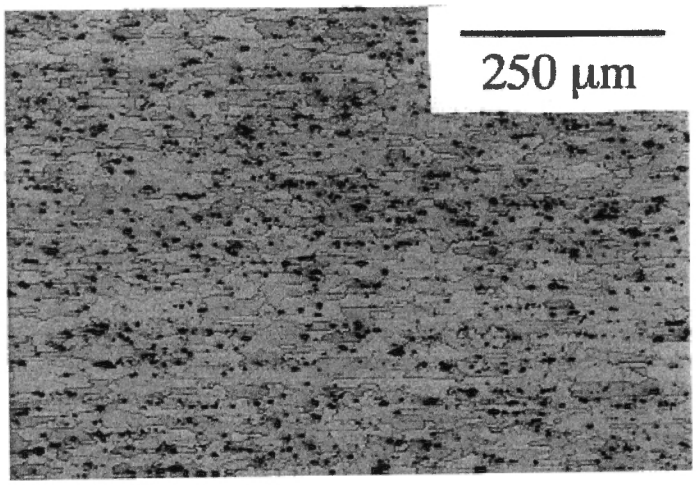

- Electroetch

Electroetching (EE) is used before viewing with polarized light (PL) to reveal the grain structures in some aluminium alloys.

92 ml HBF_4
14 gm H_3BO_3
2 litres H_20

specimen is the anode
stainless steel cathode
12-20 VDC

Alloy Families

The following information is a summary of our knowledge on the use of etchants for revealing various structures in aluminium alloys. These general suggestions may not work for all alloys in a given family. Please call or e-mail for suggestions for specific problems.

1xxx Alloys

- 20 s G/S, or 0.5% HF for 10 s to highlight constituents
- 45 s EP +PL for grain structure

2xxx Alloys

- 45 s G/S for typical structure; addition of 10 s Keller's might be helpful
- 45 s EP + PL for grain structure
- 5 s Keller's for grain structure in 2024-T3; see example in Figure 7

3xxx Alloys

- 0.5% HF in water for 10 s helps to outline constituents
- 60 s EP+PL for grain structure

4xxx Alloys

- - 1% HF in water for 20 s to highlight Si particles; or G/S + Keller's

5xxx Alloys

- 45 s EP+PL to reveal grain structure
- 180 s using 40% $H_3 PO_4$ at 95°F will highlight shear bands.

6xxx Alloys

- 60-120 s EP+PL to reveal grain structure in 6063, 6061-T4
- 180 s 1%HF in water for grain structure in 6061-T6
- 60 s in 25% HNO_3 at 70°C will highlight precipitate in some alloys.
- Hot caustic etches can be tried as a last resort for grain structure in 6xxx alloys

7xxx Alloys

- 45 s G/S or perhaps 120 s EP+PL for grain structure in 7475-T7 type materials
- 10 s G/S will highlight precipitate distribution and can be useful for phase identification.

APPENDIX 7 OPERATION OF A MULLENS TESTER

Process	*Performing a Burst Strength Test*					
Department	Foil	Document No.	SP	4	08	003
Written by	Matt Mansell	Authorised by	Department Manager			
Issue Date	1 (07-Dec-2000)	Date Authorised				
Previous Issue Date	12/08/98	Signature				

The burst test offers an indication of the alloy-temper combination of a sample of foil.

- Obtain an A4 size sample of the foil you want to test. Ensure sample is free of creasing.
- Switch the burst strength tester "ON" at the power point.
- Check the digital pressure gauge by switching the toggle switch to "CHECK". Digital readout should be 1185.
- Place the foil under the glass bulb and clamp it into place by bringing the chrome lever on top of the bulb down firmly in a clockwise direction.
- Turn the large chrome knob in the direction of the arrow and release it to return.
- The digital gauge should hold the burst strength value for 10 seconds. Record this value on the checklist. (NOTE: The gauge may not hold the vale if less than 60. In this case, switch the toggle to "CHECK" and reset the readout to "000". Repeat the burst test).
- Unclamp and remove sample. Ensure no foil remains under the glass bulb.

APPENDIX 8 OPERATION OF A ERICKSON TESTER[39]

Process	*Determination of Alloy Temper using the Erickson Test*					
Department	Foil	Document No.	SP	4	07	007
Written by	Matt Mansell	Authorised by	Department Manager			
Issue Date	1 (07-Dec-2000)	Date Authorised				
Previous Issue Date	22/11/00	Signature				

Measuring Frequency

- An Erickson Test is to be performed on each coil slit on the 756 slitter.
- The feed coil and tail of each subsequent run is to be tested.
- The 756 operator is responsible for conducting the tests.

Testing Method

- Slab outside layer from feed coil, cut a 50mm wide strip from the edge.
- Place the strip of foil through the slot in the Erickson machine.
- Wind the handle in the clockwise direction to firmly clamp foil into place. Make sure that the foil fully covers the hole in the clamping head.
- Set the scaled ring to zero by turning the ring until the '0' on the ring lines up with the line on the pointer.
- Push the knurled lock ring toward the centre and turn the handle slightly to lock it into place.
- Turn the handle slowly (clockwise) and watch in the mirror to see when the coil punctures. Stop as soon as the foil punctures.
- Read the number off the scaled ring and record it on the timesheet.
- Compare the result to the alloy temper combination. If outside of specification, refer to **RP407001.**

APPENDIX 9 BINDING ENERGY FOR OXYGEN, CARBON, ALUMINIUM, SILICON, MANGANESE AND IRON

Oxygen **O**
Atomic Number 8

Handbook of X-ray Photoelectron Spectroscopy

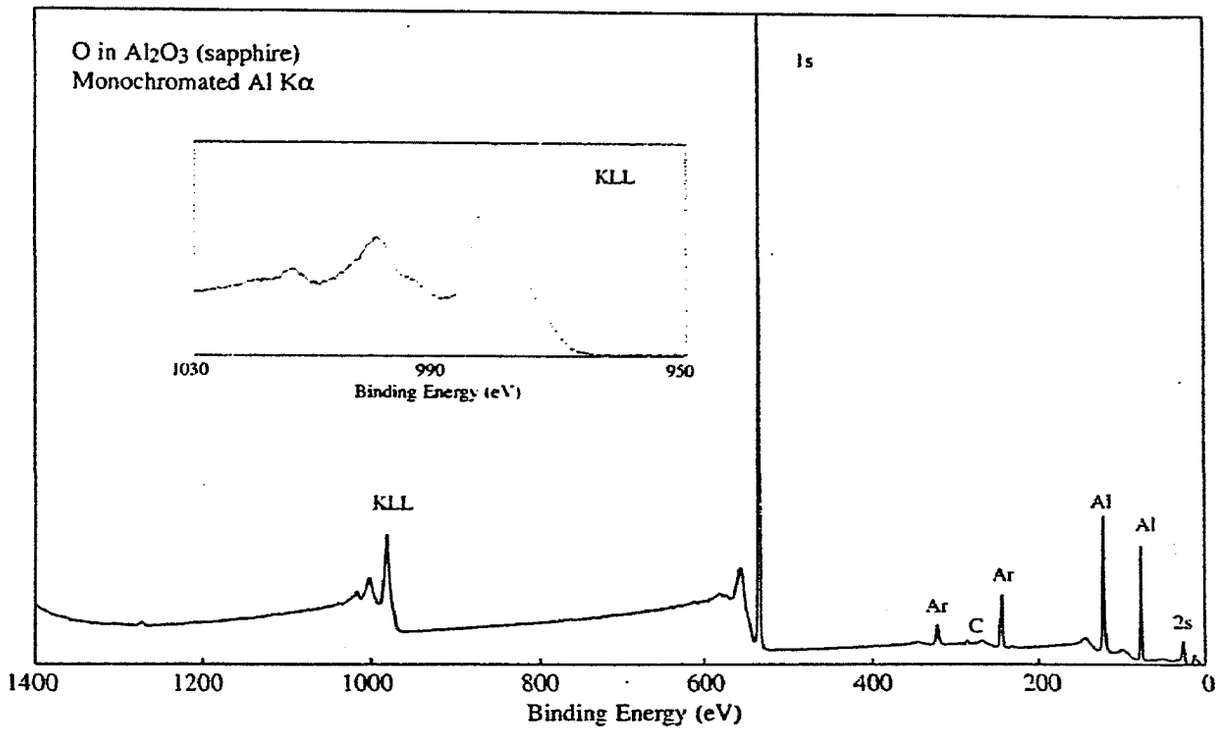

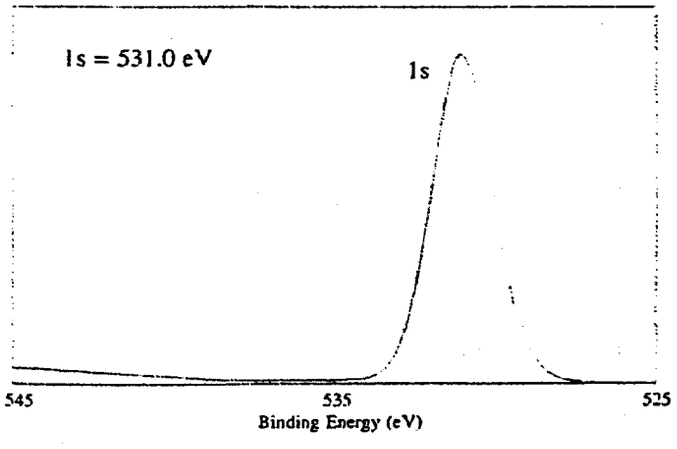

Line Positions (eV)

Photoelectron Lines

1s	2s
531.	23

Auger Lines

KL_1L_1	KL_1L_{23}	$KL_{23}L_{23}$	
1013	999	978	(Al)
780	766	745	(Mg)

Oxygen O

Atomic Number 8

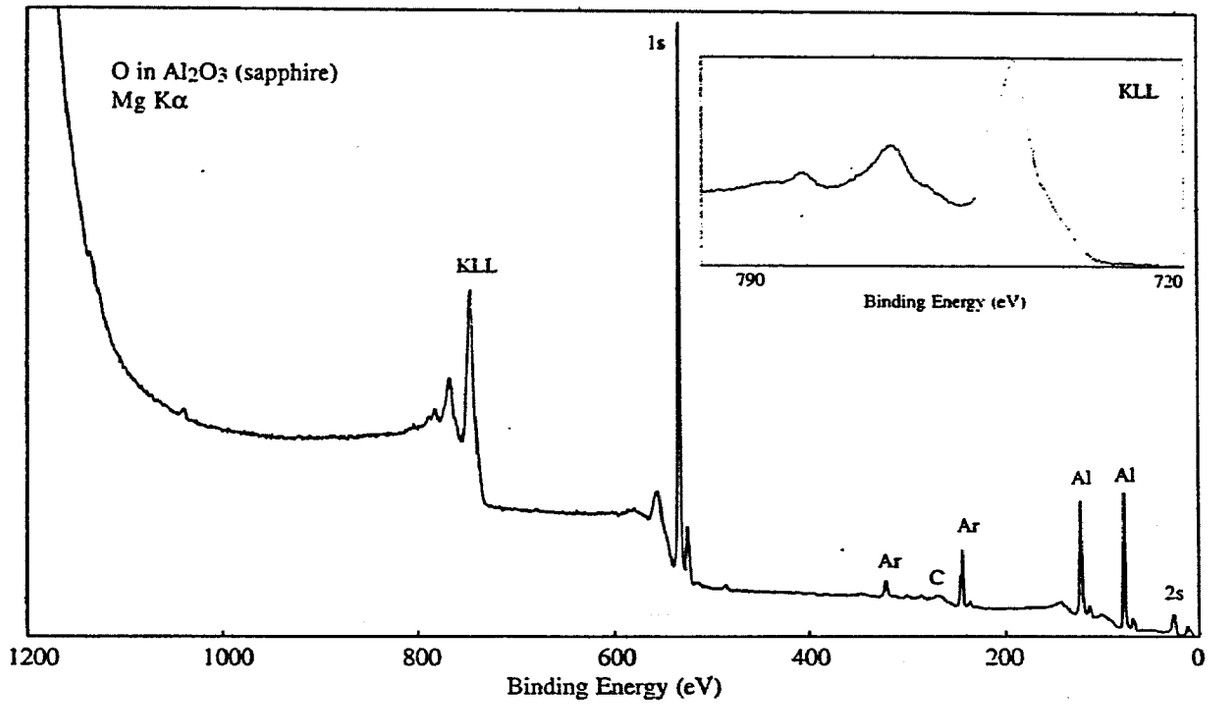

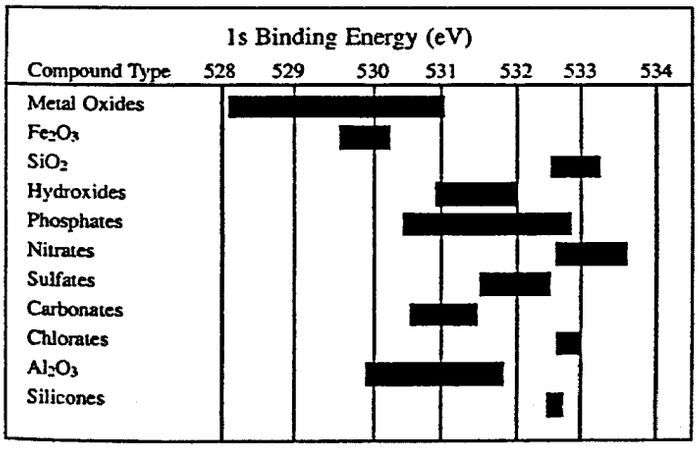

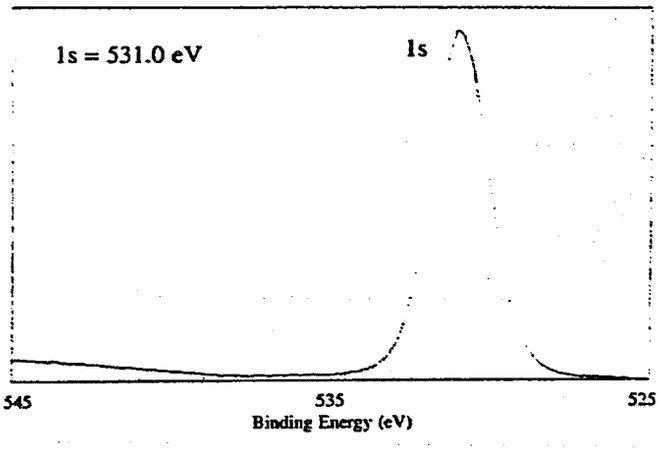

Carbon C

Atomic Number 6

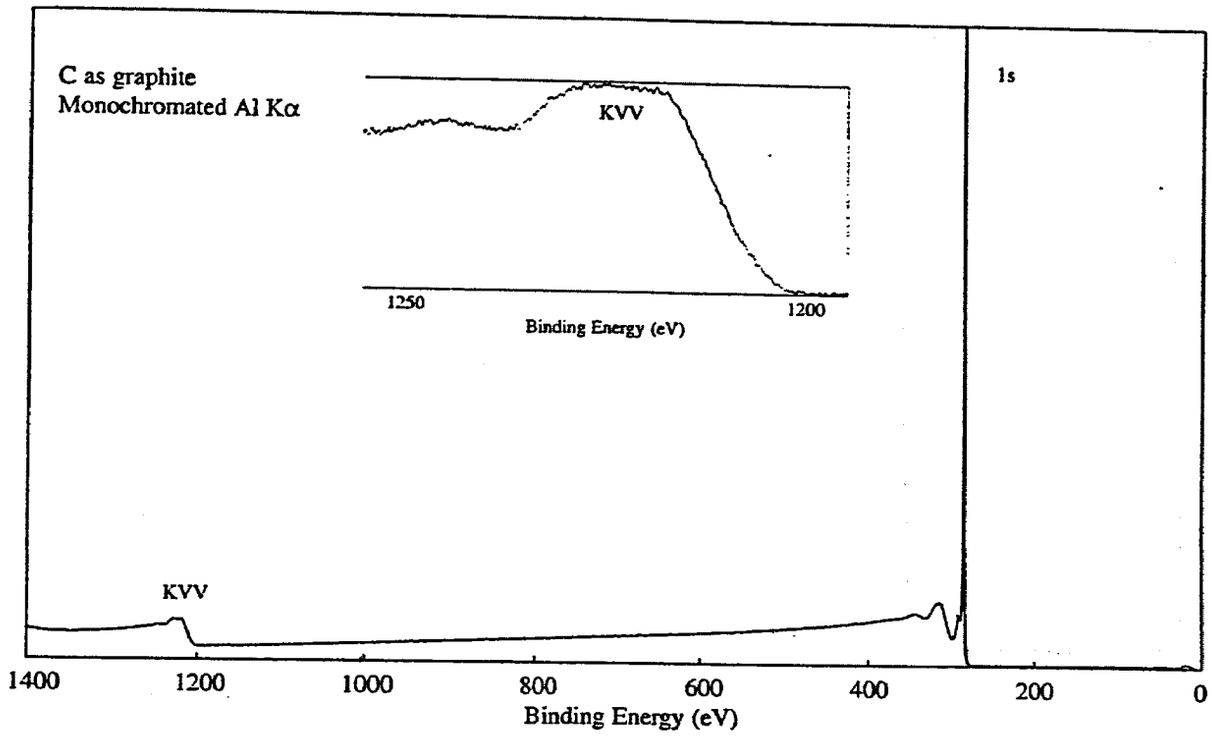

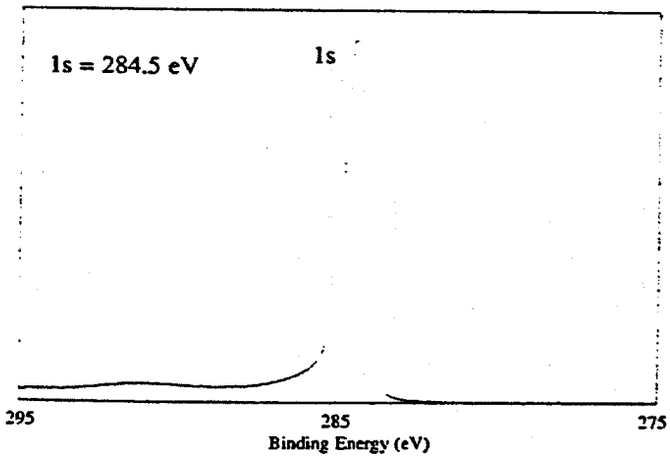

Line Positions (eV)

Photoelectron Lines

1s	
285	

Auger Lines

KVV	
1223	(Al)
990	(Mg)

Carbon C

Atomic Number 6

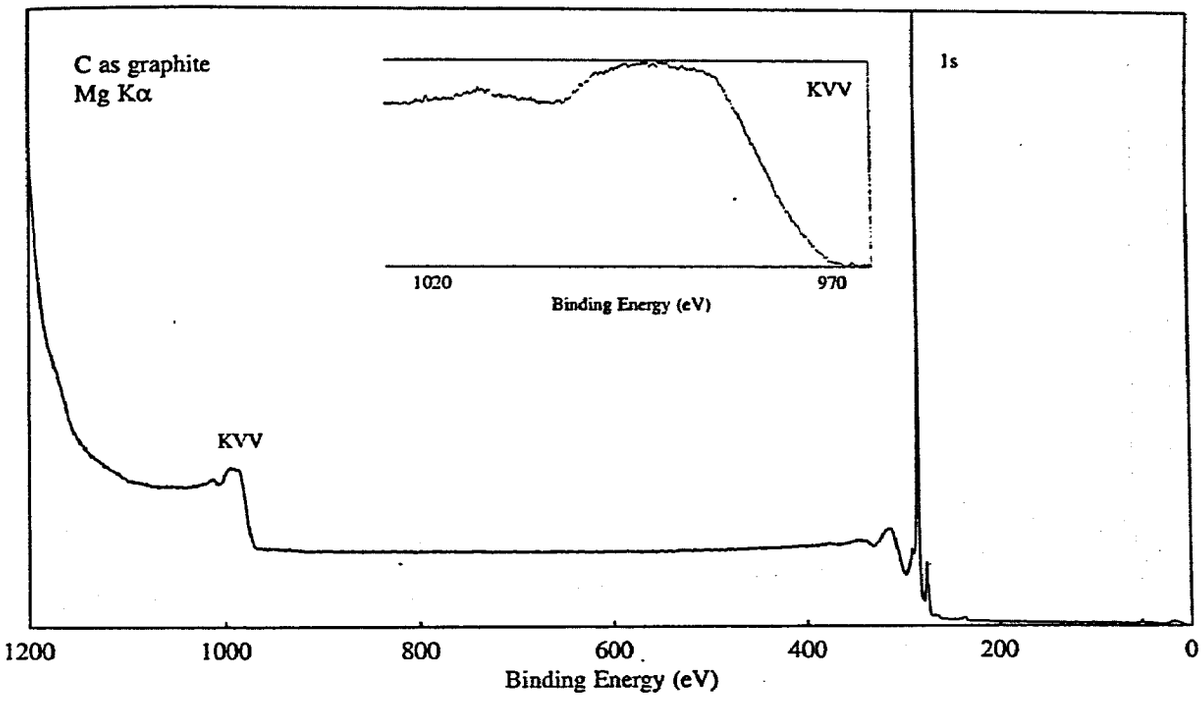

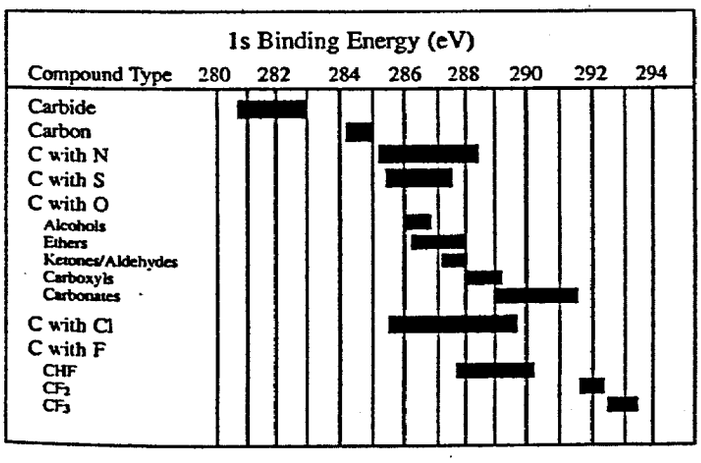

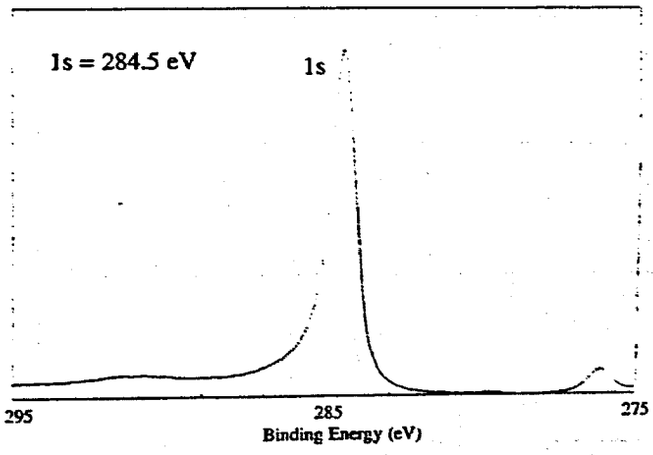

Aluminum Al

Atomic Number 13

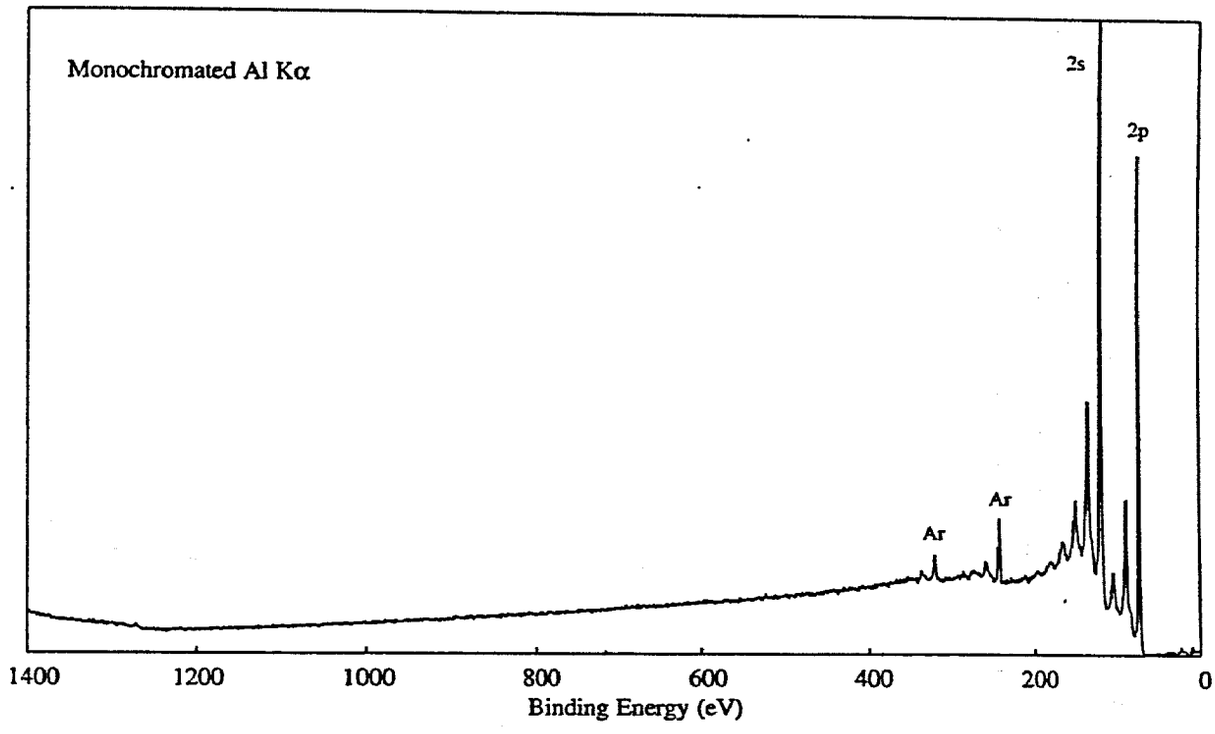

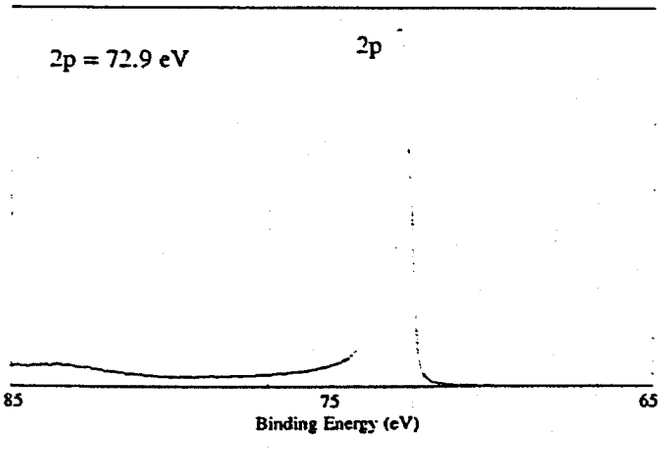

Line Positions (eV)

Photoelectron Lines

2s	2p
118	73

Auger Lines

$L_{23}M_1M_{23}$

1419 (Al)

1186 (Mg)

Aluminum Al

Atomic Number 13

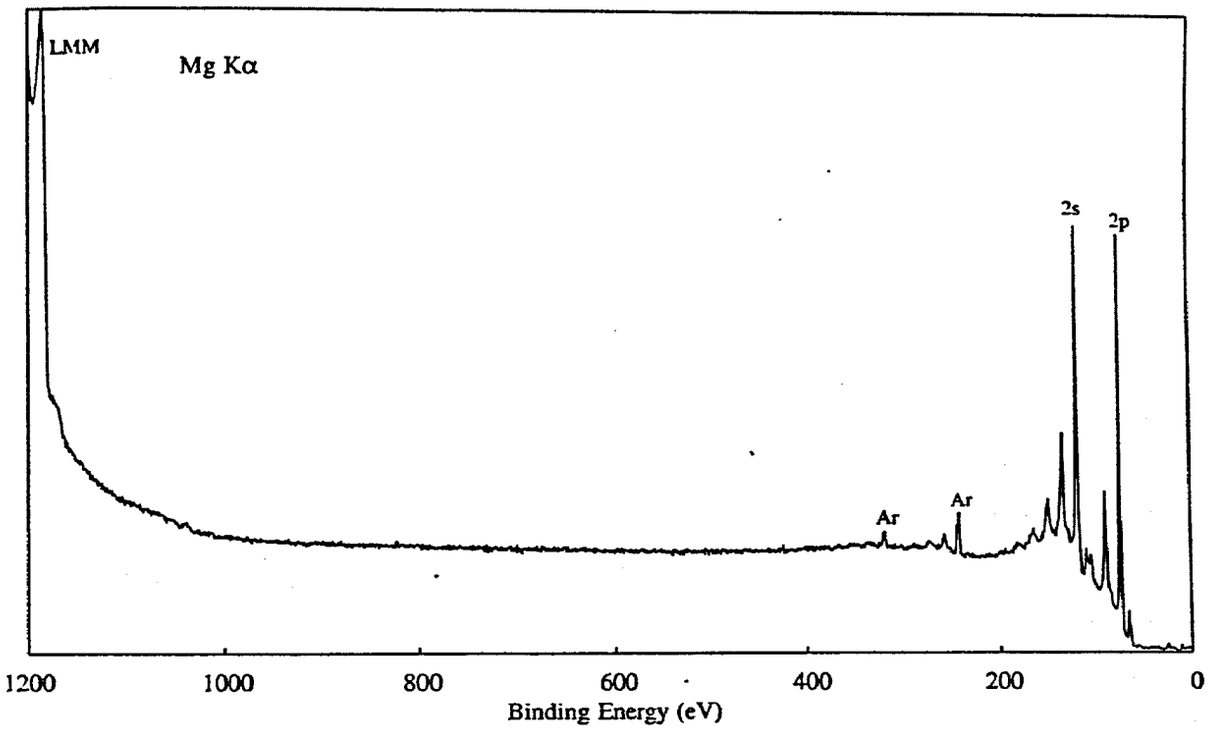

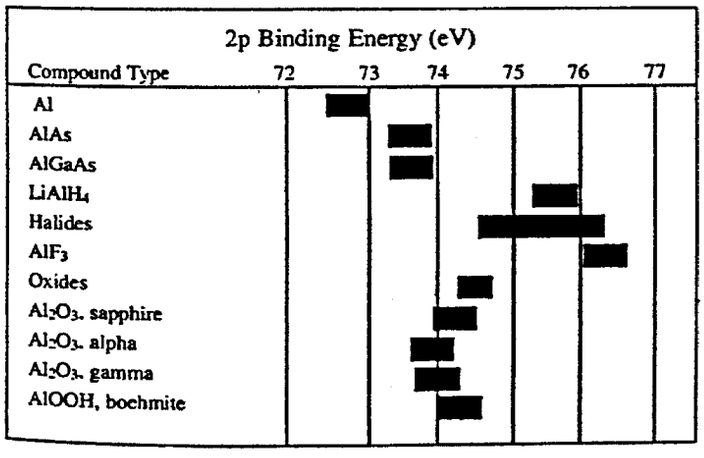

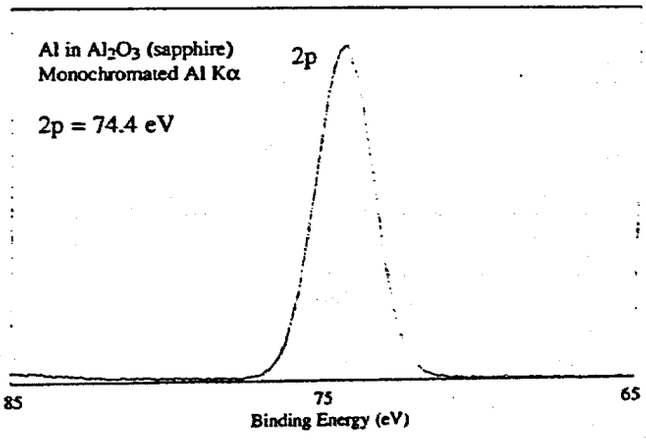

Silicon Si

Atomic Number 14

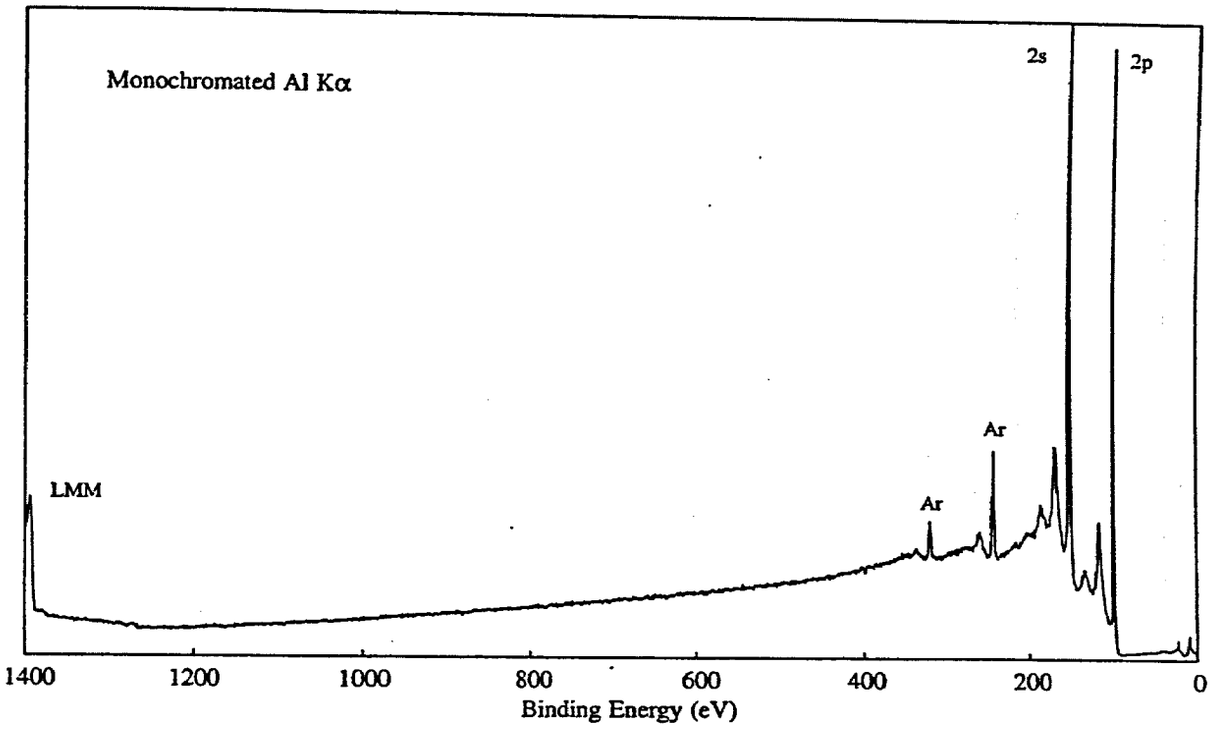

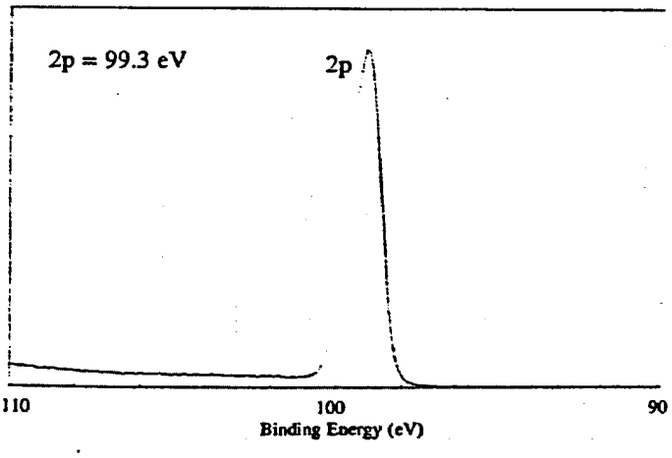

Line Positions (eV)

Photoelectron Lines

2s	2p
151	99

Auger Lines

$L_{23}M_{23}M_{23}$

1394	(Al)
1161	(Mg)

Silicon Si

Atomic Number 14

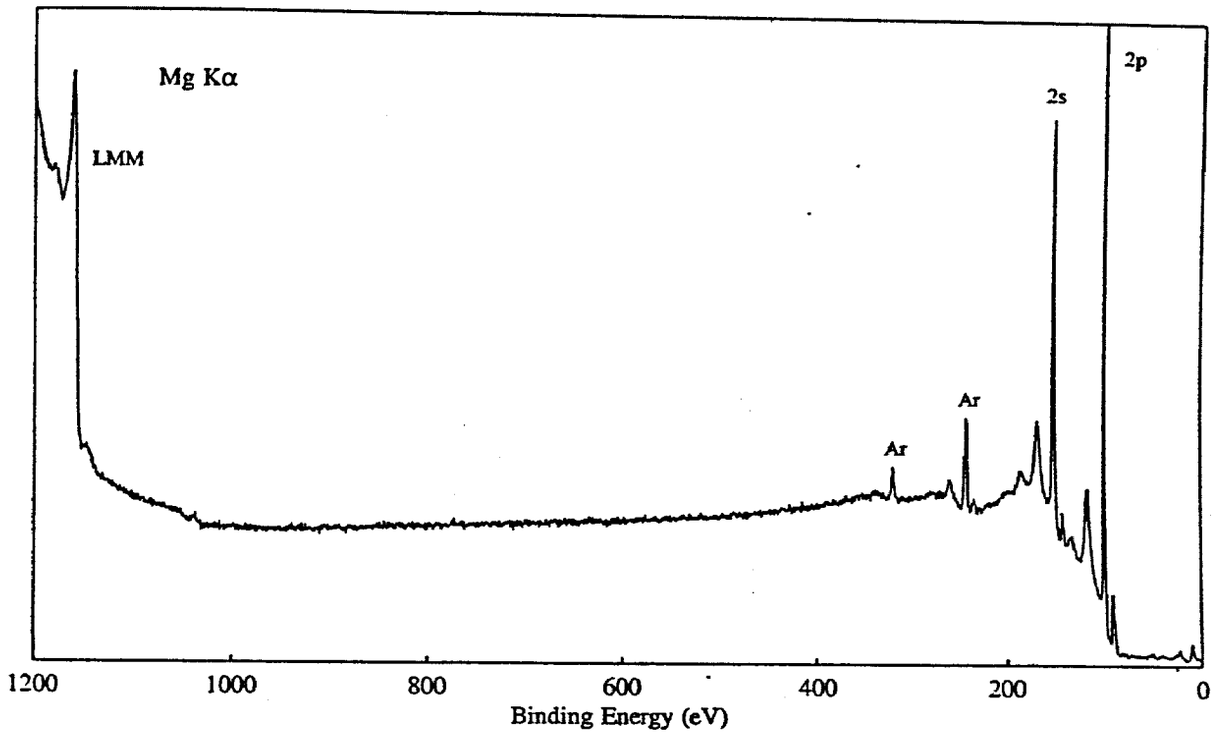

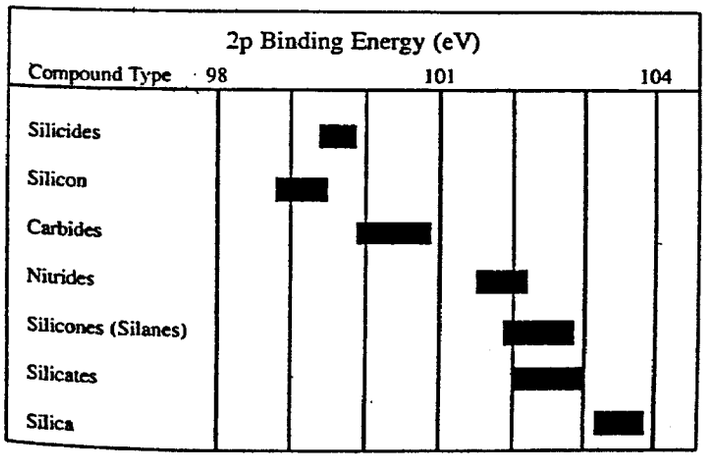

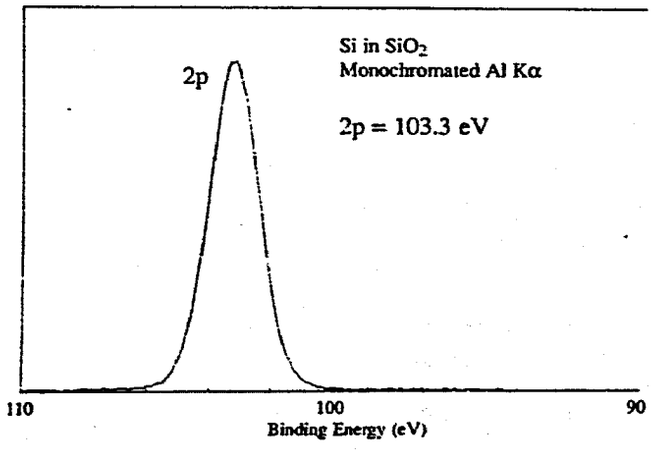

Manganese Mn

Atomic Number 25

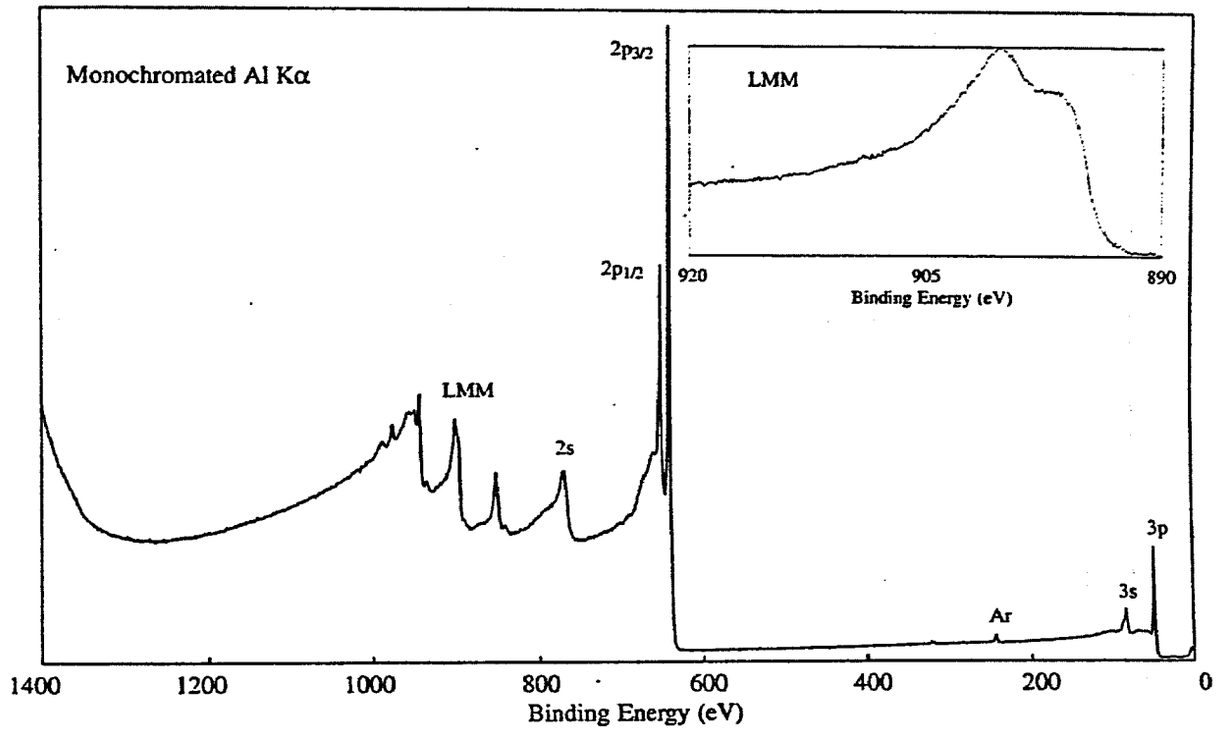

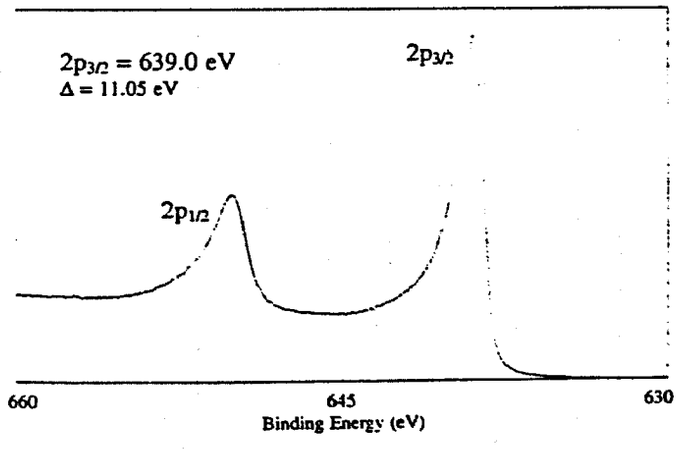

Line Positions (eV)

Photoelectron Lines

2s	2p1/2	2p3/2	3s	3p
769	650	639	83	48

Auger Lines

$L_{23}M_{23}M_{23}$	$L_3M_{23}M_{45}$	$L_3M_{45}M_{45}$	
944	900	852	(Al)
711	667	619	(Mg)

Manganese Mn

Atomic Number 25

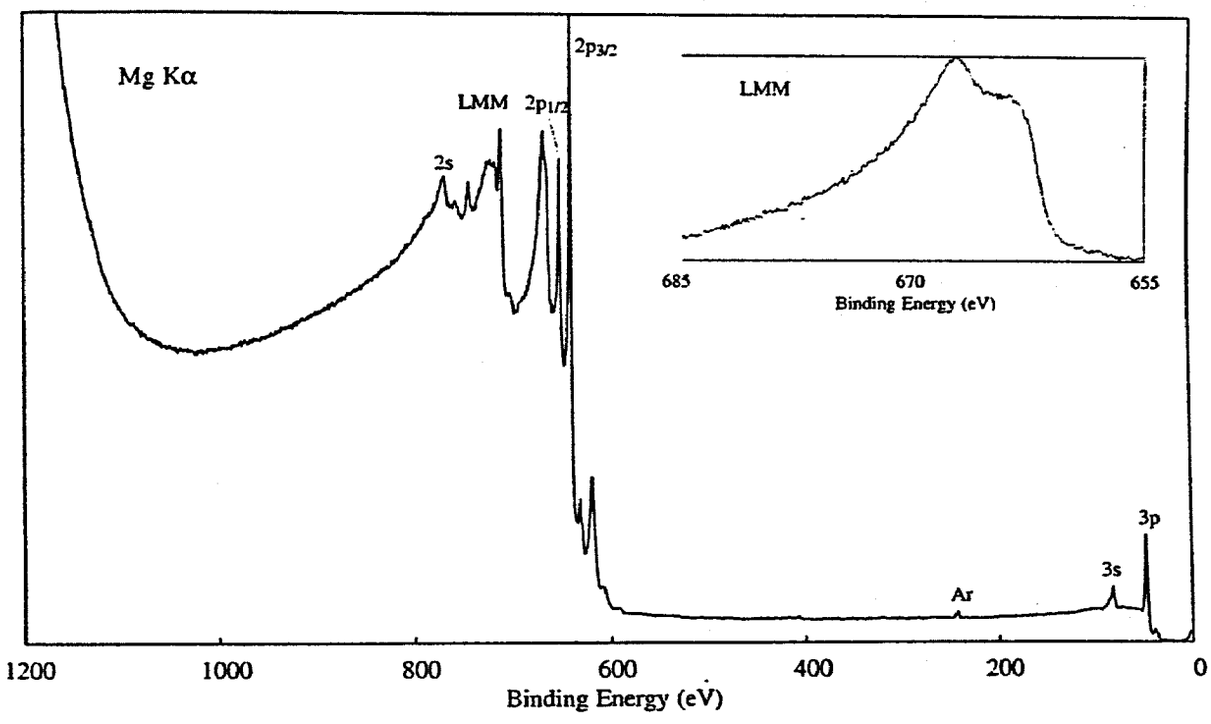

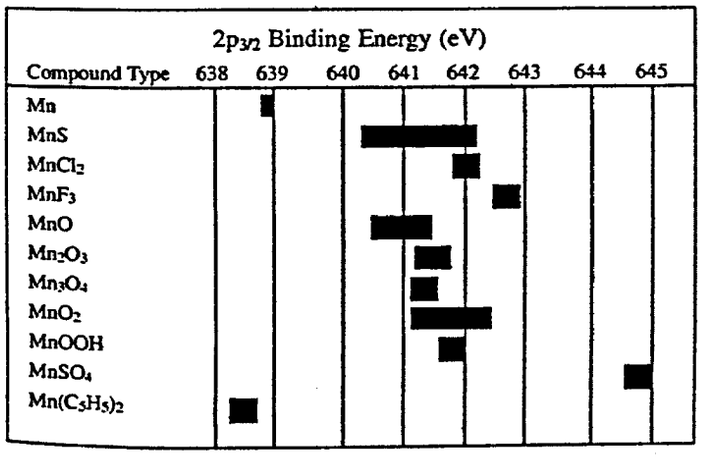

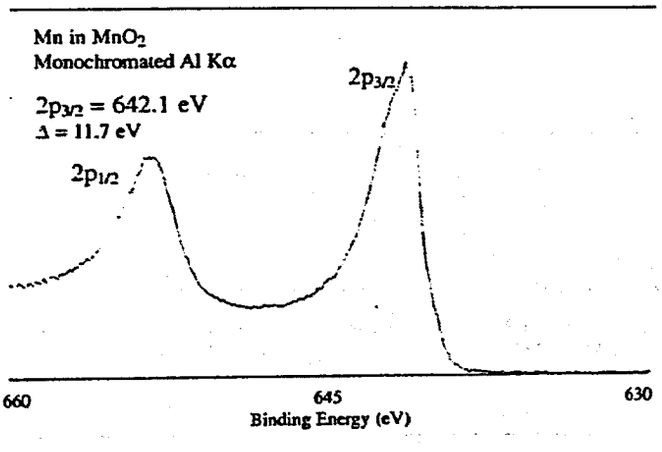

Iron Fe

Atomic Number 26

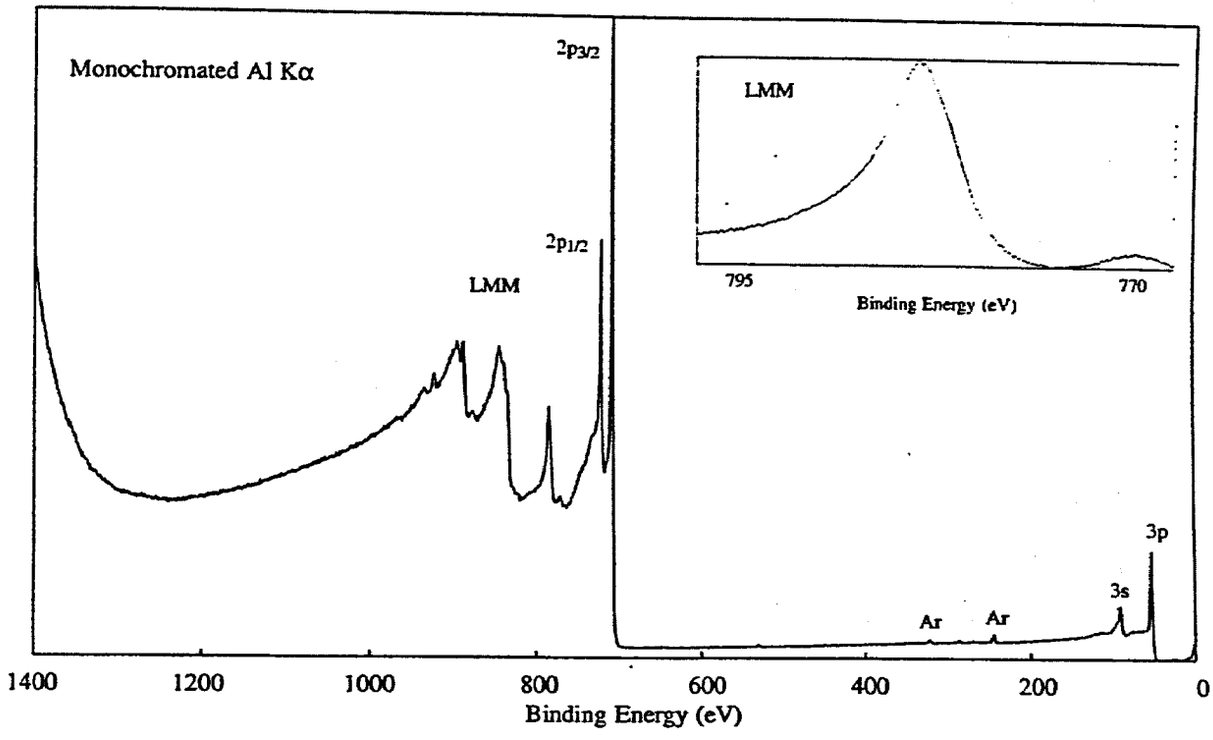

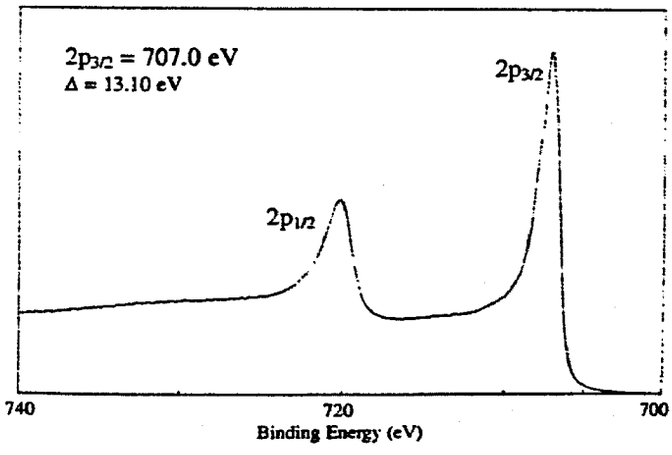

Line Positions (eV)

Photoelectron Lines

2s	2p1/2	2p3/2	3s	3p
845	720	707	92	53

Auger Lines

$LM_{23}M_{23}$	$L_3M_{23}M_{45}$ (^1P)	$L_3M_{45}M_{45}$	
888	839	784	(Al)
655	606	551	(Mg)

Iron Fe

Atomic Number 26

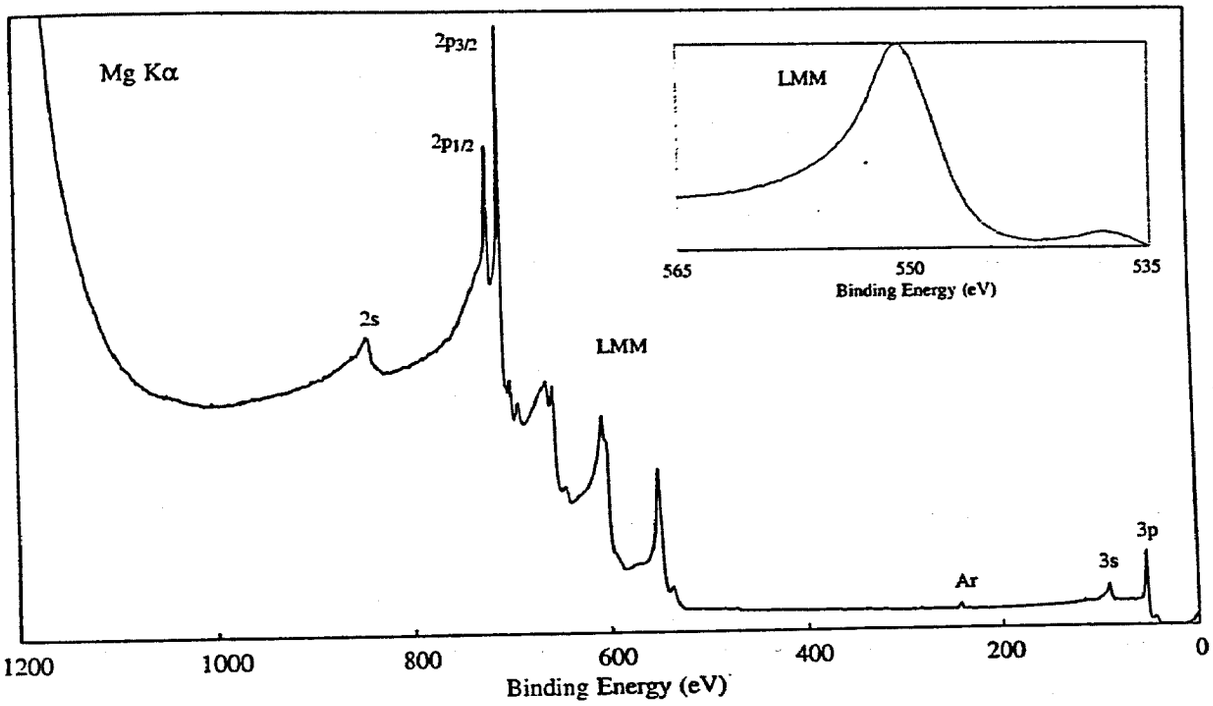

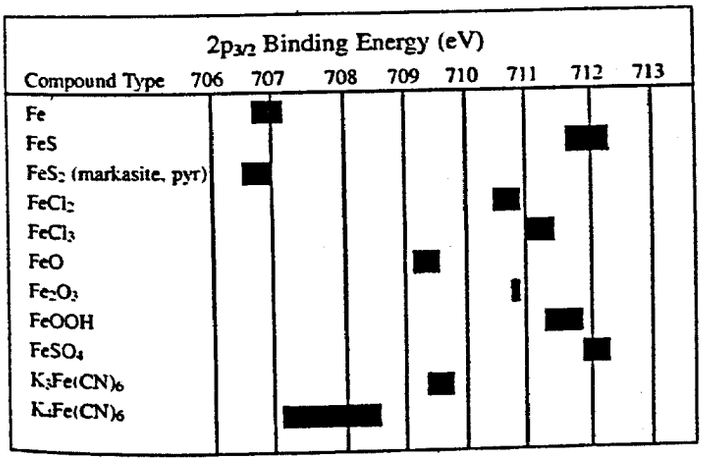

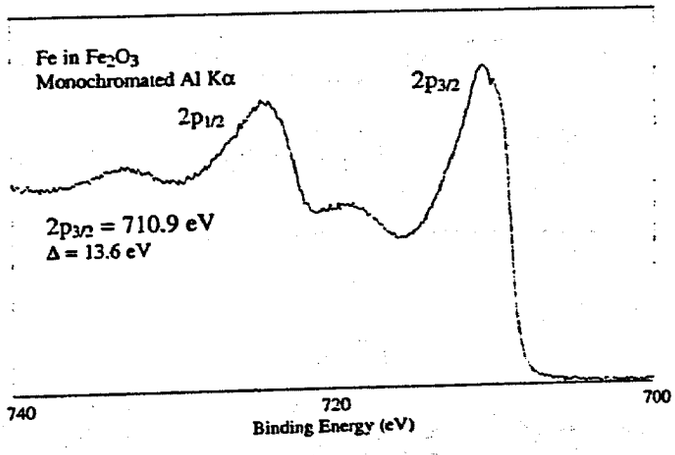

APPENDIX 10 8150 COMPOSITION[60]

Facsimile Transmission Cover Sheet

ALCOA

FROM
ALUMINUM COMPANY OF AMERICA
ALCOA TECHNICAL CENTER
Fax No. 412-337-5307

TO: MATT MANSELL

FAX NO.: (011) 61-2-96320258

DATE: 98-06-1

NO. PAGES 2 (INCLUDING COVER SHEET)

FROM: MILT MILNER

RE: REGISTRATION ACCEPTANCE LETTER FOR 8150 ALLOY

SEE ATTACHED. REGARDS —

Milt

The Aluminum Association

900 19th St., N.W.
Washington, D.C. 20006

Phone (202) 862-5100
Telex 710 822 1129
FAX (202) 862-5164

June 8, 1998

TO: Signatories to the Declaration of Accord

RE: International Registration of a New International Alloy Designation 6150

Ladies and Gentlemen:

Since there were no objections, alloy designation 6150 with the following chemical composition limits is assigned for international registration.

REGISTERED COMPOSITION LIMITS

Silicon	0.30
Iron	0.9-1.3
Manganese	0.20-0.7
Titanium	0.05
Others, Each	0.05
Others, Total	0.15
Aluminum	Remainder

This alloy has been developed for use as general household foil and semi-rigid packaging foil.

Sincerely,

Parvaneh Shaflee
Assistant Manager, Produce Standards

cc: Technical Committee on Product Standards
J. Green
P.V. Mara
P. Pollak
A.N. Andersen
PN98-58 Project File
Revisions to the 1997 Edition of Blue Sheets
Project Completion File

H:\SDA\PN98-58.doc

APPENDIX 11 SURFACE SCAN INFORMATION

Quantification Table for Experiment A:\ROUGH

Peak	Centre	SF	Pk Area	Tx. Function	Norm Area	[AT]%
? 1s	686.46	4.43	291.364	3704.9	0.00032	0.103
Mn ox	640.11	9.17	102.770	3618.2	0.00005	0.017
Mn 2p3	638.80	9.17	230.773	3615.8	0.00012	0.039
) 1s	534.01	2.93	10881.979	3436.0	0.01764	5.663
) 1s	533.07	2.93	28050.594	3434.5	0.04546	14.59!
) 1s	532.17	2.93	54026.020	3433.0	0.08754	28.10!
In ox	485.80	14.80	81.652	3359.8	0.00003	0.008
In 3d5	484.62	14.80	506.236	3358.0	0.00016	0.052
: 1s	290.43	1.00	928.875	3085.9	0.00428	1.376
: 1s	287.74	1.00	630.503	3082.5	0.00291	0.933
: 1s	286.24	1.00	7736.036	3080.6	0.03567	11.45!
Al ox	75.48	0.54	10673.379	2835.2	0.08986	28.85!
Al 2p > metal	73.02	0.54	1079.728	2832.6	0.00914	2.935
Al 2p	72.56	0.54	2159.457	2832.1	0.01828	5.869

XPS wide A:\ROUGH
ANALYSER CAE = 100eV STEP = 1 eV SCANS = 2 TIME = 4m 30.20s
SOURCE Al K-alpha Large Area XL
LABEL

19/09/2001

UNSW Surface Science

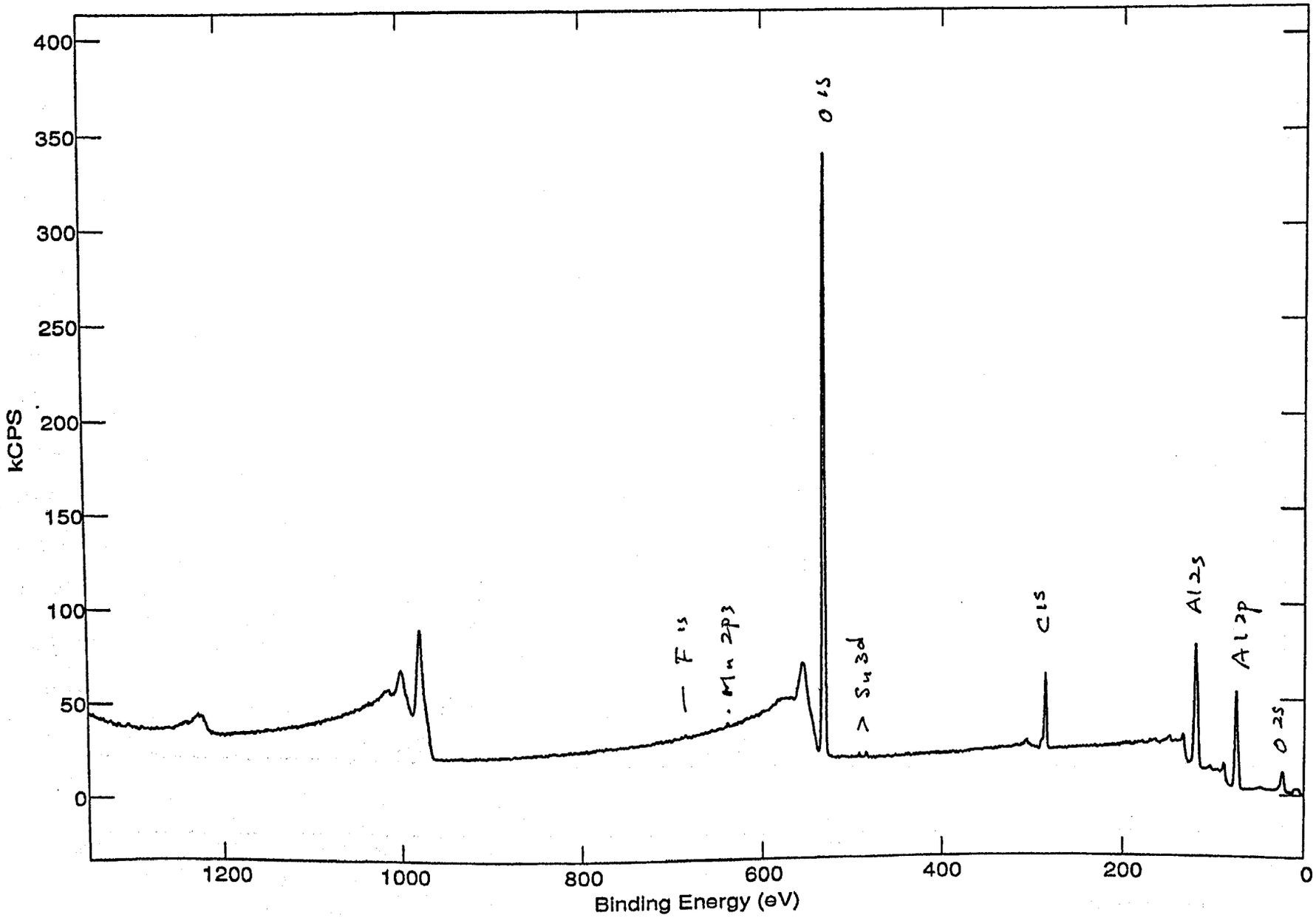

XPS	A A:\ROUGH	19/09/2001
ANALYSER	CAE = 20eV STEP = 100 meV SCANS = 5 TIME = 1m 20.50s	UNSW Surface Science
SOURCE	Al K-alpha Large Area XL	
LABEL		

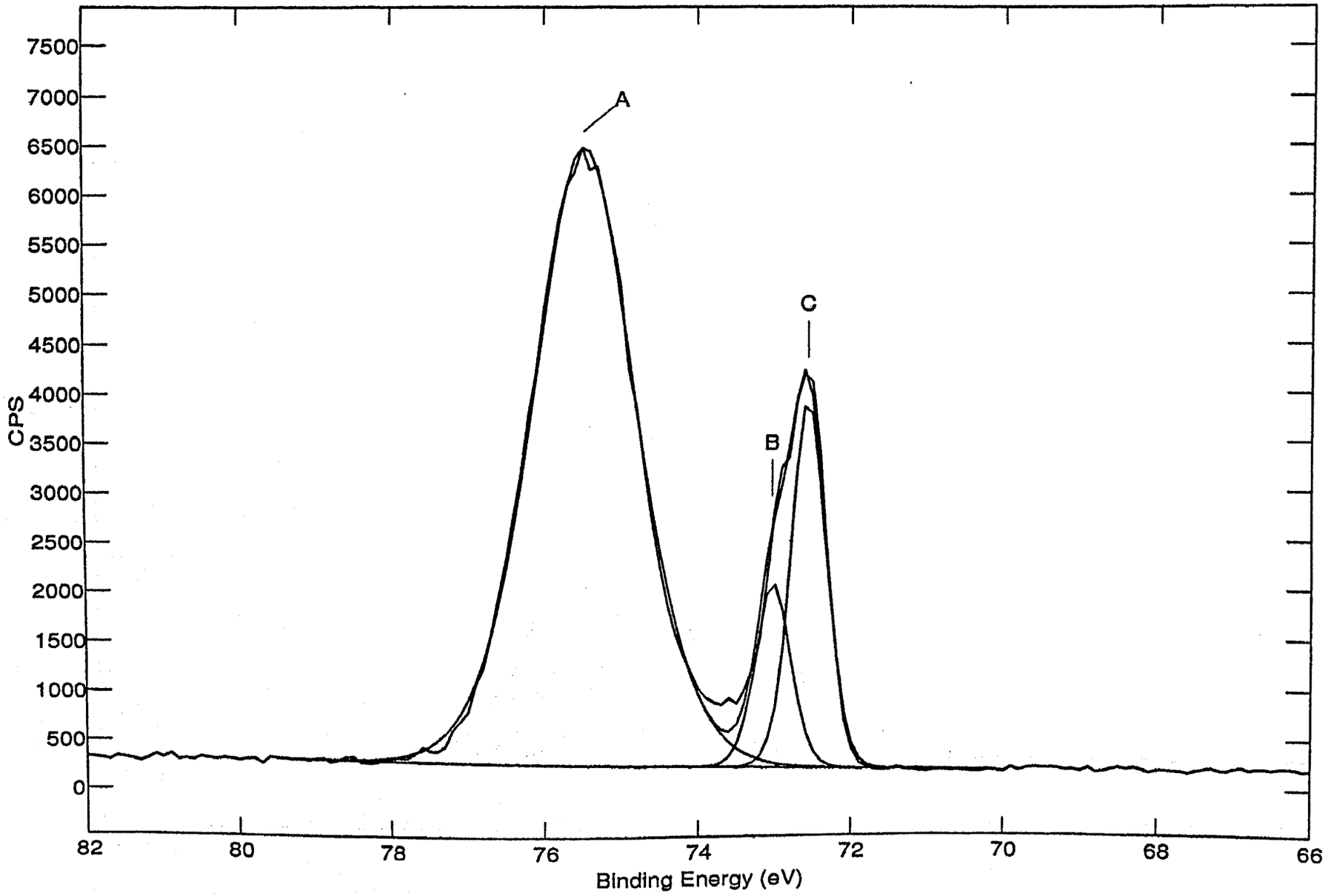

A:\ROUGH\AL2P.DTS

XPS	A A:\ROUGH	19/09/2001
ANALYSER	CAE = 20eV STEP = 100 meV SCANS = 3 TIME = 48.30s	UNSW Surface Science
SOURCE	Al K-alpha Large Area XL	
LABEL		

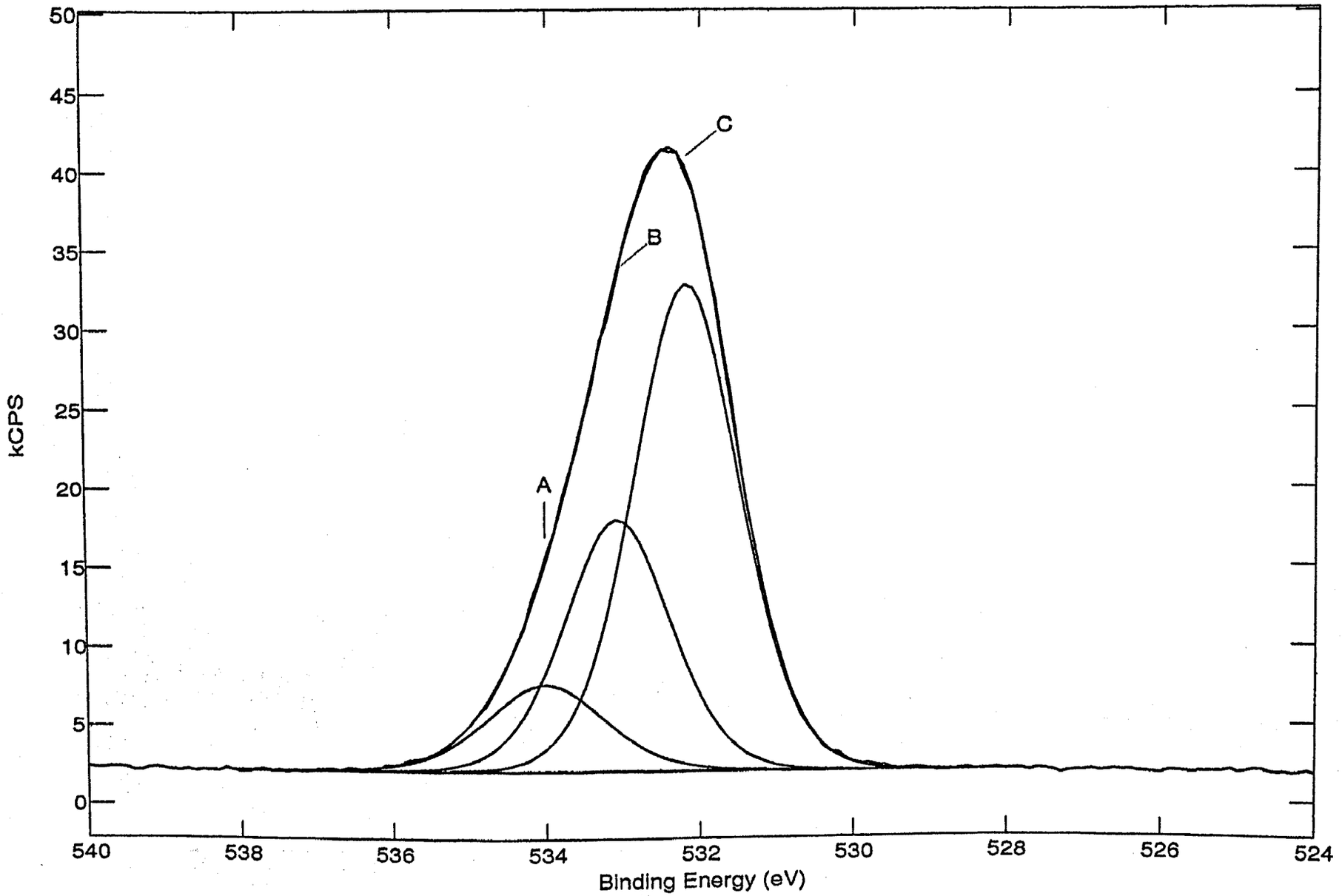

A:\ROUGH\O1S.DTS

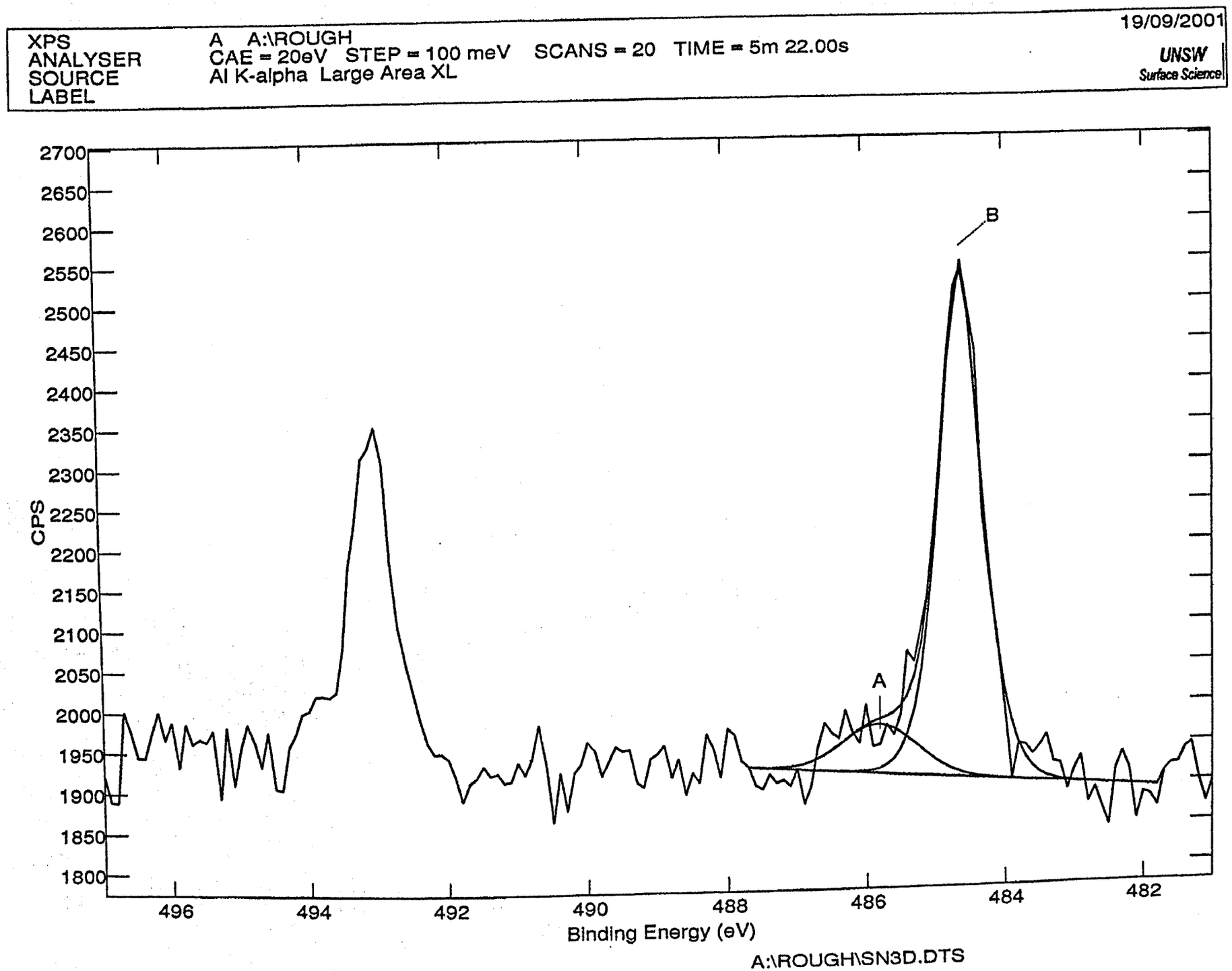
XPS
ANALYSER
SOURCE
LABEL
A A:\ROUGH
CAE = 20eV STEP = 100 meV SCANS = 20 TIME = 5m 22.00s
Al K-alpha Large Area XL
19/09/2001
UNSW
Surface Science
2700
2650
2600
2550
2500
2450
2400
2350
2300
2250
2200
2150
2100
2050
2000
1950
1900
1850
1800
CPS
A
B
496
494
492
490
488
486
484
482
Binding Energy (eV)
A:\ROUGH\SN3D.DTS

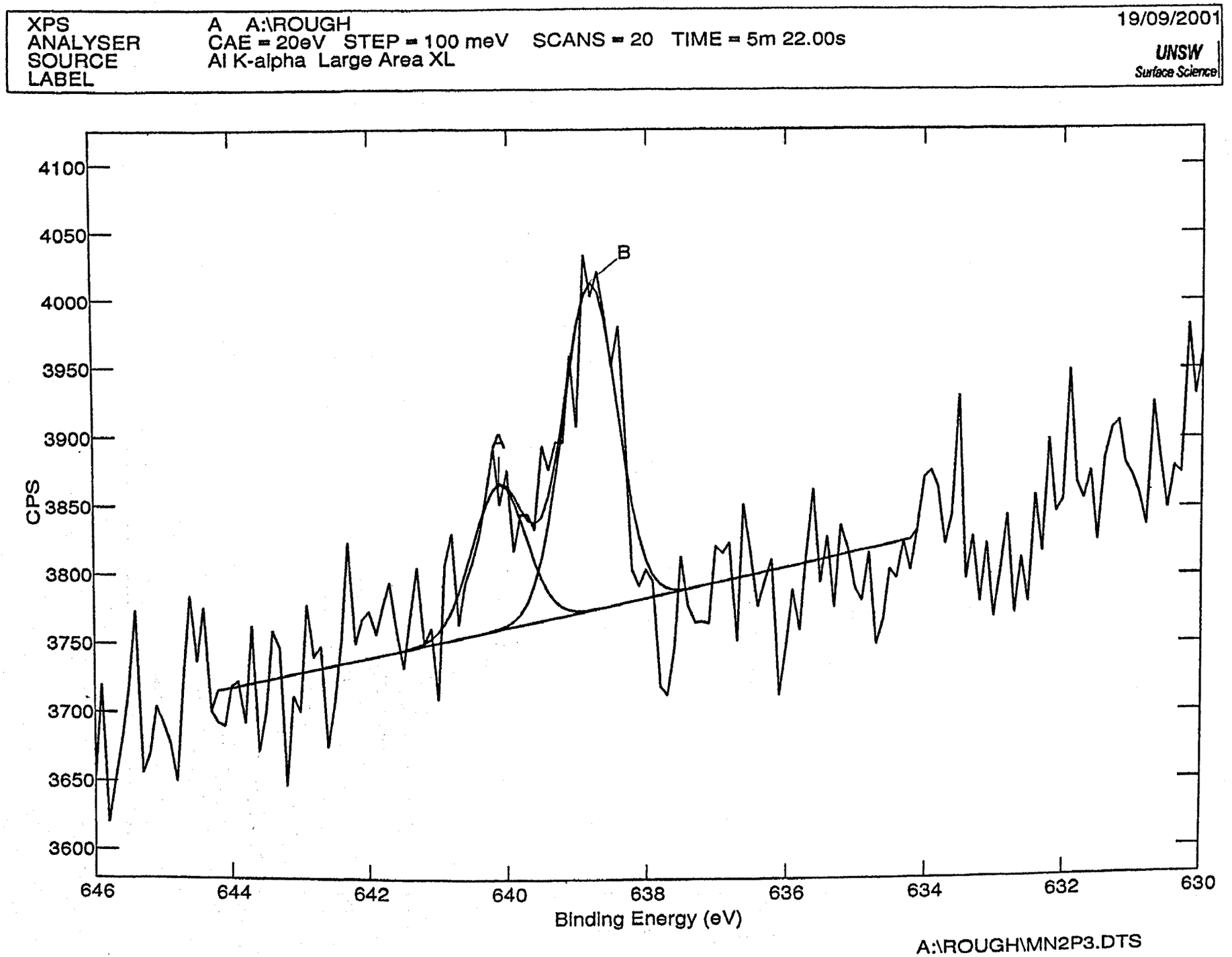
XPS
ANALYSER
SOURCE
LABEL
A A:\ROUGH
CAE = 20eV STEP = 100 meV SCANS = 20 TIME = 5m 22.00s
Al K-alpha Large Area XL
19/09/2001
UNSW
Surface Science
4100
4050
4000
3950
3900
3850
3800
3750
3700
3650
3600
CPS
A
B
646
644
642
640
638
636
634
632
630
Binding Energy (eV)
A:\ROUGH\MN2P3.DTS

XPS	A A:\ROUGH	19/09/2001
ANALYSER	CAE = 20eV STEP = 100 meV SCANS = 20 TIME = 5m 22.00s	UNSW Surface Science
SOURCE	Al K-alpha Large Area XL	
LABEL		

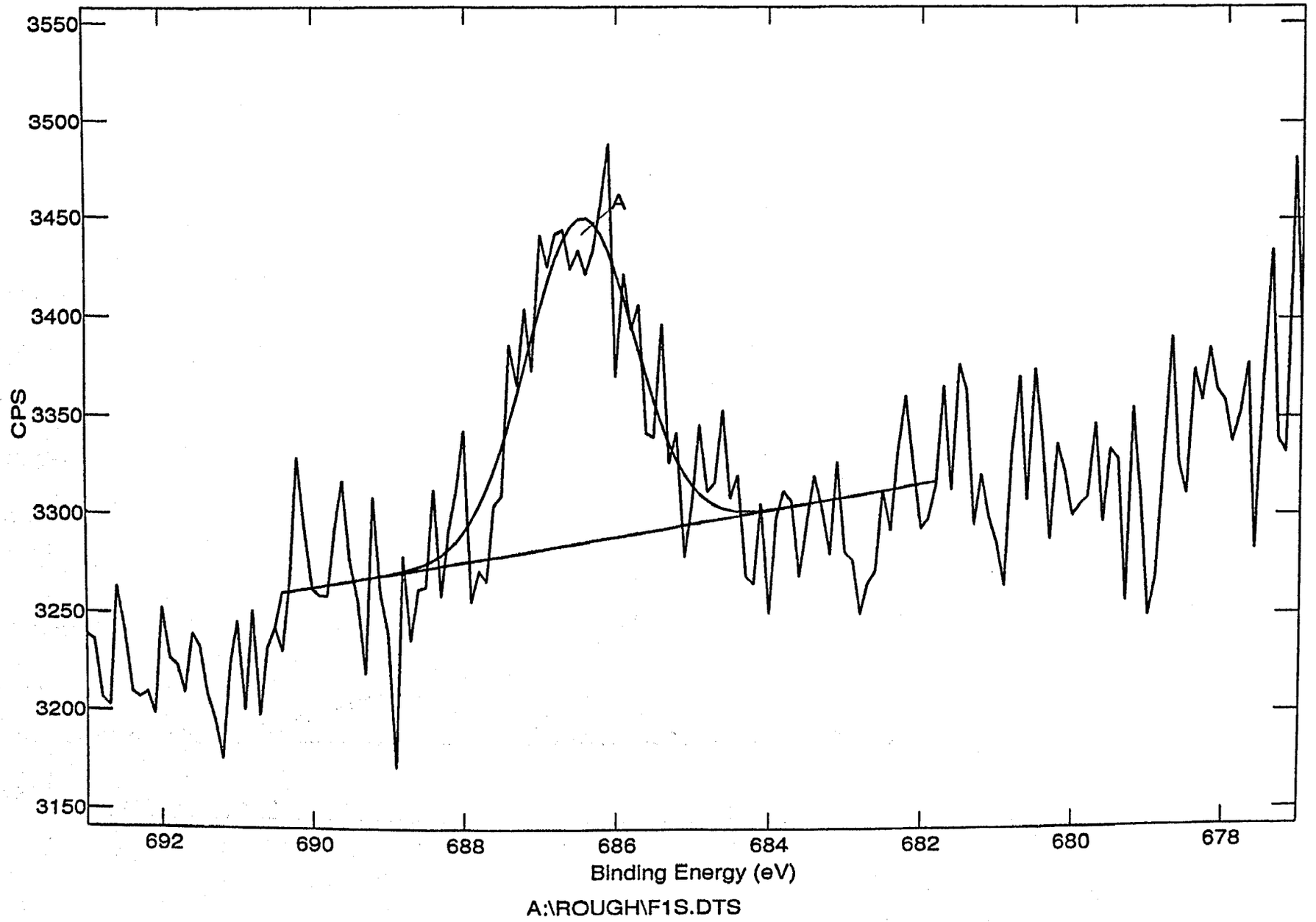

A:\ROUGH\F1S.DTS

XPS	A A:\ROUGH	19/09/2001
ANALYSER	CAE = 20eV STEP = 100 meV SCANS = 8 TIME = 2m 8.80s	
SOURCE	Al K-alpha Large Area XL	UNSW Surface Science
LABEL		

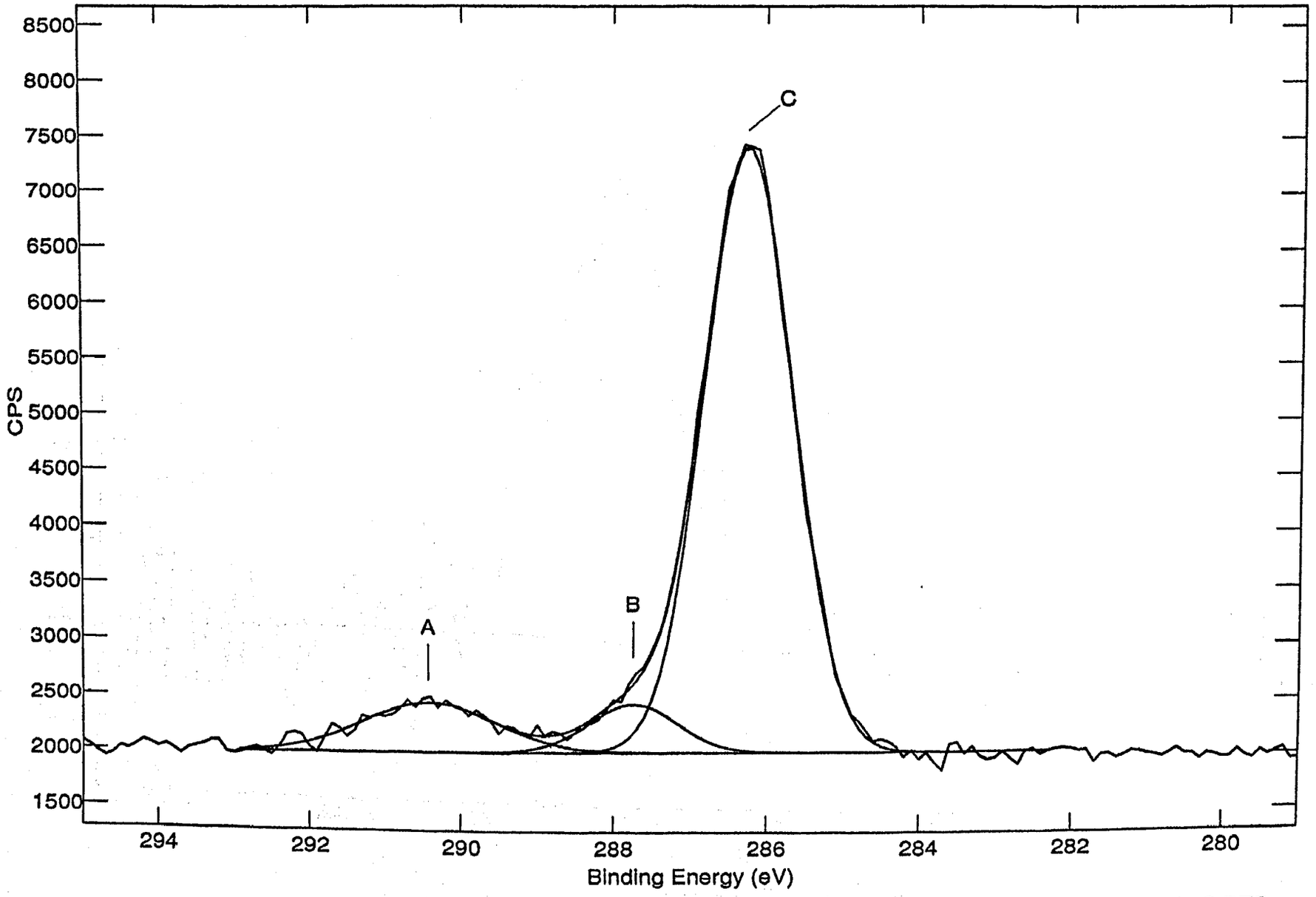

A:\ROUGH\C1S.DTS

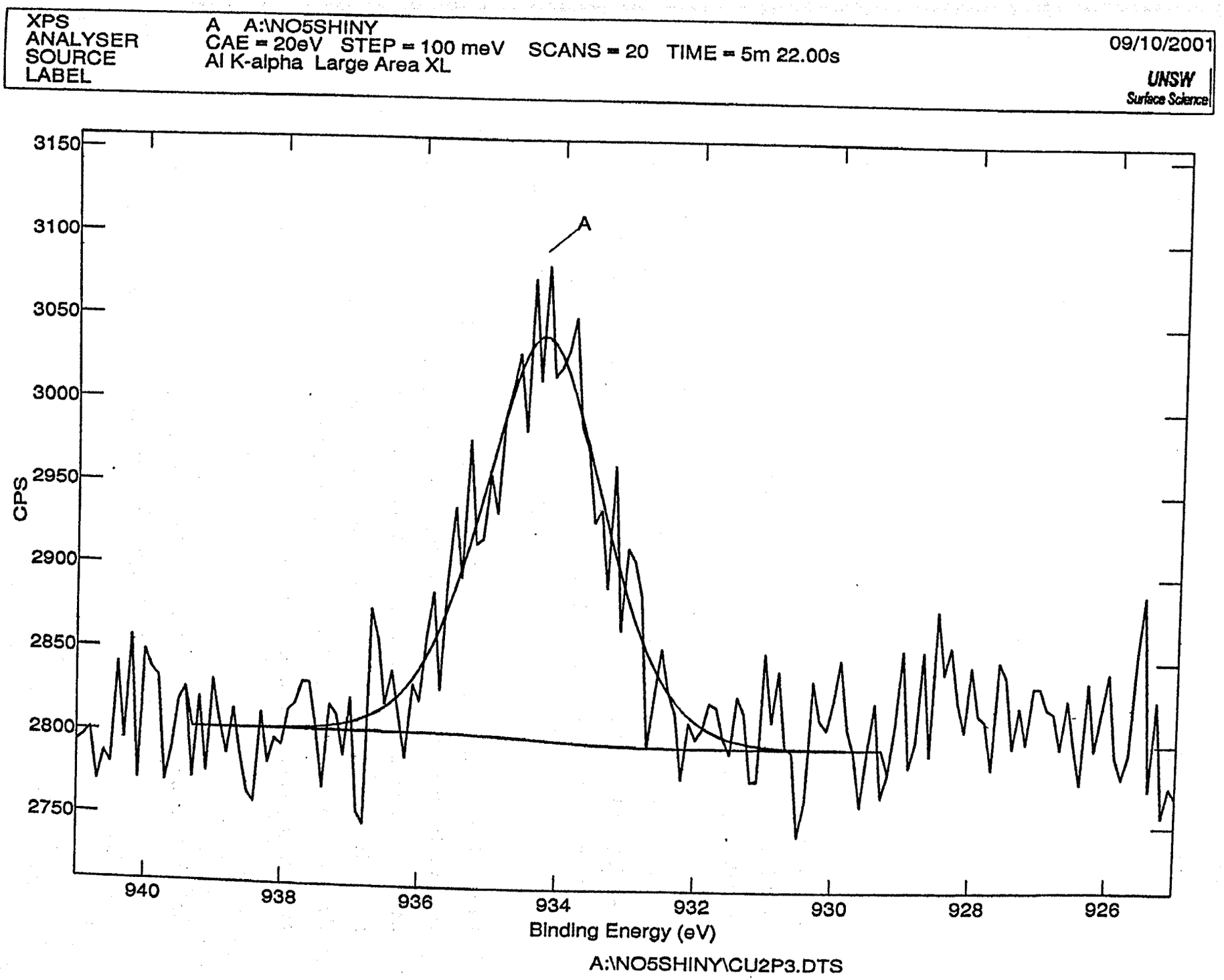
XPS
ANALYSER
SOURCE
LABEL
A A:\NO5SHINY
CAE = 20eV STEP = 100 meV SCANS = 20 TIME = 5m 22.00s
Al K-alpha Large Area XL
09/10/2001
UNSW
Surface Science
A
CPS
3150
3100
3050
3000
2950
2900
2850
2800
2750
940
938
936
934
932
930
928
926
Binding Energy (eV)
A:\NO5SHINY\CU2P3.DTS

APPENDIX 12 RECOVERY AND RECRYSTALLISATION

A. Classification of Phenomena

To fully understand this subject it is necessary to understand the terms used in this area. Recovery and recrystallisation deal with the mechanisms by which metals and alloys repair structural damage caused by mechanical deformation, resulting in changes in physical and mechanical property changes. These repair mechanisms are thermally activated and thus the material has to be heated. This is termed *annealing*[26].

The term *recovery* is often applied in two senses. The first is the partial restoration of physical and mechanical properties to the original values equal to that before deformation. The second embraces all changes all changes that do not involve the sweeping of the deformed structure by migrating high-angle grain boundaries. The structure remains but the density and distribution change. Stresses resulting from metal-working processes are called *residual stress* and are removed by heat-treatment. When the stress is uniform over long distances they are termed *long-range* and their removal is termed *stress-relief*[26] .

Recrystallisation involves the alteration of the grain structure in a deformed material through the passage of high-angle grain boundaries through the material. *Primary recrystallisation* entails the *nucleation* of new grains, often at the grain boundaries. These grains then *grow* until all the deformed structure is consumed. The grain boundaries then continue to uniformly migrate with this referred to as *grain growth.* If some grains grow very large due to selective boundary migration, the term *secondary recrystallisation* is used[26] .

When a reference state is fully recrystallised and the material contains none of the original grains, the term *fully annealed* is applied.

B. Recovery

When a material is worked, part of the energy expended during deformation is stored within the material as defects. Except at very low temperatures, many of the point defects anneal out, with the principal remaining defects usually as dislocation pairs. Any low dislocation densities associated with the deformation are due to the ease of cross slip, climb, and dislocation unpinning at nodes[41].

The mechanical properties alter during deformation, and subsequent annealing at elevated temperatures partially restores the properties back to original values by dislocation climb and rearrangement. This is termed *static recovery (SRV).* If the softening process occurs during deformation, *dynamic recovery (DRV)* is said to occur. The initial rate of recovery softening is quick at first but slows with time. This effect can be accelerated and the total degree of recovery enhanced if the anneal is applied under strain, be it artificially induced or an operational consequence such as creep or fatigue[26].

SRV occurs between intervals of deformation leading to a decrease in dislocation density within a region while increasing the neighbouring sub-boundary density, as well as a corresponding small decrease in flow stresses. In DRV, dislocations are annihilated and rearranged into neatly arrayed low energy walls that are defined polygonised subgrains. Under rapid deformation conditions, the process is most pronounced in FCC metals, especially aluminium, due to their high stacking-fault energy in which dislocation is rapid[26].

SRV can assist in nucleation by reducing the dislocation density while increasing neighbouring sub-boundary density, whereas DRV keeps the sub-boundary density and spacing as well as the internal subgrain density constant hindering recrystallisation. Table A compares dynamic to static recovery[42].

The mechanism of microstructural recovery in aluminium is termed *Polygonisation*. In polygonisation the crystal breaks up into a number of strain-free subgrains, each preserving the local orientation of the original bent crystal. This process requires thermal activation and determines the rate of polygonisation. A detailed survey of the mechanism and kinetics of polygonisation is found in a review by Hibbard and Dunn[43].

DRX	*SRX*
Mechanisms of DRX (when $\varepsilon \geq \varepsilon_{cd}$ and $\sigma \geq \sigma_c$) and SRX (after $\varepsilon \geq \varepsilon_{cs}$) are similar: (i) Nucleation at critical microstructural features (only one cell out of 10^3–10^6 in the substructure) which consist of (a) a mobile boundary possibly formed from a wall of high ρ_s and ϕ_s by thermally activated spreading or absorption of dislocations and (b) an adjacent volume of very low ρ_s (ii) Growth dependent on difference between the energy in the interior and that in the surrounding substructure	
Both are accelerated (grain size decreased) by a less recovered substructure with more deformation, micro and shear bands related to decreased stacking fault energy and particles of 0.6 μm or larger	
Retarded by concurrent strain which builds a substructure in the growing deforming grains, reducing the differential driving force	Even though SRV aids nucleation by enlarging low ρ_s regions and ϕ_s, SRX is retarded by SRV of substructure, reducing the driving force
DRX grains stop growing because of the internal substructure. New wave of DRX follows	SRX growth stops on impingement and complete consumption of substructure. Grain growth follows
Nucleation starts as ε or σ increase to critical ε_{cd} or σ_c, as θ decreases	Nucleation is faster when ε or σ are higher and θ lower ($\varepsilon_{cs} \geq \varepsilon_{cd}$)
After deformation, DRX nuclei continue to grow (metadynamic recrystallization) but soften fully only after the steady state region	After DRX has started, SRX still nucleates after straining is stopped until steady state is reached
Accelerated by increasing $\dot{\varepsilon}$ (finer grain size); ε_{cd} increased, becoming greater than or equal to ε_s and so no DRX	Accelerated by increasing $\dot{\varepsilon}$ and ε up to ε_s or to ε_{cd} (reduced SRV)
Retarded by decreasing $\dot{\varepsilon}$ because of increasing DRV until, in creep, $\varepsilon_{cd} \geq \varepsilon_s$	Similarly retarded, ε_{cs} becomes much greater than or equal to ε_s
If near ε_{cd} or σ_c, stress relaxation causes but stress decrease inhibits DRX	Enhanced by stress relaxation delaying SRV but retarded by $\sigma \leq \sigma_d$
Accelerated by increasing T_d even though DRV increases and ε_{cd} decreases more rapidly. As T_d decreases, ε_{cd} increases rapidly	Accelerated by increasing $T_d = T_m$. At fixed T_m, decreasing T_d reduces DRV and decreases ε_{cs}
No DRX in Al since $\varepsilon_s < \varepsilon_{cd}$	Delayed by lower T_m, enhancing SRV

Table A - Comparison of Dynamic and Static Recovery[42]

The amount of recovery is a function of the kinetics of recovery, time, temperature, and the nature of the material itself. Complete recovery generally occurs only in lightly deformed crystals, with greater deformation resulting in less property change and hence less recovery. The most important parameter that affects the extent of recovery is the stacking-fault energy. This parameter affects the extent to which dislocations dissociate, determines the rate of dislocation climb and is generally the rate-controlling process during recovery. In metals and alloys with high stacking-fault energy such as aluminium and iron, climb is significant and significant recovery can occur[26].

Particles such as $MnAl_6$ reduce recovery by pinning dislocations in the walls and by locking the subgrain boundary nodes. SRV slows as strain energy diminishes during annealing, but DRV rises with decreasing strain, increasing temperature and stacking fault energy until it balances strain hardening interactions[26].

C. Recrystallisation

Introduction

Recrystallisation in aluminium alloys has been the subject of much investigation through the years, with importance being placed on control of grain size, properties and texture. Unlike recovery, recrystallisation causes the mechanical and physical properties of the deformed metal to return completely to that of the annealed state, but at a much quicker rate than recovery[26].

The grain size is a balance between nucleation and growth rates, increasing with work-hardening and temperature respectively. As most nuclei form at or near grain boundaries, smaller original grain size enhances nucleation. In aluminium, lightly strained fine grained samples are either heated very slowly or passed slowly through a sharp temperature gradient to induce nucleation. Grain spacing below 2nm impede rather than assist recrystallisation nucleation[26] .

Constituents play an important role in grain size control, with coarse widely spaced constituents promoting fine grain structures on recrystallisation. Subgrains form at lattice rotations within the metal matrix and have a highly misorientated random alignment making them effective recrystallisation nuclei sites[31].

Dispersoids or second phase particles have the opposite effect to constituents. Grain size is increased due to fine particles acting as pinning points for the low angle subgrain boundaries stabilizing the structure impeding subgrain growth. Similar detrimental effects occur when precipitation and recrystallisation occur concurrently, with the relative kinetics of each determining the influence of precipitation on recrystallisation. If precipitation occurs before recrystallisation, cell walls and subgrain boundaries inhibit the formation of nuclei yielding large recrystallized grains. If the reverse occurs then interference is minimal[31,26].

Solute elements have a strong influence on recrystallisation. The effects of additions up to 1% for Cu, Si, Fe, Mn, Mg, and Zn have all been studied. Fe and Mn rapidly reduce the amount of recrystallisation, Cu and Si have little effect, and Zn and Mg tend to accelerate recrystallisation. Generally the addition of solute elements increase recrystallisation temperature, but at the same time decreases the tendency for DRV. This apparently contradictory statement is not fully understood[32].

Nucleation Models

The nature of the nucleation process has been argued and discussed many times over the last few years, with the major obstacle being the difficulty in observing a nucleus under a microscope. In recent years, various methods have been developed to overcome this problem. All indicate that the mechanism of nucleation is intimately linked with the structure of the deformed metal, and more specifically the degree of heterogeneity of orientation within each deformed grain[26] .

Metallographic evidence has established that nuclei are formed in regions where the dislocation concentration and strain hardening are greatest. A certain local concentration of elastic energy described at threshold strain is required to bring about a nucleus, with the process of nucleation being thermally activated[26] .

Many models that account for nucleation have been developed in recent years. From studies on aluminium, iron and copper it would appear that moderate degrees of deformation favour coalescence as the initial process for turning a subgrain into a nucleus[44,45].

Coalescence of neighbouring subgrains involves the 'evaporation' of the dislocations constituting the sub-boundaries between them, involving both slip and glide. One subgrain grows substantially larger than its neighbours resulting in a steep orientation gradient. The enlarged subgrains act as a nucleus growing at their neighbour's expense with nucleation taking place predominantly at grain boundaries and at deformation bands, Figure A[46].

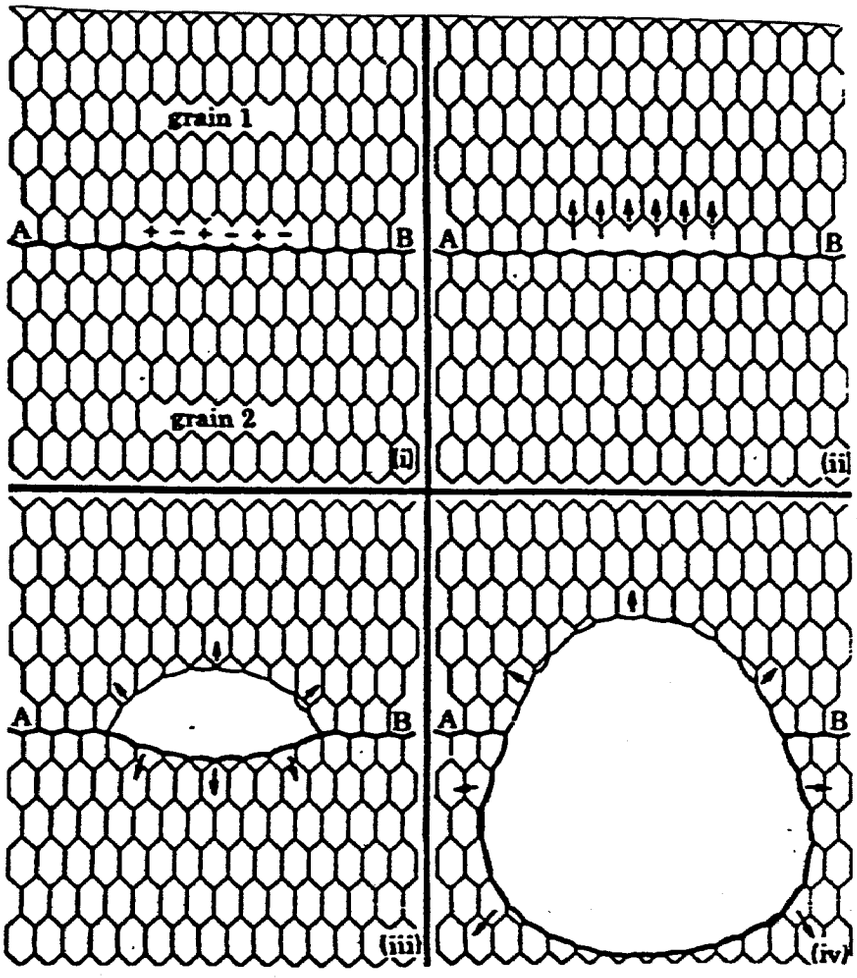

Figure A - Nucleation Involving Subgrain Coalescence[26]

The nucleation stage requires the formation of a critical-sized, strain-free subgrain with a higher mobility boundary. Formation and growth of subgrains will occur throughout the deformed material by recovery process. The most critical feature for the formation of a successful nucleus is the formation of a high mobility boundary. This requires that subgrains form within a region in which local severe gradients in orientation are present. Large constituent particles very effectively introduce such lattice rotations during deformation. Subgrains forming in this region are, compared to the rest of the deformed matrix, highly misorientated and random. This is commonly referred to as particle simulated nucleation (PSN)[46].

D. Dynamic Recrystallisation (DRX) versus Static Recrystallisation (SRX)

In dynamic recrystallisation, a large number of dislocations are eliminated by the migration of high angle boundaries. This only occurs when dislocation density reaches such high levels that recrystallisation occurs. DRX is the predominant softening mechanism in the hot working of all FCC metals, as well as aluminium.

Static recrystallisation occurs after deformation and is found to follow the Johnson-Mehl equation. Johnson and Mehl 1939 developed a relationship for the fraction recrystallized in a given time using the terms N, the rate of nucleation, and G, the rate of growth of the recrystallisation nuclei. Independently, Avrami and Kolmogorov also developed a similar theory at around the same time. Collectively this theory is known as the JMAK theory and is used to describe SRX[47].

$$f(t)=1-\exp(-(\pi/3)NG^3T^4) \qquad (a)$$

Lower temperatures reduce the efficacy of dynamic recrystallisation, until at 320-360 °C reductions greater than 85% result in SRX occurring during the self-annealing stage because of the high energy stored in the alloy[48]. Table B compares SRX and DRX.

The two processes DRX and SRX in aluminium have been carefully compared by McQueen with the conclusion that DRX is constrained by the internal substructure where-as SRX continue to grow until impingement[42]. Increasing strain rate at constant temperature increases minimum strain required for DRX, whilst decreasing minimum strain for SRX. This is due to the rate of strain accumulation that is much higher in SRX. Discontinuous grains nucleate similarly for both SRX and DRX. Particle enhanced nucleation and particle stabilized continuous recrystallisation is possible[42]. For more information on the classification and determination of restoration mechanisms in the hot working of aluminium alloys, see McQueen et.al. and references there-in[49].

DRV (during ϵ)	*SRV (after ϵ)*
Mechanisms of DRV and SRV are similar: dislocation cross-slip, climb, annihilation, rearrangement into orderly arrays; deformation temperature T_d, annealing temperature T_a	
Higher level is more polygonized: larger subgrains, *i.e.* d_s, lower density, more regular walls, *i.e.* lower ρ_w, and lower interior density ρ_i; increases as the stacking fault energy increases	
Rate defined by the current substructure, T_d, $\dot{\epsilon}$ and external stress. In the steady state regime above ϵ_s, DRV attains constant d_s, ρ_w, ϕ_w, ρ_i and σ_s	Rate defined by current substructure, T_a and the internal stress fields only. In anneal, rate decreases with time as driving force decreases (ρ and ρ_w decrease and d increases)
Makes the substructure uniform, unknitting walls and reknitting elsewhere to maintain an equiaxed substructure with the dimensions dictated by stress	Stage 1: fairly homogeneous reduction in wall and interior density. Stage 2: heterogeneous rise in d_s and ϕ_w under local driving forces
DRV at T_d gives higher polygonization than cold work plus anneal at T_d	In holding at T_d after hot working, SRV greatly softens the DRV substructure
Reduced stress causes DRV to be greater and more uniform than SRV	Stress relaxation reduces recovery compared with SRV (with $\sigma = 0$)
A low θ usually associated with a high average DRV but does not reveal the degree of heterogeneity	SRV during unloaded interval decreases σ and increases θ on reloading (thus a high θ associated with high recovery state)

Table B Comparison of Dynamic and Static Recrystallisation[42]

E. Particle Effects

Particles in metallic matrixes are usually divided into groups based on size and distribution. Coarse particles are defined as having a diameter greater than 1μm, fine particles are less than 1μm. Dispersion is based on the nearest-neighbour particle centre-to-centre distance[50].

The effects of second phase particles on primary recrystallisation, often termed Particle Stimulated Nucleation (PSN) has been reviewed in recent years by many workers such as Humphreys, Hansen and Bay, and Doherty and Martin[51,52,53]. The key conclusions are as follows;

i) Acceleration of recrystallisation occurs when large particles are present. The deformation zone around the large particle has a higher stored energy and larger misorientations than in the matrix. Higher particle density results in smaller recrystallised grain sizes.

ii) Retardation of recrystallisation occurs in the presence of fine particles where the mean spacing (Δ_3) is of the order of the sub-grain size. Fine dispersions retard sub-grain coarsening inhibiting nucleation.

iii) Nucleation originates in the deformation zone, but not always at the particle/matrix interface. Nucleation occurs by a rapid polygonisation process involving sub-boundary migration.

iv) Particles barely affect the growth of recrystallised grains, suggesting that retardation of recrystallisation is largely a consequence of the inhibition of nucleation implying further that particles affect the final grain size, depending on nucleation rates.

Factors Affecting PSN

There are many factors that affect particle role in primary nucleation. The major factors are outlined below,

a) The Deformed State

Particle size has been shown to affect the sites at which nucleation occurs. Alloys with particles less than 0.1μm have a much lower rate of recrystallisation nucleation than single phase alloys. Humphreys believed that this was due to more homogenous slip in alloys leading to fewer sites for nucleation[54]. Large particles stimulate recrystallisation nucleation with lattice rotations believed to be the nucleation mechanism[51].

Particles that deform with the matrix have been shown to affect recrystallisation behaviour via inhomogeneous slip. In non-deformable particles, Ashby demonstrated that geometrically necessary dislocations are generated at the particles[55]. Distribution of dislocations is a function of particle size and strain as shown in figure B[53]. The two criteria for growth beyond the nucleus into the deformation zone are sufficient misorientation in the deformation zone and the driving force for nucleation must be sufficient for the nucleus to grow.

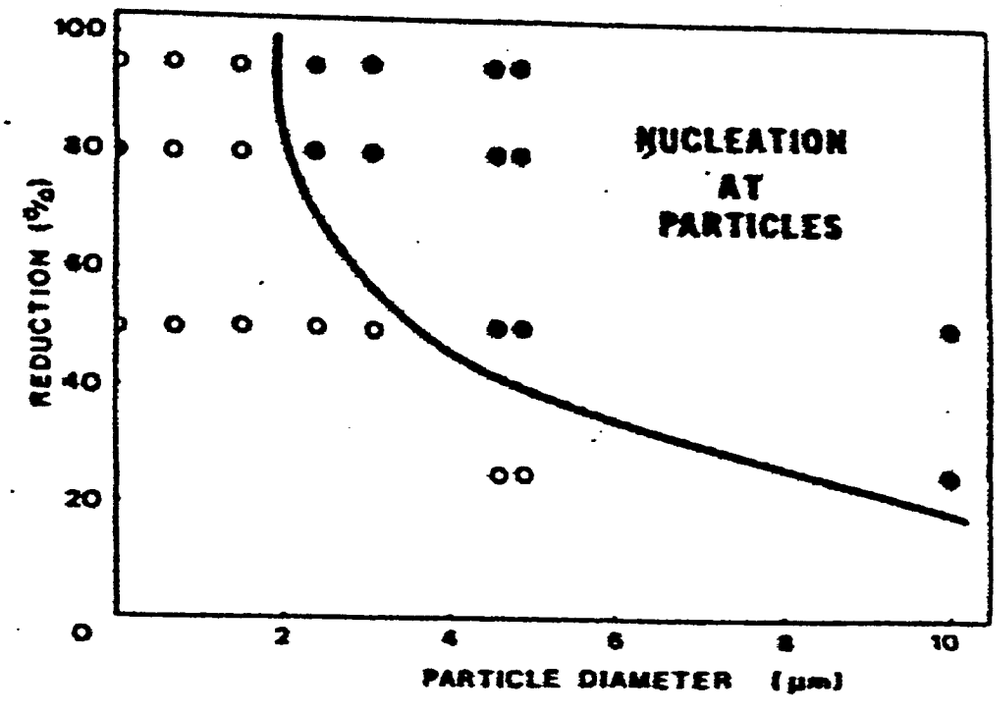

Figure B Conditions of Strain and Particle Size for which PSN occurs in Al-Si [51]

Deformation temperature has been shown to affect the formation of the deformation zone and growth of the nucleus beyond the particle. Humphreys and Kalu showed that critical strain rate is dependent on temperature, with dislocations able to climb around particles without forming deformation zones[56].

b) Particle Distributions

A recent study in the distribution of critically size particles in an aluminium matrix showed that nucleation is preferred at sites of particle clustering[57]. Large particles with small spacings inhibit recrystallisation by particle pinning effects. A retarding force referred to as Zener drag arises from the reduction in interface energy that occurs when a particle is situated on a boundary[58].

Many commercial alloys contain both large and small particles. Fine dispersions will tend to pin grain growth, reducing the driving for recrystallisation, whilst large particles stimulate nucleation. Recent work by Lloyd on aluminium-magnesium and A-A 5083 concluded that in the Al-Mg alloy, low particle contents resulted in nuclei developing from sub-grains that grow in high deformation regions[59]. In A-A 5083 particles larger than 1μm are effective as nuclei with finer dispersoids inhibiting the growth of new grains. In the alloys, shear bands are not a major source of nucleation.

REFERENCES

[1] Personnel communication with Ray Hamilton, Superintendant technical support, AARP 20th November 2003

[2] J.A. Treverton and M.P. Thomas, "Surface Contaminants on annealed aluminium foil and their effects on adhesion," Int. J. Adhesion and Adhesives, 9, 4, Oct. 1989

[3] T.L. Williams, "Some Studies of the Annealing Behaviour of Coiled Light Gauge Aluminium Foil", Thesis – University of New South Wales, 1992

[4] J. D. Andrade, "Surf. And Interf. Aspects of Biomed. Polymers", Vol. 1, Plenum Press NY, Chap. 5, 1985.

[5] A.J. Swift, "Modern Surface Analysis in Materials Science," Metals and Materials, pp. 688-692, Nov. 1988.

[6] J.F. Moulder, W.F. Stickle, P.E. Sobol, and K..D. Bomben, "Handbook of X-ray Photoelectron Spectroscopy", Ed. By J. Chastain and R.C. King jr, Pub. By Physical Electronics, Inc., 6509 Flying Cloud Drive, Eden Prairie, Minnesota 55344, USA.

[7] Internal Memo – M. Mansell, "Increased rolling speeds", 5th June 2002

[8] Personnel corrspondance with the Department of Surface Chemistry – NSW, and Department of Physics – UTS.

[9] British Patent Specification 1479429

[10] J. D. Livingston in "Material Science Engineering", Vol. 7 (1971), pages 61-70.

[11] British Patent Specification, 3,989,548; "Aluminum Alloy Products and Methods of Preperation", Figure 3.

[12] Personnel correspondence on acceptance of AA8150 registration - The Aluminium Association, June 8, 1998

[13] Personnel communication – Tom Rouns, Principle Metallurgist, ATC

[14] European Patent Specification, EP 0 750 685 B1, "Aluminium Foil", 17th March 1995

[15] Mondolfo, L.F., Aluminium Alloys: Structure and Properties, Butterworths, London 1976.

[16] Mansell, M., "Erickson Test Operation", Internal document – SOP, 2002

[17] Personnel correspondance with Dr Jennifer Russell – UNSW Dept of Surface Chemistry

[18] D.T. Clark and K.C. Tripathi, "ESCA Studies of Surfaces of Aluminium Foil", Nature Phys. Sci., 244, 135, 77-78, July 1973

[19] L.R. Morris, J.D. Thomson, "Producing Improved Metal Alloy Products (Al-Fe Alloy and Al-Fe-Si Alloy)", Alcan Int. Ltd., United States Patent No: 632091, 14th November 1975.

[20] L.R. Morris, "Aluminum Alloy Products and Methods of Preperation", Alcan Int. Ltd., United States Patent No: 471133, 17th May 1974.

[21] G.J Mahon, G.J. Marshall, R.A. Ricks, "ALUMINIUM FOIL", ALCAN INT. LTD., European Patent Specification EP 0 750 685 B1, 11th November 1998

[22] R.G. Hamerton, H. Cama and M.W. Meredith., "Development of the course intermetallic particle population in Wrought Aluminium Alloys During Ingot Casting and Thermo-mechanical Processing", Materials Science Forum Vols. 331-337 (2000), pp. 143-154

[23] R.G. Hamerton, H. Cama and M.W. Meredith., "Development of the course intermetallic particle population in Wrought Aluminium Alloys During Ingot Casting and Thermo-mechanical Processing", Materials Science Forum Vols. 331-337 (2000), pp. 143-154

[24] British Patent Specification 1479429

[25] Internal Document, S. Baumann, "Foil for Soft Packaging Laminate Composites".

[26] Cahn, R. W., "Recovery and Recrystallisation", Physical Metallurgy Vol. 2, North-Holland Physics Publishing, Oxford, 1983.

[27] Martin, J. W., Micromechanisms in Particle-hardened Alloys, Cambidge University Press, Sydney, 1980. Pp.151-164

[28] Humphreys, F. J., "The Nucleation of Recrystallisation at Second Phase Particles in Deformed Aluminium", Acta Met. 25 (1977), 1323

[29] Hansen, N. and Bay, B., "Initial Stages in Aluminium Containing Both Large and Small Particles", Acta Metall., 29, (1981) 65

[30] Doherty, R. D. And Martin, J. W., "The Effect of a Dispersed Second Phase on the Recrystallisation of Al-Cu Alloys", Journal Inst Met., 91, 332, (1962)

[31] Aluminium Alloys - Their Physical and Mechanical Properties, Vol 3, Non-Heat-Treatable Aluminium Alloys edited by Starke, E.A. and Sanders, T.H. Engineering Materials Advisory Services, Warley, U.K., 1986.

[32] Blade, J.C., "Recrystallisation in Hot Rolling of Dilute Aluminium Alloys", in Metal Science, March-April 1979.

[33] R.E. Sanders Jr, S.F. Baumann and H.C. Stumpf., "Wrought Non-Heat-Treatable Aluminum Alloys", Treatise on Materials Science and Technology, Vol 31, 1989

[34] Westengen, H., (1982b). Proc. 6th ICSMA, Pergamon Press, New York, Vol 1, pp. 461-466.

[35] Turmezey, T., Stefaniay, V., and Griger, A., "AlFeSi Phases in Aluminium"

[36] Mansell. M., "The Development of Microstructure in AA5182 During Thermomechanical Processing", Thesis, UNSW 1994

[37] Zogg, H., Timm, J., and Warlimont, H., Aluminium 55 (1979) pp. 261

[38] Baumann, S.F., "Foil for Soft Packaging Laminate Composites", internal memo SF-4563, ALCOA Techincal Centre

[39] Mansell, M., "Burst Test Operation", Internal document - SOP, 2002

[40] Personnel correspondance - The Aluminium Association, June 8, 1998

[41] Cherian, T.V., Petrokowsky, P. and Dorn, J.E., "Some observations on recovery of cold worked aluminium", in Transactions of the Metallurgical Society AIME 185: 948-56, 1949.

[42] McQueen, H.J., "Initiating Nucleation of Dynamic Recrystallisation, Primarily in Polycrystals", Material Science and Engineering A,101, 1988, p. 149-160.

[43] Hibbard Jr, W.A., and Dunn, C.G., 1957, Creep and Recovery. Asm, Metals Park, Ohio, p. 52.

[44]Faivre, "Nucleation of Recrystallisation in Compressed Aluminium: Studies by Electron Microscopy and Kikuchi Diffraction", Journal Mat Science 1979

[45] Jones, "Annealing Twinning and the Nucleation of Recrystallationat Grain Boundaries", Journal Mat Science 1981

[46] Hu, Hsun, 1981 in Metallurgical Treatises, Eds J Tien and J. F. Elliott (Met. Soc Aime)p.385

[47] Honeycombe, R. W. K., The Plastic Deformation of Metals, Arnold, 1985.

[48] Barioz, C., Brechet, Y., Legresy, J.M., Cheynet, M.C., Courbon, J., Guyot, P., and Raynaud, G.M., "Recovery of Aluminium-Magnesium Alloys", at the 3rd International Conference on Aluminium Alloys. June 1992.

[49] McQueen, H. J., Evangelista, E., and Kassner, M. E., "The Classification and Determination of Restoration Mechanisms in the Hot Working of Al Alloys", Z. Metall, 1991, H.5, pp. 336-345.

[50] Martin, J. W., Micromechanisms in Particle-hardened Alloys, Cambidge University Press, Sydney, 1980. Pp.151-164

[51] Humphreys, F. J., "The Nucleation of Recrystallisation at Second Phase Particles in Deformed Aluminium", Acta Met. 25 (1977), 1323

[52] Hansen, N. and Bay, B., "Initial Stages in Aluminium Containing Both Large and Small Particles", Acta Metall., 29, (1981) 65

[53] Doherty, R. D. And Martin, J. W., "The Effect of a Dispersed Second Phase on the Recrystallisation of Al-Cu Alloys", Journal Inst Met., 91, 332, (1962)

[54] Humphreys, F. J., "Recrystallisation Mechanisms in Two Phase Alloys", Metal Science, 13, 136, 1979

[55] Ashby, M. F., 1970. "The Deformation of Plastically Non Homogeneous Materials", Phil. Mag. 21, pp.399-424.

[56] Humphreys, F. J., and Kalu, P. N., "Dislocation-Particle Interactions During High Temperature Deformationof Two-Phase Aluminium-Alloys", Acta Metall. 35, 1987, pp.2815

[57] Koken, E., Chandrasekaran, N., Embury, J. D., and Burger, G., "The Role of Particle Distribution in Recrystallisation in Two-Phase Alloys", Mat. Scie. and Engineering., A104, 1988, pp.163.

[58] Nes, E., Ryum, N., and Hundri. O., "On the Zener Drag", Acta Metall. 33,11 (1985)

[59] Lloyd, D. J., The Influence of Particles and Deformation Structure on Recrystallisation, Microstructural Control in Aluminium Alloys Feb 27 1985, Metallurgical Society Ed Chia, E. H., and McQueen, H. J.,1985

[60] Chan, H.M., and Humphreys, F.J. (1984), Acta Met., 32, 235-243